Synchrotron Infrared Microspectroscopy of Biological Tissues: Brain Tissue from TgCRND8 Alzheimer's Disease Mice and Developing Scar Tissue in Rats

Margaret Rak

A thesis submitted to the Faculty of
Graduate Studies of the University
of Manitoba in partial fulfilment of
the requirements of the degree of

Doctor of Philosophy

Department of Chemistry
University of Manitoba
Winnipeg, Manitoba

Copyright © 2007 by Margaret Rak

Abstract

Synchrotron infrared (IR) microspectroscopy, a technique that allows the spatially resolved determination and mapping of multiple components *in situ*, was applied to the study of tissue sections. IR spectra provide information about a sample's chemical composition and conformation, such as the secondary structure of proteins. Bright synchrotron light allowed the high spatial resolution (10 microns) needed for this study. The hypothesis was that the molecular information available from IR microspectroscopy would reveal new information about Alzheimer's disease pathology and scar tissue formation.

The first project involved studying brain tissue from TgCRND8 mice, a transgenic model of Alzheimer's disease (AD), the leading cause of dementia in the ageing population. The main hallmark of AD is the deposition of plaques composed of aggregated amyloid beta (Aβ) peptide in the brain. Dense-cored and diffuse plaques in the hippocampus, cortex and caudate were IR mapped and the results correlated with histochemistry and immunostaining. Spectral analysis confirmed that congophilic plaque cores were composed of protein in a β-sheet conformation, with elevated β-sheet restricted to the core. The amide I maximum of plaque cores was 1623 cm^{-1}; there was no evidence of the high frequency (1680-1690 cm^{-1}) peak seen in *in vitro* Aβ fibrils and attributed to anti-parallel β-sheet. A significant elevation in phospholipids was found around dense-cored plaques in TgCRND8 mice ranging in age from 5 to 21 months. This was due to an increase in cellular membranes from dystrophic neurites and glial cells around the core, but could also contribute to Aβ aggregation through the interaction of newly secreted Aβ with the phospholipids. In contrast, diffuse plaques were not associated with IR detectable changes in protein secondary structure or relative concentrations of other tissue components.

In addition, focally elevated deposits of creatine, a molecule with a crucial role in energy metabolism, were discovered in AD tissue with synchrotron IR microspectroscopy. Both energy metabolism and creatine kinase activity are decreased in AD. The creatine deposits may therefore be a previously undiscovered disease marker.

A second project in this thesis was part of a Natural Sciences and Engineering Research Council Collaborative Health Research Project (NSERC-CHRP) to test the hypothesis that treatment with anti-oxidants, L-2-oxo-thiazolidine-4-carboxylate (OTC) and quercetin, following spinal surgery may reduce oxidative stress, inflammation, and scarring. In humans, excessive formation of scar tissue is the main cause of back pain following spinal surgery. The effect of OTC and quercetin was studied in rats that had undergone laminectomy. Initial synchrotron IR microspectroscopy data were collected on scar tissue from OTC, quercetin and saline (control) treated animals, sacrificed at 3 and 21 days post-surgery (n = 5 per age and treatment group). Scar tissue at 3 days post-surgery was low in collagen, and high in proteoglycans and nucleic acids. The scar tissue at 21 days post-surgery was heterogeneous, containing regions at various stages of development. However, it was marked by the deposition of collagen and a decrease of lipids, due to a reduction in the number of inflammatory cells and fibroblast in the scar. The spectral differences could therefore be correlated with the stages of wound healing. Additionally, the intrinsically polarized synchrotron light was found to affect IR spectra of fibrous 21-day-old scar tissue, rich in oriented collagen. Achilles tendon was therefore studied as a model system of oriented collagen.

List of Published Papers

1. Rak, M., Del Bigio, M. R., Mai, S., Westaway, D., & Gough, K. M. (2007) Dense-core and diffuse Aβ plaques in TgCRND8 mice studied with synchrotron FTIR microspectroscopy. Submitted.

2. Wiens, R., Rak, M., Cox, N., Abraham, S., Juurlink, B. H., Kulyk, W. M., & Gough, K. M. (2007) Synchrotron FTIR microspectroscopic analysis of the effects of anti-inflammatory therapeutics on wound healing in laminectomized rats. Anal Bioanal Chem, 387, 1679-1689.

3. Gallant, M., Rak, M., Szeghalmi, A., Del Bigio, M. R., Westaway, D., Yang, J., Julian, R., & Gough, K. M. (2006) Focally elevated creatine detected in amyloid precursor protein (APP) transgenic mice and Alzheimer disease brain tissue. J Biol Chem, 281, 5-8. (co-first author)

4. Bürklen, T. S., Schlattner, U., Homayouni, R., Gough, K. M., Rak, M., Szeghalmi, A., & Wallimann, T. (2006) The creatine kinase/creatine connection to Alzheimer's disease: CK-inactivation, APP-CK complexes and focal creatine deposits, J Biomed Biotechnol, 2006, 11 pages, available on line.

5. Gough, K. M., Rak, M., Bookatz, A., Del Bigio, M., Mai, S., & Westaway, D. (2005) Choices for tissue visualization with IR microspectroscopy. Vib Spectrosc, 38, 133-141.

6. Gough, K. M., Zelinski, D., Wiens, R., Rak, M. & Dixon, I. M. C. (2003) Fourier transform infrared evaluation of microscopic scarring in the cardiomyopathic heart: Effect of chronic AT_1 suppression. Anal Biochem, 316, 232-242.

List of Abbreviations

AD	Alzheimer's disease
ADDLs	Aβ-derived diffusible ligands
AGAT	L-arginine:glycine amidinotransferase
APP	amyloid precursor protein
ATP	adenoside triphosphate
Aβ	amyloid β peptide
BACE-1	beta-site amyloid precursor protein cleaving enzyme
BB-CK	cytosolic brain-type creatine kinase
BSA	bovine serum albumin
CA	Cornu Ammonis
CD	circular dichroism
CHRP	Collaborative Health Research Project
CK	creatine kinase
Cr	creatine
CRT	creatine transporter
DNA	deoxyribonucleic acid
FAD	familial Alzheimer's disease
FBSS	failed back surgery syndrome
FT-IR	Fourier transform infrared
GABA	gamma-aminobutyric acid
GAGs	glycosaminoglycans
GAMT	S-adenosyl-L-methionine:N-guanidinoacetate methyltransferase
GSH	glutathione
H&E	hematoxylin and eosin
IR	infrared
MCT	mercury cadmium telluride
MRS	magnetic resonance spectroscopy
NFTs	neurofibrillary tangles
NMA	N-methylacetamine
NMR	nuclear magnetic resonance
OTC	L-2-oxo-thiazolidine-4-carboxylate
PBS	phosphate-buffered saline
PCA	principal component analysis
PCr	phosphocreatine
PS1	presenilin 1
PS2	presenilin 2
RNA	ribonucleic acid
ROS	reactive oxygen species
S/N	signal-to-noise
TBS	tris-buffered saline
TGF-β	transforming growth factor β
uMtCK	ubiquitous mitochondrial creatine kinase

Acknowledgements

I would like to thank the following people without whose help and support this thesis would not be possible:

My supervisor, Dr. Kathleen Gough

The past and current members of the research group: Meghan Gallant, Marzena Kastyak, Mandy Ogg, Adriana Shegalmi, Igor Tretiakov, Lsan Tsadzu, Tammy Welshman, Richard Wiens

My advisory committee: Dr. Sabine Mai, Dr. Joseph O'Neil, and Dr. Frank Schweizer
I would like to especially thank Dr. Mai for her help with immunofluorescence

The members of the defence committee: Dr. Benedict Albensi, Dr. Hoi-Ying Holman, Dr. Sabine Mai, Dr. Frank Schweizer, and Dr. Jörg Stetefeld

Everyone in the Chemistry Department

The synchrotron beamline staff
    Dr. Bob Julian (SRC)
    Drs. Lisa Miller, Randy Smith, and Neb Marinkovic (NSLS)

AD Project
    Dr. David Westaway for providing us with the TgCRND8 Mice
    Dr. Marc Del Bigio
    Cheryl Taylor-Kashton for help with immunofluorescence
    Everyone who provided me with valuable technical assistance:
        Sharon Allen, Susan Janeczko, Terry Enno, Dr. Michael Mayne, Dr. Paul Dumas

Scar Tissue Project
        Our collaborators at the University of Saskatchewan: Nicky Cox, Suraj Abraham, Dr. Elizabeth Schultke, Dr. B. Juurlink, and Dr. W. Kulick

Financial Support
        NSERC PGS-A
        University of Manitoba Graduate Fellowship
        McCrorie-West Family Fellowship for Alzheimer Research

My family

Table of Contents

Abstract I
List of Published Papers III
List of Abbreviations IV
Acknowledgements V
Table of Contents VI
List of Figures XI
List of Tables XVI

Chapter 1. General Introduction 1
- 1.1. Infrared Spectroscopy 1
  - 1.1.1. Principles of Infrared Spectroscopy 1
  - 1.1.2. Dispersive Infrared Instruments 4
  - 1.1.3. Fourier Transform Infrared Instruments 5
    - 1.1.3.1 Principles of Fourier-Transform IR Spectroscopy 6
    - 1.1.3.2. Advantages of Fourier-Transform IR Spectroscopy 9
- 1.2. Infrared Microspectroscopy 10
  - 1.2.1. Instrumentation for IR Microspectroscopy 10
  - 1.2.2. Spatial Resolution of IR Microspectroscopy 12
  - 1.2.3. IR Microspectroscopy with a Synchrotron Source 13
- 1.3. Infrared Biospectroscopy 15
  - 1.3.1. IR Spectroscopy of Proteins 17
    - 1.3.1.1. Protein Structure Determination with IR Spectroscopy 19
  - 1.3.2. IR Spectroscopy of Lipids 21
  - 1.3.3. IR Spectroscopy of Nucleic Acids 23
  - 1.3.4. IR Spectroscopy of Carbohydrates 25
  - 1.3.5. IR Spectroscopy and Imaging of Tissues 26
    - 1.3.5.1. Preparation of Tissue Sample for IR Spectroscopy 28
  - 1.3.6. Analysis of IR Map Data 29
    - 1.3.6.1. Spectral Acquisition Parameters and Pre-processing 29
    - 1.3.6.2. Univariate and Bivariate Methods 33
    - 1.3.6.3. Multivariate Methods 33

Part 1. Infrared Microspectroscopy of AD Mouse Brain

Chapter 2. Introduction to Alzheimer’s Disease 36
- 2.1. Alzheimer’s Disease 36
  - 2.1.1. Neuropathology 37
  - 2.1.2. Pathogenesis 39
- 2.2. Aβ Plaques in Alzheimer’s Disease 42
  - 2.2.1. Aβ Plaque Morphology and Terminology 42
  - 2.2.2. Aβ Structure 43
  - 2.2.3. Visualization of AD Plaques 47

2.3. Animal Models of AD 50
    2.3.1. TgCRND8 Mice 51
2.4. IR Spectroscopy of Amyloid 53
    2.4.1. *In Vitro* IR Spectroscopy of Amyloid-forming Peptides 53
    2.4.2. *In situ* IR Spectroscopy of Amyloid 54

Chapter 3. Alzheimer's Disease Study Methods 56
3.1. Outline of the Experiments 56
    3.1.1. Animals 58
    3.1.2. Initial Mapping 59
    3.1.3. Dense-cored Plaques 59
    3.1.4. Plaque Staining 59
    3.1.5. IR Mapping Aided by Immunostaining 60
    3.1.6. Creatine in TgCRND8 Mice 61
3.2. Detailed Experimental Protocols 63
    3.2.1. Tissue Preparation 63
        3.2.1.1. Paraffin-embedded Tissue 63
        3.2.1.2. Frozen Tissue 64
    3.2.2. Congo-red Staining 64
    3.2.3. Immunostaining 65
        3.2.3.1. Immunofluorescence 65
        3.2.3.2. Immunohistochemistry 66
    3.2.4. Fluorescence Microscopy 67
    3.2.5. IR Microspectroscopy 68
        3.2.5.1. IR Data Collection 68
            3.2.5.1.1. Tissue Component IR Spectra 69
        3.2.5.2. IR Spectral Analysis and Data Processing 69
            3.2.5.2.1. Lipids 70
            3.2.5.2.2. Proteins 71
            3.2.5.2.3. Other Peaks 72
            3.2.5.2.4. Hierarchical Cluster Analysis 72

Chapter 4. Alzheimer's Disease Study Results 74
4.1. Overview 74
4.2. Brain Tissue Samples 76
4.3. Histochemistry and Immunohistochemistry 78
4.4. IR Mapping of Brain Tissue 86
    4.4.1. Processing of IR Maps 88
    4.4.2. Spectral Artifacts Associated with Brain Tissue 94
    4.4.3. IR Mapping of the Hippocampus 98
    4.4.4. IR Mapping of Plaques 107
        4.4.4.1. Processing of Plaque Maps 108
        4.4.4.2. Control Data 112
        4.4.4.3. Plaque Core Spectra 115
        4.4.4.4. Comparison of IR Mapping with Congo Red Staining 117
        4.4.4.5. Elevated Phospholipids Surround Dense-Cored Plaques 124

4.4.4.6. Hierarchical Cluster Analysis of Plaque Maps 134
4.4.4.7. Diffuse Plaques 139

Chapter 5. Alzheimer's Disease Study Discussion 149
5.1. IR Spectra Reflect Differences in Tissue Composition 149
5.2. Secondary Structure of Aβ in Plaque Cores 152
5.3. Dense-cored Plaques are Surrounded by Elevated Phospholipids 155
5.4. Diffuse Plaques Are Not Detectable by IR Spectroscopy 156

Chapter 6. Alzheimer's Disease Study Conclusions 158

Chapter 7. Creatine Deposits in AD Mouse Brain 160
7.1. Overview 160
7.2. Introduction 162
7.2.1. The Cr/PCr System 162
7.2.2. Cr/PCr System in the Brain 164
7.2.3. The Cr/PCr System and AD 165
7.2.4. Measurement of Creatine in AD Brain 166
7.3. Methods 168
7.4. Results 169
7.4.1. Identification of the Creatine Deposits 169
7.4.2. Distribution of the Creatine Deposits 173
7.5. Discussion 178
7.6. Conclusions 183

Part 2. Infrared Microspectroscopy of Scar Tissue

Chapter 8. Introduction to the Scar Tissue Study 184
8.1. Overview 184
8.2. Failed Back Surgery Syndrome 187
8.3. Wound Healing 190
8.3.1 Scar Tissue Composition 192
8.3.2. Collagen 192
8.4. Oxidative Stress and Inflammation 194
8.4.1. The Role of Inflammation in Fibrosis 195
8.5. Quercetin 197
8.6. OTC 198
8.7. IR Spectroscopy of Collagen 200
8.7.1. IR Spectroscopy of Collagen-containing Tissues 202
8.7.2. Polarized IR Spectroscopy of Collagen 203

Chapter 9. Scar Tissue Study Methods 205
9.1. Surgery and Treatment 205
9.2. Tissue Harvesting and Preparation 206
9.3. FTIR Microspectroscopy Data Collection 207
9.4. IR Data Analysis 208

9.4.1. Univariate and Bivariate Analysis 208
9.4.2. Hierarchical Cluster Analysis 210

Chapter 10. Scar Tissue Study Results 211
- 10.1. Tissue Samples 211
  - 10.1.1. H & E Stained Scar Tissue 215
- 10.2. IR Mapping of Scar Tissue 217
  - 10.2.1. Normal Muscle Tissue IR Data 217
  - 10.2.2. IR Mapping of Saline-treated 3-Day Post-surgery Scar Tissue 217
  - 10.2.3. IR Mapping of Saline-treated 21-Day Post-surgery Scar Tissue 224
    - 10.2.3.1. Developing Scar Tissue 224
    - 10.2.3.2. Fibrous Scar Tissue 228
    - 10.2.3.3. Wound Tissue Next to Degenerating Muscles 232
  - 10.2.4. IR Mapping of Scar Tissue from Treated Rats 236
    - 10.2.4.1. IR Mapping of OTC-treated 3-Day Post-surgery Scar Tissue 237
    - 10.2.4.2. IR Mapping of OTC-treated 21-Day Post-surgery Scar Tissue 239
      - 10.2.4.2.1. Developing Scar Tissue 239
      - 10.2.4.2.2. Fibrous Scar Tissue 241
      - 10.2.4.2.3. Wound Tissue Next to Degenerating Muscles 243
    - 10.2.4.3. IR Mapping of Quercetin-treated 3-Day Post-surgery Scar Tissue 245
    - 10.2.4.4. IR Mapping of Quercetin-treated 21-Day Post-surgery Scar Tissue 247
      - 10.2.4.4.1. Developing Scar Tissue 247
      - 10.2.4.4.2. Fibrous Scar Tissue 249
      - 10.2.4.4.3. Wound Tissue Next to Degenerating Muscles 251
- 10.3. The Effect of Polarized Synchrotron Light on Scar Tissue Spectra 253
  - 10.3.1. Polarized IR Spectra of Achilles Tendon 255

Chapter 11. Scar Tissue Study Discussion 260
- 11.1. Comparison of 3-Day and 21-Day Data 260
  - 11.1.1. Phosphate Stretch Region 261
  - 11.1.2. Amide I Band 262
  - 11.1.3. CH Stretch Region 264
- 11.2. IR Spectra Reflect the Molecular Composition of Scar Tissue 266
- 11.3. IR Spectra Can be Related to the Stages of Wound Healing 269
- 11.4. OTC and Quercetin-treated Scar Tissue 270
- 11.5. Effect of Polarized Synchrotron Light on Oriented Samples 271

Chapter 12. Scar Tissue Study Conclusions 273

Chapter 13. Summary and Future Work 275
- 13.1. Summary 275
- 13.2. Future Work 281
  - 13.2.1. Alzheimer’s Disease Project 281

13.2.2. Scar Tissue Project 282

Chapter 14. Appendix 1. IR Maps of Dense-cored Plaques 283

Chapter 15. Appendix 2. Additional Mouse Information 316

References 317

List of Figures

Figure 1.1. The Michelson interferometer 5
Figure 1.2. Fourier transform of monochromatic light. 7
Figure 1.3. Interferogram and spectrum. 8
Figure 1.4. The IR microscope. 11
Figure 1.5. Protein IR spectrum. 17
Figure 1.6. Phospholipid IR spectra. 22
Figure 1.7. Nucleic acid IR spectra. 24
Figure 1.8. Carbohydrate IR spectra. 25
Figure 1.9. The effect of spectral smoothing. 31
Figure 2.1. AD neuropathology. 38
Figure 2.2. Schematic of the amyloid precursor protein. 39
Figure 2.3. Aβ fibril. 45
Figure 2.4. The structure of the amyloid dye Congo red. 48
Figure 4.1. Morphology of a sagittal mouse brain section. 77
Figure 4.2. AD pathology in TgCRND8 mice. 78
Figure 4.3. Anti-Aβ immunofluorescence in 5-month-old TgCRND8 mouse. 80
Figure 4.4. Anti-Aβ immunofluorescence in 11-month-old TgCRND8 mouse. 81
Figure 4.5. Dense-cored plaques surrounded by diffuse Aβ haloes. 82
Figure 4.6. Hippocampal plaque load in TgCRND8 mice. 84
Figure 4.7. Variability of plaque morphology in TgCRND8 mice. 85
Figure 4.8. Representative IR spectrum of neuropil tissue in the cortex of a control mouse. 87
Figure 4.9. Univariate processing of an IR map. 89
Figure 4.10. Bivariate processing of an IR map. 91
Figure 4.11. Hierarchical cluster analysis. 92
Figure 4.12. Saturated plaque core spectrum. 94
Figure 4.13. Baseline distortion in plaque core spectra. 95
Figure 4.14. Spectral artifacts in IR spectra near plaque edges. 95
Figure 4.15. Spectral artifact from control tissue, where amyloid plaques are absent. 96
Figure 4.16. White matter spectra with distorted baselines. 97
Figure 4.17. A typical hippocampus from an 11-month-old TgCRND8 mouse. 99
Figure 4.18. A typical hippocampus from a 5-month-old TgCRND8 mouse. 100
Figure 4.19. A typical hippocampus from an 11-month-old control mouse. 101
Figure 4.20. A typical hippocampus from a 5-month-old control mouse. 102
Figure 4.21. An IR map in the hippocampus of a 5-month-old control mouse. 104
Figure 4.22. An IR map of β-sheet in dense-cored plaques. 109
Figure 4.23. Total integrated absorbance and amide I area. 110
Figure 4.24. CH stretch maps. 111
Figure 4.25. Phosphate stretch maps. 111
Figure 4.26. Representative IR maps in the cortex. 113-114
Figure 4.27. Plaque amide I bands. 116

Figure 4.28. Comparison of plaque sizes from IR mapping and Congo red staining. 118
Figure 4.29. Correspondence of high β-sheet content with Congo red staining. 123
Figure 4.30. Dense-cored plaque from a 5-month-old TgCRND8 mouse. 126
Figure 4.31. Dense-cored plaque from an 11-month-old TgCRND8 mouse. 127
Figure 4.32. Dense-cored plaque from a 14-month-old TgCRND8 mouse. 128
Figure 4.33. Dense-cored plaques from a 16-month-old TgCRND8 mouse. 129
Figure 4.34. Dense-cored plaques from a 17-month-old TgCRND8 mouse. 130
Figure 4.35. Dense-cored plaques from a 21-month-old TgCRND8 mouse. 131
Figure 4.36. Spectra of plaques and their surroundings. 133
Figure 4.37. Cluster analysis on the fingerprint region. 134
Figure 4.38. Cluster analysis on the amide I band. 135
Figure 4.39. Cluster analysis on the amide I and II bands. 136
Figure 4.40. Cluster analysis on the CH stretch region. 136
Figure 4.41. Cluster analysis on the amide I and II bands and the CH stretch region. 137
Figure 4.42. Cluster analysis on the phosphate stretch region. 138
Figure 4.43. Diffuse plaque in the caudate of an 11-month-old TgCRND8 mouse. 141
Figure 4.44. Diffuse plaque in the caudate of a 14-month-old TgCRND8 mouse. 142
Figure 4.45. Diffuse plaque in the caudate of a 16-month-old TgCRND8 mouse. 143
Figure 4.46. Diffuse plaques in the caudate of a 17-month-old TgCRND8 mouse. 144
Figure 4.47. Diffuse plaques in the caudate of a 21-month-old TgCRND8 mouse. 145
Figure 4.48. Control caudate maps. 146-148
Figure 7.1. Creatine structure. 163
Figure 7.2. IR spectra of creatine deposits. 170
Figure 7.3. Creatine deposit in the caudate. 171
Figure 7.4. Cr deposits are not associated with obvious disturbances in the tissue morphology. 172
Figure 7.5. Creatine deposits near dense-cored plaques. 174
Figure 7.6. Creatine deposit in the cortex. 175
Figure 7.7. Association of creatine deposits with blood-vessels and plaque edges. 176
Figure 8.1. The lamina and discs of the spinal cord vertebrae. 189
Figure 8.2. Quercetin. 197
Figure 8.3. OTC. 198
Figure 8.4. The IR spectrum of collagen. 201
Figure 10.1. Tissue section from rat which did not undergo laminectomy. 212
Figure 10.2. Typical unstained scar tissue sections. 214
Figure 10.3. H&E stained scar tissue. 216
Figure 10.4. Wound tissue in saline-treated rat, 3 days after surgery. 219

Figure 10.5. Cluster analysis of 3-day-old wound tissue on the amide I and II bands. 220
Figure 10.6. Cluster analysis of 3-day-old wound tissue on the phosphate stretch region. 222
Figure 10.7. Cluster analysis of 3-day-old wound tissue on the fingerprint region. 223
Figure 10.8. Developing scar tissue in saline-treated rat, 21 days after surgery. 225
Figure 10.9. Cluster analysis of 21-day-old wound tissue on the amide I and II bands. 226
Figure 10.10. Cluster analysis of 21-day-old wound tissue on the phosphate stretch region. 227
Figure 10.11. Cluster analysis of 21-day-old wound tissue on the fingerprint region. 228
Figure 10.12. Fibrous scar tissue in saline-treated rat, 21 days after surgery. 229
Figure 10.13. Cluster analysis of 21-day-old fibrous wound tissue. 231
Figure 10.14. Wound tissue next to degenerating muscle, 21 days post-surgery. 233
Figure 10.15. Cluster analysis of 21-day-old wound tissue next to degenerating muscle. 235
Figure 10.16. Wound tissue in OTC-treated rat, 3 days after surgery. 237
Figure 10.17. Cluster analysis of OTC-treated tissue, 3 days after surgery. 238
Figure 10.18. Developing scar tissue in OTC-treated rat, 21 days after surgery. 239
Figure 10.19. Cluster analysis of OTC-treated developing scar tissue, 21 days after surgery. 240
Figure 10.20. Fibrous scar tissue in OTC-treated rat, 21 days after surgery. 241
Figure 10.21. Cluster analysis of OTC-treated fibrous scar tissue, 21 days after surgery. 242
Figure 10.22. Wound tissue next to degenerating muscle in OTC-treated rat, 21 days post-surgery. 243
Figure 10.23. Cluster analysis of OTC-treated wound tissue next to degenerating muscle, 21 days after surgery. 244
Figure 10.24. Wound tissue in quercetin-treated rat, 3 days after surgery. 245
Figure 10.25. Cluster analysis of quercetin-treated tissue, 3 days after surgery. 246
Figure 10.26. Developing scar tissue in quercetin-treated rat, 21 days after surgery. 247
Figure 10.27. Cluster analysis of quercetin-treated developing scar tissue, 21 days after surgery. 248
Figure 10.28. Fibrous scar tissue in quercetin-treated rat, 21 days after surgery. 249
Figure 10.29. Cluster analysis of quercetin-treated fibrous scar tissue, 21 days after surgery. 250
Figure 10.30. Wound tissue next to degenerating muscle in quercetin-treated rat, 21 days post-surgery. 251

Figure 10.31. Cluster analysis of quercetin-treated wound tissue next to degenerating muscle, 21 days after surgery. 252
Figure 10.32. Effect of polarized synchrotron IR light on 21-day post-surgery scar tissue spectrum. 254
Figure 10.33. IR spectra of Achilles tendon taken with linearly polarized light. 256
Figure 10.34. Tendon spectra taken with orthogonally plane-polarized light. 257
Figure 10.35. Synchrotron IR spectra of Achilles tendon. 258
Figure 11.1. The phosphate stretch region of scar tissue IR spectra. 262
Figure 11.2. The amide I and II bands of scar tissue IR spectra. 263
Figure 11.3. The CH stretch region of scar tissue IR spectra. 265
Figure 14.1. Dense-cored plaques from a 5-month-old TgCRND8 mouse. 283
Figure 14.2. Dense-cored plaque from a 5-month-old TgCRND8 mouse. 284
Figure 14.3. Dense-cored plaque from a 5-month-old TgCRND8 mouse. 285
Figure 14.4. Dense-cored plaque from a 5-month-old TgCRND8 mouse. 286
Figure 14.5. Dense-cored plaque from a 5-month-old TgCRND8 mouse. 287
Figure 14.6. Dense-cored plaque from a 5-month-old TgCRND8 mouse. 288
Figure 14.7. Dense-cored plaques from a 5-month-old TgCRND8 mouse. 289
Figure 14.8. Dense-cored plaque from a 5-month-old TgCRND8 mouse. 290
Figure 14.9. Dense-cored plaque from a 5-month-old TgCRND8 mouse. 291
Figure 14.10. Dense-cored plaque from an 11-month-old TgCRND8 mouse. 292
Figure 14.11. Several dense-cored plaques from an 11-month-old TgCRND8 mouse. 293
Figure 14.12. A dense-cored plaque from an 11-month-old TgCRND8 mouse. 294
Figure 14.13. Several small dense-cored plaques from an 11-month-old TgCRND8 mouse. 295
Figure 14.14. A dense-cored plaque from an 11-month-old TgCRND8 mouse. 296
Figure 14.15. A dense-cored plaque from an 11-month-old TgCRND8 mouse. 297
Figure 14.16. Two dense-cored plaques from an 11-month-old TgCRND8 mouse. 298
Figure 14.17. Several large multicored plaques from an 11-month-old TgCRND8 mouse. 299
Figure 14.18. Dense-cored plaque from a 14-month-old TgCRND8 mouse. 300
Figure 14.19. Dense-cored plaque from a 14-month-old TgCRND8 mouse. 301
Figure 14.20. Dense-cored plaque from a 14-month-old TgCRND8 mouse. 302
Figure 14.21. Dense cored plaques from a 14-month-old TgCRND8 mouse. 303
Figure 14.22. Dense-cored plaque from a 14-month-old TgCRND8 mouse. 304
Figure 14.23. Dense-cored plaques from a 16-month-old TgCRND8 mouse. 305
Figure 14.24. Two-dense cored plaques from a 16-month-old TgCRND8 mouse. 306
Figure 14.25. Dense-cored plaques from a 16-month-old TgCRND8 mouse. 307
Figure 14.26. Dense-cored plaques from a 17-month-old TgCRND8 mouse. 308
Figure 14.27. Dense-cored plaques from a 17-month-old TgCRND8 mouse. 309

Figure 14.28. Dense-cored plaques from a 17-month-old TgCRND8 mouse. 310
Figure 14.29. Dense-cored plaques from a 17-month-old TgCRND8 mouse. 311
Figure 14.30. Dense-cored plaques from a 21-month-old TgCRND8 mouse. 312
Figure 14.31. Dense-cored plaques from a 21-month-old TgCRND8 mouse. 313
Figure 14.32. Dense-cored plaques from a 21-month-old TgCRND8 mouse. 314
Figure 14.33. Dense-cored plaques from a 21-month-old TgCRND8 mouse. 315

List of Tables

Table 1.1. Assignments of peaks in IR spectra of tissues 16
Table 3.1. Processing parameters used for brain IR maps 70
Table 3.2. Spectral regions used for hierarchical cluster analysis of brain tissue 73
Table 4.1. Comparison of dense-cored plaque size by Congo-red staining and IR microspectroscopy 119-121
Table 9.1. Processing parameters used for scar tissue IR maps 209
Table 9.2. Spectral regions used for hierarchical cluster analysis of scar tissue 210
Table 15.1. Information about second set of transgenic AD mice 316

Chapter 1. General Introduction

1.1. Infrared Spectroscopy

1.1.1. Principles of Infrared Spectroscopy

Infrared (IR) spectroscopy is the study of the vibrations of pairs or groups of atoms in molecules (Herzberg, 1945). IR spectra are the result of transitions between vibrational energy levels that occur when light with a frequency that corresponds to a characteristic frequency of the molecule is absorbed. ΔE, the energy difference between two vibrational energy levels, E_2 and E_1, is equal to

$$\Delta E = E_2 - E_1 = h\nu$$

where h is Planck's constant and ν is the frequency of the light. The transition between vibrational energy levels will occur when the frequency of the vibration and the frequency of the radiation are equal. This is usually radiation in the mid-infrared region which spans from roughly 2.5 to 50 micrometers or 4000 to 200 wavenumbers (cm^{-1}). Energy is transferred from the photon to the molecular vibration, such as a bond stretch or angle bend, changing the amplitude of the vibration. This can only occur if a change takes place in the dipole moment of the molecule during the vibration. The electrical field of light can then interact with the molecule and transfer its energy to the molecular vibration. For this reason, symmetric, diatomic molecules such as N_2 or O_2 are IR inactive because their dipole does not change upon bond stretching. According to quantum mechanics, only certain energy levels are allowed (McHale, 1999). However, as most molecules at room temperature are at the ground vibrational state, transitions to the first vibrationally exited state, known as fundamentals, are the most important. The probability of the transition between the two states is proportional to the square of the transition dipole moment, a principle known as Fermi's golden rule (McHale, 1999).

The process of infrared absorption can be understood by considering two atoms connected by a spring-like bond (Herzberg, 1939). The bond can stretch and contract, changing the distance between the atoms and the potential energy of the molecule. As the atoms approach, charge repulsion will increase, leading to an increase in the energy, and as they move apart, energy will also increase, until the bond breaks. The minimum potential energy occurs at the equilibrium bond length where the attractive and repulsive forces are balanced. The stretching and contracting of the diatomic molecule can therefore be modeled by the simple harmonic oscillations of a spring, and the vibrational frequency, $\mathrm{v}_{\mathrm{vib}}$ is then

$$\mathrm{v}_{vib} = \frac{1}{2\pi}\sqrt{\frac{k}{\mu}}$$

where k is the force constant, related to the stiffness of the spring or strength of the bond, and μ is the reduced mass, defined as

$$\frac{1}{\mu} = \frac{1}{M_A} + \frac{1}{M_B}$$

where M_A and M_B are the atomic masses of the individual atoms. The frequency of IR absorptions will therefore depend on the masses of the atoms and the strength of the bond. Simple harmonic motion is not obeyed exactly for real molecules, but it is a good approximation. The situation becomes more complex for polyatomic molecules, where molecular vibrations will include bond stretching, bending, twisting and rocking. A molecule with N atoms will have 3N – 6 vibrations (3N-5 if it is linear). However, depending on the symmetry of the molecule, not all of these will be allowed and others may be degenerate, occurring at the same frequency.

IR spectra provide valuable information about molecular structure. The basic structural elements of molecules such as C=O or CH_3 groups, known as functional groups, tend to absorb radiation of similar energy regardless of the structure of the rest of the molecule. This gives rise to specific peaks in the IR spectrum which can be used to identify the functional groups present in the sample. The exact shapes and positions of IR peaks are sensitive to the molecular environment. This makes IR spectroscopy useful for studying hydrogen bonding, solvent effects and molecular interactions. The spectral region from 1800 to 600 cm^{-1} contains many peaks, including those from the skeletal vibrations. It is difficult to interpret, but this region is unique for each molecule. For this reason, it is known as the fingerprint region; libraries of IR spectra are often used to unambiguously identify unknown materials. IR spectroscopy requires minimal sample preparation and is applicable to gaseous, liquid and solid samples. It is therefore widely-used in both research and industry.

IR spectra are usually recorded in absorbance mode as a function of wavenumber (cm^{-1}), the inverse of the wavelength in cm. Absorbance (A) is defined as

$$A = \log(I_0/I)$$

where I is the intensity of light after interacting with the sample and I_0 is the intensity of light with no sample present. Spectra are also sometimes recorded as transmittance (T), defined as

$$T = I/I_0$$

which gives a spectrum where the peaks appear as valleys. Absorbance and transmittance are related by

$$A = \log(1/T)$$

1.1.2. Dispersive Infrared Instruments

An IR spectrum can be collected by scanning through the wavelength range of interest and measuring the energy absorbed by the sample at selected intervals. This type of instrument, called a continuous scanning or dispersive spectrometer, consists of a source of continuous IR radiation, a monochromator and a detector. The source is usually a globar, a blackbody radiator made of a high resistance substance that emits thermal radiation when an electrical current passes through it. The monochromator contains a grating for selecting wavelengths of interest. The amount of radiation absorbed at each wavelength is measured by the detector. Most dispersive spectrometers are double-beam instruments, which measure the difference in energy between the sample and a blank reference. This type of instrument is relatively inefficient and has been almost completely replaced by interferometer-based instruments, called Fourier Transform infrared (FT-IR) spectrometers (see section 1.1.3.2 for an explanation of the advantages of FT-IR).

1.1.3. Fourier Transform Infrared Instruments

FT-IR instruments are based on the Michelson interferometer (Griffiths, 1975). The interferometer (Figure 1.1) consists of a fixed and a moving mirror, mounted at right angles to each other. A beam splitter, which reflects half the radiation and transmits half, is mounted so that half the radiation from the source is transmitted to one mirror and half is reflected to the other. Half the radiation reflected from each mirror is then recombined after either passing through or being reflected by the beamsplitter. This radiation will pass through the sample and go to the detector. The other half of the radiation will return to the source.

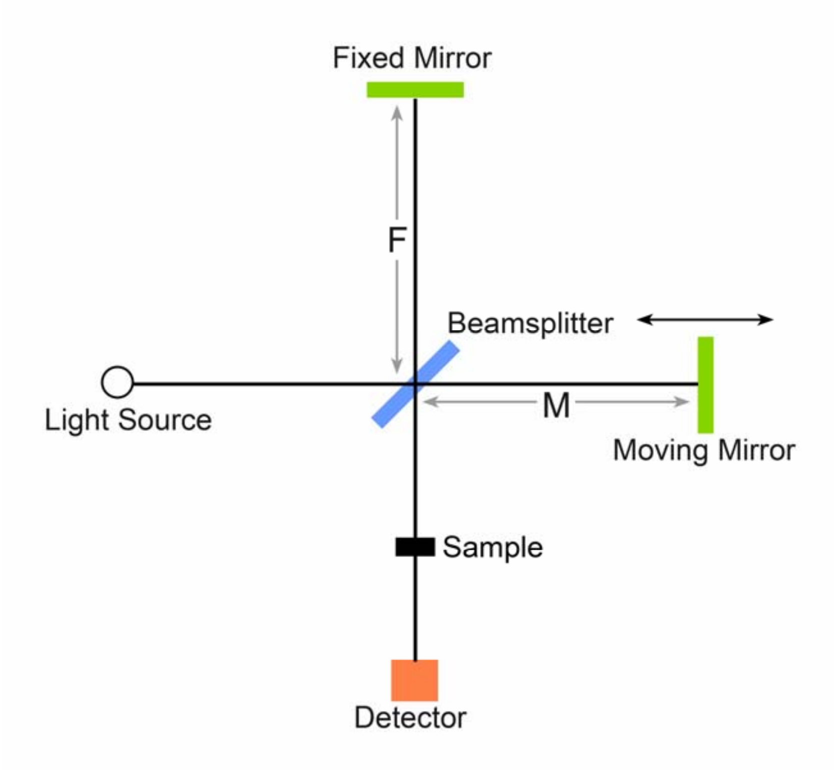

Figure 1.1. The Michelson interferometer. F is the distance between the fixed mirror and the beamsplitter, while M is the distance between the moving mirror and the beamsplitter.

1.1.3.1 Principles of Fourier-Transform IR Spectroscopy

The process of obtaining a spectrum from an FT-IR instrument can be understood by considering a monochromatic beam of perfectly collimated light, with a wavelength of λ cm and a frequency in wavenumbers of v cm^{-1} (Figure 1.2A) (Griffiths, 1975). The beamsplitter is assumed to reflect exactly half the radiation and transmit the other half. With reference to Figure 1.1, the difference in the distance traveled by the light going to the two mirrors, is 2(M – F). This optical path difference is called the retardation, represented by δ. When both mirrors are the same distance from the beam splitter, δ will be zero, and the light beams will recombine in phase. The intensity of the light recorded at the detector will be simply the sum of the intensities of the beams from the fixed and moving mirrors, and the beams are said to interfere constructively. If the moving mirror is displaced by a distance equal to $\lambda/4$ cm, the retardation will be $\lambda/2$ cm. When the beams from the two mirrors recombine, their phase difference will thus be half the wavelength, and the resulting intensity will be zero, as they will interfere destructively. However, if the moving mirror is displaced by $\lambda/2$ cm, the retardation will be λ cm, and the beams will once again be perfectly in phase. Therefore, by moving one mirror at a constant velocity, the signal at the detector will vary sinusoidaly. I(δ), the intensity at the detector measured as a function of the retardation, is just a cosine curve, which can be described as

$$I(\delta) = \tfrac{1}{2}\, I(v)\cos 2\pi v\delta$$

where I(v) is the intensity of the beam as a function of v (Figure 1.2B). The factor of ½ is needed because only half of the light from the source reaches the detector, while the other half is returned to the source.

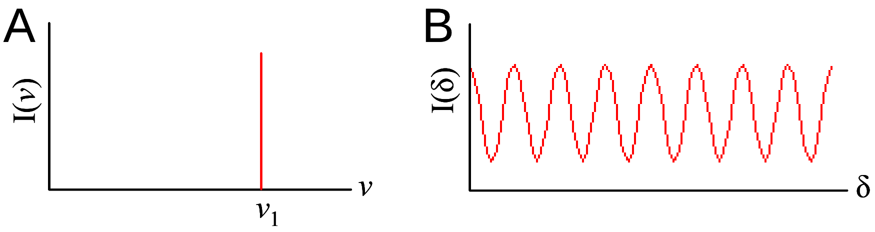

Figure 1.2. Fourier transform of monochromatic light. (A) Spectrum and (B) interferogram for a monochromatic source.

It is impossible to find a beamsplitter that transmits exactly 50% of the radiation and reflects the other 50%. The optical components, as well as the IR amplifiers and detectors, do not respond in exactly the same way to all frequencies of light. Therefore the amplitude of the interferogram is not only dependent on the radiant power of the beam, but also on detector response, amplifier characteristics and the efficiency of the beamsplitter. A frequency-dependent factor, H(v), has to be introduced into the above equation:

$$I(\delta) = \tfrac{1}{2}H(v)I(v)\cos 2\pi v\delta$$

By substituting B(v) for ½H(v)I(v), the expression for I(δ), modified by the limitations of the instrument, is obtained:

$$I(\delta) = B(v)\cos 2\pi v\delta$$

The plot of I(δ) as a function of δ is called the interferogram, while the plot of B(v), the energy as a function of v, is known as the spectrum. The data is measured as the interferogram but the spectrum is required by the researcher. Fortunately, the interferogram is mathematically related to the spectrum by the Fourier transform. The cosine Fourier transform of the above equation is

$$B(v) = I(\delta)\cos 2\pi v\delta$$

and the two above equations are called a cosine Fourier transform pair.

When the source emits more than one frequency, the interferogram is the sum of the interferograms for each frequency. With a continuous source, such as a globar, the interferogram is represented by the integral:

$$I(\delta) = \int_{-\infty}^{+\infty} B(v)\cos 2\pi v\delta \cdot dv$$

and the spectrum, the cosine Fourier transform of the above equation, is

$$B(v) = \int_{-\infty}^{+\infty} I(\delta)\cos 2\pi v\delta \cdot d\delta$$

With this many wavelengths, they will all be in phase in just one position, known as the centreburst of the time-domain spectrum or interferogram (Figure 1.3A). FT-IR spectroscopy can be considered as time-domain spectroscopy, because the entire spectrum is collected as a function of retardation, or time, as the mirror moves at a constant velocity (Figure 1.3A), and is then translated mathematically into the frequency domain (Figure 1.3B) using a Fourier transform. Dispersive spectroscopy, on the other hand, is regarded as frequency-domain spectroscopy because energy is recorded directly as a function of wavelength.

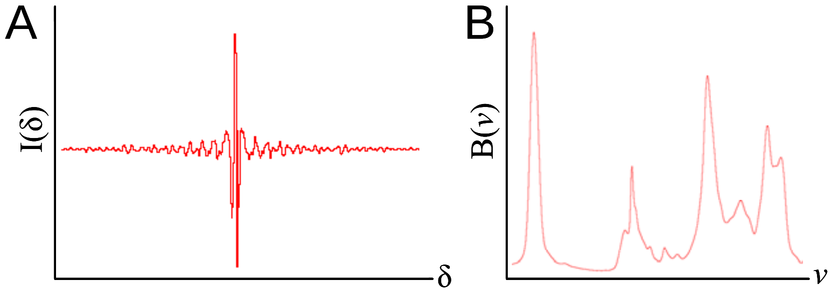

Figure 1.3. Interferogram and spectrum. (A) An interferogram collected in the time domain, as a function of mirror displacement. (B) Fourier transformation converts the interferogram into a conventional, frequency-domain spectrum (part of phosphatidylcholine spectrum shown).

1.1.3.2. Advantages of Fourier-Transform IR Spectroscopy

FT-IR interferometers are much faster and more sensitive than dispersive spectrometers (Griffiths et al, 1977). Since many FT-IR spectra can be obtained in the time needed to obtain one conventional spectrum, a large number of spectra can be acquired and averaged, resulting in an increase of the signal-to-noise ratio. This is known as the Fellgett or multiplex advantage. The FT-IR spectrometer has no slit through which radiation is selected and thus the power reaching the detector is much larger than in regular IR spectrophotometers. This is called the Jaquinot or throughput advantage and it also increases the signal-to-noise ratio. Because FT-IR instruments use internal laser calibration, they have higher wavenumber accuracy and reproducibility, resulting in the Connes or precision advantage. Because of these many advantages, FT-IR instruments have now almost completely replaced dispersive instruments.

1.2. Infrared Microspectroscopy

IR microspectroscopy involves connecting an IR microscope to a FT-IR interferometer, so that spectra of small areas of a sample can be collected. This technique combines the spatial resolution of microscopy with the molecular-level information of IR spectroscopy (Frazer, 1950; Reffner & Martoglio, 1995). By sampling in a grid pattern, or raster scanning, the spatial heterogeneity of the sample can be studied. A chemical image or map can be created by representing the distribution and intensity of peaks of interest on a color scale. This is called functional group or chemical mapping. The resulting chemical image can be correlated to the sample morphology. As this technique is non-destructive, the sample is available for other analyses. Sample preparation is minimal. The sample is sectioned, placed on the appropriate substrate and examined without any processing, so that nothing is added or taken away from it except water.

1.2.1. Instrumentation for IR Microspectroscopy

The factors that will influence the performance of an IR microspectroscope include the optics, light source and detector (Reffner, 1998). An IR microspectroscope includes a FT-IR interferometer with a connected microscope accessory, or a microscope with a built-in interferometer (Figure 1.4A, B). To allow mapping, the instrument has a computer-controlled sample stage. The IR microspectroscope resembles a conventional light microscope. The main difference is that the refracting optics (the condenser and objective lenses) are replaced with Schwarzschild optics (Reffner, 1998), made of highly-reflective aluminum coated mirrors. Those optics are capable of forming visible light images just like conventional microscope lenses, so that suitable areas for IR analysis can be identified. Most IR microspectroscopes can operate in either transmission or reflectance-absorbance (usually called reflectance) mode. In transmission mode, the light from the source passes through the sample and on to the detector (Figure 1.4C). In reflectance mode, the light passes through the sample, is reflected from the substrate, and passes through the sample again before going to the detector (Figure 1.4D).

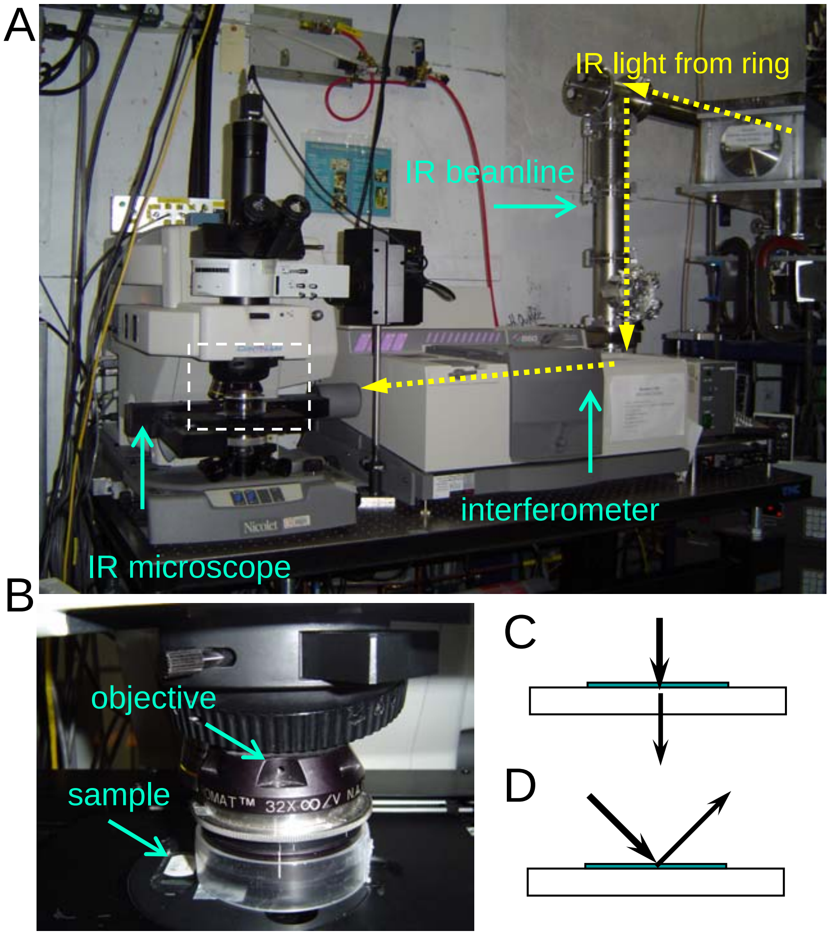

Figure 1.4. The IR microscope. (A) The experimental set-up at a synchrotron IR beamline (NSLS, U10B). Light from the synchrotron ring travels through the beamline into the interferometer, and then into the IR microscope. (B) A close-up of the sample stage (white outline in A). The path of the light through the sample with the (C) transmission and (D) reflectance set-ups.

IR microspectroscopes usually use mercury cadmium telluride (MCT) detectors, as they have high sensitivity and low noise, and operate over the mid-infrared region. Focal plane array detectors have also been applied to IR microspectroscopy (Lewis et al, 1995). These arrays of detector elements, originally developed for military applications, allow spectra to be collected from a number of pixels at the same time, speeding up the data collection process.

The light source for IR microspectroscopy is usually a conventional globar, built into the FT-IR interferometer. Synchrotron IR sources, discussed below, can also be used, and provide numerous advantages.

1.2.2. Spatial Resolution of IR Microspectroscopy

The spatial resolution of IR microspectroscopy is defined with an aperture, but is limited by the wavelength of the light and the brightness of the light source. When the size of the aperture is close to the wavelength of light, diffraction effects come into play and there is spectral contamination from the surrounding regions of the sample. The actual sample area studied is then not equal to the area that is defined by the aperture and seen with the shorter wavelengths of visible light (Miller & Smith, 2005). This leads to blurring between pixels.

Spatial resolution can be improved by using confocal apertures, which limit diffraction effects (Carr, 2001). One aperture is used above the sample to define the sample area illuminated by the light, and another below it to limit the field of view of the detector. For reflectance measurements, a single aperture is used to get the confocal effect, as the light passes through the aperture, is reflected off the sample, and passes out again through the same aperture. With a confocal system, the diffraction limit is approximately λ/2, compared to 2λ/3 for a non-confocal system, where λ is the wavelength of light (Carr, 2001). This is reached when the aperture size is equal to the wavelength of interest (Carr, 2001). However, as the size of the aperture is reduced, diffraction leads to a reduction in photon flux, and therefore spectral quality. Thus, with a conventional globar source, the best spatial resolution that can be achieved is ~20 µm, well below the diffraction limit for the mid-infrared region. However, if a very bright light source, such as a synchrotron is used, the resolution becomes dependent on wavelength and diffraction-limited resolution is possible.

1.2.3. IR Microspectroscopy with a Synchrotron Source

A synchrotron is a particle accelerator in which electrons travel at close to the speed of light. The path of the electrons is bent by magnetic fields generated by large magnets placed around the ring. The change in path causes the electrons to accelerate and emit electromagnetic radiation, known as synchrotron radiation or light (Wiedemann, 2003). Synchrotron light has several unique properties. It is low noise, polarized, highly collimated and spans from high energy x-rays to the infrared region. Most importantly it is very bright. In the IR region, it is around 1000 times more intense than a blackbody source such as a globar (Smith, 2002).

IR microspectroscopy with a synchrotron source was first attempted at the National Synchrotron Light Source (Brookhaven National Laboratory. Upton, NY) and shown to give better spatial resolution with higher signal to noise compared to a globar source (Carr et al, 1995). Diffraction-limited spatial resolution (where the aperture size is equal to the wavelength of interest) is possible (Carr, 2001; Smith, 2002; Dumas et al, 2004). Therefore, at 3000 cm^{-1}, the spatial resolution is 3 µm, but at 1000 cm^{-1}, it is only 10 µm. Spatial resolution will not be increased if the aperture defines a region smaller than the wavelength. The light will appear to originate from the diffraction-limited region of the sample (Carr, 2001). The full advantage of a confocal microscope becomes apparent with a synchrotron source (Carr, 2001), as there is less contamination from first and second order peaks of the point spread function at the diffraction limit. Therefore, IR microspectroscopy with a synchrotron source provides the best possible spatial resolution and signal-to-noise ratio (Miller & Smith, 2005).

1.3. Infrared Biospectroscopy

IR spectroscopy has been used for decades to study biological molecules (Parker, 1983). Peak frequencies are sensitive to the structure and environment of the atoms involved in the vibration. The fast time response of IR (on the level of milliseconds, and with very specialized equipment even femtoseconds) (Smith & Palmer, 2002) allows information to be collected about dynamic processes. IR spectroscopy can be used to monitor the conformational changes that accompany reactions, ligand binding, folding, unfolding, and aggregation. There are several factors that make IR spectroscopy widely used in the study of biomolecules. It is fast, easy, sensitive, and quantitative. IR is applicable to a wide variety of samples including solids (such as films or crystals), liquids and solutions. As the frequency of a band depends on the mass of the molecules involved, individual bonds of interest can be studied by using isotopic substitution. Only small amounts of sample (around 100 μg) are required to obtain IR spectra (Surewicz et al, 1993) and even very large molecules like proteins can be studied. IR is also a non-destructive technique, so the sample is available for other analyses. The main disadvantage is that water has strong absorption in the mid-infrared region, but this can be remedied by using deuterium oxide as the solvent, as the substitution of the water hydrogens for deuterium shifts the water bands to different parts of the spectrum. Alternatively, short path lengths can be used and the water signal digitally subtracted.

Table 1.1 summarizes the main IR spectral peak positions of biological molecules. The region from 3700 to 3100 cm^{-1} contains broad peaks due to O-H and N-H stretching, while the C-H stretching vibrations dominate the region from 3100 to 2800 cm^{-1}. The C=O stretching vibrations of lipid and nucleic acid ester groups are found at

1740-1715 cm^{-1}. The region from 1700 to 1500 cm^{-1} contains the amide I and II bands of proteins. Several bands due to C-H deformation modes are found between 1470 to 1350 cm^{-1}, while a band due to the C=O stretching of COO^- is found at 1390 cm^{-1}. The region below 1400 cm^{-1} is generally much more complicated, containing many overlapping bands. The amide III band of protein is found between 1310 and 1240 cm^{-1}. The asymmetric P=O stretch of phosphodiesters occurs at 1250 to 1220 cm^{-1} and the symmetric P=O stretch at 1090 to 1085 cm^{-1}. The C-O-P-O-C stretch of phosphodiester bonds is found at 1060 cm^{-1}. As well, the region between 1200 and 900 cm^{-1} contains the C-O stretch and ring vibrations of carbohydrates.

Table 1.1. Assignments of peaks in IR spectra of tissues

Peak Position (cm^{-1})	Assignment (Parker, 1983; Mantsch & Chapman, 1996)
3400-3500	O-H stretching
3300-3200	N-H stretching (Amide A of proteins)
3082	N-H stretching (Amide B of proteins)
3015	=C-H stretching of unsaturated fatty acids
2956	Asymmetric CH_3 stretching
2922	Asymmetric CH_2 stretching
2871	Symmetric CH_3 stretching
2851	Symmetric CH_2 stretching
1738	C=O stretching of esters
1715	C=O stretch of carbonic acids
1600-1700	Amide I of proteins (exact position depends on secondary structure)
1550-1520	Amide II of proteins
1515	Tyrosine band
1466	C-H deformation of CH_2
1455	Methyl asymmetric bend
1394	Symmetric C=O stretch of COO^- of amino acid side chains and fatty acids
1310-1240	Amide III of proteins
1200-900	Sugar ring modes: C-O and C-C stretching, C-O-H and C-O-C deformations of carbohydrates
1250-1220	Asymmetric P=O stretching of PO_2^- groups
1090-1085	Symmetric P=O stretching of PO_2^- groups
1060	C-O-P-O-C stretch of phosphodiester bonds
970	Phosphodiester chain vibration

1.3.1. IR Spectroscopy of Proteins

Proteins are linear polymers of amino acids linked through the peptide bond, and folded into three-dimensional structures. Proteins have many functions, including structural elements, enzymes, receptors and transporters. IR spectroscopy is widely used to study proteins (Barth & Zscherp, 2002). N-methylacetamine (NMA) was used as a model compound for the normal mode analysis of the polypeptide backbone vibrations, as it is the smallest molecule to contain the trans-peptide group (Krimm & Bandekar, 1986). With modifications, the results could be translated to proteins. The modes of the peptide backbone, found in the region usually studied by mid-IR, include the Amide A, B, I, II, and III bands, as well as a skeletal vibration mode (Figure 1.5). (The spectrum in figure 1.5 and the spectra in Figures 1.6 to 1.8 were acquired in the lab by me. See section 3.2.5.1.1. for experimental details.)

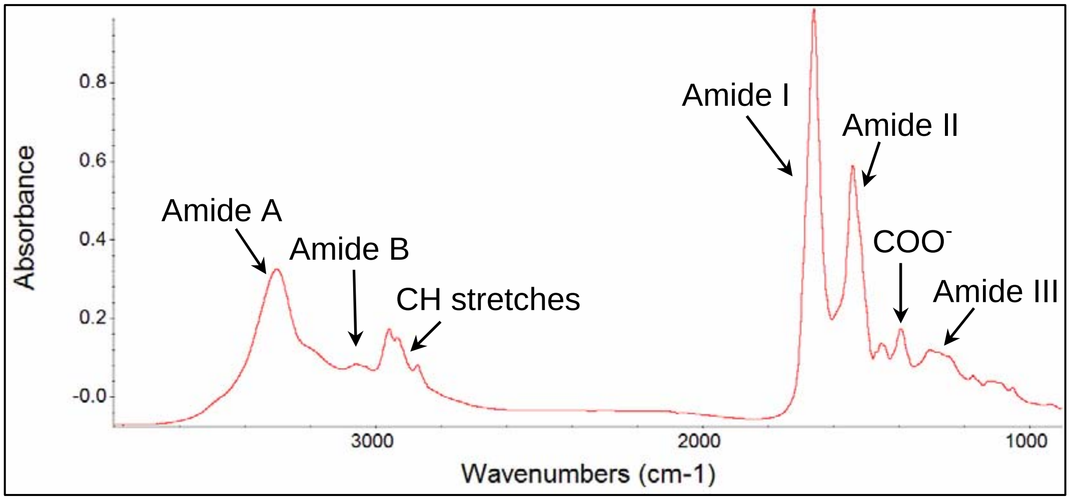

Figure 1.5. Protein IR spectrum. Thin film of bovine serum albumin, a typical globular protein.

The amide modes are assigned to various vibrations of the peptide backbone (Krimm & Bandekar, 1986). The NH stretching vibration of proteins is found as a Fermi resonance doublet between 3300 and 3000 cm^{-1}. The two components are known as the amide A and B modes. The amide A component is due to NH stretching and is mainly localized in the NH bond. The amide B band is an overtone or combination band of the Amide II mode. These bands are seldom studied as they are insensitive to the conformation of the polypeptide backbone. The Amide I vibration is found between 1600-1700 cm^{-1}. It is due to C=O stretching with small contributions from out-of-phase CN stretching, CCN deformation and NH in plane-bending. The position of this vibration is dependent on the protein secondary structure, and is therefore often used for secondary structure analysis. The Amide II band, at around 1540 cm^{-1}, is the out-of-phase combination of the NH in-plane bend and the CN stretch, with minor contributions from the CO in-plane bend, and CC and NC stretches. The Amide III mode occurs at 1400-1200 cm^{-1}, and is the in-phase combination of the NH in plane bend and the CN stretch, with some contributions from CO in-plane bending, and CC stretching. Skeletal stretching vibrations are found at 1200 to 880 cm^{-1}. In NMA, this results in a NC stretching mode and a mixed mode, but the situation is more complex for polypeptides, with a number of weak modes appearing in that region, depending on the side-chains. The remaining modes include Amide IV (CO in-plane bend and CC stretch, with some CNC deformation), Amide V (out-of-plane NH bend and CN torsion), Amide VI (CO out-of-plane bend with some CN torsion) and Amide VII (NH out-of-plane bend, CN torsion and CO out-of-phase bend). They are found at lower frequencies (700-200 cm^{-1}), outside of the region usually studied in the mid-IR.

The main force responsible for the dependence of amide I peak position on protein secondary is hydrogen bonding (Surewicz et al, 1993). The frequency of a vibration depends on the strength and polarity of the bond. Thus, anything that affects the bond, such as hydrogen bonding, will be reflected in the spectrum. Hydrogen bonding will generally shift the position of stretching vibration to lower wavenumbers (Colthup et al, 1975). The strength of the hydrogen bonding between N-H and C=O groups of the peptide backbone will depend on their geometry and therefore different secondary structures will have hydrogen bonding of different strengths that will be reflected in the spectra. Transition dipole coupling, a dipole-dipole coupling interaction between oscillating transition dipoles of neighboring amide groups, has been proposed as the cause of the observed splitting in the amide I band of anti-parallel β-sheet (Krimm & Bandekar, 1986)

The spectra of proteins are dominated by the backbone amide bands, but the amino acid side chains also contribute to protein spectra. Some of these, such as Asn, Gln, and Lys have side-chain absorptions in the amide I and II region (Krimm and Bandekar, 1986).

1.3.1.1. Protein Structure Determination with IR Spectroscopy

Proteins can adopt a variety of secondary structures (α-helix, β-sheet, random coil and turns) defined by the dihedral angles of the peptide backbone. The analysis of protein structure by IR spectroscopy goes back over 5 decades, when it was recognized that the position of the amide band is dependent on the secondary structure (Ambrose and Elliott, 1951). Amide peak positions were assigned to certain secondary structures through empirical observation and theoretical calculations (Miyazawa and Blout, 1961). An amide I maximum between 1662-1650 cm^{-1} indicates α-helix; 1650-1640, unordered structure; 1640-1620, β-sheet; maxima above 1660 cm^{-1} are associated with β-turns

(Bandekar, 1992; Surewicz et al, 1993). The anti-parallel β-sheet displays a characteristic splitting of the Amide I band into an intense low frequency component at 1625 cm^{-1}, and a weak high frequency component at 1695 cm^{-1}. However, the relationship between Amide I peak position and secondary structure does not exist for every protein; for some proteins, the secondary structure predicted from the amide I band position does not correspond to the actual structure (Wilder et al, 1992).

Secondary structure analysis of proteins is most often based on the amide I band. This band is the sum of all the amide I vibrations from every peptide group in the protein. The peak position of each contributing vibration will be dependent on its conformation. Therefore, the amide I band is broad and very complex. In order to obtain structural information about the protein, two main approaches have been developed. The first method relies on peak resolution enhancement, via Fourier-self deconvolution or second derivative techniques, to obtain structural information from the amide I band. Fourier self-deconvolution can be applied to IR spectra to resolve the amide I band into the underlying components (Kauppinen et al, 1981) that are then assigned to known secondary structure elements (Byler and Susi, 1986). Second derivatization may also be used to resolve the amide I band (Susi and Byler, 1983). The resolved bands can then be assigned to the various types of secondary structures, the position of which is established empirically from spectra of proteins and polypeptides with known x-ray diffraction structures, as well as from normal-mode calculations on model compounds (Krimm and Bandekar, 1986). The other major approach involves using a pattern-recognition method based on a calibration set of spectra from proteins whose structure is known (Dousseau &

Pezolet, 1990; Lee et al, 1990). The advantage of this approach is that the frequencies of bands due to specific structural elements do not need to be known.

IR spectroscopy does not provide the type of residue-specific structural information available from x-ray crystallography (Turk & Johnson, 2001) or nuclear magnetic resonance (NMR) spectroscopy (Downing, 2004). However, these techniques are often not possible if crystals of the protein cannot be obtained or the molecule is too large for NMR. IR structural analysis is useful for obtaining an average conformation that can be used to estimate the relative percentage of peptide bonds contributing to each secondary structure in the protein, even through the conformation of specific amino acid residues cannot be found from IR spectra.

1.3.2. IR Spectroscopy of Lipids

Lipids are a class of water insoluble compounds that act as membrane components and energy stores. The building blocks of most lipids are fatty acids, composed of a long hydrocarbon tail (14-24 carbon groups long) and carboxyl head group. Two fatty acids linked to a polar head group are the main component of biological membranes. Membrane lipids are classified according to their head group, and include glycerophospholipids, sphingolipids, and sterols such as cholesterol. The lipids form bilayers, with the hydrophilic head groups pointing outwards, and the hydrophobic acyl chains pointing towards each other.

IR spectroscopy has been applied to the study of membrane lipids (Casal & Mantsch, 1984). Information can be obtained on chain packing, conformational order, phase transition between gel and liquid crystal phases and interactions with membrane proteins. The spectra of lipids (Figure 1.6) are dominated by the acyl vibrations including the C-H stretching bands at 3100-2800 cm^{-1} and the methylene and methyl bending vibrations between 1500 and 1350 cm^{-1}. The assignment of vibrations due to the acyl chain is well known, thanks to work on n-paraffins (Snyder & Schachtschneider, 1963). The most important head group bands are the C=O stretches between 1740 and 1715 cm^{-1}. The rest of the bands will depend on the head group. For phospholipids, the phosphate stretch bands are found at around 1250 to 1220 cm^{-1} and 1090 to 1080 cm^{-1}.

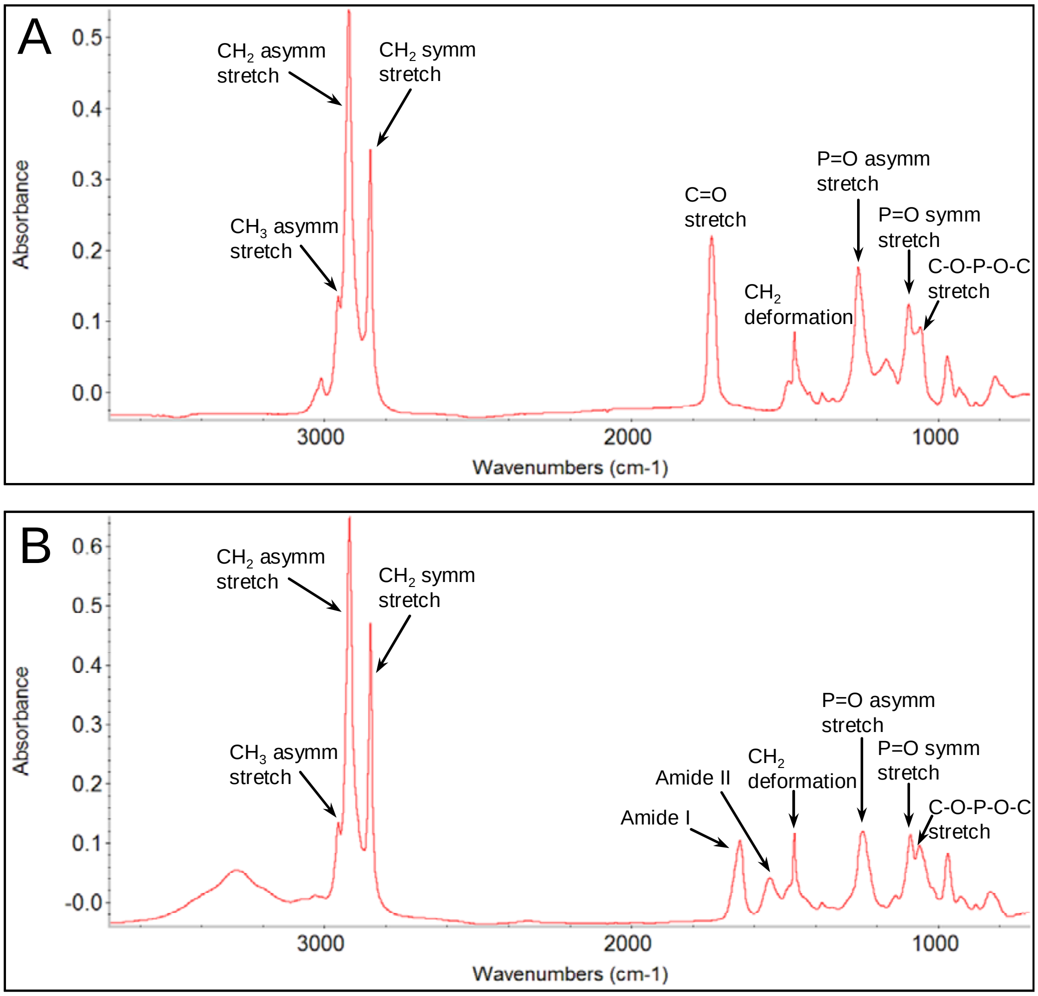

Figure 1.6. Phospholipid IR spectra. (A) Phosphatidylcholine, the main constituent of cell membranes. (B) Sphingomyelin, which makes up the myelin sheet and is a major constituent of brain tissue. Note the presence of an amide I and II band due to an amide group in the headgroup.

1.3.3. IR Spectroscopy of Nucleic Acids

Nucleotides, composed of a nitrogenous base (pyrimidine or purine), a pentose sugar and a phosphate group, are the building blocks of nucleic acids. The nucleotides are linearly connected through phosphodiester bonds. Deoxyribonucleic acid (DNA) contains the genetic information of the cell. It is transcribed into ribonucleic acid (RNA), the template for protein synthesis. Nucleotides such as adenosine triphosphate are also important carriers of energy.

IR spectroscopy has been used for structural studies of nucleic acids (Liquier & Taillandier, 1996). The IR spectra are sensitive to base-pairing, base-stacking and interactions with small molecules. Therefore, IR spectroscopy can be used to monitor changes in structure, such as those caused by the formation or melting of the double helix. The IR spectra of isolated nucleic acids (Figure 1.7) contain a number of well-defined peaks, due to the bases, sugars, phosphate groups and the sugar-phosphate backbone (Liquier & Taillandier, 1996). The base pair peaks are found in the region from 1700 to 1500 cm^{-1}. It has been proposed that the nuclear DNA of mature cells is so tightly packed that it is opaque in the mid-infrared region, and any peaks due to nucleic acids of the cell are due to RNA in the cytoplasm (Chiriboga et al, 1998). However, at other points of the cell cycle when the DNA in the nucleus unwinds, it will contribute to the spectrum of the cell (Chiriboga et al, 1998).

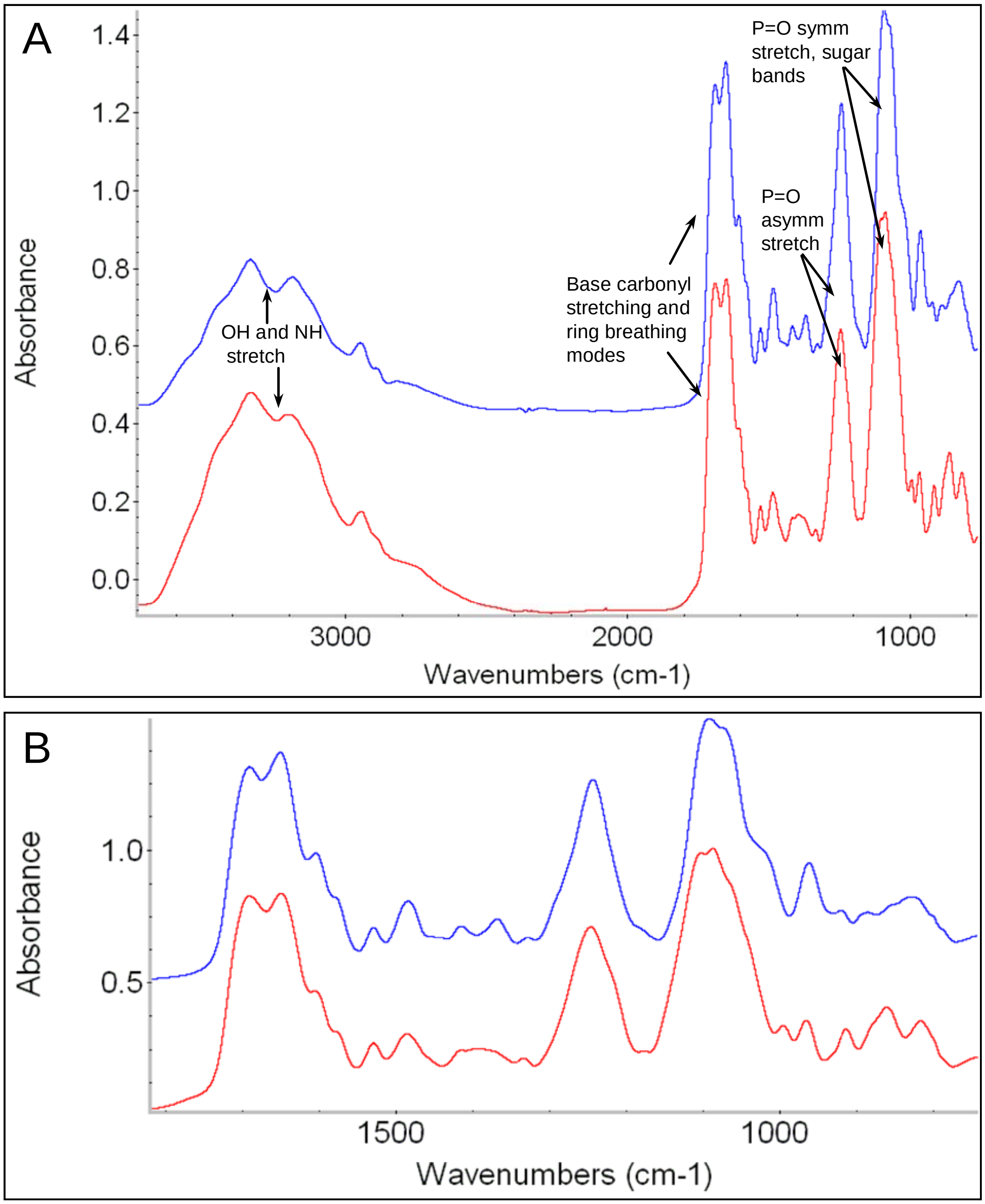

Figure 1.7. Nucleic acid IR spectra. (A)The IR spectra with the main peaks indicated and (B) the close-up of the fingerprint region of isolated RNA (red) and DNA (blue).

1.3.4. IR Spectroscopy of Carbohydrates

Carbohydrates are a class of molecules with the formula $(CH_2O)_n$. They provide the cell with energy and structural elements and are a constituent of many larger molecules such as glycoproteins and glycolipids. The basic unit is called a monosaccharide. Polysaccharides known as glycosaminoglycans are constituents of the extracellular matrix. IR spectroscopy is useful in the study of carbohydrates (Brandenburg & Seydel, 2002). The spectra of sugars are dominated by a broad O-H stretch band at around 3400 cm^{-1} (Figure 1.8). Sugars also have a number of peaks between 1200 and 900 cm^{-1}, due to C-O and C-C stretching, and C-O-H and C-O-C bending. These bands are characteristic of the type and conformation of the carbohydrate, as well as the glycosidic bond between the monosaccharide subunits of oligosaccharides (Kacurakova & Mathlouthi, 1996).

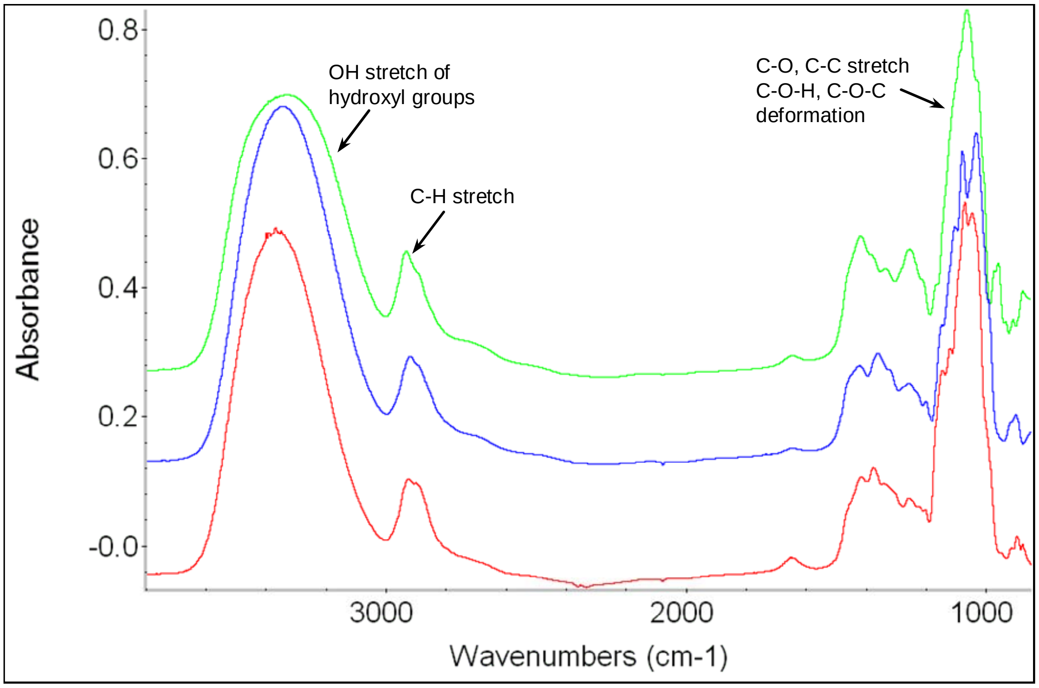

Figure 1.8. Carbohydrate IR spectra. Mannose (green), glucose (blue) and lactose (red).

1.3.5. IR Spectroscopy and Imaging of Tissues

Although the study of isolated biomolecules is very useful, it is often of interest to study them in their biological environment, *in situ*. Cells and tissues are composed of countless types of molecules but the resultant spectra look surprisingly simple due to the near-degeneracy of vibrations from specific functional groups. Unfortunately, due to this overlap, individual molecules cannot generally be monitored. The average molecular composition of the sample can however be probed with IR, by analyzing bands due to the functional groups found in lipids, proteins and other molecules of interest. By taking spectra of adjacent regions, IR microspectroscopy can be used to create spectral maps of the chemical composition. A few researchers use the term IR imaging to describe data collected with a focal plane array and IR mapping to describe data collected by raster scanning the sample with a point detector. However, as the end result is the same, in this work the terms IR map and image will be used interchangeably.

IR microspectroscopy was applied to biological problems soon after its development almost 60 years ago (Fraser, 1950). With the development of Fourier transform IR spectrometers, synchrotron IR sources and focal plane arrays, great improvements have been made in both the quality of data and speed of data collection. IR microspectroscopy has been applied to the study of both normal and diseased cells and tissues. One of the earliest examples involved imaging the differences in white and grey matter in normal brain, based on the lipid content (Wetzel & LeVine, 1993). IR imaging has been used to study silicone inclusions in breast tissue biopsies (Kidder et al, 1997), mineralization and collagen maturity in bone tissue (Camacho et al, 1999), the penetration of chemical compounds into skin (Mendelsohn et al, 2000), chemical modification in hair (Dumas & Miller, 2003) and the distribution of collagen in cardiomyopathic heart (Gough et al, 2003). IR microspectroscopy has been used to image the distribution of various components in living cells in their normal state and during division, as well as to study apoptotic and necrotic cells (Jamin et al, 1998; Holman et al, 2000; Jamin et al, 2003). Attempts have been made to use IR microspectroscopy as a diagnostic tool, for example in cancer (Lasch et al, 2002), scrapie (Kneipp et al, 2002) and the identification of microorganisms (Naumann, 2000).

1.3.5.1. Preparation of Tissue Sample for IR Spectroscopy

Sample preparation for IR spectroscopy and imaging of tissue and cells is generally minimal. The samples have to be mounted on IR compatible substrates. For measurements in transmittance mode, IR transparent windows such as KBr, ZnSe, CaF_2 or BaF_2, are used. Gold-coated mirrors or commercially available IR-reflecting MirrIR slides (Kevley Technologies, Chesterland, OH) are used for measurements in reflectance mode. Cells are generally placed directly on the substrate. Tissue sections have to be cut into sections of the appropriate thickness before being mounted on the substrate and desiccated. The tissue is preserved by freezing and thin sections are made by cryotoming. In this way, nothing is added or taken away from the sample, except water.

The sample preparation will affect the quality of the data. Anything that alters the composition or physical integrity of the sample will affect the IR spectra. Therefore, it is generally best to avoid post-mortem delays that will result in autolysis of the tissue. Chemical treatments to the sample, such as the fixation and paraffin-embedding commonly employed with conventional staining, should also be avoided. Paraffin embedded samples are saturated with a mixture of alkane hydrocarbons, that after sectioning, are removed with polar solvents. Although this will preserve the tissue morphology and some molecules such as proteins, non-polar molecules like lipids will be removed.

1.3.6. Analysis of IR Map Data

In order to utilize the information obtained from IR biospectroscopy and imaging, several issues must be considered. First, the complex IR spectra of biological samples, made up of many IR bands, have to be interpreted. Second, the vast amount of data obtained from IR mapping has to be processed, efficiently and consistently. Data analysis involves extracting chemical information from the peak positions, shapes and intensities of the individual spectra, and then displaying this information as an image so that the IR data can be correlated with sample morphology. This involves processing the IR map data to create false-color images that represent aspects of the sample's chemistry. The same map can be processed on different features to illustrate different aspects of the sample's composition.

Software, created either independently or by IR microscope manufacturers, allows the data to be processed in bulk. The software provides the user with numerous options for pre-processing and analyzing the data that will be discussed below.

1.3.6.1. Spectral Acquisition Parameters and Pre-processing

The types of analyses that can be attempted on a data set are determined by the spectral quality. This will be affected by the instrumental settings and type of sample, but sometimes improvements can be made with spectral pre-processing methods.

Most FT-IR spectrometers allow the user to select several parameters for data collection (such as spectral resolution, zero-filling, number of scans co-added, and apodization function) that will affect the quality of the final data. With reference to data collection, the spectral resolution refers to the spacing of data points. In biological samples, the peaks are usually quite broad, and use of a higher spectral resolution than required will result in noisier spectra. However, using a resolution that is too low will result in a loss of detail as real peaks may not be resolved. A spectral resolution of 4 or 8 cm^{-1} is generally adequate for tissue samples. Zero-filling introduces zeroes to the end of the interferogram, which after the Fourier transform results in interpolated data points being added between the real data points. This creates the illusion of smoother spectra, but is not advisable as the raw data is altered. The number of spectra collected will affect the signal-to-noise ratio (S/N). The more spectra co-added, the better the data, but this will increase the collection time. Apodization is needed in FTIR because the Fourier transform function requires an infinite data set but the interferogram measured by the interferometer is limited by the finite distance that the mirror can be moved. When the Fourier transform function is applied to the finite interferogram, the peaks in the resulting spectrum have significant side lobes. A number of apodization functions, such as boxcar, triangular, and Happ-Genzel, can be used to reduce the appearance of these side lobes. However, the more the function reduces the side lobes, the more it reduces the resolution by broadening the peaks. The most popular apodization function in biological spectroscopy is the Happ-Getzel function, because it maximizes side lobe reduction while minimizing resolution reduction.

IR map data is often pre-processed before analysis is attempted. This involves the same protocols used to pre-process single spectra, except that they are applied at once to all the spectra in the map. Common pre-processing methods include water vapour and CO_2 subtraction, baseline correction, normalization and smoothing. Care must be taken when applying these methods. Smoothing, for example, involves reducing the effect of noise on spectral appearance, but it also decreases spectral resolution. The degree of smoothing will depend on the number of neighboring data points used to calculate each smoothed point. The bigger that number, the greater the loss of spectral detail, as illustrated in Figure 1.9.

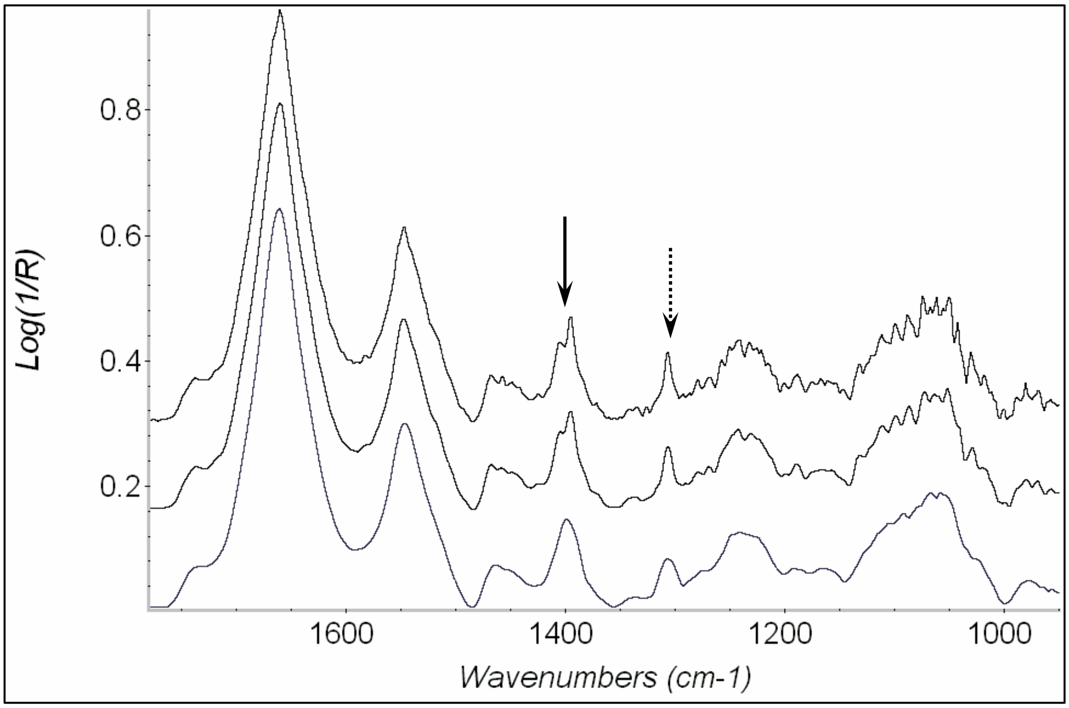

Figure 1.9. The effect of spectral smoothing. A noisy spectrum (top), smoothed using 7 (middle) and 15 (bottom) data points. Oversmoothing can result in a loss of spectral detail, especially apparent with closely-spaced doublets (solid arrow) and sharp peaks (dotted arrow), and the appearance of artifacts caused by the smoothing of noise.

As IR spectra of biological samples are made up of a number of overlapping bands, band narrowing methods are often applied to resolve the underlying peaks. In principle, by narrowing the bands, peaks due to overlapping components should be separated. The two main approaches involve deconvolution and derivatization. Derivatization has been used to resolve overlapped peaks in IR spectra for decades (Collier & Singleton, 1956). First derivative spectra show the rate of change of the slope, and as they cross the x-axis at the peak maxima of the original spectra, are often useful for finding the exact location of peak maxima. Second derivative spectra show the rate of change of the curvature of the original spectra. As the maxima occur at the same wavenumbers as in the original peaks (except in the negative direction), second derivatives are often used to resolve broad bands. Derivatives depend on the rate of change of the slope, so sharp bands are magnified and broad bands reduced in amplitude. Therefore, first or second derivative spectra are commonly used to reduce baseline effects and increase the "resolution" of IR data. However, derivatization will magnify the effect of sharp peaks due to noise, so that the spectra are often smoothed before being derivatized. A commonly used method of finding derivatives, the Savitzky-Golay algorithm, actually incorporates a smoothing procedure (Savitzky & Golay, 1964). The effect of this is that the spectral resolution is actually lowered. Small peaks and shoulders may be hidden, and false maxima created through the smoothing of noise. The derivatization process also leads to the creation of artifactual peaks on both sides of the real peak (Maddams & Mead, 1982; Hawkes et al, 1982; Maddams & Southon, 1982).

Fourier self-deconvolution can also be used to reduce the width of IR bands (Kauppinen, 1981). Fourier self-deconvolution requires that assumptions about the band shape and position be made. Different results are obtained depending on the methods employed. Care must be taken with Fourier self-deconvolution as spectral artifacts can be introduced and noise can be magnified (Griffiths & Pariente, 1986). For the aforementioned reasons, the data pre-processing methods mentioned in this section will not be employed in this research.

1.3.6.2. Univariate and Bivariate Methods

Once the data collection parameters have been selected and pre-processing decisions have been made, there are several approaches to analyzing the data obtained from IR mapping. Univariate methods involve representing the area of a single peak, or just the peak height, on a false color scale. This method allows the presence or relative intensity of a functional group of interest to be displayed. Therefore, this technique is often called functional group or chemical imaging. One can also create a map based on peak area (or peak height) ratios, which constitutes bivariate analysis. This is often used to display the relative changes in tissue components, and as a simple way of normalizing the effects of sample thickness, by ratioing the area of a peak due to one component against another whose relative amount is assumed not to change much across the sample. When calculating peak heights or areas, a baseline on both sides of the peak of interest is often used to minimize baseline variation. Univariate and bivariate methods require that the identity of the peaks used be known. In complex biological samples, the broad, overlapped peaks can make assignment to specific functional groups impossible, and more sophisticated, multivariate methods may be employed.

1.3.6.3. Multivariate Methods

Multivariate methods use mathematical algorithms in order to classify the spectra into groups based on their similarity. The results can then be used to create color images that show the spatial distribution of similar spectra. The identity of individual peaks does not need to be known, as the spectra are classified based on their shapes. These methods can therefore highlight subtler spectral differences that are the result of underlying variations in the composition of the sample.

Several cluster analysis methods are commonly used to analyze IR map data (Lasch et al, 2004). In hierarchical cluster analysis, objects (spectra) are grouped into successive clusters. The similarity between spectra is calculated using distance matrix calculations, and then clusters of similar spectra are created with a clustering algorithm. K-means clustering is a non-hierarchical method where the objects are placed into a user-specified number of clusters. An object can only belong to one group at a time. Fuzzy c-means clustering is also a non-hierarchical method but each object can belong to more than one cluster to different extents (between 0 and 1).

Principal component analysis (PCA) is a data reduction method that can be used to represent the variability in the data with a lower number of variables. This method has been applied to create spectral images from IR map data by displaying the location of principal components on a color scale (Lasch & Naumann, 1998). Artificial neural networks, a data modeling method that uses an interconnected group of artificial neurons to group data based on a training data set, has also been used to created IR images (Schmitt & Udelhoven, 2001). Artificial neural networks require a data set of spectra with known identities in order to “train” the network.

The best solution is to analyze the data with several methods, including univariate, bivariate, and multivariate methods, and compare the results obtained with each. Although several of the multivariate methods were tried in this research, hierarchical cluster analysis was found to be the most useful and was therefore applied to the data. The data processing methods used in this study will be discussed in more detail in Chapter 4.

Part 1. Infrared Microspectroscopy of AD Mouse Brain

Chapter 2. Introduction to Alzheimer's Disease

2.1. Alzheimer's Disease

Alzheimer's disease (AD) is a progressive neurodegenerative disorder, accompanied by memory loss and dementia. In the Canadian population, AD is estimated to affect 5.1% of individuals over 65, while for those over 85, this increases to 26.0% (Canadian Study of Health and Aging Working Group, 1994). The condition was first described in 1906 by the German neuropsychiatrist, Alois Alzheimer. AD is one of several neurodegenerative diseases, such as amyotrophic lateral sclerosis, Parkinson, Huntington, and Creutzfeldt-Jacob diseases, marked by the deposition of protein aggregates in the brain (Selkoe, 2003; Forman et al, 2004). They are collectively known as conformational diseases, as they involve the misfolding of normally-soluble proteins.

AD can be divided into the sporadic, or late-onset, form, and the much rarer familial AD (FAD) (Selkoe, 2001). The causes of sporadic AD are still unclear. It likely is a multifactorial disease, as a variety of unrelated environmental and genetic factors can increase its likelihood. Risk factors include age, head trauma, and cardiovascular disease (Morris, 1997; Stampfer, 2006) while the regular use of non-steroidal anti-inflammatory drugs (such as ibuprofen, aspirin, naproxen, celecoxib, rofecoxib) appears to be protective (Gasparini et al, 2004). Certain polymorphisms of the apolipoprotein E gene, which codes for a lipid-transport protein, are also associated with AD susceptibility. The ε4 allele is associated with the highest incidence of AD, while the ε2 with the lowest (St. George-Hyslop & Petit, 2005). Recently, reduced expression of the SORL1 gene, which codes for a protein involved in protein trafficking, was found to be associated with late-onset AD (Rogaeva et al, 2007).

The symptoms of FAD are similar to sporadic AD, except that they appear much earlier. FAD is connected with specific, inherited genetic mutations. They include mutations in the presenilin 1 (PS1) gene on chromosome 14 (Sherrington et al., 1995), the presenilin 2 (PS2) gene on chromosome 1 (Rogaev et al, 1995, Levy-Lahad et al, 1995) and the amyloid precursor protein (APP) gene on chromosome 21 (Goate et al, 1991). Individuals with Down's syndrome, having three copies of chromosome 21 and thus three copies of the APP gene, develop AD symptoms at an early age (Armstrong, 1994).

2.1.1. Neuropathology

Macroscopically, brains from individuals with AD show a reduction of volume and enlarging of the ventricles, due to a loss of grey matter. Microscopically, the pathological features of AD include aggregated protein deposits called plaques and neurofibrillary tangles (NFTs). NFTs (Figure 2.1A) are intraneuronal bundles of hyperphosphorylated tau, a microtubule-associated protein, bound into paired helical filaments. Plaques (Figure 2.1B) are extracellular protein deposits, whose main constituent is the amyloid β peptide (Aβ) (Glenner & Wong, 1984; Masters et al, 1985). The Aβ peptide has also been shown to accumulate intraneuronally, which may be an early step in the pathogenesis of AD (Wirths et al, 2004). Other pathological features include neuron and synapse loss, glial cell activation (microglia and astrocytes), and congophilic angiopathy, or the deposition of amyloid protein in the small blood vessels.

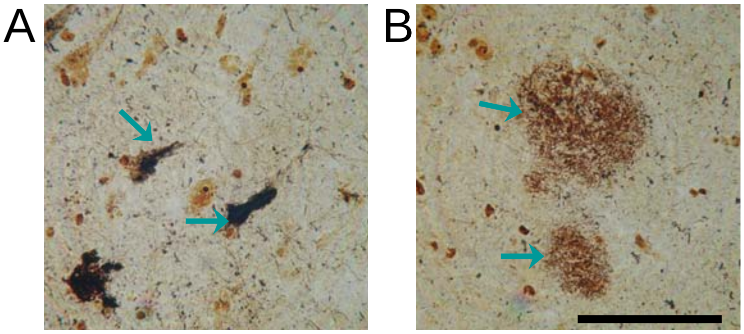

Figure 2.1. AD neurpathology. Post-mortem brain tissue from a human patient with AD, stained with Bielschowsky silver to show (A) neurons with neurofibrillary tangles, and (B) plaques, in the CA1 region of the hippocampus (images of tissue analyzed by Mandy Ogg (Ogg, 2002)). Scale bar 100 = µm.

The Aβ peptide was identified as the main constituent of plaques only 20 years ago (Masters et al, 1985). Aβ is 39 to 43 amino acids long and is cleaved from the amyloid precursor protein (APP). The 40 and 42 amino-acid peptides are the predominant components of plaques, but are also present in the cerebrospinal fluid and blood of normal individuals. APP is a highly conserved transmembrane protein with a poorly understood function. It can be up to 770 amino acids long, with APP695, APP751 and APP770 being the most common variants. APP can be cleaved by three protein secretases: α, β and γ (Figure 2.2). The α-secretase cleaves APP in the Aβ domain, preventing formation of the plaque-forming peptide. Cleavage of APP by β-secretase, followed by γ-secretase, forms the Aβ peptide. β-Secretase, or BACE-1 (beta-site APP cleaving enzyme) is a membrane-spanning aspartyl protease (Vassar & Citron, 2000). γ-Secretase, also an intermembrane aspartyl protease, is a complex of several proteins, including presenilins 1 and 2 (De Stropper, 2003). The position of cleavage by γ-secretase is variable. Aβ40 is the main species formed, followed by Aβ42. Although these two forms of Aβ have many properties in common, their aggregation properties are different (Bitan et al, 2003; Yan & Wang, 2006; Lim et al, 2007). In vitro, Aβ42 is known to aggregate much faster than Aβ40 and is more neurotoxic. The longer fragment accounts for only around 10% of the total Aβ, but is believed to play a central role in AD pathogenesis (Selkoe, 2001). Aβ42 is the main form of the Aβ peptide in plaques (Selkoe, 2001). Transgenic mice expressing Aβ42 develop dense-cored and diffuse plaques and vascular amyloid deposits, while mice expressing only Aβ40 fail to do so (McGowan et al, 2005).

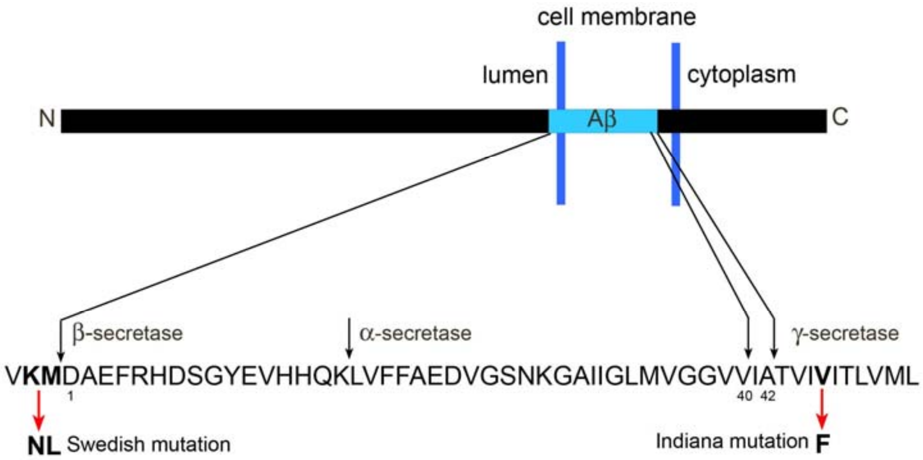

Figure 2.2. Schematic of the amyloid precursor protein. The location of the Aβ peptide is shown in blue, and its amino acid sequence, with the secretase cleavage sites, is shown at the bottom. The Swedish and Indiana mutations, responsible for some types of familial AD, are also shown.

2.1.2. Pathogenesis

There are numerous theories on the cause of sporadic AD. Roles have been proposed for inflammation, oxidative damage and disorders in energy metabolism, all of which have been identified in AD (Beal, 1995; Butterfield et al, 2002; Markesbery & Carney, 1999). However, plaques and NFT have attracted the most attention. The relative importance of plaques and tangles in Alzheimer disease is poorly understood and has been widely debated. Each has been suggested as the cause of the disease process, or merely a symptom (Hardy & Selkoe, 2002; Mudher and Lovestone, 2002; Smith et al, 2002). This is further complicated, because both or only one may be found in post-mortem brain tissue from demented, as well as cognitively normal, individuals (Braak & Braak, 1991). NFTs increase in number throughout the disease process and their number correlates with the duration of dementia, while the correlation with plaque load is poor (Inglesson, 2004).

FAD cases provide strong evidence for the central role of Aβ in AD. All of the mutations leading to FAD result in increased levels of the Aβ peptide, especially the more amyloidogenic Aβ42 (Scheuner et al, 1996; Citron et al, 1997). As well, individuals with FAD display NFTs, but no mutations in the genes for tau have been found. On the other hand, mutations in genes for tau protein on chromosome 17 lead to neurodegenerative conditions called tauopathies marked by NFT accumulation and neurodegeneration, but not Aβ plaques (Froelich-Fabre & Bhat, 2004; Goedert & Jakes, 2005). Similarly, transgenic mutant human tau mice accumulate phosphorylated, conformationally changed tau protein, but have no plaques (Ikeda et al, 2005; Goedert & Jakes, 2005). Injection of Aβ42 into transgenic tau mice enhances NFT formation (Gotz et al, 2001). Double mutant tau/APP mice, obtained from crossing transgenic tau and APP mice, develop more NFT pathology than the mice with the tau mutation alone (Lewis et al, 2001). This suggests that APP or Aβ may have an effect on NFT formation. As well, transgenic mice expressing mutant APP and presenilin-1 (and therefore accelerated Aβ plaque deposition compared to mutant APP mice) have phosphorylated, conformationally changed tau accumulation in the dystrophic neurites surrounding plaque cores (Samura et al, 2006). This strongly indicates that NFTs are a secondary feature of AD.

The toxicity of Aβ appears to be dependent on its aggregation. *In vitro*, Aβ fibrils have been shown to be toxic to cells, while amorphous Aβ was harmless (Lorenzo, 1994). The neurotoxicity of amyloid peptides was associated with amyloid fibril formation and the development of β-sheet secondary structure (Pike et al, 1995). However, the theory that pre-fibrillar intermediates are the more neurotoxic elements in AD is gaining acceptance (Lansbury, 1999; Watson et al, 2005). Soluble, prefibrillar intermediates, such as protofibrils and Aβ-derived diffusible ligands (ADDLs), are also neurotoxic (Walsh, 1999; Chromy, 2003). Aβ oligomers, ADDLs and fibrils are all toxic to cultured neurons, but by distinct mechanisms (Deshpande et al, 2006). Aβ oligomers and ADDLs bind to synaptic contacts and cell membranes and cause neuronal death, with the oligomers acting more rapidly. The fibrils cause neuritic dystrophy and significantly less cell death, on a much longer time scale than the smaller aggregates (Deshpande et al, 2006). This may explain the correlation between soluble Aβ species and disease progression, and the fact that the correlation between fibrillar amyloid load and neurological dysfunction is poor (Klein, 2001). It is however important to note that the Aβ peptide is found in the cerebrospinal fluid from normal individuals, which suggests that it may have a normal physiological role, such as regulation of synaptic activity (Pearson & Peers, 2006).

2.2. Aβ Plaques in Alzheimer's Disease

2.2.1. Aβ Plaque Morphology and Terminology

Aβ plaques are morphologically heterogeneous. Various, sometimes contradictory, classifications and names are used (Armstrong, 1998; Selkoe, 2001; Adlard & Vickers, 2002). However, the two main types are diffuse and dense-cored plaques. Diffuse plaques (sometimes erroneously called pre-plaques or pre-amyloid) are amorphous or non-fibrillar deposits of the Aβ peptide that lack a core and dystrophic neurites. Diffuse plaques are generally not associated with neurodegeneration or glial activation, and do not disturb the structure of the neuropil and dendrites (Wisniewski et al, 1998; Adlard & Vickers , 2002). Diffuse plaques do not stain with the amyloid dyes Congo-red or thioflavin, which implies that the Aβ peptide is not in the aggregated amyloid conformation (see section 2.2.2.). Dense-cored plaques, sometimes called cored neuritic or classic, have a core of Aβ peptide in the highly-aggregated amyloid conformation. They are often associated with dystrophic or degenerating neurites, microglia, reactive astrocytes and neuropil threads. The dystrophic neurites may contain paired helical filaments and are immunoreactive for tau protein. The cores may be surrounded by a halo of non-fibrillar Aβ. Some authors also describe compact or burnt out plaques, consisting of an isolated amyloid core (Cummings et al, 1998). However, analysis with confocal microscopy has revealed that these are actually dense-cored plaques (Dickson & Vickers, 2001). Fibrillar or primitive plaques have also been described. They are composed of distinct Aβ fibrils emanating from the centre, but lack a central amyloid core (Dickson & Vickers, 2001). These plaques are Congo red positive.

The presence of several types of plaques has led some authors to conclude that one type (diffuse) can evolve into another (dense cored). However, this theory is unlikely as all plaque types are present in both pre-clinical and end-stage AD (Dickson and Vickers, 2001), and the proportion of diffuse plaques may actually increase with disease progression (Wegiel et al, 2001). The different plaque types may therefore be formed by different processes. Diffuse plaques, for example, may be of neuronal origin, while dense-cored plaques may be formed by microglia (Wisniewski et al, 1998). Regional differences in plaque type are also found. Some brain regions, such as the caudate and the molecular layers of the cerebellum and dentate gyrus, only develop diffuse plaques even in advanced AD (Wegiel et al, 2001). This suggests that tissue-specific factors may affect plaque formation (Morris, 1997).

2.2.2. Aβ Structure

The Aβ peptide can form a variety of aggregates, including amyloid. Amyloid is the generic term for any proteinaceous extracellular deposit with a characteristic cross β-pleated sheet fibril structure (Glenner et al., 1974). Amyloids are insoluble under physiological conditions and are fairly resistant to proteolytic digestion. They stain with the dye Congo red, which then shows birefringence when viewed under cross-polarized light with the amyloid appearing bright green against a dark background (Glenner et al., 1972). Electron microscopy of amyloid reveals unbranched fibrils (70-120 Å in diameter) while a cross β-sheet conformation is indicated by X-ray crystallography (Glenner et al., 1972). Amyloids can be formed from different, unrelated proteins that are normally soluble. They are found in a number of pathological states and in various organs, i.e. the pancreas in diabetes and the brain in AD and Parkinson’s disease. The dense-cored or neuritic plaques found in Alzheimer’s disease show all the properties of classic amyloid. Amyloid fibril formation may be a common property of all proteins. Under the right conditions, many soluble proteins, not associated with amyloid diseases, have been shown to aggregate into β-sheet fibrils (Gazit, 2002; Taboada et al, 2006).

The general model of amyloid, the cross-β fibril, is based on fiber x-ray diffraction data (Figure 2.3) (Serpell, 2000). The fibrils are made of β-sheets, arranged perpendicular to the fiber axis (cross-β), with the hydrogen bonds parallel to the axis. The hydrogen bonding distance between β-strands is 0.47-0.48 nm, while the distance between the β-sheets is 1.07 nm. However, the exact molecular structure of amyloid fibrils is still not known (Lansbury, 1992). For example, it is unclear whether the β-sheets are parallel or antiparallel, and how similar are the amyloid fibrils formed by different peptides (Serpell, 2000; Tycko, 2003).

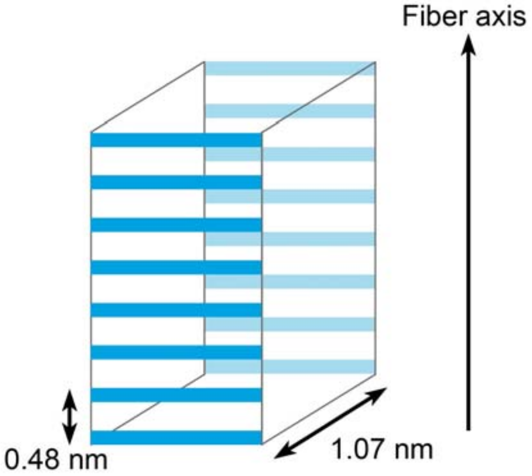

Figure 2.3. Aβ fibril. A model for the cross-β fibril, proposed on the basis of x-ray diffraction from amyloid fibrils. The intersheet distance is 1.07 nm and the hydrogen-bonding distance between β-strands is 0.48 nm (based on Serpell, 2000).

As a result of its central role in AD, the *in vitro* structure of various segments of the Aβ peptide has been studied extensively (Serpell, 2000). However, the structure is still poorly understood, as its tendency to aggregate and form insoluble fibrils makes Aβ unsuitable for study by methods such as single crystal X-ray crystallography, which would establish the structure unambiguously. Instead, techniques such as electron microscopy, solid state NMR spectroscopy, fiber x-ray diffraction, circular dichroism (CD) and FT-IR spectroscopy have been used (Lansbury, 1992; Halverson, 1990; Inoue, 1999; Tycko, 2003; Kirkitadze, 2001).

In vitro, Aβ can adopt a variety of structures, depending on its environment (solvent, pH, concentration) and time in solution (Serpell, 2000; Petkova, 2005). It can aggregate, changing from soluble monomers to highly aggregated fibrils that show all the properties of classical amyloid. The process appears to start when the soluble peptide, in an α-helix or random coil conformation, undergoes a conformational switch to a β-sheet structure, which then self-aggregates (Serpell, 2000). Various intermediate states exist along the way. Although the aggregation process has been extensively studied, it is still incompletely understood and there are some conflicting results. An oligomeric intermediate high in α-helix may precede formation of the β-sheet structure (Kirkitadze, 2001). However, the formation of β-sheet is always associated with the process of fibrillogenesis (Lansbury, 1999). Fragments of Aβ peptide adopt β-sheet structure when they precipitate, i.e. β-sheet formation is associated with insolubility (Halverson, 1990).

Two identified, soluble intermediates are the protofibrils and ADDLs. Protofibrils are flexible, fibrillar assemblies less than 200 nm in length and 4-11 nm in diameter (Harper, 1997; Walsh, 1997). Protofibrils form amyloid fibrils with time; circular dichroism analysis indicates that they are high in β-sheet (Walsh, 1999). ADDLs are globular oligomers (trimers to 24mers) of Aβ (Chromy, 2003).

The problem with *in vitro* studies is that they are not representative of what happens *in vivo*. During *in vitro* studies, a single, synthetic peptide, usually at fairly high concentrations, is incubated in a solvent, such as a water-based buffer. *In vivo*, the molecular environment is much more complex, containing many molecules that could modulate the aggregation process. High resolution electron microscopy indicates that, *in situ*, the structure of amyloid fibrils may be much more complex than *in vitro*, and may include other substances, such as heparin sulphate, chondroitin sulphate proteoglycans, amyloid P component and apolipoprotein E (Inoue, 1999).

2.2.3. Visualization of AD Plaques

Plaques in post-mortem tissue are commonly visualized with a variety of histochemical stains or immunostaining with specific antibodies (Westermark et al, 1999). Histochemistry of plaques relies on either silver impregnation methods or amyloid dyes. Silver impregnation methods include Bielschowsky, periodic acid-methenamine, Campbell-Switzer-Martin, Gallays, Globus, and Bodian staining (Yamaguchi et al, 1989; Vallet et al, 1992). The Bielschowsky method is widely used for diagnostic purposes, because it stains all the pathological elements of AD such as plaques, dystrophic neurites and neurofibrillary tangles, as well as normal neuronal processes. However, it is quite sensitive to experimental conditions (Litchfeld & Nagy, 2001). The Bielschowsky and periodic acid-methenamine methods can reveal diffuse plaques (Yamaguchi et al, 1989), as well as the cored plaques revealed by the other silver methods.

The amyloid dyes, such as Congo red and thioflavin S and T, stain amyloid plaque cores. These dyes bind to the general cross-β pleated sheet structure of amyloid fibrils, rather than to the specific amino-acid sequence of the proteins. The Congo red method is widely used because it is sensitive and simple to perform. Congo red (Figure 2.4) is a symmetrical sulfonated azo dye. It is believed to bind to the regular cross-β sheet structure of amyloids by intercalation (Carter and Chou, 1998).

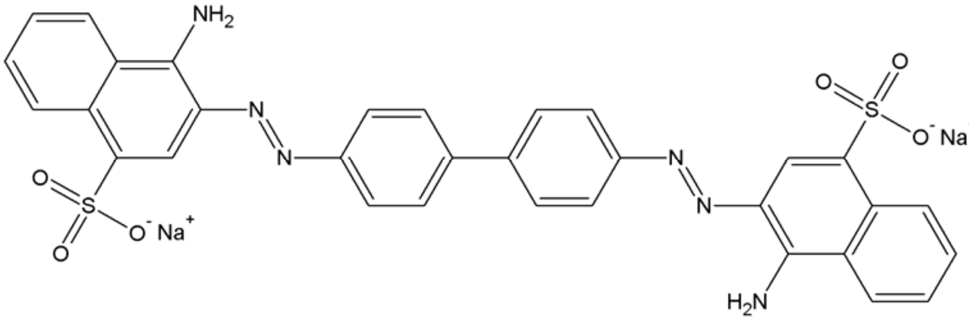

Figure 2.4. The structure of the amyloid dye Congo red.

Congo red-stained amyloid is pinkish-red and produces an apple-green birefringence under polarized light that is a characteristic of amyloids. The birefringence is believed to result from the highly organized binding of the Congo red molecules to the amyloid fibrils, as the dye molecules are oriented in a parallel and linear manner along the fibril (Westermark et al, 1999). Congo red-stained amyloid exhibits red fluorescence under UV light illumination (Puchler et al., 1985), which is useful for the detection of very small amyloid deposits (Linke, 2000). The thioflavin dyes, thioflavin S and T, also stain the amyloid cores of plaques (Westermark et al, 1999). However, the green fluorescence produced when thioflavin binds to amyloid needs to be viewed with a fluorescence microscope and fades with time.

Immunostaining with antibodies raised against Aβ is highly specific and more sensitive than silver stains, especially for diffuse deposits (Gentleman et al, 1989). The production of specific antibodies and their application for the visualization of proteins are standard techniques (Harlow and Lane, 1988). Most protocols involve treating the tissue with a fixative, usually containing formaldehyde, to prevent degradation. Sometimes an epitope retrieval step, to reveal the antigen site of the protein of interest, is required. This could involve enzymatic digestion, heat treatment, or for amyloids, formic acid treatment.

A blocking step to prevent non-specific binding of the antibody to the tissue may also be required. The tissue is incubated with a solution of proteins, such as bovine serum albumin, non-immune serum, or skim milk, to block non-specific binding. The sample is then incubated with the primary antibody. The antibody could be polyclonal, binding to multiple epitopes on the antigen, or monoclonal, binding to a single epitope. The resulting antibody-antigen complex can then be visualized with fluorescent or chromogenic dyes. Although the primary antibody itself could be labeled, a labelled secondary antibody can also be used.

Histochemistry and immunostaining are extremely valuable in studying tissues and cells. They are widely used in both research and diagnosis. However, most protocols are time-consuming and the results can be highly dependent on the experimental protocols and the quality of reagents.

2.3. Animal Models of AD

There is no natural equivalent of AD found in mice or other small animals. For many years, scientists had to rely on autopsy tissue from AD patients, a situation that made studying the sequence of events leading to AD almost impossible. For this reason, FAD mutations have been exploited to create transgenic mouse models of AD (Wong et al, 2002; Dodart et al, 2002; Phinney et al, 2003). In order to create transgenic AD mice, the genes for human APP, PS1 and PS2 (generally containing FAD-associated mutations) are engineered to express in mice (Treuting et al, 2002). The resulting mouse models display AD-like pathology with various levels of success. The genetic background of the mice, the choice of gene expression promoter, and the gene construct used in the creation of the model all affect the phenotype of the resulting AD mouse (Dodart et al, 2002). As well, species specific factors, the much shorter lifespan of the mice compared to humans, and the complex multifactorial nature of AD may limit the ability of the mouse models to mimic all aspects of AD (Dodart et al, 2002; Phinney et al, 2003). Depending on the model, the AD mice may exhibit plaques (diffuse and/or neuritic), cognitive deficits, astrocytosis, microglial activation and changes in cytoskeletal proteins, including tau. However, the failure of the mice to display all the features of human AD, including NFTs, has led some to question their usefulness in modeling the human disease (Dodart et al, 2002). Differences in the post-translational modification of Aβ in human and mouse plaques have been noted (Kuo et al, 2001; Kalback et al, 2002). The Aβ peptides in the mouse plaques lack the extensive post-translational modifications, such as isomerization, N-terminal degradation, racemization, pyroglutamyl formation, oxidation, and formation of covalently-linked dimmers, that are found in human Aβ plaques (Kuo et al, 2001;

Kalback et al, 2002). Nevertheless, the mice have proven themselves very useful in research, especially in the testing of potential therapies (Schenk et al, 1999; Janus et al, 2000; Chauhan et al, 2005).

2.3.1. TgCRND8 Mice

The TgCRND8 mouse was created at the Centre for Research in Neurodegenerative Diseases at the University of Toronto (Chishti et al, 2001). It expresses a double mutant form of human amyloid precursor protein (βAPP_{695}), with the "Swedish" mutation (K670N/M671L) and the "Indiana" mutation (V717F), expressed in the C3H/C57 background strain. These mutations are found at the N- and C-boundaries of the Aβ fragment, near the β- and γ-secretase cleavage sites (Figure 2.2). They favor the cleavage of APP into the amyloidogenic Aβ fragment, ensuring robust AD-type pathology in the mouse. The expression of APP in the brain is controlled by the hamster PrP gene promoter. APP and its cleavage products, Aβ40 and Aβ42, are detected in the brain and their levels increase with age. At 6 months, the levels of Aβ40 and Aβ42 are 190 and 510 times, respectively, the levels measured at 4 weeks (Chishti et al, 2001).

TgCRND8 mice have been thoroughly characterized with conventional histological and immunological methods (Chishti et al, 2001). They have normal hippocampal size and neuronal structure, but show early, robust plaque pathology. At just over two months, most of the animals have multiple plaques, and plaque loads continue to increase with age (Chishti et al, 2001). The cortex and hippocampus are affected earliest. The first plaques stain with thioflavin S and Congo red, indicating that the Aβ peptide is in the amyloid conformation. At just over three months of age, the plaques become heterogeneous in size and some have diffuse Aβ haloes. In older animals, there is great variety in plaque size and structure and some plaques are multi-cored. Diffuse plaques appear first in the olfactory bulb when the mice are over three months old, and at eight months in the caudate, molecular layer of the dentate gyrus, and cerebellum. They are found in the cortex by ten and a half months.

Dense-cored plaques in TgCRND8 mice are often accompanied by dystrophic neurites, as well as microglia and astrocytes, indicative of an inflammatory response. (Chishti et al, 2001). At four months, glutamatergic, GABAergic (gamma-aminobutyric acid) and cholinergic dystrophic neurites are found in the plaque periphery (Bell et al, 2003). In seven-month-old TgCRND8 mice, activated microglia infiltrate plaques, while hypertrophic astrocytes surround them (Belluci et al, 2006). The plaques are associated with neuronal degeneration and axonal damage. Dense-cored plaques in the white matter are accompanied by demyelination and a decrease in axonal staining (Belluci et al, 2006). At 7 months, there is a reduction in cholinergic neurons in TgCRND8 mice, compared to littermate controls and 2 month old TgCRND8 mice, which do not yet have plaques (Belluci et al, 2006).

The neuropathology in TgCRND8 mice is accompanied by behavioral symptoms. The mice show deficits in spatial learning, as measured by the Morris water maze test for spatial memory, from three months of age (Chishti et al, 2002; Janus et al, 2000). Behavioral testing revealed that cognitive impairment coincides with plaque development and progresses with age (Hyde et al, 2005).

2.4. IR Spectroscopy of Amyloid

2.4.1. *In Vitro* IR Spectroscopy of Amyloid-forming Peptides

Amyloid-forming peptides acquire β-sheet secondary structure upon aggregation (Gorman and Chakrabartty, 2001; Halverson et al, 1990; Serpell, 2000). The sensitivity of IR spectroscopy to changes in protein secondary structure has therefore been exploited to study amyloid forming peptides and proteins.

The IR spectra of amyloid fibrils have several features in common. Glenner et al studied a number of amyloid forming peptides and proteins (insulin, glucagon, Bence Jones protein fragments, and amyloids isolated from spleen, livers and kidneys). The amide I of all these β-pleated sheet proteins had a maximum at 1630+/- 3 cm^{-1}, as well as a shoulder at around 1650 cm^{-1}, indicative of some unordered and/or α-helical structure. The proteins in which the β-sheets were arranged in an anti-parallel fashion, such as the immunoglobulin VL fragment had an additional shoulder at 1696 cm^{-1}. This feature was absent in parallel β-sheet proteins, such as insulin fibrils (Glenner et al, 1974).

Similar results have been found for the AD plaque-forming Aβ peptide. IR spectroscopy has been used to study the Aβ peptide under various conditions to monitor the effects of solvents, pH, aggregation time and various mutations (Fraser et al, 1992; Fabian et al, 1993). Aggregated Aβ show a splitting of the amide I band into two peaks at around 1625 and 1685 cm^{-1}. When conditions favor unaggregated structure, the amide I band is generally centered at 1640-1650 cm^{-1}, indicating α-helical or unordered conformation.

The Aβ fibrils are most likely formed from intermolecular β-sheet, with the hydrogen bonds formed between peptides arranged in an anti-parallel fashion (Fabian et al, 1993). In fact, the amide I bands of globular β-sheet proteins are different from the intermolecular cross-β structure of amyloids. Generally, amyloid fibrils (formed from various proteins and peptides) have amide I maxima from 1611 to 1630 cm^{-1}, while globular β-sheet proteins have amide I maxima of 1630 to 1643 cm^{-1} (Zandemeneghi et al, 2004).

2.4.2. *In Situ* IR Spectroscopy of Amyloid

In situ IR studies of amyloid have been fairly limited. The first IR spectra of amyloid recorded *in situ* were of deparaffinized tissue sections of the amyloid produced by thyroid medullary carcinoma (O'Leary & Levin, 1985). Both β-sheet and disordered conformations were seen in the amyloid deposit. Choo et al analyzed two plaques in human AD brain using synchrotron IR microspectroscopy (Choo et al, 1996) and found that plaques had a predominantly β-sheet structure, while the surrounding tissue was mostly α-helical. The spectra of plaque core differed from in-vitro spectra of amyloid fibrils. Ogg studied tissue from several AD patients, with emphasis on hippocampal neurons, however several plaques were also IR mapped (Ogg, 2002). Miller et al looked at thioflavin stained human AD plaques with synchrotron IR microspectroscopy and synchrotron X-ray fluorescence (Miller et al, 2006). Some co-localization of increased Cu and Zn levels with plaques, high in β-sheet by IR, was reported.

All of the *in situ* AD studies found a maximum of 1630-1632 cm^{-1} for plaque cores. This corresponds to an increase in β-sheet protein structure associated with plaques. However, it differs from in-vitro spectra of Aβ-peptide, indicating that tissue-specific factors alter the structure. Changes in other IR bands, associated with plaques, have not been reported.

Chapter 3. Alzheimer's Disease Study Methods

An overview of the experiments is given in the first section. The second section describes the specific details of the experimental protocols employed.

3.1. Outline of the Experiments

The main goal of this thesis was to use synchrotron IR microspectroscopy to study brain tissue from TgCRND8 mice, a transgenic model of AD (Chishti et al, 2001). The hypothesis was that the high-resolution spectral information provided by that technique would provide new insights into the pathological processes of AD. The exact goals and hypotheses changed as I learned more about AD and the transgenic mouse model. This thesis was therefore composed of several parts, which are described in detail below.

1) Mapping of hippocampal neurons

> The initial hypothesis was that spectral differences, specifically an increased absorbance in the spectral region attributed to β-sheet proteins, exist between hippocampal CA neurons of transgenic AD and control mice. This hypothesis was based on previous work done on human AD samples by Mandy Ogg, a M. Sc. student in Dr. Gough's laboratory (Ogg, 2002). Neuronal spectra were compared in a blinded manner. This approach was unsuccessful, as the neurons are not affected in this transgenic AD model.

2) Identification of dense-cored plaques

> The hypothesis was that the dense objects found in TgCRND8 mouse brain, which were non-transparent when viewed under visible light, were in fact

dense-cored plaques. The IR spectra of these objects showed the presence of highly aggregated β-sheet protein. When the tissue was stained with the amyloid dye Congo red after mapping, these objects were confirmed to be dense-cored plaques. IR data processing protocols were modified in order to visualize the plaques and related pathological changes.

3) Mapping of dense-cored and diffuse plaques

The hypothesis was that IR would reveal spectral differences in and around both dense-cored and diffuse plaques, as well as changes that occurred with age. Serial sections were immunostained with anti-Aβ antibodies in order to identify the regions for IR spectroscopic mapping. Both diffuse and dense-cored plaques, some of which had a halo of diffuse Aβ around the dense core, were mapped. The initial data were collected on a set of 5 and 11-month-old mice. A second set of much older mice was obtained later, and analyzed in the same way.

4) Discovery of focally-elevated creatine deposits

An unusual spectral signature was found in some of the IR maps from the transgenic AD mice. This was identified as creatine, a molecule with a crucial role in energy metabolism. An initial analysis of this unusual, and previously unreported, anomaly was therefore undertaken.

3.1.1. Animals

The TgCRND8 (Tg(K670N/M671L+V717F)8 (C3H/C57)) mice and gender-matched littermate controls were provided by Dr. David Westaway from the Centre for Research in Neurodegenerative Diseases (CRND, University of Toronto). The first set included TgCRND8 mice and non-transgenic littermates at 5 months (3 TgCRND8 and 5 controls) and 11 months (4 TgCRND8 and 4 controls). Subsequently, a second set of several much older animals was obtained (see Table 15.1 in Appendix 2). They included 14-month-old animals (2 TgCRND8 and 2 controls) and one TgCRND8 plus one control at 16, 17 and 21 months. All animals were bred at the CRND.

The first set of 16 animals was sent from the CRND and the tissue was processed at the University of Manitoba by Dr. Marc Del Bigio and Dr. Michael Mayne (Department of Pathology). Half of each brain was processed for conventional histochemistry and immunostaining. Sections from each animal were stained to demonstrate plaque pathology. The other half was frozen and cryosectioned for IR analysis. I was initially provided with two or three sections from each animal mounted on MirrIR slides, and adjacent sections stained with hematoxylin and eosin, to help with examining the tissue morphology. The remaining tissue was stored at -70 ^{o} C until needed. The second set of older mice was provided at a later date by Dr. Westaway. The animals were processed by members of Dr. Gough's group, including me, with the help of Dr. Del Bigio. The tissue was treated in the same way as for the first set of animals.

3.1.2. Initial Mapping

IR mapping was initially performed in the hippocampus of each sample, as this region is affected earliest by AD in both transgenic mice and human patients. Several maps were collected in the hippocampus of each 5 and 11-month-old animal, both control and transgenic. The maps included the CA1, CA3, and dentate gyrus neurons, the neuropil and the white matter of the corpus callosum. Mapping was also performed in the cortex and the caudate. Data were collected in similar regions of control and transgenic mice.

3.1.3. Dense-cored Plaques

Dense-cored plaques were mapped in the hippocampus and cortex of the 5 and 11-month-old animals. After mapping, the tissue was stained with Congo red to visualize the aggregated amyloid of plaque cores. All the IR mapped samples, including those from the older mice prepared at a later time, were stained with the amyloid dye Congo red after mapping. The exact dimensions of the Congo-red positive plaques were measured and correlated with the IR data.

3.1.4. Plaque Staining

The initial staining done by Dr. Del Bigio, as well as the IR mapping, demonstrated the significant heterogeneity of the plaques. It became obvious that the IR analysis had to be directly correlated with conventional staining methods. I cut more sections from the frozen tissue from the 5 and 11-month-old mice. I developed an immunostaining protocol with the help of Dr. Sabine Mai (Manitoba Institute of Cell

Biology, University of Manitoba) using antibodies against the Aβ peptide. With this method, all plaque types, including dense-cored (some of which had a halo of diffuse Aβ) and purely diffuse, could be visualized. I stained serial sections with Congo red and anti-Aβ immunofluorescence, in order to gain a better understanding of the plaque morphology.

Although the immunofluorescence gave excellent results, the time-consuming imaging and eventual fading of the signal made this method impractical. I therefore developed a protocol using chromogenic detection, where the antibody-antigen complex is visualized with a coloured substance that can be viewed with conventional light microscopy. The resulting sections could be examined and photographed with light microscopy. Qualitatively, both methods were effective in visualizing both dense cored and diffuse plaques in TgCRND8 mouse brain.

3.1.5. IR Mapping Aided by Immunostaining

The TgCRND8 mice exhibited both dense-cored and purely diffuse plaques. The latter were invisible in the unstained tissue. Therefore, serial sections were immunostained to identify diffuse plaques, and the corresponding regions on MirrIR were IR mapped. Mapping of diffuse plaques was performed in the caudate, where they are the predominant type. Initially, I used immunofluorescence, but immunostaining with chromogenic detection was more practical. The best protocol involved cutting several sections adjacent to both sides of the section on MirrIR. These sections were placed on glass slides and stored at -70° C until needed. The serial sections on both sides of the IR section were immunostained for the Aβ peptide, while sections serial to those were stained with Congo red.

Diffuse plaques were mapped in the 11-month-old mice, and in the older mice from the second set. Corresponding regions in the caudate of control animals were mapped as well. No diffuse plaques were mapped in the 5-month-old mice as they were very rare at that age and no suitable regions for mapping were identified. Dense-cored plaques were also mapped in the same samples from mice of all ages.

3.1.6. Creatine in TgCRND8 Mice

In the course of IR mapping of transgenic mouse brain, I found an unusual spectral signature in many maps from TgCRND8 mice. This signature was identical to one found in human brain by Mandy Ogg (Ogg, 2002). A spectral library search, performed by Dr. Paul Dumas (LURE-CNRS, France) identified it as creatine, a molecule with a central role in energy metabolism. I re-analyzed my data, and found that the focally elevated creatine deposits were only found in AD mice. However, up to that point, only mapping of isolated areas of interest had been done, whether plaques or normal tissue. It therefore became clear that larger regions in both the control and transgenic mice had to be surveyed systematically in order to gain a better understanding of the distribution of the creatine deposits. I worked with Meghan Gallant (Master's student, Dr. K. Gough laboratory) on preparing new samples and collecting more IR data.

Some of the larger creatine deposits were visible in sections mounted on gold-coated slides, viewed in reflectance mode, as a slight difference in tissue texture, most likely due to the way the light reflects off them. Therefore, much of the subsequent mapping for creatine was done on the samples mounted on gold. One section was placed on glass, and later stained with Congo red to visualize dense-cored plaques. The adjacent section was placed on gold and IR mapped. The third adjacent section, mounted on glass, was immunostained with anti-Aβ antibody with chromogenic detection. The creatine deposits are discussed in detail in Chapter 7.

3.2. Detailed Experimental Protocols

The following sections describe the various protocols employed for this research.

3.2.1. Tissue Preparation

The animals were killed by cervical dislocation (i.e. the neck was broken with a blunt instrument). The brains were extracted and bisected sagitally along the midline. One half of the brain was covered in OCT compound (Sakura, Tokyo, Japan) or HistoPrep (Fisher), placed cut-side down on a small piece of cork and frozen in liquid nitrogen. It was stored at −70° C. The other half was placed in cold 3% paraformaldehyde in 0.1 M PBS for fixation, then dehydrated and embedded in paraffin. The animals were treated in accordance with the guidelines of the Canadian Council on Animal Care and the protocols were approved by the University of Toronto and the University of Manitoba

3.2.1.1. Paraffin-embedded Tissue

Paraffin embedded brain halves were used for general examination of tissue pathology prior to IR mapping. The tissue was cut into 6 μm sections in the sagittal plane, 0.5 mm from the midline and placed on glass slides. Sections from each animal were stained with hematoxylin and eosin, modified Bielschowsky silver stain, or Congo red. Immunohistochemical staining against ubiquitin (rabbit polyclonal, Dako, Carpinteria, CA) was also performed to detect dystrophic pathology associated with the plaques. The staining was performed by technicians in Dr. Del Bigio's laboratory.

3.2.1.2. Frozen Tissue

The frozen brains were used for IR microspectroscopy and anti-Aβ immunostaining. For IR microspectroscopy, the unfixed, flash-frozen tissues were cryotomed at 8 μm, placed on IR reflective slides (Low-e MirrIR^{TM}, Kevley Technologies, Chesterland, OH) or gold-coated silicone wafers (manufactured by Dr. P. de Stasio, SRC, University of Wisconsin) and desiccated at room temperature. Additional sections for immunostaining were placed on glass slides and stored at −70 °C until needed.

3.2.2. Congo-red Staining

This protocol, based on the alkaline, alcoholic method of Puchtler et al (Puchtler et al, 1962), was used for both frozen sections on glass and dried sections on MirrIR. For the dried sections, step 1 was omitted. The kit for performing Congo red staining was purchased from Sigma Diagnostics.

1) Frozen sections were defrosted at room temperature for several minutes.
2) Sections were fixed in absolute ethanol for 7 minutes and placed in water for 2 minutes.
3) The sections were counterstained in Mayer's hematoxylin (Sigma) for 10 minutes, and rinsed in tap water for 5 minutes.
4) The sections were placed in an alkaline sodium chloride solution (Sigma, 40 mL of 80% alcohol solution saturated with sodium chloride, mixed with 0.4 mL of 0.25 mol/L sodium hydroxide right before use) for 20 minutes.
5) The sections were placed in an alkaline Congo red solution (Sigma, 40 mL of solution, containing 0.2% Congo red dissolved in 80% alcohol saturated with sodium chloride, mixed with 0.4 mL of 0.25 mol/L sodium hydroxide right before use and filtered) for 20 minutes.
6) Sections were rinsed in three changes of absolute ethanol, cleared in xylene, mounted with Permount (Fisher) and coverslipped.

3.2.3. Immunostaining

Cryosections were immunostained with anti-Aβ antibodies and visualized with immunofluorescence or chromogenic detection, using standard protocols. Monoclonal antibody 4G8 (Signet Laboratories, Dedham, MA), which binds to amino acids 17 to 24 of the human Aβ peptide, was used for most staining (Kim et al, 1988). This antibody was especially good for the visualization of diffuse amyloid in this mouse model (Chishti et al, 2001). Additional sections were stained with anti-Aβ antibodies 6E10 (Signet Laboratories, Dedham, MA) and BAM-10 (Abcam, Cambridge, MA). All antibodies showed similar staining patterns. The protocols are given in the sections below. The antibody dilutions for immunofluorescence were 1 in 100 (Section 3.2.3.1), while for immunohistochemistry they were 1 in 2000 (Section 3.2.3.2).

Sections from age-matched mice not expressing the human APP gene were used as negative controls. The primary antibody was omitted from some sections of TgCRND8 and control mice, to exclude non-specific binding of the secondary antibody to the tissue.

3.2.3.1. Immunofluorescence

The following protocol, adapted from Fukasawa et al (Fukasawa et al, 1997) to be suitable for Aβ detection (Westermark et al, 1999), was used:

1) Sections mounted on glass were removed from the freezer and allowed to come to room temperature.
2) Sections were fixed in 3.7% formaldehyde buffered with PBS for 30 minutes.
3) The sections were washed in two changes of PBS.
4) The epitope was retrieved in 70% formic acid for 30 minutes.
5) The sections were washed in three changes of PBS.
6) The sections were blocked in 1% BSA in PBS for 30 minutes.

7) Excess blocking buffer was wiped carefully from the slide and 50 µL of primary antibody diluted in blocking buffer was placed over the tissue section and covered with a coverslip.
8) The sections were incubated for 2 hours at room temperature.
9) The coverslip was carefully removed and the slides washed three times in PBS.
10) 50 µL of Alexa Fluor ® 488 goat anti-mouse IgG secondary antibody (Molecular Probes, Eugene, OR), diluted in blocking buffer (1 in 200 dilution), was placed over the tissue and covered with a coverslip.
11) The sections were incubated for 30 minutes in the dark.
12) The coverslip was carefully removed and the slides washed three times in PBS.
13) The sections were counterstained with 4',6-diamidino-2-phenylindole (DAPI). 100 µL of 1µg/mL DAPI was placed over the tissue, covered with a coverslip and incubated for 5 minutes in the dark.
14) The coverslip was removed, excess DAPI shaken off and a drop of anti-bleach placed over the tissue.
15) The section was covered with a coverslip, blotted gently with tissue, and stored covered in a 4°C refrigerator until imaging with fluorescence microscopy (see section 3.2.4.).

3.2.3.2. Immunohistochemistry

The primary antibody was also detected with the StreptABComplex-horseradish peroxidase-conjugated Duet kit (Dako) visualized with diaminobenzidine (DAB), according to the manufacturer's protocol (steps 12 to 22). The following standard protocol, adapted for Aβ detection (Westermark et al, 1999), was used.

1) Sections mounted on glass were removed from the freezer and allowed to come to room temperature.
2) Sections were hydrated twice in TBS for 5 minutes to remove bound IgGs, thus decreasing background.
3) Sections were fixed in 3.7% formaldehyde buffered with PBS for 30 minutes.
4) The sections were washed in two changes of TBS.
5) The epitope was retrieved in 70% formic acid for 30 minutes.
6) The sections were washed in three changes of TBS.
7) The sections were blocked in 1% BSA in PBS for 30 minutes.
8) Excess buffer was tapped off and sections were covered with 0.6% hydrogen peroxide in methanol for 5 minutes.
9) Sections were rinsed with distilled water and placed in TBS for 5 minutes.
10) Sections were blocked with 20% nonimmune goat serum in 1% BSA in TBS for 30 minutes.
11) Excess blocking buffer was tapped off, and 50-100 µL of primary antibody diluted in 1% BSA in TBS was applied and incubated for an hour.

12) The sections were rinsed with TBS and placed in TBS bath twice for 5 minutes.
13) The sections were covered with biotinylated goat antibody to mouse/rabbit immunoglobulins diluted in TBS, and incubated for 20 minutes.
14) The sections were rinsed with TBS and placed in TBS bath twice for 5 minutes.
15) The sections were covered with StreptABComplex/HRP diluted in TBS, and incubated for 20 minutes.
16) The sections were rinsed with TBS and placed in TBS bath twice for 5 minutes
17) Sections were incubated with diluted DAB+ (Dako) solution for 1 minute.
18) The sections were rinsed with distilled water and placed in a distilled water bath for 1 minute.
19) Sections were counterstained for 3 minutes in Mayer's hematoxylin.
20) The sections were rinsed in tap water and incubated in a tap water bath for 1 minute to develop the counter stain.
21) The sections were dehydrated by being placed for 2 minutes in 70% ethanol, 2 minutes in absolute ethanol, and 2 minutes in xylene.
22) The sections were mounted with Permount (Fisher) and coverslipped.

3.2.4. Fluorescence Microscopy

Dense-cored plaques stained with Congo red after IR mapping and immunofluorescence-stained sections were examined with fluorescence microscopy. The slides were imaged on a Zeiss Axiophot microscope equipped with a SenSys digital camera (Photometrics, Tucson, AZ), and MacProbe v4.4 software (Applied Imaging, San Jose, CA). Images of plaques in the cortex, hippocampus and caudate putamen were taken at 40× magnification. Afterwards, 20× images were taken of adjacent areas of the entire hippocampus and of the part of the cortex and caudate putamen that was imaged. These images were pasted together to create an image of the fluorescent staining pattern of the area of interest.

Images of Congo red-stained plaques (which had been IR mapped prior to staining) at 40× magnification were obtained on the Zeiss Axiophot microscope, both in brightfield mode and fluorescence mode using a FITC filter set (absorption maximum, 495 nm; emission maximum, 525 nm). The red fluorescence under UV light illumination

(Puchtler et al, 1985) was more sensitive than examination under visible light for detection of very small Congo red stained amyloid (Linke, 2000). Plaque dimensions in Congo red and antibody stained sections were measured with MacProbe v4.4 software, calibrated with a stage micrometer slide.

3.2.5. IR Microspectroscopy

3.2.5.1. IR Data Collection

Data collection was performed at the Synchrotron Radiation Centre (SRC, the University of Wisconsin) and at the National Synchrotron Light Source (NSLS, Brookhaven National Laboratories). IR maps were recorded on a Nicolet Magna 500 FTIR with Nicolet Nic-Plan IR microscope (SRC) or a Nicolet Magna 860 FTIR with a Spectra Tech Continuum IR microscope (NSLS). A few maps were collected with a new Nicolet Continuum IR microscope installed at the SRC in the fall of 2006. All spectra were collected in reflectance mode from 4000 to 800 cm^{-1} at 4 cm^{-1} spectral resolution, using Happ-Genzel apodization. From 16 to 128 spectra were coadded, depending on the operating conditions, to achieve acceptable signal-to-noise ratio. Spectral maps were collected by raster scanning across the area of interest, using a step size of 10 μm and an aperture of 12x12 μm. The spectra were saved in log(1/R) format. In reflectance mode, the light passes through the sample and is then reflected back by the slide, making two passes through the tissue. The absorbance is therefore defined as log(1/R), where R is the ratio of the reflectance of the sample and the reflectance of a blank.

3.2.5.1.1. Tissue Component IR Spectra

In order to aid with the interpretation of tissue IR data, spectra of a number of isolated tissue components were collected. They included a protein (bovine serum albumin), phospholipids (phosphatidylcholine, sphingomyelin), sugars (mannose, glucose, lactose) and nucleic acids (baker's yeast RNA, calf thymus DNA). Samples containing 10 mg/ml of each component were made by dissolving the appropriate amount of the component in water, or for the phosphatidylcholine and sphingomyelin, in 1:1 methanol/chloroform. A small amount of the solution (50 μm) was placed on an IR transparent window and dried under vacuum. Infrared spectra were collected on a Nicolet Nexus 870 interferometer, at 4 cm^{-1} spectral resolution, using Happ-Genzel apodization. An average of 128 or 256 spectra were co-added for each sample.

3.2.5.2. IR Spectral Analysis and Data Processing

IR maps were analyzed with OMNIC/Atlμs software (ThermoNicolet), on original, unprocessed spectra. Smoothing, derivatization and Fourier self-deconvolution were not employed, in order to avoid the introduction of artifacts. Numerous methods of processing the data were tried, based on well-established assignment of IR bands in biospectroscopy (Parker, 1983; Mantsch and Chapman, 1996). The areas or heights of peaks due to specific components, and their ratios, were represented on a false color scale. The exact univariate and bivariate methods used to process brain tissue maps are outlined in Table 3.1. Several of the bands were ratioed with the amide I band. This gave a better picture of the distribution of components in regions where the tissue was very dense, such as plaque cores. However, in most instances, maps of peaks ratioed against the amide I were almost identical to those of unratioed bands, as the amount of protein in normal tissue was fairly constant.

Table 3.1. Processing parameters used for brain IR maps

Function	Peak 1 (cm^{-1})	Baseline (cm^{-1})	Peak 2 (cm^{-1})	Baseline (cm^{-1})	Display limits**
Lipid					
CH_2 peak height	2922	2998-2760			0.12-0.45
CH_2/CH_3 peak area ratio*	2940-2912	3007-2814	2978-2951	3007-2814	1.3 to 2.4
Peak area ratio: CH_2/Amide I	2940-2912	2998-2760	1700-1600	1806-900	0.01-0.25
Protein					
Amide I peak area	1700-1600	1806-900			40-90
Peak area ratio to detect amide I shift*	1636-1646	1770	1662-1652	1770	0.6-0. 95
Peak area ratio to detect plaques	1662-1652	1806-900	1630-1620	1806-900	0.8-2.2
Other Peaks					
1080 cm^{-1} peak area	1130-1014	1145-900			4.5-12
Peak area ratio: 1080 cm^{-1}/amide I	1130-1014	1145-900	1700-1600	1806-900	0.04-0.3
1230 cm^{-1} peak area	1275-1205	1290-1185			3.1-4.8
Peak area ratio: 1230 cm^{-1}/amide I	1275-1205	1290-1185	1700-1600	1806-900	0.04-0.1
Total peak area or chemigram	3999-900	3999-900			300-1500

* Method developed by Mandy Ogg (Ogg, 2002)
** The display limits used in most maps. Conditions during data collection could require the use of adjusted display limits (see section 4.4.1 and Chapter 13).

3.2.5.2.1. Lipids

Membrane lipids, made of long acyl chains, have strong peaks due to CH stretches that can be used to image the lipid content of brain tissue. The CH stretch bands can be used to distinguish the myelin-coated nerve cell fibres of white matter from the grey matter based on their higher lipid content (Wetzel & LeVine, 1993). Chemical maps showing the lipid content of tissue were therefore created using the peak height at 2922

cm^{-1}. As the position of this peak was shown to be very constant, the peak height, rather than the peak area could be used. Other molecules, like proteins and sugars, also have functional groups that will give rise to absorptions in the CH stretch region. However, these molecules do not contain the type of long acyl chains found in lipids, where the proportion of CH_2 groups relative to CH_3 groups is very high. Therefore, as the proportion of lipids (with their long acyl chains) increases in tissue relative to other components, the intensity of the CH_2 stretching peaks increases relative to the CH_3 stretching peaks. Neuronal nuclei in the gray matter can be distinguished from the surrounding neuropil on the basis of the CH_2/CH_3 peak height ratio (Ogg, 2002).

3.2.5.2.2. Proteins

The amide I is the strongest vibration due to proteins. It overlaps with peaks due to nucleotide base pairs, but as the amount of protein in cells is many times larger than the amount of nucleic acids, the total area of this peak (1700-1600 cm^{-1}) can be used to image the protein content of the sample. The shape and position of the amide I band is strongly dependent on the protein secondary structure (Bandekar, 1992). Amide I maxima between 1662-1650 cm^{-1} are generally assigned to α-helix; 1650-1640 to random coil; 1640-1620 to β-sheet (Bandekar, 1992; Krimm & Bandekar, 1986; Surewich et al, 1993). Thus, a ratio of an area due to one protein conformation to the area of another, represented on a false color scale, can be used to image the average proteins secondary structure of the tissue (Ogg, 2002). A ratio of peak area from 1646 to 1636 cm^{-1}, to the area from 1662 to 1652 cm^{-1}, was used to image the normal variations in protein secondary structure in the brain due to various tissue types, such as white matter, gray matter and neurons. Images of the distribution of highly aggregated β-sheet due to plaques were based on the ratio of the amide I area from 1662 to 1652 cm^{-1} (α-helix) to the area from 1630 to 1620 cm^{-1} (β-sheet).

3.2.5.2.3. Other Peaks

The 1080 cm^{-1} peak contains contributions from the phosphate symmetric stretch modes of phospholipids and nucleic acids, as well as carbohydrate C-O stretching bands. The 1230 cm^{-1} peak includes phosphate asymmetric stretch and amide III modes. Maps showing the relative intensities of these bands were created from integrated peak areas from 1130 to 1014 cm^{-1} and 1275 to 1205 cm^{-1}, respectively.

The physical integrity of the tissue was imaged using the total integrated intensity under all peaks. This produces a false-color total intensity image, called a chemigram by the Atlμs software (ThermoNicolet). Unusually strong integrated intensity indicated the presence of a fold in the tissue or very dense plaque cores, while low integrated intensity indicated thinner or torn tissue.

3.2.5.2.4. Hierarchical Cluster Analysis

Hierarchical cluster analysis was performed with CytoSpec software using D-values distance matrix calculations and Ward's hierarchical clustering algorithm (Lasch et al, 2004). The spectral regions used are shown in Table 3.2. They included the amide I and II bands, the CH stretch region, the fingerprint region and various combinations thereof. The analysis was done on both the original spectra, as well their second derivatives, which may emphasize subtle variations in peak curvatures while minimizing baseline effects (Gough et al, 2005). Second derivatization was attempted because it is widely used with chemometric methods such as cluster analysis. However, as it did not prove to be useful (see section 4.4.4.6), it was not employed in this study.

Table 3.2. Spectral regions used for hierarchical cluster analysis of brain tissue

Region	**Wavelength Range (cm^{-1})**
Amide I	1700-1600
Amide I and II	1700-1500
Fingerprint region	1700-1010
Phosphate and sugar region	1335-1010
CH stretch region	2998-2830

Chapter 4. Alzheimer’s Disease Study Results

4.1. Overview

The goal of this project was to use synchrotron IR microspectroscopy to study changes in the molecular composition of brain tissue from a transgenic mouse model of AD. The hypothesis was that the information provided by IR microspectroscopy would provide new insights into the pathological processes of AD. IR spectra provide information about chemical composition and conformation, such as protein secondary structure, while AD is associated with the formation of protein aggregates, known as plaques, in the brain. The use of synchrotron light gives the highest spatial resolution possible with mid-IR light (3 to 10 microns) for studying heterogeneous biological tissue samples.

Initially, IR mapping was performed in the hippocampus, a part of the brain severely affected by AD. When this region was studied in human samples, spectral differences were found between post-mortem tissue from normal, early AD and AD samples (Ogg, 2002). However, very limited information was available on the human subjects. The diagnosis of AD was based on tissue pathology, and the immediate cause of death was the only clinical information available about each subject. Analysis of a transgenic mouse model, with its clearly defined disease state and available littermate controls, was therefore undertaken as the central project of this thesis. The use of an animal model also allowed the disease to be studied at various stages.

Data was collected from two sets of animals. The initial set included 5 control and 3 TgCRND8 mice at 5 months, and 4 control and 4 TgCRND8 mice at 11 months. The second set included two controls and two TgCRND8 mice at 14 months, as well as one control and one TgCRND8 mouse at 16, 17 and 21 months. The tissue was analyzed by IR mapping, and the results were correlated with conventional histochemistry and immunostaining. Initial IR maps in the first set of animals included the neuropil, hippocampal neurons and corpus callosum white matter. Aβ plaques, however, were the focus of this study. Dense-cored and diffuse plaques were IR mapped in both sets of animals. The regions of the brain studied included the hippocampus, cortex and caudate, as these were the areas that exhibited extensive plaque pathology.

4.2. Brain Tissue Samples

IR mapping was performed on desiccated, 8 μm thick sections mounted on the appropriate substrate. The number of sections used per animal ranged from 2 to 6. Even though the sections were unstained, the overall morphology could be identified as the white matter fibers looked very different from the smooth grey matter. Figure 4.1A shows an unstained sagittal section from a control mouse. The hippocampus, cortex, caudate and other regions can be identified from the patterns formed by the white matter. The nuclei of neurons are also generally distinguishable from the neuropil (Figure 4.1B). The hippocampus, a part of the temporal lobe, was studied especially closely as it is the region of the brain most severely affected by AD. It has a highly organized structure that includes the densely-packed neurons in the dentate gyrus and the CA1 and CA3 fields of the Cornu Ammonis (CA) (Figure 4.1C).

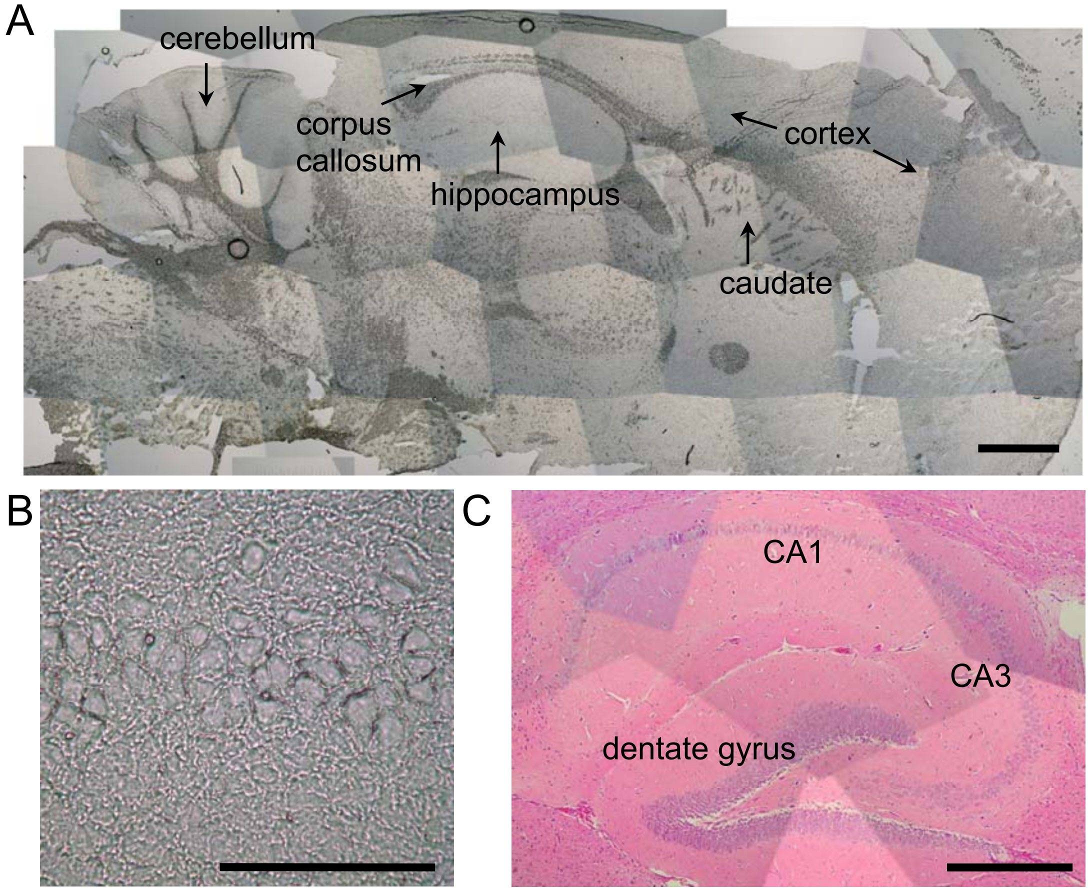

Figure 4.1. Morphology of a sagittal mouse brain section. (A) Whole unstained section from a 5-month-old control mouse mounted on MirrIR. Scale bar = 1000 µm. (B) A close-up of hippocampal CA1 neurons in an unstained section. Scale bar = 100 µm. (C) A hematoxylin (blue-purple) and eosin (pink) stained hippocampus. The locations of the CA1, CA3 and dentate gyrus neurons (blue-purple staining) are indicated.
Scale bar = 400 µm.

4.3. Histochemistry and Immunohistochemistry

Brain tissue from TgCRND8 mice and non-transgenic littermate controls was evaluated by histochemistry and immunohistochemistry. The gross morphology of TgCRND8 and littermate control brains was identical. Closer examination revealed AD plaques in the TgCRND8 mice. Dense-cored plaques were visible in the unstained tissue, since their density obscures the light when illuminated from below (Figure 4.2A). Histological and immunological stains revealed further pathology in the TgCRND8 mice.

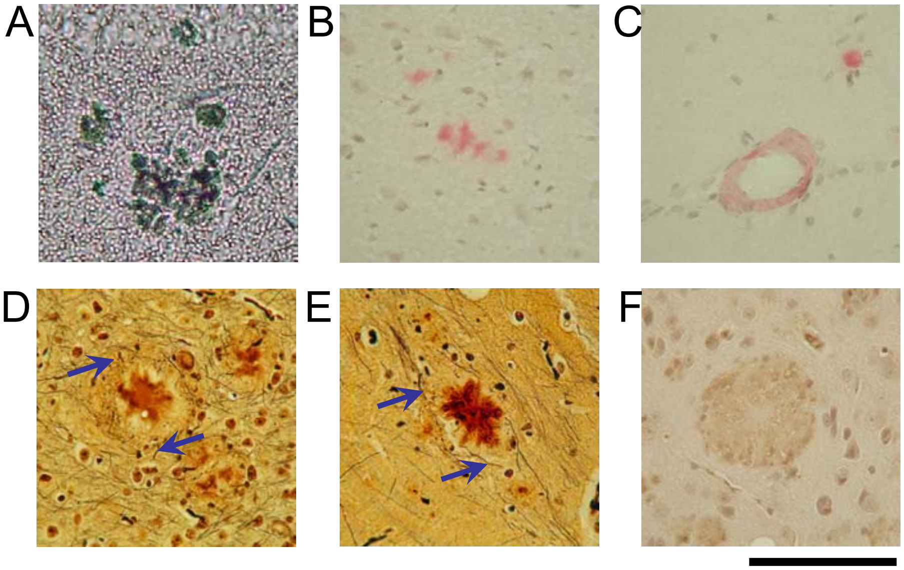

Figure 4.2. AD pathology in TgCRND8 mice. (A) An unstained dense-cored hippocampal plaque on a MirrIR slide. Tissue from an 11-month-old TgCRND8 mouse stained with Congo red to show (B) plaque cores and (C) vascular amyloid in the hippocampus. Bielschowsky silver-stained plaques in the (D) cortex and (E) hippocampus of an 11-month-old TgCRND8 mouse. Arrows point to dystrophic neurites. (F) A plaque in the cortex of an 11-month-old TgCRND8 mouse immunostained with an anti-ubiquitin antibody. Scale bar = 100 µm.

In all transgenic brains, the Congo red stain revealed multiple dense-cored plaques, primarily in the cortex and hippocampus, measuring up to 60 microns in diameter (Figure 4.2B). Many blood vessels in transgenic mice 11 months and older were

Congo red positive, indicating the presence of vascular amyloid deposits (Figure 4.2C). Fibrillar amyloid in cores was confirmed by birefringence under polarized illumination (not shown). In the Bielschowsky silver stained sections, plaque cores stained dark brown and had a feathered edge (Figure 4.2D and E). The cores were surrounded by a halo of abnormal neuropil and darkly-staining dystrophic neurites (Figure 4.2D and E, arrows). Weak immunoreactivity to ubiquitin, a feature of protein deposits in many neurodegenerative disorders (Lowe et al, 2001) was associated with the plaques (Figure 4.2F).

Anti-Aβ immunostaining with antibody 4G8 (with both fluorescent and chromogenic detection) was employed to visualize the Aβ peptide in plaques. Unlike Congo red, which only stains highly aggregated amyloid, anti-Aβ antibodies bind to an epitope on the Aβ peptide, regardless of its aggregation state. Immunostaining therefore revealed the dense plaque cores, the haloes of diffuse Aβ surrounding some cores, and the purely diffuse plaques (Figures 4.3 and 4.4).

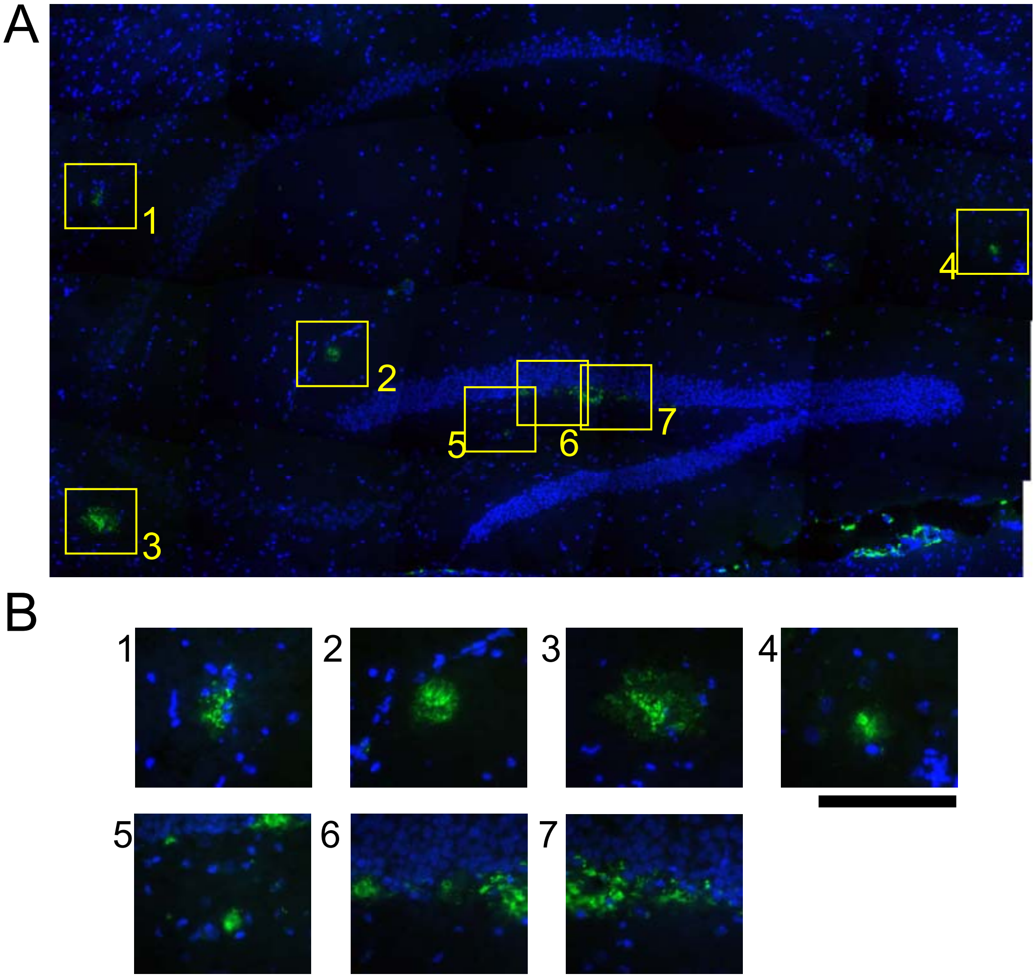

Figure 4.3. Anti-Aβ immunofluorescence in 5-month-old TgCRND8 mouse. (A) The entire hippocampus immunostained with antibody 4G8 to reveal plaques (green) and nuclear dye DAPI (blue). (B) Close-up images of plaques outlined in yellow boxes in (A). Scale bar for B = 100 μm.

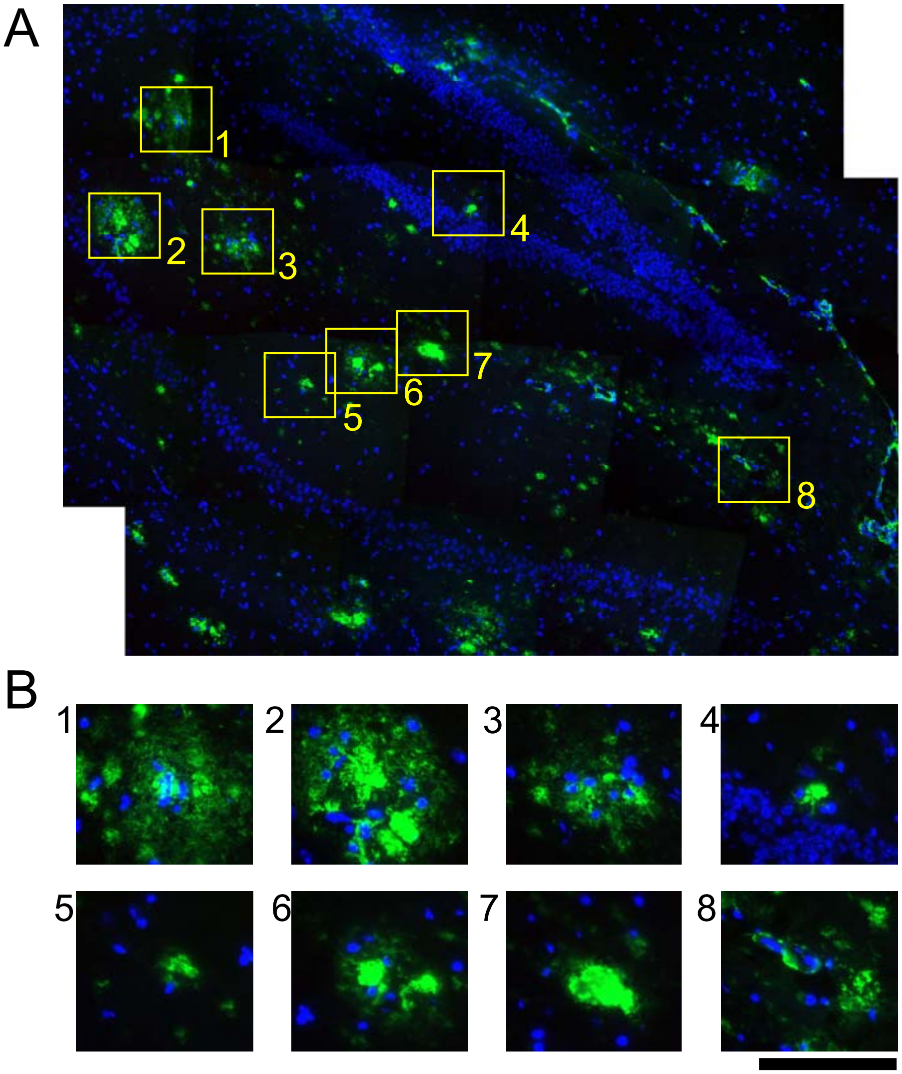

Figure 4.4. Anti-Aβ immunofluorescence in 11-month-old TgCRND8 mouse. (A) The entire hippocampus immunostained with antibody 4G8 to reveal plaques (green) and nuclear dye DAPI (blue). (B) Close-up images of plaques outlined in yellow boxes in (A). Scale bar for B = 100 µm.

Staining of serial sections with anti-Aβ immunofluorescence and Congo red illustrated different aspects of plaque morphology. Figure 4.5A-C shows a large multi-cored plaque common to both sections. The cores are Congo red positive (Figure 4.5A, B), and surrounded by diffuse immunostaining (Figure 4.5C), demonstrated with antibody 4G8. The contrast between the cores and haloes of plaques is demonstrated especially well with another anti-Aβ antibody, BAM-10 (Figure 4.5D and E).

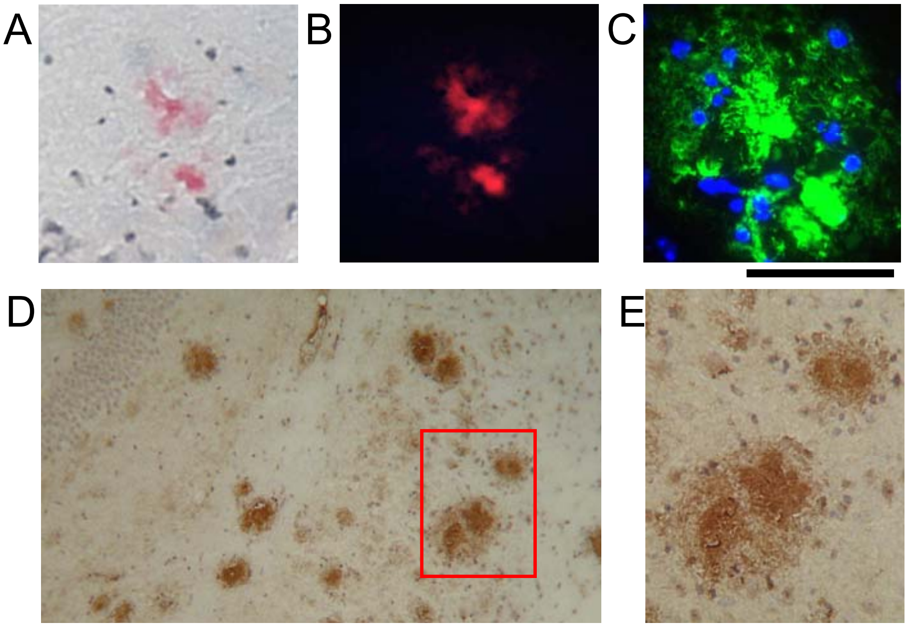

Figure 4.5. Dense-cored plaques surrounded by diffuse Aβ haloes. A plaque in the hippocampus of an 11-month-old TgCRND8 mouse stained with Congo red, viewed with (A) normal illumination and (B) fluorescence. The same plaque in a serial section examined with (C) immunofluorescence against Aβ with antibody 4G8 (green) and nuclear dye DAPI (blue). In a 17-month-old TgCRND8 mouse, the diffuse halo of Aβ surrounding the cores is visible after immunostaining with anti-Aβ antibody BAM-10, at (D) x10 and (E) x40 magnification. Scale bar = 100 µm for A-C, E.

The age of the mice in this study ranged from 5 to 21 months, with plaques present in all transgenic animals. Their number and size increased with age, as illustrated by hippocampi from TgCRND8 mice immunostained with anti-Aβ antibody 4G8 (Figure

4.6A-F). Plaques were never found in the littermate controls, even at 21 months (Figure 4.6G).

In 5-month-old mice, plaques were sparse and found mostly in the hippocampus and cortex, very rarely in the caudate. Most were small (10 to 30 μm diameter, Congo red or Bielschowsky staining) and associated with a single, Congo red positive core. In the 11-month-old mice, the plaques were more numerous, often multi-cored and heterogeneous in size (10 to 60 μm) and shape, and sometimes surrounded by diffuse anti-Aβ immunostaining. Aβ-positive diffuse plaques, not associated with a congophilic core, were found in the caudate, cortex and hippocampus. Diffuse plaques were the predominant form in the caudate grey matter of 11-month-old mice, in agreement with previous reports (Chishti et al, 2001). Diffuse immunostaining was also found in the molecular layer of the dentate gyrus. The oldest TgCRND8 mice (14 to 21 months) exhibited extensive plaque pathology. Large, multi-cored plaques and diffuse immunostaining were abundant.

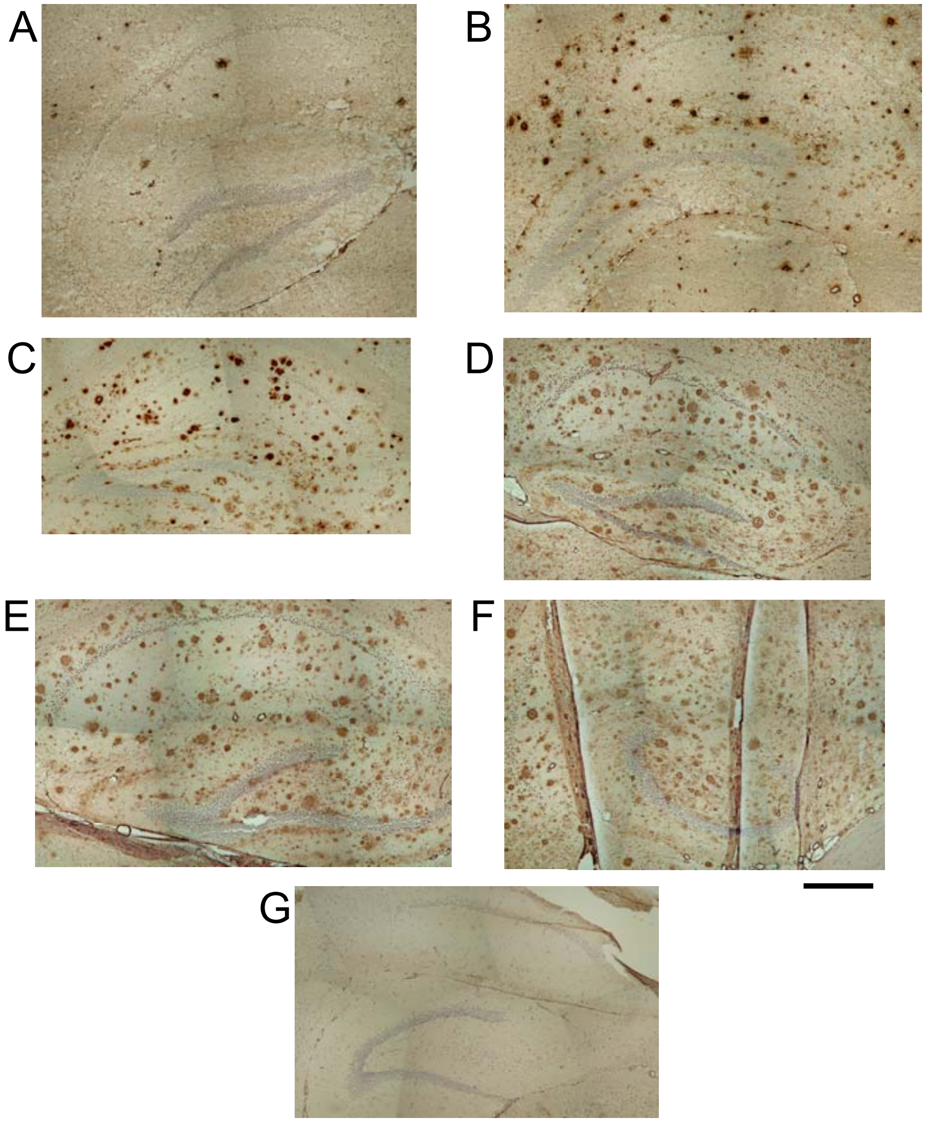

Figure 4.6. Hippocampal plaque load in TgCRND8 mice. Hippocampi in TgCRND8 mice immunostained with anti-Aβ antibody 4G8 at (A) 5 months, (B) 11 months, (C) 14 months, (D) 16 months, (E) 17 months, and (F) 21 months. (G) A 21-month-old littermate control stained with the same protocol has no plaques. Scale bar = 400 μm.

Closer examination of immunostained plaques revealed their significant structural heterogeneity; this was especially obvious in the older mice. Figure 4.7 shows typical plaques in the (Figure 4.7A-C) hippocampus, (Figure 4.7D-F) cortex, and (Figure 4.7G-I) caudate of a single 14-month-old TgCRND8 mouse. The plaques in the hippocampus and cortex are mostly dense-cored. They range in size from 10 to over 100 µm, and can be either single or multi-cored. Some plaques are surrounded by varying amounts of diffuse Aβ. The plaques in the caudate are mostly diffuse; they too are variable in size.

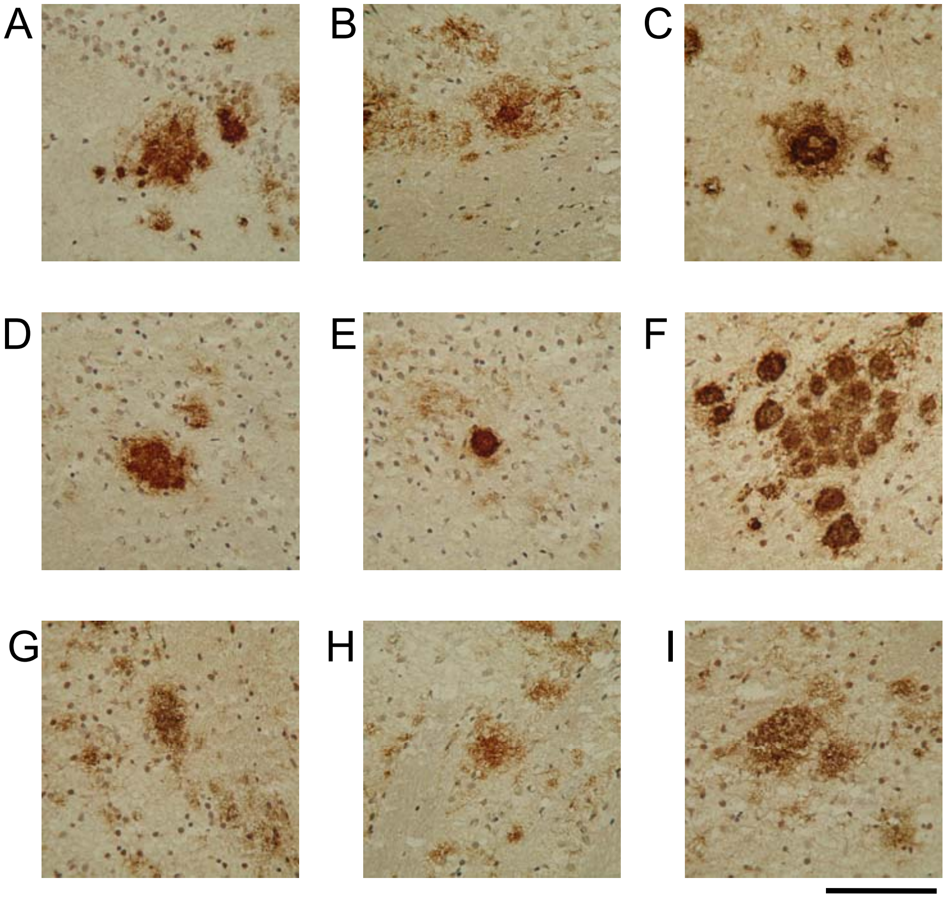

Figure 4.7. Variability of plaque morphology in TgCRND8 Mice. Brain tissue from a 14-month-old TgCRND8 mouse immunostained with anti-Aβ antibody 4G8. Dense-cored plaques in the hippocampus (A, B, C) and cortex (D, E, F), and diffuse plaques in the caudate (G, H, I). Scale bar = 100 µm.

4.4. IR Mapping of Brain Tissue

IR mapping was performed in the hippocampus, cortex and caudate of TgCRND8 and control mice. IR spectra of mouse brain (Figure 4.8) show absorption peaks due to the functional groups of the biological molecules (Parker, 1983; Mantsch & Chapman, 1996). Tissue spectra look simple, but are actually the sum of the spectra of millions of different molecules that make up living organisms. Usually, the most intense peak is the amide I band of proteins, found at around 1660 cm^{-1}, followed by the amide II peak at 1550 cm^{-1}. The amide III, found at 1240 cm^{-1} is much weaker. This peak overlaps with the asymmetric phosphate stretch. Similarly, the peak centered at 1080 cm^{-1} is due to the overlap of symmetric phosphate stretch and phosphodiester C-O-P-O-C stretch, with various sugar bands. The phosphate peaks are due to the membrane phopholipids and, to a smaller extent, nucleic acids. The peaks at 2956 and 2922 cm^{-1} are due to asymmetric CH_3 and CH_2 stretching, while the weaker peaks at 2871 and 2851 cm^{-1} are due to symmetric CH_3 and CH_2 stretching, respectively. Most of the intensity of the CH stretching peaks is due to the acyl chains of lipids. The C=O stretch of lipid esters is found at 1738 cm^{-1}. The broad absorbance at 3330 cm^{-1} is due to NH and OH stretching. The exact shapes and intensities of the peaks are a reflection of molecular composition. Spectra of brain tissue (Figure 4.8) are dominated by the peaks of proteins and phospholipids, as these are the main components of brain.

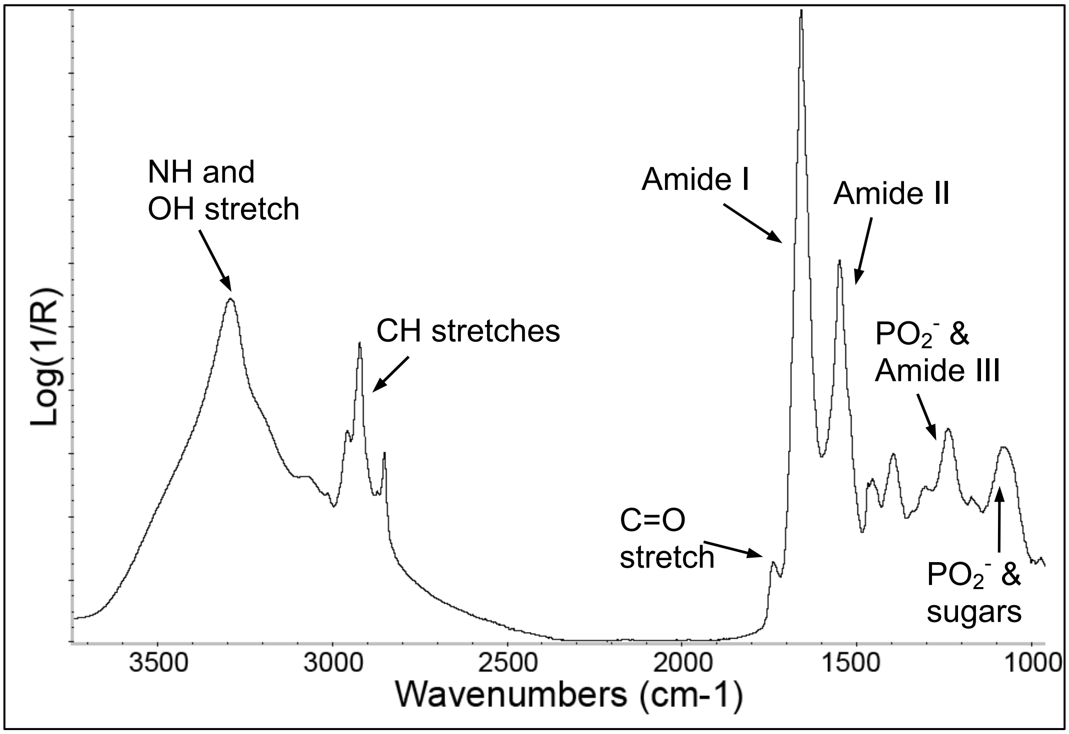

Figure 4.8. Representative IR spectrum of neuropil tissue in the cortex of a control mouse.

4.4.1. Processing of IR Maps

In order to extract useful information from IR maps, it is necessary to represent the chemical information available in the individual spectra as images. The spectral results can then be correlated with sample morphology. A number of approaches were employed to process IR maps. The methods were based on known peak assignments (Parker, 1983; Mantsch and Chapman, 1996) but were fine-tuned through trial and error to give the best contrast possible. The data analysis protocols employed could be divided into three main categories; univariate, bivariate and multivariate. An example of each will be shown below, as applied to an IR map of the corpus callosum and CA1 region of the hippocampus of a control mouse. The exact details of the protocols employed to process the maps are given in Table 3.1 in the Methods section.

Univariate methods are based on peak heights or areas. The value calculated for each pixel in the IR map is represented on a false color scale. This approach is used to display peak intensity changes (and therefore relative concentrations of functional groups) across the IR map. With this protocol, for example, the relative intensity of the CH_2 peak (Figure 4.9A), due mostly to the acyl chains of lipids, can be used to create a false color image (Figure 4.9B). In the spectral map (Figure 4.9B), the dark blue region (high CH_2 intensity) corresponds to the corpus callosum white matter, the darker region on the left side of the corresponding photomictrograph (Figure 4.9C). The red, yellow and green regions correspond to neuropil, and the white regions (very low intensity of CH_2) show the CA neurons, which are indicated with red arrows in the corresponding photomicrograph (Figure 4.9C). It is important to note that IR microspectroscopy is a semi-quantitative method, as the exact sample thickness is not known. However, the relative changes in band intensity across the spectral map can be imaged. The scale bars simply show which colors represent relatively high or low peak intensities in the map. The display limits for each processing method are given in Table 3.1.

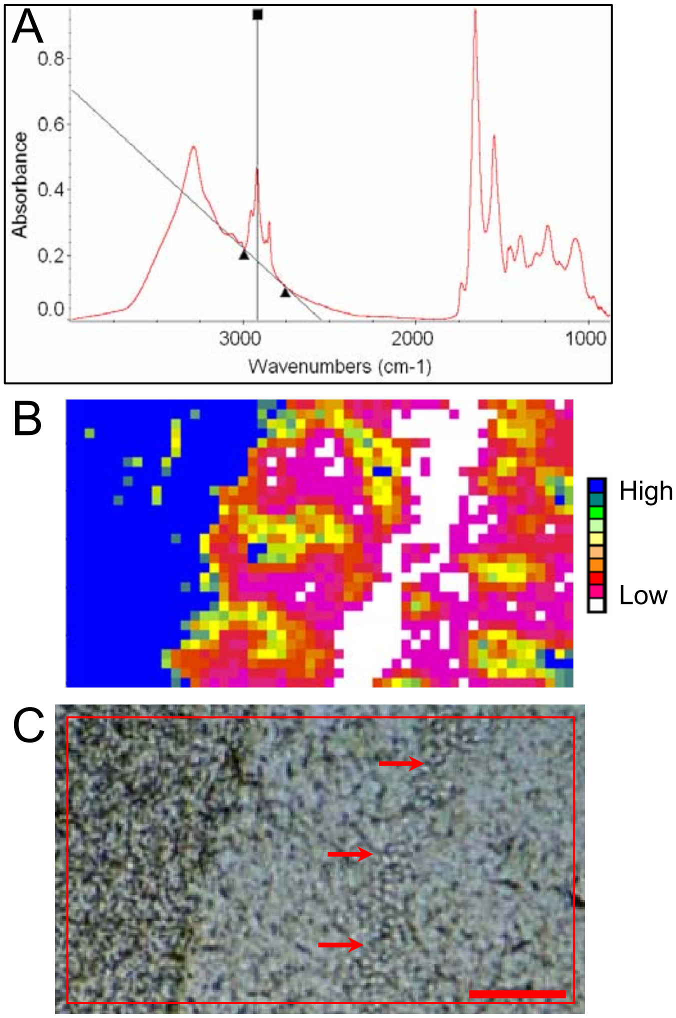

Figure 4.9. Univariate processing of an IR map. (A) An IR spectrum of brain tissue, with the method used to find the CH stretch peak height at 2922 cm^{-1} illustrated. The baseline is set on both sides of the peak, in order to reduce the effect of baseline variations. (B) The resulting functional-group map, with the legend bar for the false-color scale. (C) The photomicrograph of the IR mapped region. The white matter is the darker region in the left third of the image, and the red arrows point to the line of CA1 neuron nuclei. Scale bar = 100 μm.

Bivariate methods are based on the ratios of peak heights or areas, which are also represented on a false color scale. This method can represent the relative change in intensity between two peaks. This is also useful in displaying changes in the composition of the sample. For example, changes in the average protein secondary structure in a map can be mapped by ratioing amide I band areas attributable to the different secondary structures (Ogg, 2002). As well, images based on the CH_2/CH_3 ratio can be used to visualize the densely-packed CA or dentate gyrus neuronal nuclei in the neuropil (Figure 4.10). The loosely-spaced neuronal nuclei in other regions of the brain, such as the cortex, are generally harder to visualize, as the spatial resolution of synchrotron IR microspectroscopy is similar to the size of the nuclei, and the resulting spectra generally contain contributions from the nuclei and the surrounding neuropil. The CH_2/CH_3 ratio can be used to image the CA neuron nuclei because they contain very little lipid. The neuropil, a mixture of dendrites, axons and glial cell processes, is rich in bilayer membranes, and therefore phospholipids. White matter contains a large percentage of sphingomyelin, a phospholipid that forms an insulating sheath around axons. As the proportion of lipids (with their long acyl chains) increases in tissue relative to other components, the intensity of the CH_2 stretching peaks increases relative to the CH_3 stretching peaks. This ratio will therefore be very different for tissues containing almost no lipid, such as neuronal nuclei, and tissues relatively high in lipid, such as neuropil and white matter (Figure 4.10) (Ogg, 2002). However, it will not be effective for imaging changes in total lipid concentration because the ratio between the CH_2 and CH_3 peaks stays the same; it is the amount and not the composition of lipid that is changing. Thus, this method could not be used to image the elevation of lipids in white matter or even normal variations in lipid levels in the neuropil.

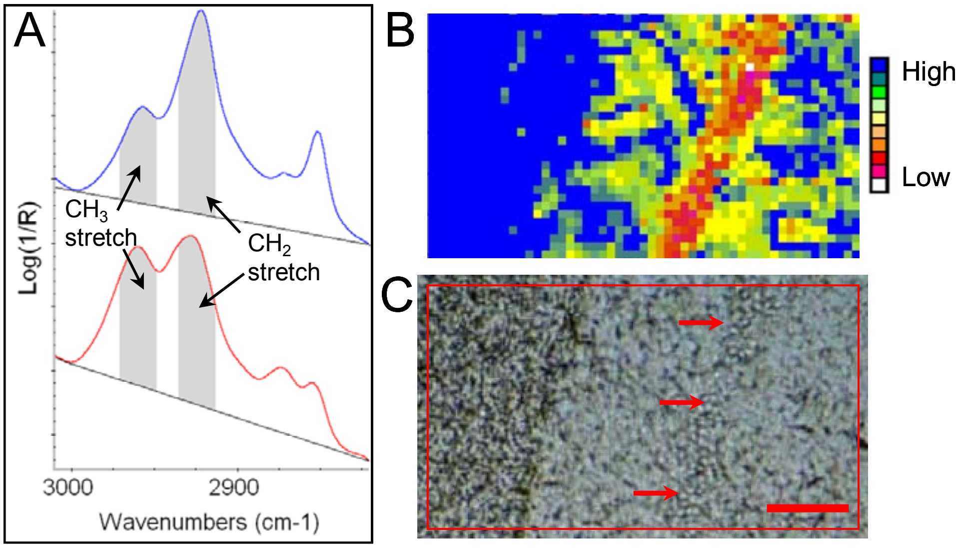

Figure 4.10. Bivariate processing of an IR map. (A) The CH stretch region of neuropil (blue) and neuronal nuclei (red), with the areas of the CH_3 and CH_2 peaks shown in grey. (B) An IR map of hippocampal tissue processed to show the CH_2/CH_3 ratio. The regions with a low ratio (red) correspond to CA1 neuronal nuclei in the corresponding photomicrograph (C) (arrows). Scale bar = 100 µm.

The IR maps were also processed with multivariate methods. Hierarchical cluster analysis, using D-values distance matrix calculations and Ward's hierarchical clustering algorithm, were found to give the best results. Cluster analysis is a valuable tool in IR spectral data analysis. Because it does not require that the identity of peaks is known, it can be used for exploratory data analysis. Hierarchical cluster analysis groups the spectra based on similarity. The results of cluster analysis on the map from Figures 4.9 and 4.10 are presented in Figure 4.11.The analysis was based on the CH stretch region from 2998 to 2830 cm^{-1}. The results of clustering are represented as dendrograms (Figure 4.11A). In principle, the number of possible clusters ranges from two to the number of spectra grouped (where each cluster contains one spectrum). In the example in Figure 4.11A, the horizontal black line in the dendrogram indicates that three main clusters were chosen. This seems like a reasonable choice, as the dendrogram splits into two broad categories, of which one has two major sub-groups. Spectra in the same cluster are represented by the same color in the resulting image (Figure 4.11B), and an average spectrum for each cluster is produced (Figure 4.11C).

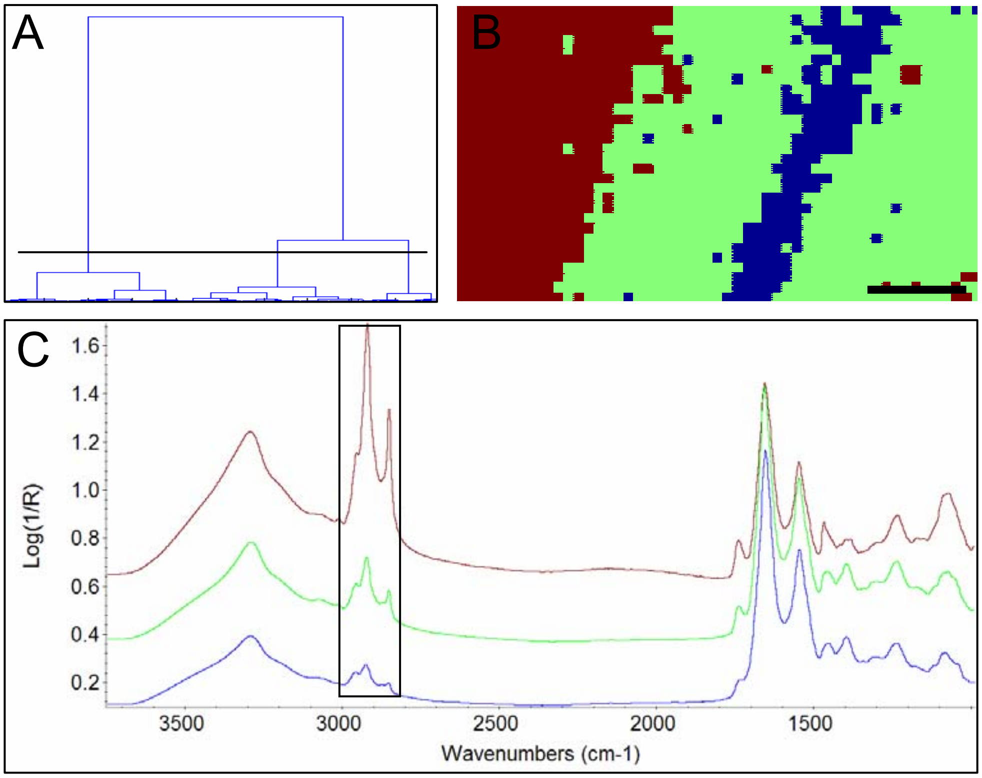

Figure 4.11. Hierarchical cluster analysis. An IR map (the same as in Figures 4.9 and 4.10), containing white matter, neuropil and CA1 neurons, clustered on the CH stretch region from 2998 to 2830 cm^{-1}. (A) A dendrogram, (B) cluster analysis image and (C) corresponding average spectra for each cluster. Scale bar = 100 µm.

In this map, the three clusters illustrate the corpus callosum white matter, the grey matter neuropil, and CA neurons in the grey matter (see photomicrograph of the mapped tissue in Figure 4.9C or 4.10C). When just two clusters are selected, the white and grey matter are distinguishable. Choosing four clusters distinguished the neuronal nuclei, neuropil, and two white matter regions, with higher and lower lipid contents, respectively. It is up to the user to decide how many clusters to use, so the process is somewhat arbitrary. Nevertheless, the images obtained with this method appear simpler than those created through functional group mapping, as a fixed number of clusters, rather than a color scale, is used. As more than one band can be considered simultaneously, the resulting images can show changes in several components at the same time. This is in contrast to the univariate and bivariate methods presented in Figures 4.9 and 4.10.

4.4.2. Spectral Artifacts Associated with Brain Tissue

Before presenting the results of IR mapping in more detail, it is important to consider the spectral artifacts that can arise. Generally, the quality of the spectra obtained from brain tissue is very good as long as the integrity of the tissue is not affected by tears or folds. The two areas where spectral problems tended to arise were white matter and dense-cored plaques.

Plaque cores are composed of very dense amyloid and at times the signal can oversaturate the detector. This leads to artifacts in some of the stronger bands, such as the amide I (Figure 4.12).

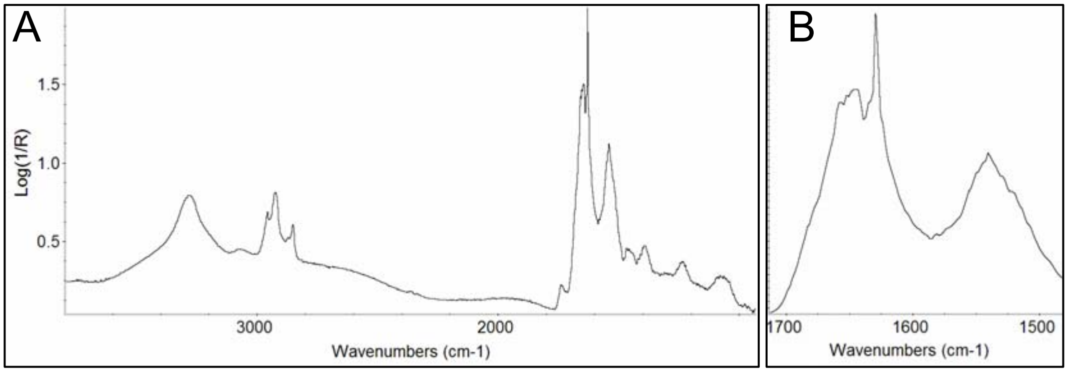

Figure 4.12. Saturated plaque core spectrum. (A) The whole spectral region, and (B) a close-up of the amide I and II bands.

Scattering of light off plaque cores can lead to baseline problems. The sinusoidal baselines that arise in the spectra of plaque cores are highly variable and cannot be easily corrected (Figure 4.13). Their effects on spectra can be significant and the shapes, intensities, and position of bands can be distorted. This became an important consideration when interpreting plaque data, particularly the regions surrounding the dense-cored plaques.

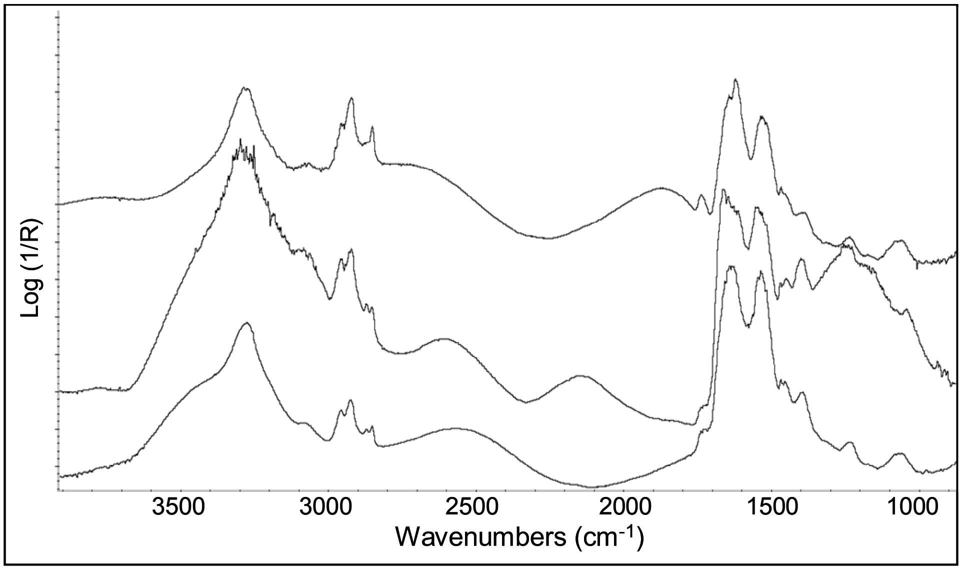

Figure 4.13. Baseline distortion in plaque core spectra.

Similar, but generally less severe, baseline problems are also associated with plaque edges (Figure 4.14). The shape of the amide I band profile can be perturbed, leading to spectra that appear to have elevated β-sheet protein levels (Figure 4.14B). Preliminary analyses that did not take baseline anomalies into account led to the incorrect conclusion that a significantly larger amount of aggregated Aβ could be detected with IR than with Congo red staining. However, when more and better quality IR maps were collected, it became obvious that this was just a spectral artifact.

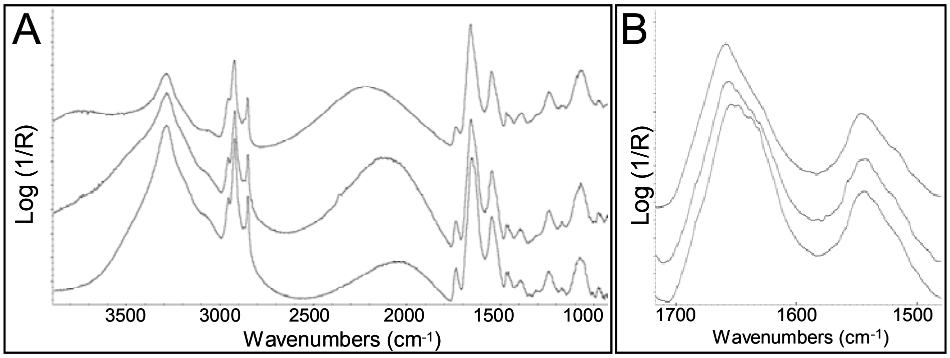

Figure 4.14. Spectral artifacts in IR spectra near plaque edges. The sinusoidal baseline (A) can distort the shape of the amide I band (B).

The shape of the amide I band in that case is due to the baseline problems, rather than actual changes in the secondary structure of protein. This can be illustrated by considering a spectrum from a control mouse (where no aggregated protein is found) which also has baseline problems due to bad tissue quality (Figure 4.15A). Its amide I (Figure 4.15B) is similarly distorted to those in Figure 4.14. The spectra in and around plaque cores were therefore carefully reviewed in order to take the spectral artifacts into consideration during the spectral analysis.

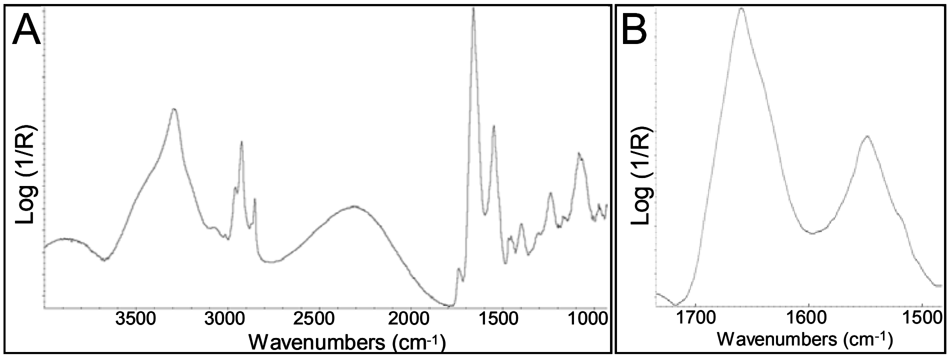

Figure 4.15. Spectral artifact from control tissue, where amyloid plaques are absent. The baseline problem (A) can distort the shape of (B) the amide I band.

Baseline artifacts are also often found in the spectra of white matter, which is made up of closely packed, lipid rich myelin sheaths (Figure 4.16, three top spectra). However, the majority of white matter spectra have flat baselines (Figure 4.16, bottom spectrum).

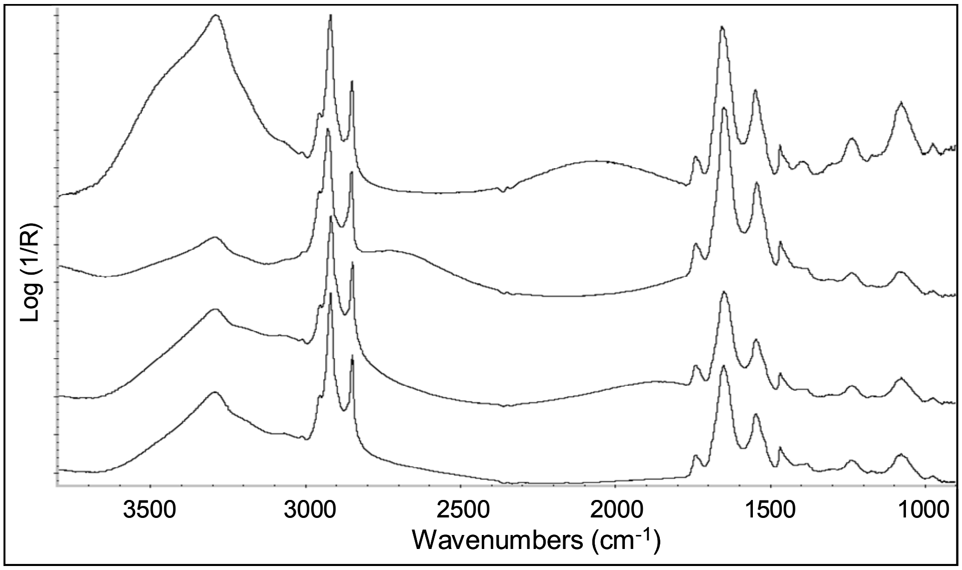

Figure 4.16. White matter spectra with distorted baselines. The top three spectra have sinusoidal baselines that distort the spectrum, while the bottom spectrum is free of artifacts.

The above artifacts are unpredictable and extremely variable. Spectral artifacts due to scattering or dispersion are often a feature of mid-IR spectra of tissue samples, especially those collected in reflectance mode (Mohlenhoff et al, 2005; Romeo & Diem, 2005). They are a direct result of the physical state of the sample, as the texture of a sample can influence light scattering (Kohler et al, 2005). It is therefore necessary to carefully examine the IR data and take the artifacts into consideration during analysis.

4.4.3. IR Mapping of the Hippocampus

The initial sample group consisted of 5 littermate control and 3 TgCRND8 mice at 5 months, and 4 control and 4 TgCRND8 mice at 11 months. The hippocampus is the region of the brain most severely affected by AD. Human AD hippocampi had been studied previously in Dr. Gough's group with IR microspectroscopy (Ogg, 2002). Based on the results of that study, the initial (and eventually disproved) hypothesis was that the relative amount of β-sheet in the CA neurons would be higher in the transgenic AD mice, and this amount would be higher in the 11-month-old animals compared to the 5-month-old animals. IR mapping was therefore started in this region. Several maps (4 to 11 per sample, depending on size) were collected throughout the hippocampus for each sample. They included the CA1, CA3 and dentate gyrus neurons, neuropil, as well as at least one map in the white matter of the corpus callosum.

Typical data from control and TgCRND8 hippocampi at both ages are presented in Figures 4.17 to 4.20. The entire unstained hippocampus is presented, with the location of the mapped regions outlined by red boxes. Processed IR maps are shown beside the map location. A ratio of peak area from 1646 to 1636 cm^{-1} to the area from 1662 to 1652 cm^{-1}, was used to image average β-sheet/α-helix content (maps marked a), as had been done for the human data (Ogg, 2002). Blue pixels have elevated β-sheet content compared to the red pixels. The maps were also processed for the CH_2/CH_3 ratio to visualize neuron nuclei (maps marked b). Red pixels indicate a low ratio, or that the amounts of CH_2 groups compared to CH_3 groups was low, while blue pixels indicate a high ratio. Neuronal nuclei, with their low lipid content, are therefore displayed in red. The CH_2 peak height was used to visualize the total lipid content (maps marked c).

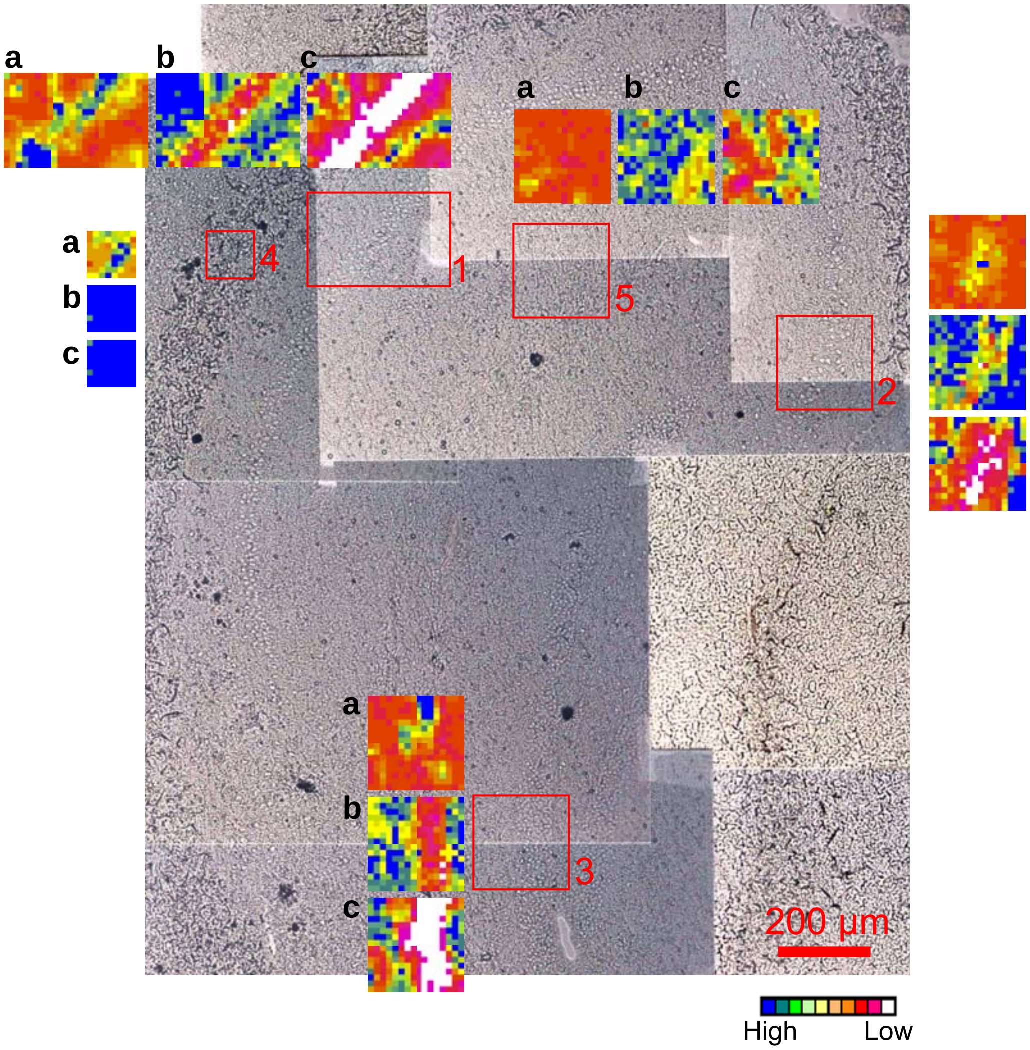

Figure 4.17. A typical hippocampus from an 11-month-old TgCRND8 mouse. Maps are processed for (a) β-sheet to α-helix ratio, (b) CH_3/CH_2 ratio to visualize neurons, and (c) CH_2 peak height to visualize lipid levels. Map 1 includes the CA1 neurons, map 2 the CA3 neurons, map 3 the dentate gyrus neurons, map 4 some of the white matter, and map 5 the internal region of the hippocampus.

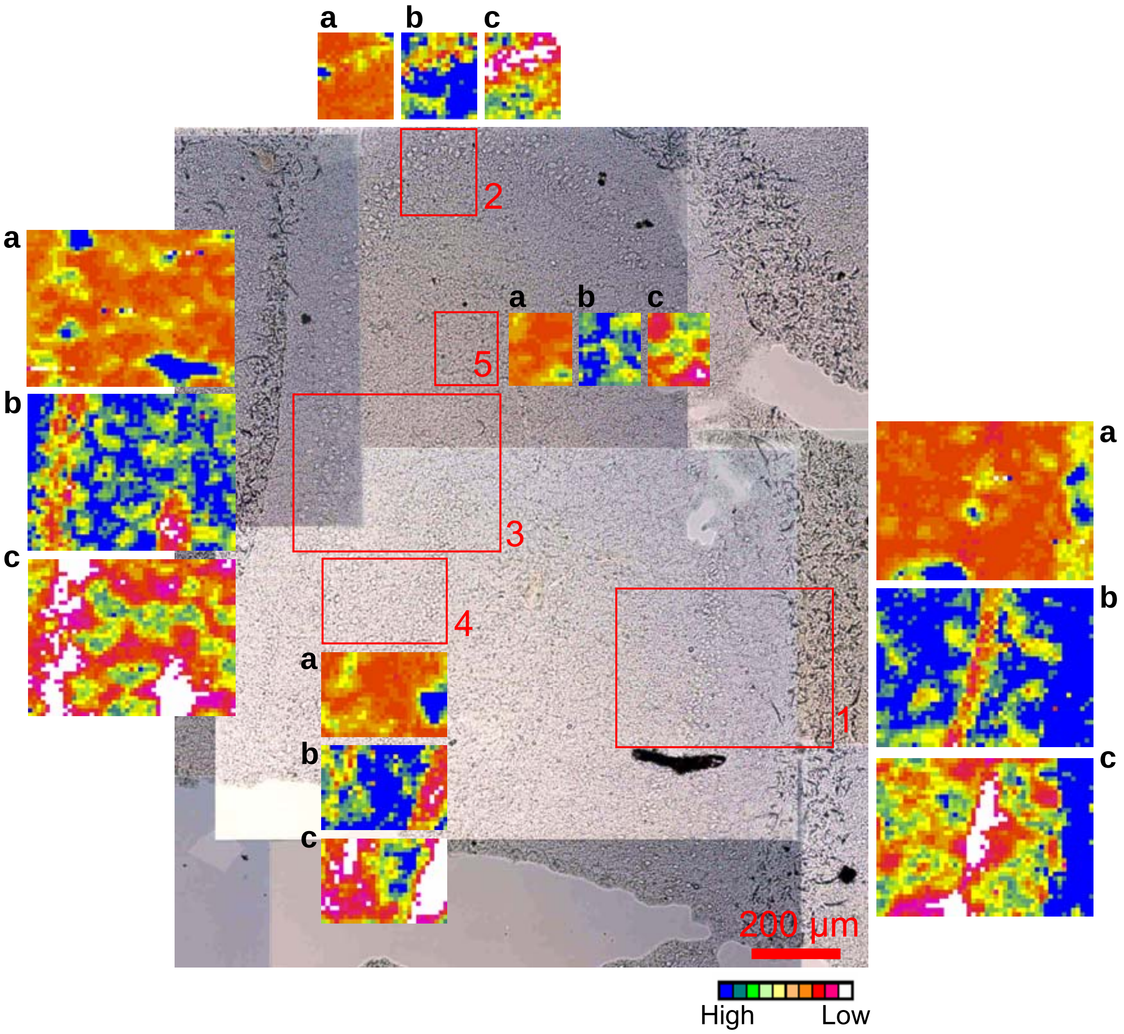

Figure 4.18. A typical hippocampus from a 5-month-old TgCRND8 mouse. Maps are processed for (a) β-sheet to α-helix ratio, (b) CH_3/CH_2 ratio to visualize neurons, and (c) CH_2 peak height to visualize lipid. Map 1 includes the CA1 neurons and white matter, map 2 the CA3 neurons, map 3 the CA3 and dentate gyrus neurons, map 4 the dentate gyrus and map 5 the internal region of the hippocampus.

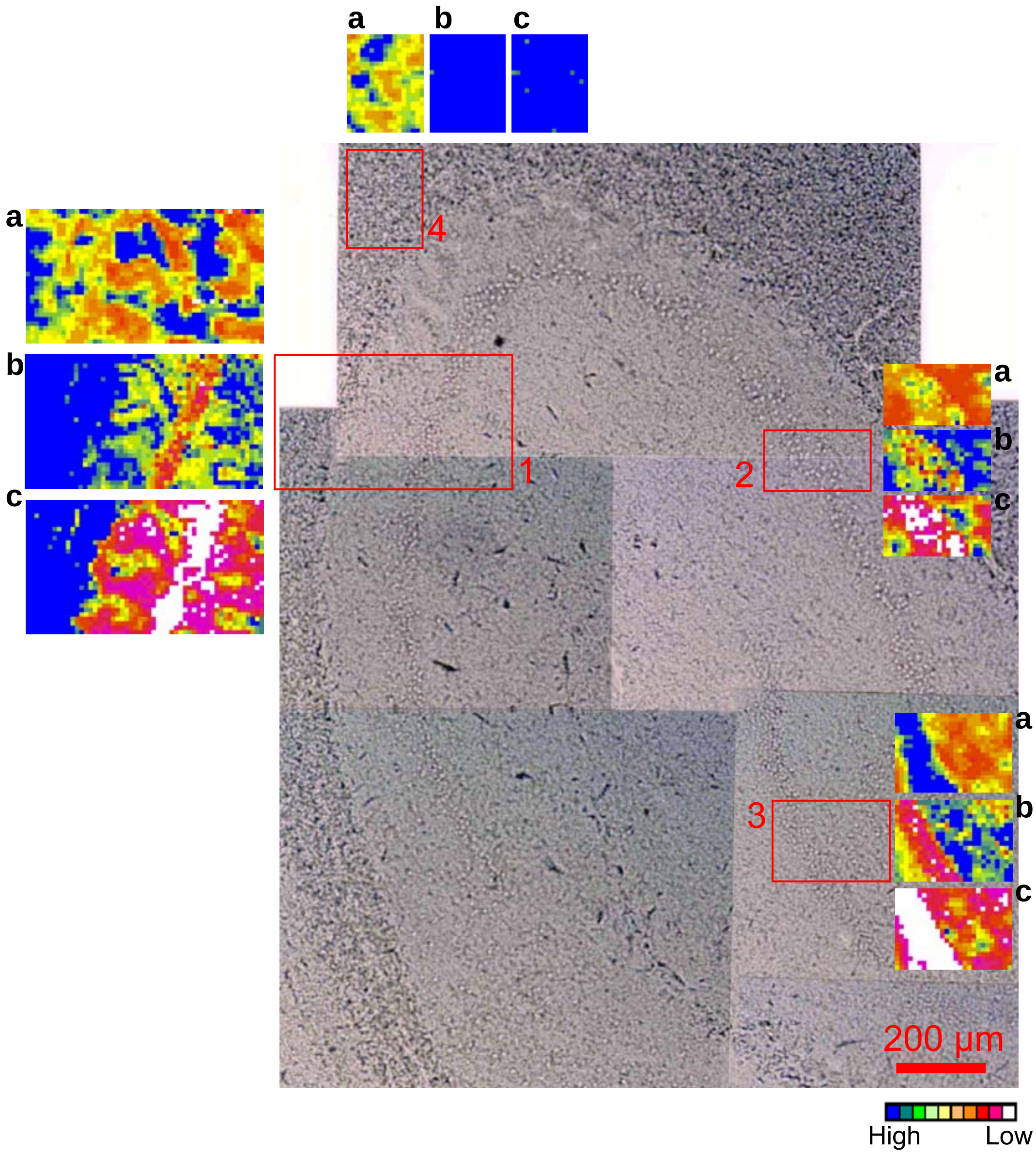

Figure 4.19. A typical hippocampus from an 11-month-old control mouse. Maps are processed for (a) β-sheet to α-helix ratio, (b) CH_3/CH_2 ratio to visualize neurons, and (c) CH_2 peak height to visualize lipid. Map 1 includes the CA1 neurons and white matter, map 2 the CA3 neurons, map 3 the dentate gyrus neurons, and map 4 some of the white matter.

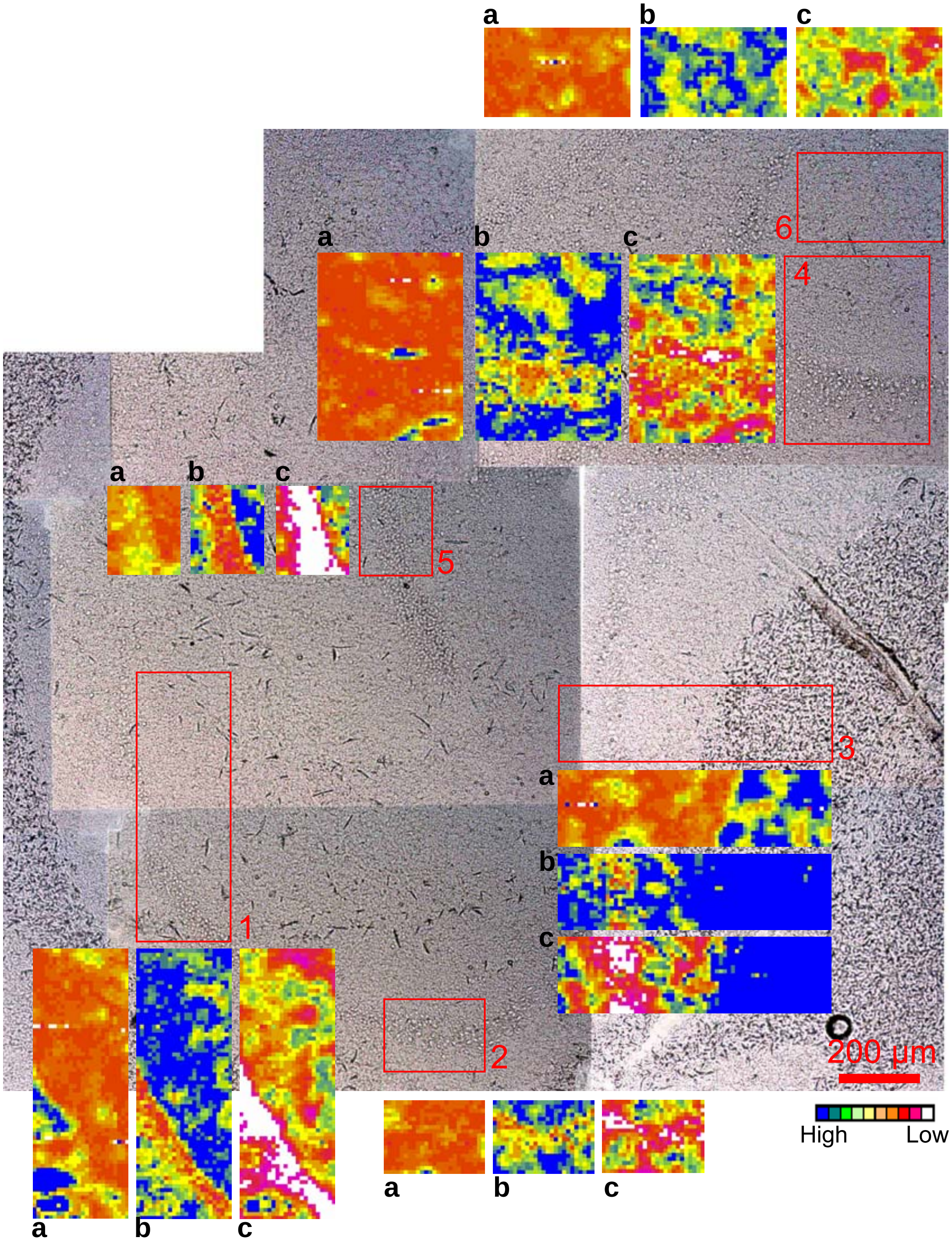

Figure 4.20. A typical hippocampus from a 5-month-old control mouse. Maps are processed for (a) β-sheet to α-helix ratio, (b) CH_3/CH_2 ratio to visualize neurons, and (c) CH_2 peak height to visualize lipid. Map 1 includes the CA1 neurons, maps 2 and 4 the CA3 neurons, map 3 the CA3 neurons and white matter, map 5 the dentate gyrus neurons, and map 6 the internal region of the hippocampus.

The neurons appeared to have increased amounts of β-sheet in both control and AD animals of all ages, compared to the neuropil. The white matter also appeared to have higher β-sheet in all animals. These results did not correspond to the AD status or age of the animal. The reason for the increased β-sheet in the neurons became clear when the spectra were studied more closely.

Figure 4.21A shows representative spectra of white matter (blue), neuropil (green) and neuron (red), from a map in a 5-month-old control animal. This map, shown previously as map 3 in Figure 4.20, contains neuropil, white matter and closely-packed CA3 neurons (Figure 4.21B).

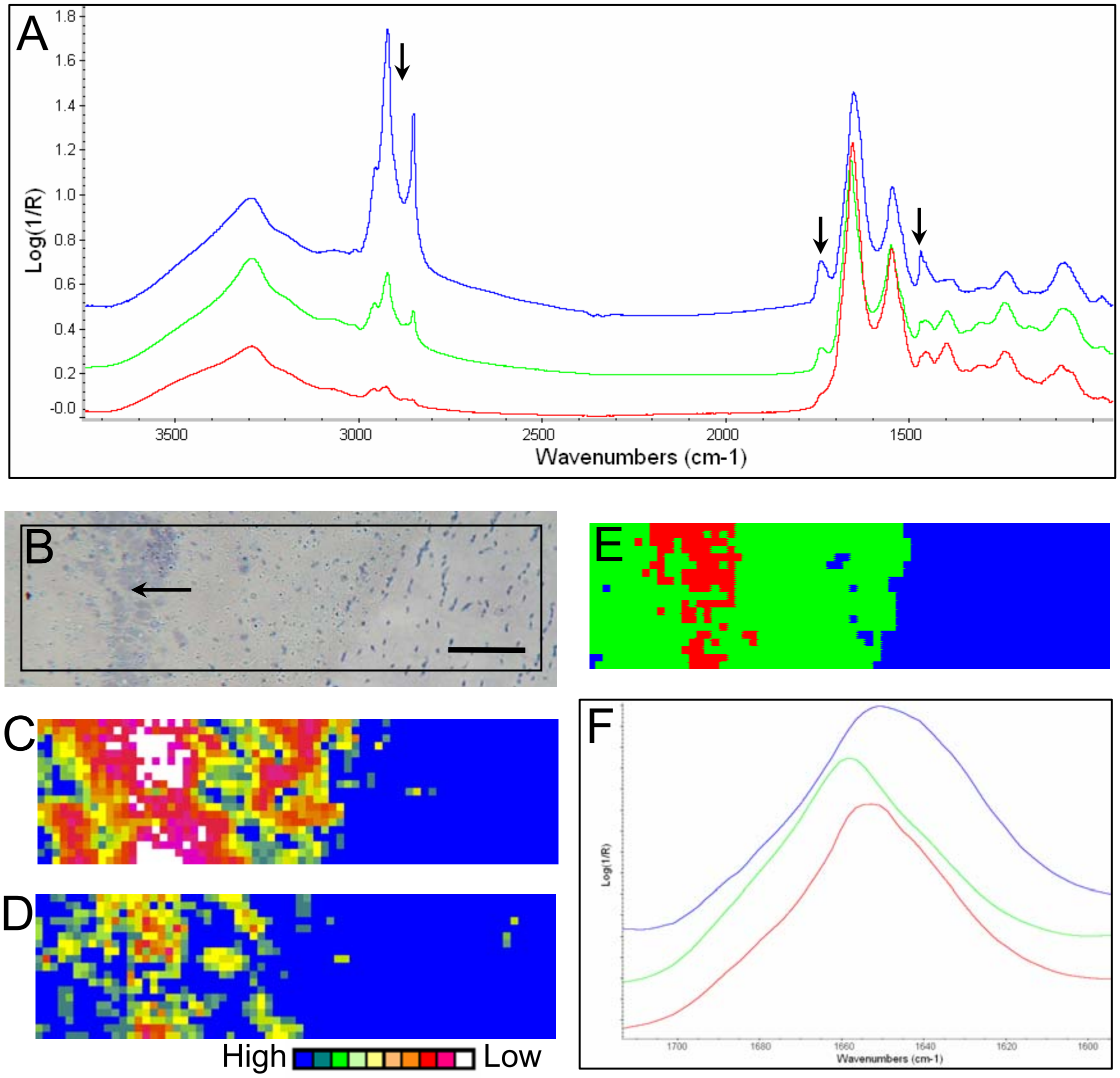

Figure 4.21. An IR map in the hippocampus of a 5-month-old control mouse. (A) Representative IR spectra of white matter (blue), neuropil (green) and neuronal nuclei (red). Arrows point to the main lipid bands. (B) Tissue stained with hematoxylin after IR mapping, showing neuropil, neurons (arrow) and white matter (right side). Nuclei of neurons and glia stain blue. (C) The map processed for CH_2 peak height to visualize total lipid. The nuclei are low in lipid and the white matter high, while the neuropil is intermediate but variable. (D) The map processed to show the CH_2/CH_3 ratio, which is low for the neuronal nuclei. Color legend applies to C and D. (E) The IR map, processed using hierarchical cluster analysis on the CH stretch region. The colors correspond to those in A and F. Note the good correspondence between the cluster map and tissue morphology in the stained micrograph in B. (F) A close up of amide I bands from A. Scale bar = 100 µm.

The peaks due to lipid, such as CH and C=O stretches and CH deformations are highest in the white matter (Figure 4.21A, blue spectrum, arrows). The protein content of white matter is lower than that of neuropil and neuronal nuclei, indicated by lower amide I and II absorbances. The neuronal nuclei have very low lipid levels, while their protein content is high (Figure 4.21A, red spectrum). Neuropil has intermediate amounts of both constituents (Figure 4.21A, green spectrum). The map based on the height of the CH_2 stretch peak shows the high content of lipid in the white matter (Figure 4.21C). Within grey matter, the CH_2/CH_3 peak height ratio can be used to distinguish neuronal nuclei from the surrounding neuropil (Figure 4.21D). Figure 4.21E shows a spectral map created using hierarchical cluster analysis based on the CH stretch region (2998 to 2830 cm^{-1}). The clustering algorithm readily distinguishes between the tissue types based on their spectra. There is very good correspondence between the neuronal nuclei (Figure 4.21B, vertical band in the left-hand side of the stained image) and the red pixels in the IR cluster map below (Figure 4.21E). Although the data presented in Figure 4.21 is from a 5-month-old control, similar results were found in all the animals studied, whether control or TgCRND8, at both 5 and 11 months.

Figure 4.21F shows a close-up of the amide I bands. The amide I of neuropil (green) has a maximum at ~1658 cm^{-1}, indicating that most proteins are in a predominantly α-helical conformation. The band shape is symmetrical. The amide I spectral profiles of neurons and white matter are distinct from neuropil, indicative of tissue-specific differences in the protein secondary structure. The amide I band of white matter (blue) is centered between 1658 and 1650 cm^{-1}, and is broader than the amide I of neuropil and neurons. Sphingomyelin, the main constituent of white matter, contains an amide group. It has an amide I band at 1645 cm^{-1} (Figure 1.6A in Chapter 1) which could broaden the white matter amide I. Neuron amide I maxima (red) are variable between 1658 and 1652 cm^{-1}, with a slight shoulder between 1640-1630 cm^{-1}. These band shapes still point to mostly α-helical structure, with what could be an increase in random coil or β-sheet, compared to neuropil. Thus, when the maps are processed with the method used to display elevated β-sheet in human AD neuron spectra (Ogg, 2002), an increase in β-sheet appears to be observed (maps marked a in Figures 4.17 to 4.20). However, as this is the case for control and transgenic animals, it actually reflects normal differences in the tissue composition rather than AD related changes. As it stands, changes to the neurons, such as intraneuronal accumulation of Aβ, have not been reported in this mouse model.

Thus, neuron IR maps were not useful in distinguishing between AD and control mice. The above data were however useful for ascertaining the normal spectral (and therefore compositional) variability of the tissue. This is important when studying changes that are due to pathological processes.

4.4.4. IR Mapping of Plaques

Plaques are the main pathological feature of AD and were the focus of this research. IR maps of plaques were collected in the hippocampus, cortex and caudate of mice of all ages. The maps included dense-cored and diffuse plaques, as well as normal-looking neuropil, neurons and white matter from transgenic animals. The maps ranged in size from 10000 μm^2 to 144000 μm^2, with at least 10 plaque maps collected per animal. Dense-cored plaques for IR mapping were selected by visual inspection, as the core and distortions in the surrounding tissue were readily apparent when viewed with light microscopy. The diffuse plaques were visually indistinguishable from normal tissue in the unstained sections. Therefore, it was necessary to use adjacent anti-Aβ immunostained sections (on both sides of the IR mapped section) to guide the selection of diffuse plaques for mapping.

As the goal was to compare diffuse and dense-cored plaques, it was of paramount importance to distinguish between true diffuse plaques, and the haloes of diffuse amyloid surrounding plaque cores buried deeper in the tissue. Examination of adjacent sections stained with Congo red and anti-Aβ antibody 4G8 showed that this was frequently the case in the hippocampus and cortex, where dense-cored plaques are the predominant type. The study was therefore confined to diffuse plaques in the caudate, where they were the principal form of Aβ deposit.

Overall, 79 dense-cored and 20 diffuse plaques in the 11-month-old and 26 dense-cored plaques in the 5-month-old TgCRND8 mice were mapped. The diffuse plaques were very rare in young mice and suitable regions for mapping could not be identified. Diffuse and dense-cored plaques in five aged mice with advanced pathology, and comparable regions in littermate controls, were also mapped. This was done to determine whether the diffuse plaques would develop IR detectable β-sheet conformation in the later stages of disease, as well as to study older dense-cored plaques. The number of plaques mapped in the 14, 16, 17 and 21 month TgCRND8 mice, respectively, included 22, 12, 34 and 23 dense-cored plaques, and 11, 12, 10 and 7 diffuse plaques. Multi-cored plaques were counted as one, and diffuse plaques were counted if there was anti-Aβ immunostaining in both adjacent sections.

4.4.4.1. Processing of Plaque Maps

The general principles of processing IR map data discussed in section 4.4.1. apply to the maps of dense cored plaque. However, as the spectra of plaque cores presented some challenges (see section 4.4.2.), the methods used had to be adjusted. Several of the most useful methods will be shown below, applied to a representative map of a multicored plaque in the cortex of a 21-month-old TgCRND8 mouse. These methods were applied to maps of plaques and control tissue. The exact spectral regions employed are listed in Table 3.1 in the Methods section. Each processed map is accompanied by a label that designates that method in the figures that follow. The results of the data processing will be presented in more detail in the following sections.

The ratio of the peak area from 1646 to 1636 cm^{-1} (due to globular β-sheet) to the area from 1662 to 1652 cm^{-1} (due to α-helix) was good for imaging differences in protein secondary structure in non-plaque tissue. This method was however not ideal for imaging plaques, as the amide I maximum of plaque cores was found at 1623 cm^{-1}. As the goal was to visualize the plaques and not the normal variations in protein secondary structure, a new method was developed. In order to display the location of cored plaque, the region from 1662 to 1652 cm^{-1} was ratioed against the region from 1630 to 1620 cm^{-1}, due to highly aggregated β-sheet. This was represented on a false-color scale. A high ratio meant that the content of α-helical protein was high and of β-sheet low. This was the case for normal neuropil, which usually was displayed as blue. A low ratio indicated that there was higher absorbance in the β-sheet region of the spectrum. This was true of plaque cores, which generally displayed in red and white. The regions employed in this analysis were based on the known assignments of amide I peak positions of the various protein secondary structures (Bandekar, 1992). An example is shown in Figure 4.22. Note the excellent correspondence between the pink Congo red staining (A) and the elevated β-sheet content in the IR map, shown by the red and white pixels (B). The numbers on the axes of the IR maps are added by the Altμs software but are difficult to read, so a scale bar has been included in all the figures containing IR maps.

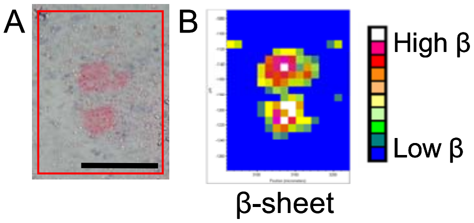

Figure 4.22. An IR map of β-sheet in dense-cored plaques. (A) Plaques in the cortex of a 21-month-old TgCRND8 mouse, Congo red stained after mapping. (B) The IR map processed for protein secondary structure based on the amide I band. The plaques show high levels of β-sheet protein (red) while the surrounding tissue is mostly α-helical (blue). Scale bar = 100 μm.

As variations in the quality of the sample affect the quality of the spectra, the total integrated absorbance of the whole spectrum (known as the chemigram) was therefore imaged (Figure 4.23A). Low values are due to tears in the tissue, while unusually high values are associated with folds. These regions of the map could then be ignored in the analysis. Dense regions of the sample, such as plaque cores, were also sometimes associated with increased absorbance. The overall protein content of the sample was imaged using the area of the amide I band (Figure 4.23B). The cores of plaques generally contained high amounts of protein.

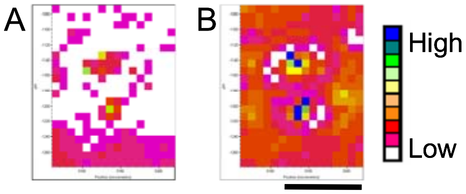

chemigram amide I area

Figure 4.23. Total integrated absorbance and amide I area. The above IR map, (A) processed for total integrated absorbance, and (B) the area of the amide I band. Scale bar = 100 μm.

The greater density of the plaque cores was an issue when imaging the relative concentrations of various components in and around the cores. A conventional solution is to “normalize” the spectra, so that the total absorbance of each spectrum in the map is the same. However, this can mask the differences in total intensity that arise because of actual changes in the sample. Better results could be obtained by ratioing the peak area of the component of interest against the amide I band. However, for most maps, the images based on the unratioed and ratioed methods were almost identical. Of course, it is necessary to be careful with this method when the relative amounts of protein to other components change in the tissue by a great amount, such as when the map contains regions of white matter that are high in lipid and low in protein. The maps of lipid, and the 1230 and 1080 cm^{-1} peak distributions are therefore shown both unratioed and ratioed.

The lipid content was imaged on the CH stretch region. Images based on the asymmetric CH_2 stretch peak height (Figure 4.24A) gave almost the same results as those based on that peak's area ratioed against the amide I band (Figure 4.24B). Images based on the CH_2/CH_3 ratio were good for the visualization of differences between tissue that contained lipid, such as neuropil, and tissue with no or very little lipid, such as plaque cores (Figure 4.24C). However, as mentioned previously, this method was not effective for imaging variations in lipid levels in lipid-containing tissue, because if the amount, but not composition, of the lipid was changing, the ratio between the CH_2 and CH_3 peaks stayed the same. This method was therefore not generally used for plaque maps.

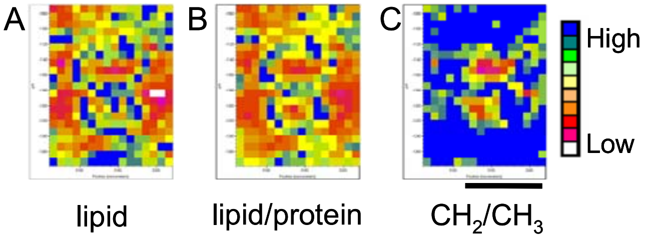

Figure 4.24. CH stretch maps. The above map processed for (A) the height of the asymmetric CH_2 stretch peak, (B) the ratio of the CH_2 stretch peak area to the amide I peak area, and (C) the CH_2/CH_3 ratio. Scale bar = 100 µm.

The areas of the peaks at 1080 cm^{-1} (symmetric phosphate stretch and carbohydrate C-O stretches) and 1230 cm^{-1} (asymmetric phosphate stretch and amide III) were also imaged (Figure 4.25). The ratioed and unratioed maps were very similar.

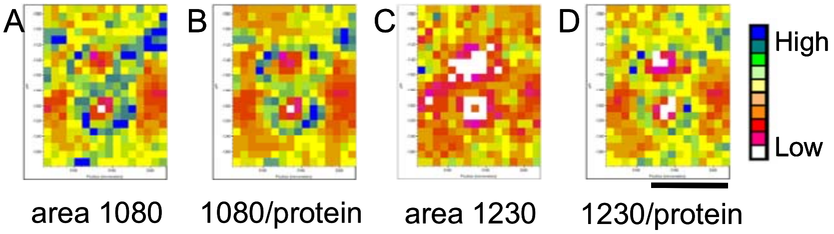

Figure 4.25. Phosphate stretch maps. The IR map processed for (A) the area of the 1080 cm^{-1} band, (B) its ratio to the amide I band, (C) the area of the 1230 cm^{-1} band, and (D) its ratio to the amide I band. Scale bar = 100 µm.

It is important to note that bands in tissue spectra cannot often be assigned to a specific component because of the degeneracy of absorbances from different molecules.

4.4.4.2. Control Data

Before the plaque data can be presented and discussed, it important to show some control data. Maps were also collected in the hippocampus, cortex and caudate of control mice, and areas free of plaques in TgCRND8 mice. These maps were processed in exactly the same way as the plaque maps, in order to demonstrate the variation in the composition of normal brain tissue. As an example, representative maps in the cortex of control and TgCRND8 mice at 5 and 11 months are shown in Figure 4.26. In the transgenic mice, plaque-free regions were selected. The maps have been processed with the methods developed to process maps of dense-cored plaques, to make comparison between the data easier. The maps from all animals show variability in their chemical composition. However this variability is not due to the disease status. It is rather a result of the normal differences in composition. A co-localization is seen between the distribution of increased intensity in several bands, including CH stretch and the bands at 1230 and 1080 cm^{-1}. The intensity of the CH stretch peak is mostly attributable to the acyl chains of lipids, and the two other bands are assigned to phosphate stretching. All these bands are therefore due to the vibrations of membrane phopholipids, which appear to be heterogeneously distributed.

(A) 5-month-old TgCRND8 Mouse Cortex

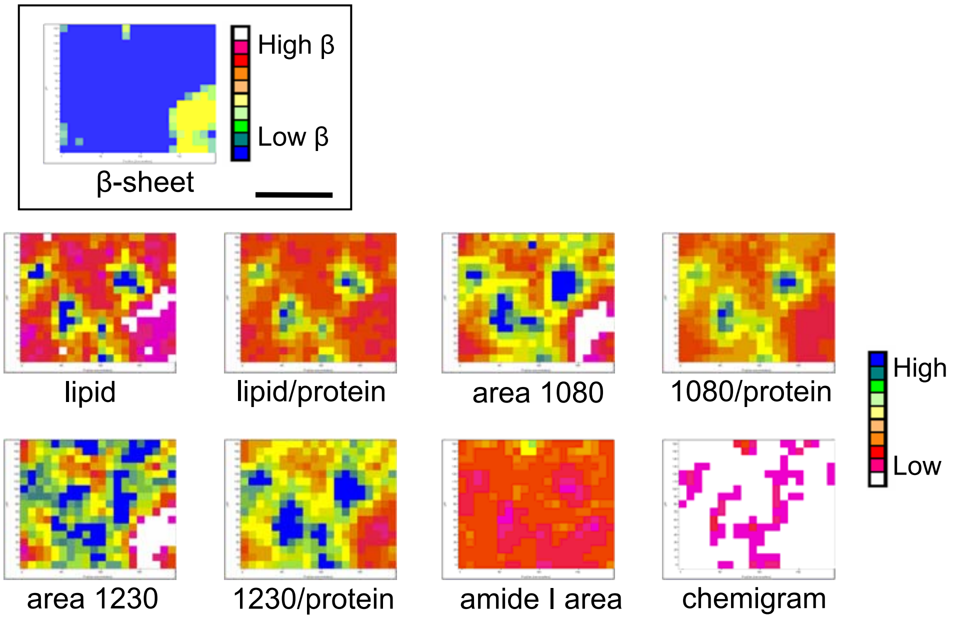

(B) 5-month-old Control Mouse Cortex

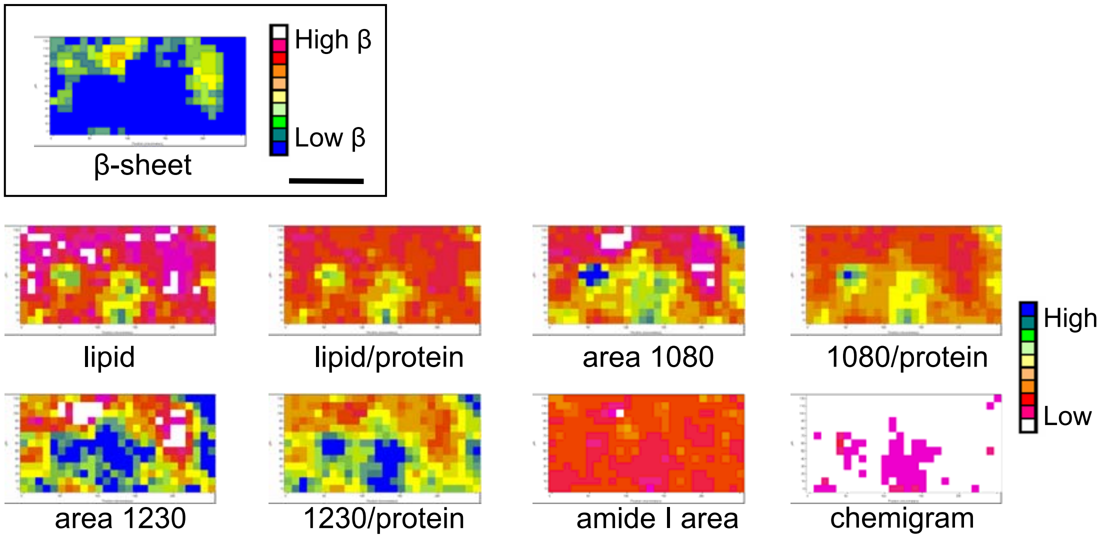

Figure 4.26. Representative IR maps in the cortex. Maps from (A) 5-month-old TgCRND8, (B) 5-month-old control, (C) 11-month-old TgCRND8, and (D) 11-month-old control, processed with the methods outlined in Table 3.1. Figure continued on the next page. (Blacked-out regions in D correspond to an interruption in data collection by a beam fill or re-injection of electrons into the synchrotron). Scale bar = 100 μm

(C) 11-month-old TgCRND8 Mouse Cortex

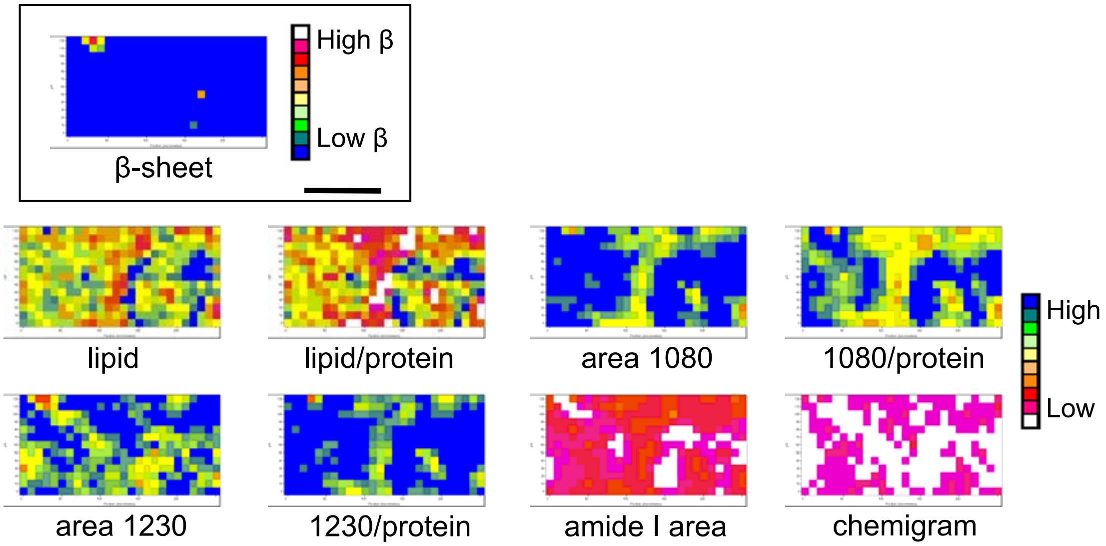

(D) 11-month-old Control Mouse Cortex

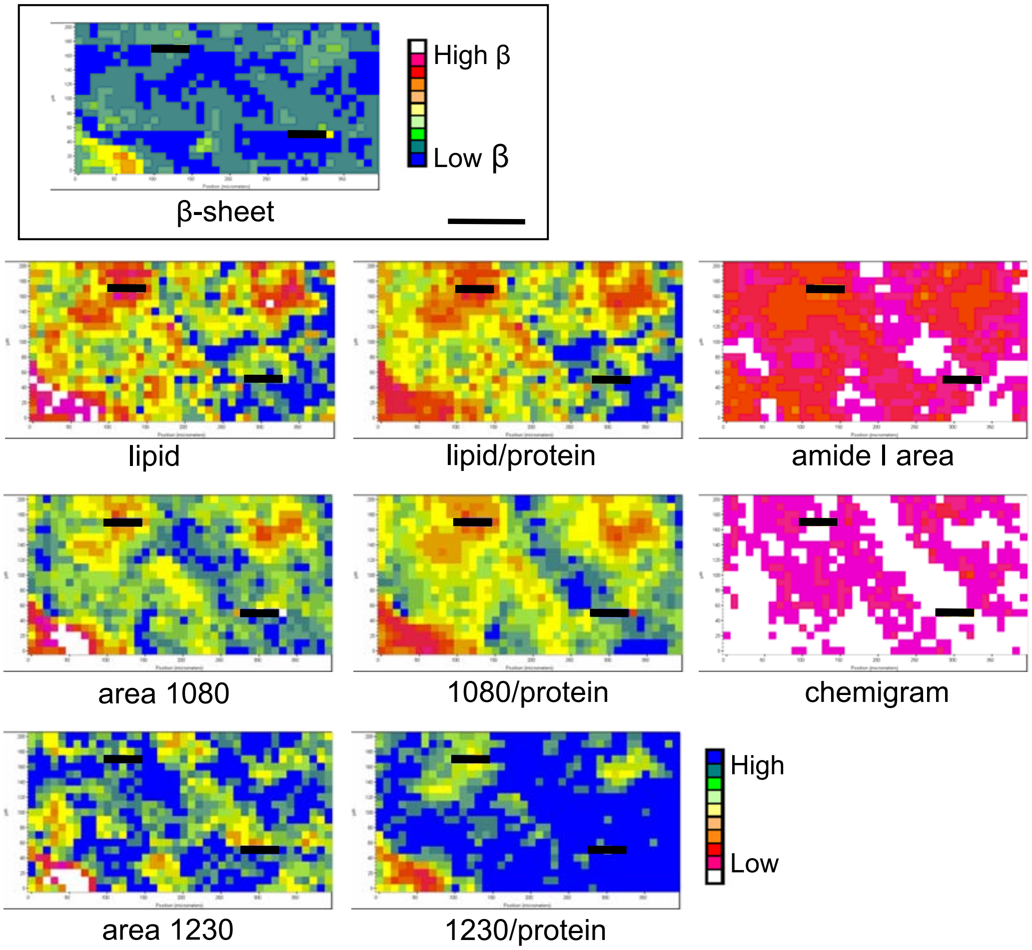

4.4.4.3. Plaque Core Spectra

Figure 4.27 shows the amide I region of typical dense-cored plaque spectra. Amide I bands of dense-cored plaques display increased intensity in the region of the spectrum corresponding to β-sheet. The top spectrum (Figure 4.27, spectrum A) was taken from the centre of a large plaque, and shows an intense peak at 1623 cm^{-1}, indicative of highly aggregated β-sheet, with a broad shoulder in the higher wavenumber region of the spectrum (1660-1640 cm^{-1}), indicative of some α-helical and/or random coil structure. It may be significant that there was no evidence of a peak at 1680 to 1690 cm^{-1}, indicative of anti-parallel β-sheet (Glenner et al, 1974; Krimm and Bandekar, 1986), and commonly observed in *in vitro* amyloid IR spectra (Fabian et al, 1993; Lansbury, 1992). Spectra taken closer to the plaque periphery show either a doublet (Figure 4.27, spectrum B), or a maximum at 1658 cm^{-1} and a shoulder centered between 1630 and 1620 cm^{-1} (Figure 4.27, spectrum B). As the aperture used was 12x12 μm square and the plaques have irregular, rounded shapes with dimensions ranging from 10 to over 100 μm , it is expected that many spectra of the plaque edge will contain contributions from the plaque core as well as the mostly α-helical surrounding tissue, which will both be reflected in the spectra. However, the centers of large plaque cores should be free of these contributions and are expected to be a true chemical signature of plaque cores. The IR spectral profiles of regions distant from the plaques in the transgenic brain tissue are identical to those of control tissue (Figure 4.27, spectrum D).

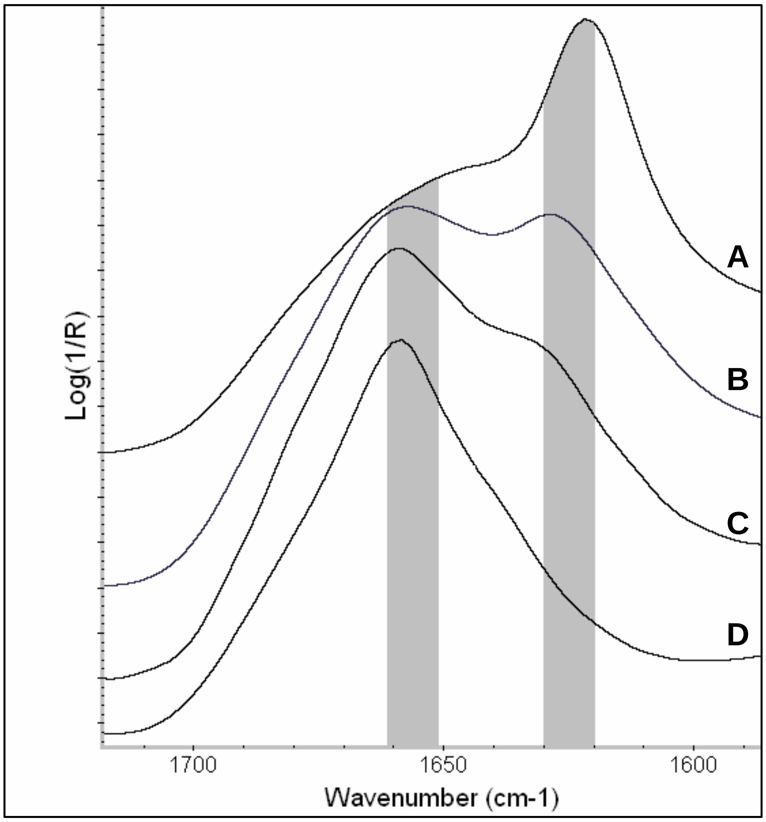

Figure 4.27. Plaque amide I bands. Spectrum of plaque core (A) shows an intense maximum at 1623 cm^{-1}, indicating highly aggregated amyloid. Plaque edge spectra show either a doublet (B) or a shoulder (C) indicating a mixture of α-helix and β-sheet protein. Normal neuropil tissue (D) has an amide I maximum at 1658 cm^{-1}, indicating mostly α-helical proteins. Shaded bars show the spectral regions that are integrated and ratioed to illustrate β-sheet composition in IR maps.

The shaded regions in Figure 4.27 show the amide I peak areas that were ratioed to produce false-color images representing the relative α-helix to β-sheet ratio in spectral maps. This method can be used to visualize dense-cored plaques, such as those seen in the micrograph of tissue stained with the amyloid dye Congo red following IR mapping (Figure 4.28B). In the corresponding false-color image (Figure 4.28A), the high β-sheet plaque cores show up as red and white, while the surrounding tissue is blue and green. As can be seen, there is excellent correspondence between Congo red staining and high β-sheet content.

4.4.4.4. Comparison of IR Mapping with Congo Red Staining

Following IR mapping, all sections on MirrIR were stained with the amyloid dye Congo red. This stain is known to bind to proteins that have aggregated to form amyloid (Glenner et al, 1972). All of the mapped plaques were then imaged using the red fluorescence of Congo red. This was more sensitive than examination under visible light (where the color of Congo red ranges from pink to light red) for the detection of very small amyloid deposits (Linke, 2000).

A semi-quantitative comparison was performed on the data for 18 dense-cored plaques in the 5 month, 52 in the 11 month, 19 in the 14 month, 7 in 16 month, 7 in 17 month and 9 in 21 month TgCRND8 brain, based on Congo red stain fluorescent images and exact pixel dimensions in IR. Only the best quality data were chosen. The IR maps had to be of sufficiently good quality (high signal to noise, baselines relatively free of artifacts) and the tissue had to be undamaged by the staining process.

Figure 4.28 shows the process used to correlate the spectral data with Congo red staining. The IR map was processed for high β-sheet content using the amide I ratio method illustrated in Figure 4.27. The pixels corresponding to high β-sheet were then carefully reviewed, as baseline problems can distort the peak shapes (see section 4.4.2), and the pixels showing real elevated β-sheet (Figure 4.28A) were outlined. The number of pixels in the vertical and horizontal direction was then counted, and this was deemed to constitute the height and width of the plaque by IR. Similarly, the height and width of the Congo red positive regions in the fluorescent images of the stained sample was also measured (Figure 4.28B). This defined the height and width of the plaque by Congo red staining. The results are summarized in Table 4.1.

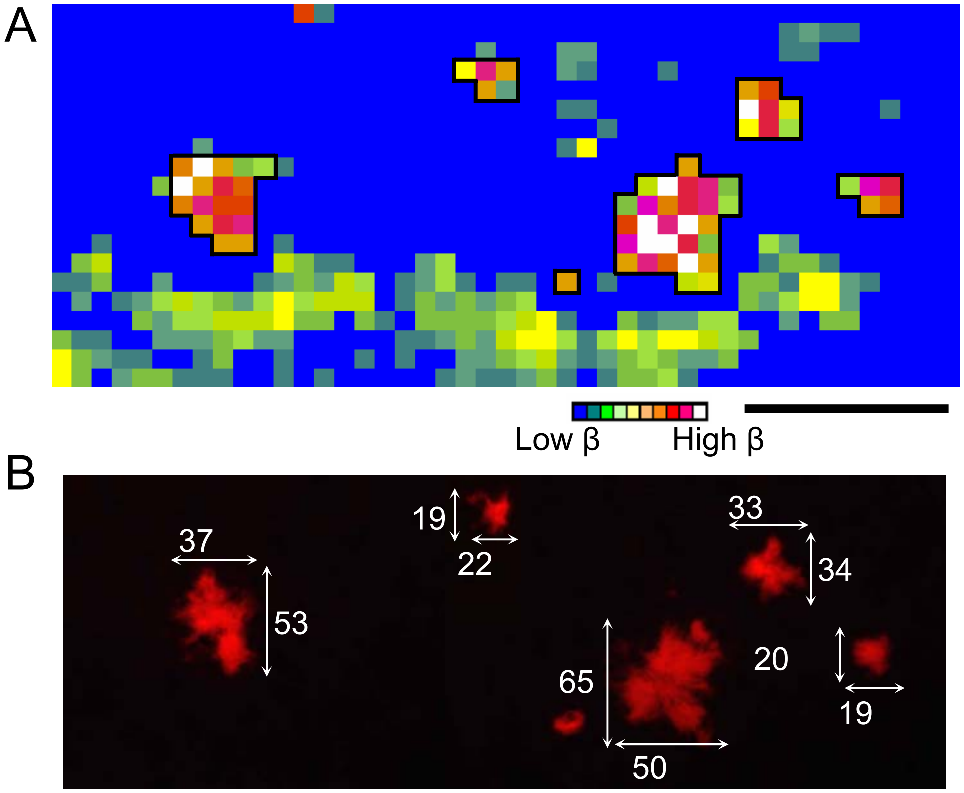

Figure 4.28. Comparison of plaque sizes from IR mapping and Congo red staining. (A) An IR map processed for high β-sheet content (red). The pixels containing elevated β-sheet are outlined in black. (B) Congo red fluorescence of the mapped tissue, stained after IR data collection, with the sizes of the plaques indicated. The plaques show up as red, against a black background. Pixel size 10 µm, scale bar = 100 µm.

Table 4.1. Comparison of dense-cored plaque size by Congo-red staining and IR microspectroscopy

Age in months	Congo red width (μm)	Congo red height (μm)	IR width (μm)	IR height (μm)	Step size (μm)	Width difference (μm)	Height difference (μm)
5	13	15	24	12	12	11	-3
	22	16	36	12	12	14	-4
			30	20	10	8	4
			24	24	12	2	8
	17	14	24	24	12	7	10
	12	11	20	10	10	8	-1
	12	22	24	12	12	12	-10
			20	10	10	8	-12
			12	24	12	0	2
	17	15	24	36	12	7	21
			24	24	12	7	9
			30	30	10	13	15
	10	12	20	20	10	10	8
	34	27	30	30	10	-4	3
	30	32	30	30	10	0	-2
	30	31	30	30	10	0	-1
	38	24	40	20	10	2	-4
	23	24	20	30	10	-3	6
	39	25	30	30	10	-9	5
	20	22	20	10	10	0	-12
	41	36	20	30	10	-21	-6
	20	37	20	30	10	0	-7
	21	17	29	20	10	8	3
	29	35	30	30	10	1	-5
11	13	15	24	36	12	11	21
	37	34	60	48	12	23	14
	31	24	48	36	12	17	12
	33	20	48	36	12	15	16
	32	37	50	50	10	18	13
	12	18	10	10	10	-2	-8
	49	55	48	60	12	-1	5
	15	14	24	24	12	9	10
	40	38	48	48	12	8	10
	41	20	60	36	12	19	16
	18	35	30	50	10	12	15
	17	13	24	24	12	7	11
	16	18	36	24	12	20	6
	27	23	48	36	12	21	13
	17	16	24	24	12	7	8
	90	48	108	60	12	18	12
	21	19	24	36	12	3	17
	14	15	24	36	12	10	21
	12	19	24	24	12	12	5
	43	38	60	60	12	17	22

	19	17	24	24	12	5	7
	33	29	40	40	10	7	11
	40	37	50	40	10	10	3
	18	28	20	30	10	2	2
	54	44	60	60	10	6	16
	37	48	40	60	10	3	12
	23	23	40	30	10	17	7
	43	39	52	39	13	9	0
	14	15	20	20	10	6	5
	13	17	24	24	12	11	7
	25	26	36	36	12	11	10
	11	13	12	24	12	1	11
	22	21	24	36	12	2	15
	19	15	24	24	12	5	9
	11	14	12	24	12	1	10
	31	34	36	48	12	5	14
	8	10	24	12	12	16	2
	14	17	36	36	12	22	19
	9	12	12	12	12	3	0
	31	35	40	40	10	9	5
	19	23	10	20	10	-9	-3
	67	42	50	50	10	-17	8
	43	47	30	40	10	-13	-7
	25	25	20	20	10	-5	-5
	25	17	20	20	10	-5	3
	21	21	20	30	10	-1	9
	31	38	30	40	10	-1	2
	20	27	30	30	10	10	3
	19	15	10	10	10	-9	-5
	12	13	10	10	10	-2	-3
	20	14	30	20	10	10	6
	25	20	40	30	10	15	10
14	19	18	20	20	10	1	2
	13	13	10	10	10	-3	-3
	13	11	20	10	10	7	-1
	20	17	20	20	10	0	3
	23	17	20	20	10	-3	3
	15	20	20	20	10	5	0
	46	49	50	50	10	4	1
	14	11	20	10	10	6	-1
	13	12	10	20	10	-3	8
	13	20	20	20	10	7	0
	32	22	30	20	10	-2	-2
	29	24	40	30	10	11	6
	15	11	10	20	10	-5	9
	15	13	10	10	10	-5	-3
	8	8	10	10	10	2	2
	17	16	20	20	10	3	4
	14	14	20	10	10	6	-4
	15	20	20	10	10	5	-10
	30	21	30	20	10	0	-1
16	77	72	70	70	10	-7	-2
	15	27	30	30	10	15	3

	19	15	20	20	10	1	5
	19	17	20	20	10	1	3
	61	56	60	60	10	-1	4
	17	15	20	20	10	3	5
	44	27	50	30	10	6	3
17	65	79	70	70	10	5	-9
	55	42	50	50	10	-5	8
	22	19	30	20	10	8	1
	33	34	30	30	10	-3	-4
	19	20	30	20	10	11	0
	37	53	50	50	10	13	-3
	50	65	60	70	10	10	5
21	26	20	30	20	10	4	0
	45	40	50	50	10	5	10
	38	43	40	50	10	2	7
	44	40	40	40	10	-4	0
	49	48	50	50	10	1	2
	42	43	50	40	10	8	-3
	18	19	20	20	10	2	1
	59	57	60	60	10	1	3
	90	55	90	50	10	0	-5

The sizes of the plaques varied between the two methods, but not within the resolution of the technique. The spatial resolution of IR mapping was determined by the size of the aperture, generally 12x12 µm. With IR mapping, the size of the plaque had to be a multiple of the aperture size. A pixel that either included some normal tissue and some plaque or included just plaque was counted to be part of the plaque. The size of a plaque was therefore “spread-out” as all pixels with elevated β-sheet were counted to be part of the plaque. Different results could therefore be obtained for the same plaque mapped at different times, depending on how the plaque fit into the pattern of raster scanning across the sample. Taking into account the spatial resolution of the techniques, where spectral artifacts were not a problem, there was no significant difference between the extent of the plaque core as defined by either Congo red or IR mapping. The difference between the two methods was never greater than two pixels. The correspondence between Congo red staining and IR mapping was excellent, as can be seen from the examples in Figure 4.29. Super-imposition of IR maps over scaled micrographs of Congo red-stained tissue showed that each pixel with elevated β-sheet contained at least some tissue that stained with Congo red. In plaques consisting of a congophilic core with a diffuse halo of Aβ indicated by immunostaining, elevated β-sheet was restricted to the core. The presence of elevated β-sheet in the IR maps was therefore always associated with Congo red staining, and vice versa, confirming the specificity of the stain for aggregated amyloid (Glenner et al, 1972; Puchtler et al, 1962).

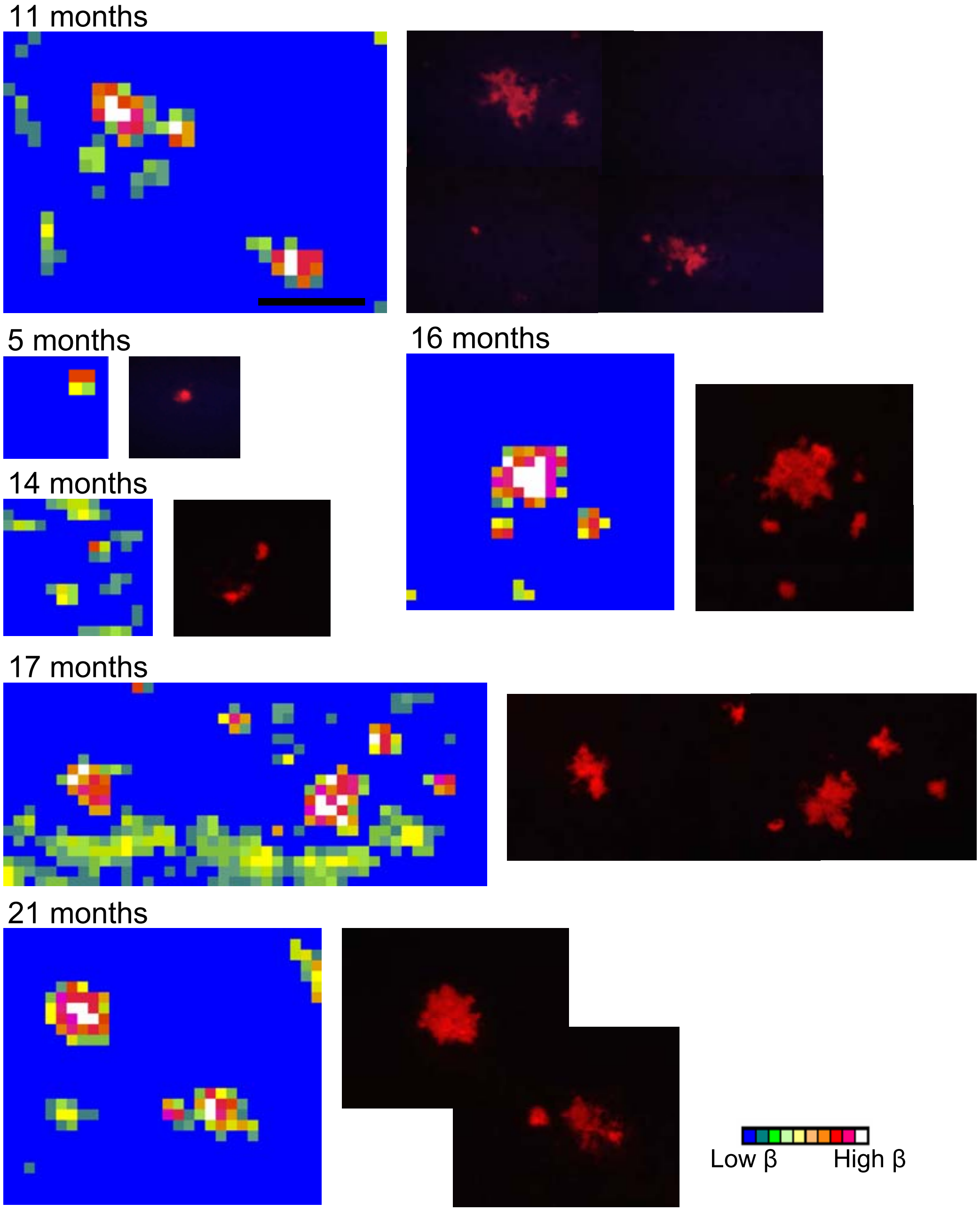

Figure 4.29. Correspondence of high β-sheet content with Congo red staining. Examples of dense-cored plaques at all ages studied. The IR maps are processed to show elevated β-sheet based on the amide I band. The plaques show high levels of β-sheet (red and white) while the surrounding tissue is mostly α-helical (blue). The tissue stained with Congo red after IR mapping, visualized with fluorescence. Scale bar = 100 μm.

4.4.4.5. Elevated Phospholipids Surround Dense-Cored Plaques

An advantage of IR microspectroscopy is that changes in the relative proportions of multiple tissue components can be visualized, *in situ*, based on their spectral signatures, without the use of stains or other probes. The distribution of absorbance peaks due to all the major tissue components was examined in the maps. One strikingly consistent factor was the increased intensity in the CH stretch, 1080 cm^{-1}, and 1230 cm^{-1} bands around congophilic plaque cores. Typical dense-cored plaque maps from each age group are presented in Figures 4.30 to 4.35. A micrograph of the tissue, Congo-red stained after mapping, is shown for each map. Where available, serial sections immunostained with anti-Aβ antibodies are also shown. For some maps, sections on both sides of the mapped section are available, but for others only one is. Each map is processed for elevated β-sheet to show the location of plaque cores. The maps are also processed to show the distribution of other peaks of interest. The methods used to process plaque data and the assignments of the mapped bands are discussed in detail in Section 4.4.4.1.

Although the ages of the mice ranged from 5 to 21 months, several facts about the dense-cored plaques were consistent for all age groups. In all of the figures, the Congo red staining corresponds to elevated β-sheet. The cores were surrounded by elevated intensity in the CH stretch, 1080 cm^{-1}, and 1230 cm^{-1} peaks, bands attributable to phospholipids (see Figure 1.6). Although the intensity of these peaks does vary with normal tissue morphology, an unmistakable and significant increase associated with dense-cored plaques was observed, in mice at all ages (Figures 4.30 to 4.35 and Appendix 1). The increase was most pronounced around the larger plaques, but was also found around the smaller plaques (10-20 μm cross-section). This elevation is due to an increase in membrane-containing structures around dense-cored plaques, as phospholipids serve mainly as components of lipid bilayer membranes. Additionally, the chemigram, or total absorbance, shows greater intensity in the cores of the plaques, demonstrating the density of the amyloid. The intensity of the amide I band is also higher in the plaque cores. Additional data is presented in Appendix 1 (Chapter 14). The data in the following figures and the Appendix show the morphological variability of the plaques, as well as the features that are always consistent, such as the elevation of phospholipids around the amyloid core.

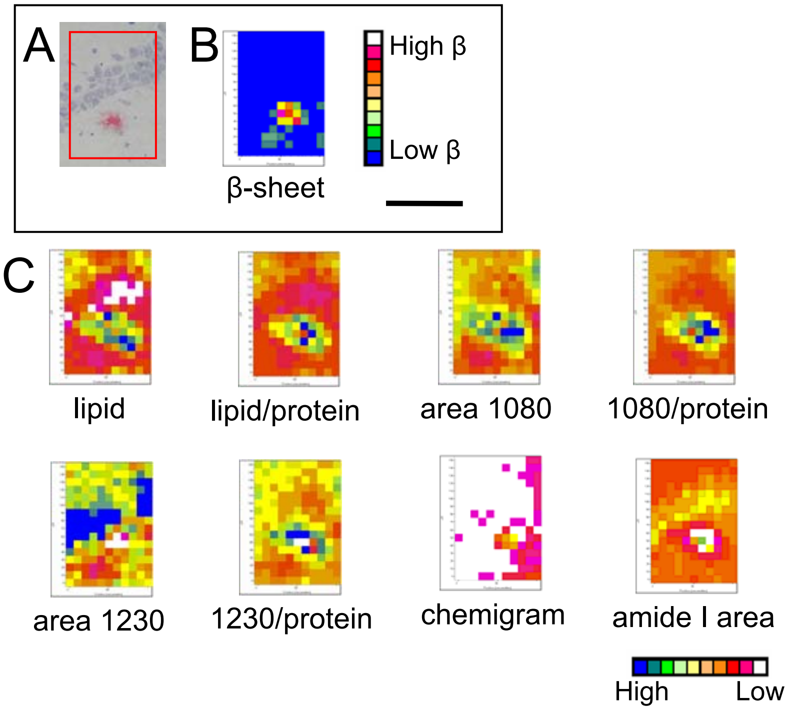

Figure 4.30. Dense-cored plaque from a 5-month-old TgCRND8 mouse. (A) A photomicrograph of the mapped region, stained with Congo red after IR mapping. The plaque is located near the CA1 neurons of the hippocampus. (B) The map processed to show elevated β-sheet proteins. (C) The map processed with the methods outlined in Table 3.1. In spite of its small size and the early stage of the disease progress, the plaque is surrounded by elevated phospholipids, indicated by increased intensity around the plaque core in the lipid, lipid/protein, area 1080, 1080/protein, area 1230 and 1230/protein maps. The area 1230 map also shows increased intensity (blue) that corresponds to the neuron nuclei (blue spots in Congo red micrograph). This is not seen in the 1230/protein map, where the area of the 1230 cm^{-1} band was ratioed against the amide I band, while the increased intensity around the plaque core is still seen. This is because the neuron nuclei are high in proteins, as indicated by increased intensity in the amide I area map (yellow), relative to the neuropil (orange to red), and the 1230 cm^{-1} band contains contributions from the protein amide III band, as well as the asymmetric phosphate stretching. Scale bar = 100 μm.

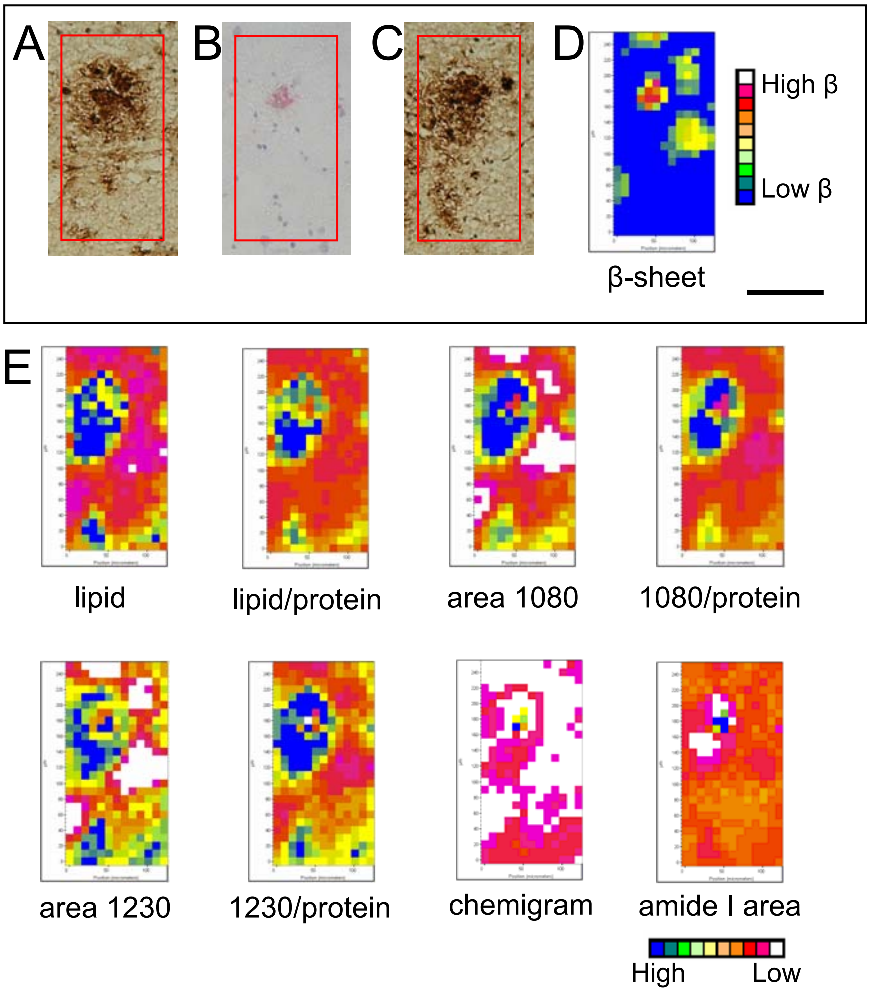

Figure 4.31. Dense-cored plaque from an 11-month-old TgCRND8 mouse. Photomicrographs of (A, C) serial sections immunostained with antibodies against the Aβ-peptide and (B) the mapped region, stained with Congo red after IR mapping. The plaque is found in the central region of the hippocampus. The amyloid core is small, but serial anti-Aβ immunostaining shows a large halo of diffuse amyloid surrounding the core and extending downward. (D) The map processed to show elevated β-sheet proteins. (E) The map processed with the methods outlined in Table 3.1. The plaque core is surrounded by elevated phospholipids in an oval pattern, indicated by increased intensity around the plaque core in the lipid, lipid/protein, area 1080, 1080/protein, area 1230 and 1230/protein maps. Some non-plaque associated elevated phospholipids are found in the lower part of the map. Scale bar = 100 µm.

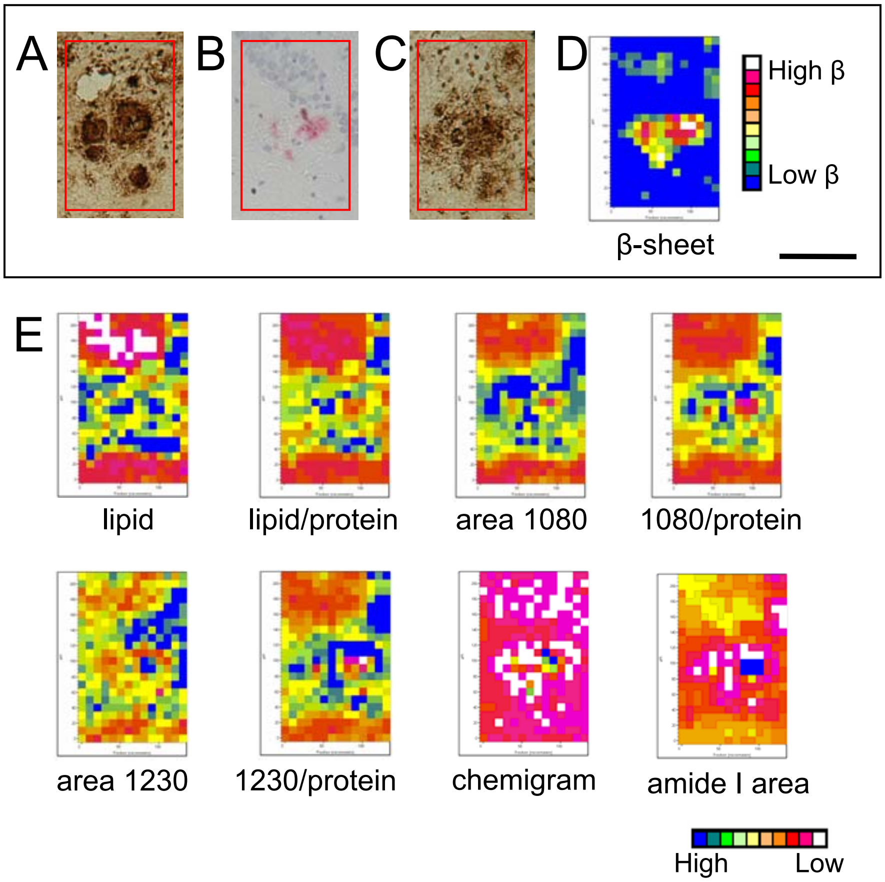

Figure 4.32. Dense-cored plaque from a 14-month-old TgCRND8 mouse. Photomicrographs of (A, C) serial sections immunostained with antibodies against the Aβ-peptide and (B) the mapped region, stained with Congo red after IR mapping. The multicored plaque is found near the CA1 neurons of the hippocampus. In the Congo red-stained micrograph, the plaque core can be seen to displace the neurons. Some diffuse amyloid is found around and between the individual amyloid cores. (D) The map processed to show elevated β-sheet proteins. (E) The map processed with the methods outlined in Table 3.1.The plaque is surrounded by large amounts of elevated phospholipids, indicated by increased intensity around the plaque core in the lipid, lipid/protein, area 1080, 1080/protein, area 1230 and 1230/protein maps. Scale bar = 100 μm.

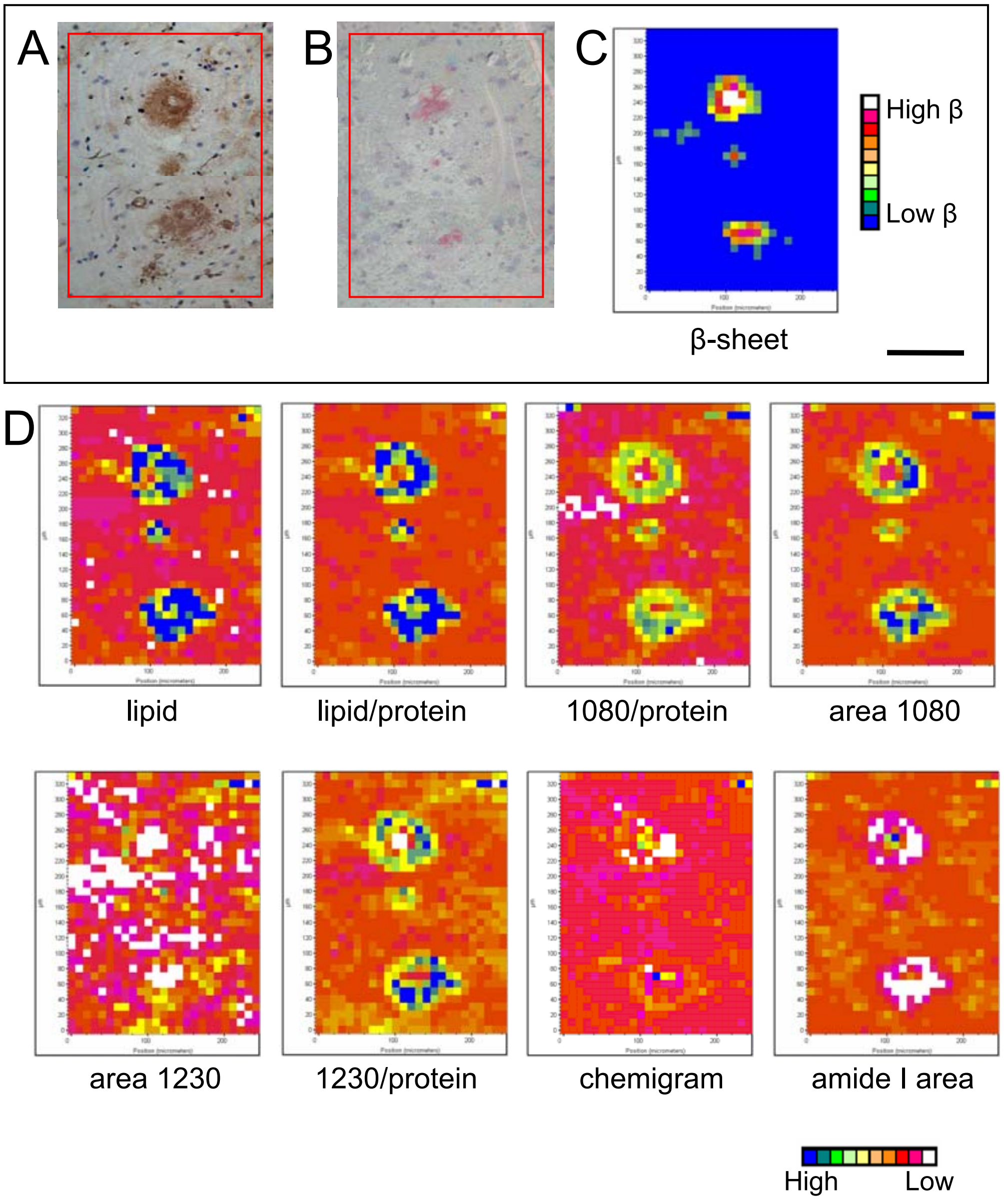

Figure 4.33. Dense-cored plaques from a 16-month-old TgCRND8 mouse. Photomicrographs of (A) a serial section immunostained with antibodies against the Aβ-peptide and (B) the mapped region, stained with Congo red after IR mapping. The three single-cored plaques are found in the cortex. (C) The map processed to show elevated β-sheet proteins. (D) The map processed with the methods outlined in Table 3.1. The two larger plaques are surrounded by large rings of elevated phospholipids, indicated by increased intensity around the plaque core in the lipid, lipid/protein, area 1080, 1080/protein, area 1230 and 1230/protein maps. The tiny plaque in the middle is also surrounded by a ring of elevated phospholipids, but only one pixel thick around the core. Scale bar = 100 μm.

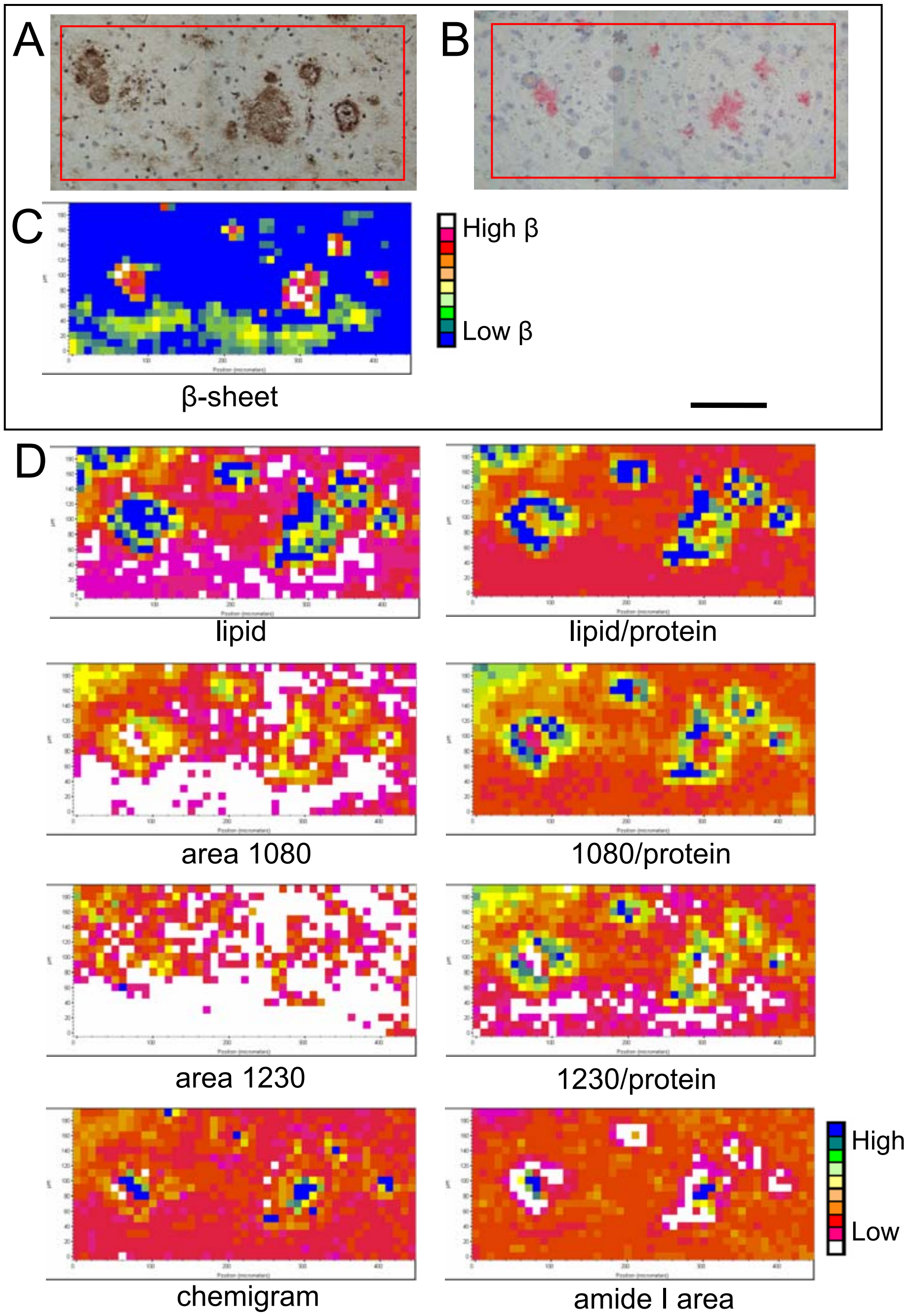

Figure 4.34. Dense-cored plaques from a 17-month-old TgCRND8 mouse. Photomicrographs of (A) a serial section immunostained with antibodies against the Aβ-peptide and (B) the mapped region, stained with Congo red after IR mapping, showing several plaques of various sizes in the cortex. (C) The map processed to show elevated β-sheet proteins. (D) The map processed with the methods outlined in Table 3.1. All plaques are surrounded by elevated phospholipids, indicated by increased intensity around the plaque core in the lipid, lipid/protein, area 1080, 1080/protein, area 1230 and 1230/protein maps. Scale bar = 100 μm.

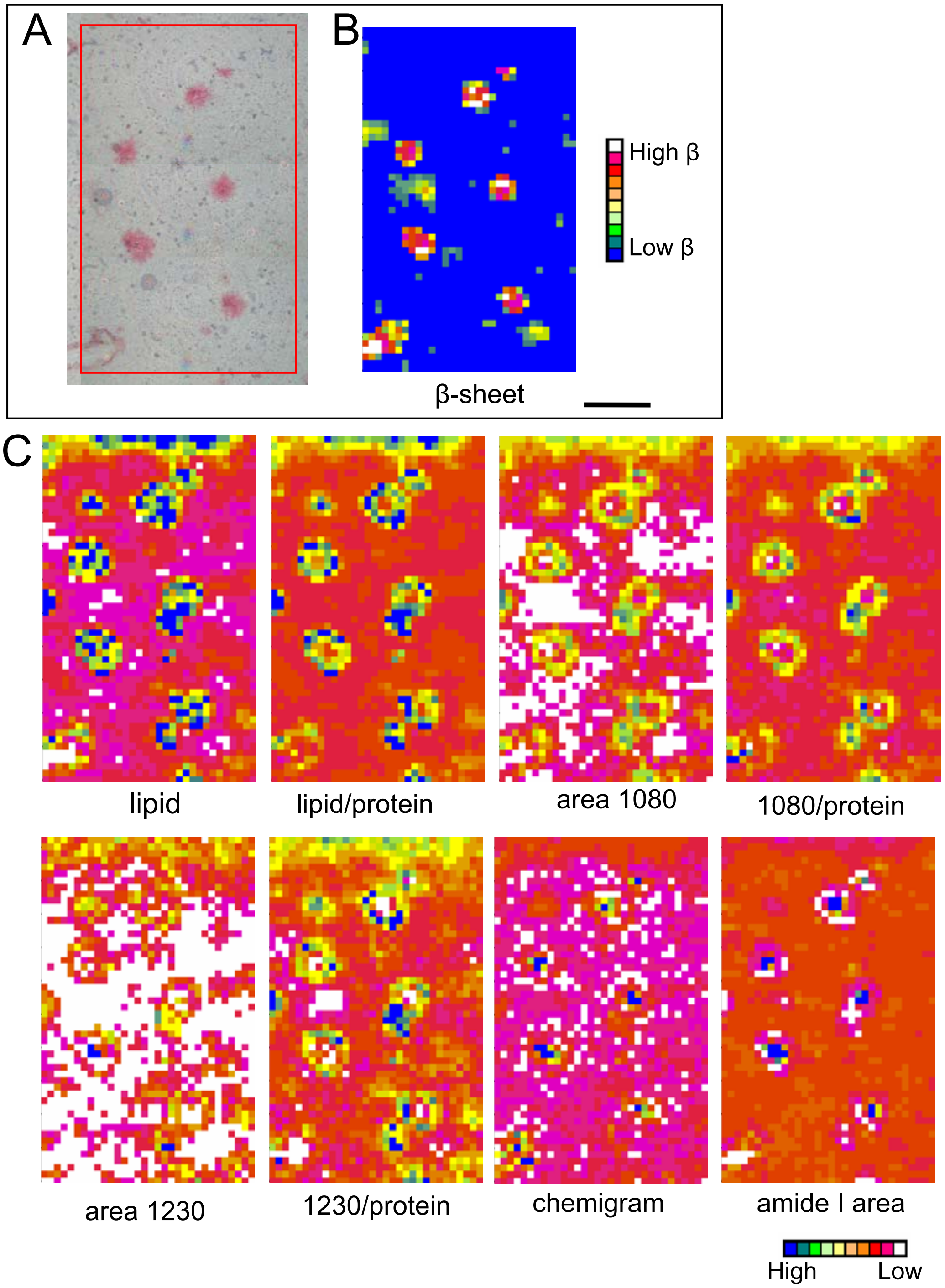

Figure 4.35. Dense-cored plaques from a 21-month-old TgCRND8 mouse. (A) A photomicrograph of the mapped region, stained with Congo red after IR mapping. The plaques are found in the central region of the hippocampus. Note the congophilic blood vessel in the lower-left corner of the map. (B) The map processed to show elevated β-sheet proteins. (C) The map processed with the methods outlined in Table 3.1. All plaques are surrounded by elevated phospholipids, indicated by increased intensity around the plaque core in the lipid, lipid/protein, area 1080, 1080/protein, area 1230 and 1230/protein maps. Scale bar = 100 μm.

Typical spectra of plaque core, normal neuropil and the region of elevated lipid around the plaque core are shown in Figure 4.36. The core (red) shows increased intensity in the amide I band and decreased intensity of the bands due to other tissue components such as the CH stretches and the bands at 1080 and 1230 cm^{-1}. This demonstrates elevated protein content in plaque cores and the exclusion of other components, compared with healthy tissue. The spectrum of the region surrounding the plaques (green) has elevated intensity in the CH stretch, and the 1080 and 1230 cm^{-1} bands, compared to normal neuropil (blue). The bands at 1080 cm^{-1} and 1230 cm^{-1} are assigned to symmetric and asymmetric phosphate stretching, respectively. However, the spectral region from 1300 to 900 cm^{-1} is very complex, containing many overlapping absorptions. For example, various carbohydrate vibrations are found between 1200 and 900 cm^{-1}, and the presence of carbohydrate residues has in fact been reported in the periphery of amyloid plaques with lectin histochemistry (Szumanska et al, 1987). Nevertheless, the high correlation between the chemical maps based on the intensity of the CH_2 stretch peaks, the 1080 cm^{-1} peak and the 1230 cm^{-1} peak leads to the conclusion that there is an increase in phospholipids around plaque cores. This is confirmed by the elevation of other lipid peaks, such as the C=O stretch at 1740 cm^{-1} and the CH deformation band at 1466 cm^{-1} (Figure 4.36, green spectrum). This elevation does not appear to be due to displacement of normal tissue by plaque core, as the total absorbance around the plaque core is not higher than for normal neuropil.

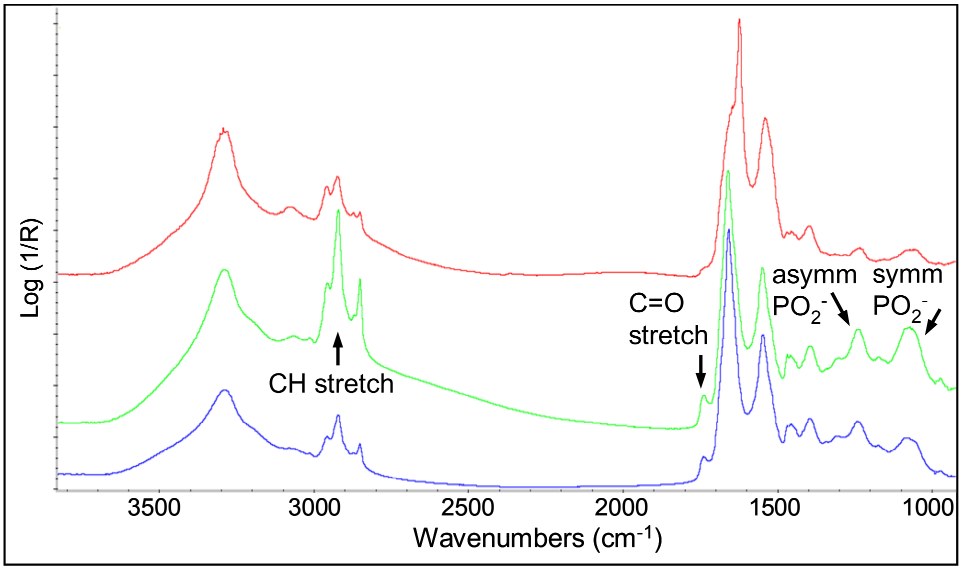

Figure 4.36. Spectra of plaques and their surroundings. Normalized spectra of plaque core (red), plaque edge (green), and normal neuropil further from plaque (blue). Arrows indicate the phospholipid peaks.

4.4.4.6. Hierarchical Cluster Analysis of Plaque Maps

A multivariate method like cluster analysis can be used to objectively group spectra. The results given by this method for plaque maps were compared to the results of the simple functional group analyses. Clustering was based on several spectral regions, listed in Table 3.2 in the Methods section. The results of cluster analysis on a typical map of a dense-cored plaque in the cortex of a 21-month-old TgCRND8 mouse are presented below. This is the example map from Section 4.4.4.1.

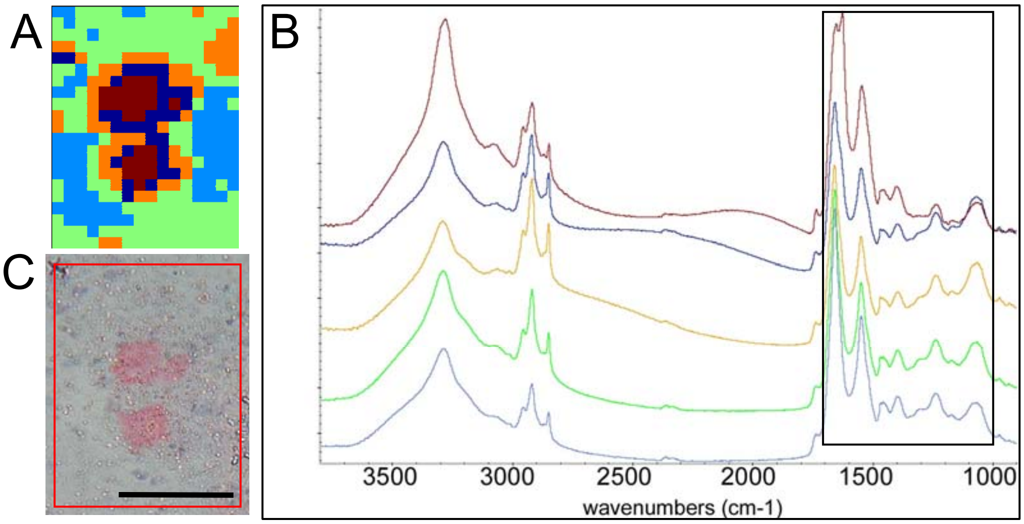

Figure 4.37. Cluster analysis on the fingerprint region. (A) Image and (B) corresponding average spectra created by hierarchical cluster analysis on the spectral region from 1700 to 1010 cm^{-1}. (C) The mapped tissue, stained with Congo red after IR data collection.

Clustering on the spectral region from 1700 to 1010 cm^{-1} distinguished the main pathological changes associated with plaques. Figure 4.37 shows (A) the cluster image, (B) the corresponding average spectra, and (C) the tissue stained with Congo red after mapping. The spectrum of plaque core (brown) has an amide I maximum at 1623 cm^{-1}, and the phospholipid peaks have lower intensities. The spectra surrounding the plaque (dark blue and orange) are high in phospholipids, indicated by increased intensity of the

CH and phosphate stretching bands. The spectra closest to the core (dark blue) have a sinusoidal baseline that distorts the shape of the amide I band. The spectra of the surrounding neuropil (green and light blue) have amide I maxima at 1659 and 1658 cm^{-1}, and intermediate amounts of phospholipids. Thus, the cluster map permits distinction of the plaque core, the elevation of phospholipids around the core, and the surrounding neuropil in just one image. Univariate and bivariate methods can only show one aspect of the sample chemistry at a time.

The results of hierarchical cluster analysis will vary depending on the spectral region chosen for the analysis. Cluster analysis based on the amide I band (Figure 4.38) or both the amide I and II bands (Figure 4.39), could distinguish the plaque core, the distortion of the amide I by baseline effects around the plaque core and the surrounding neuropil. The results of these two methods are similar but not the same. For this particular map, clustering on the amide I alone resulted in three main clusters, while using both the amide I and II gave 4 main clusters.

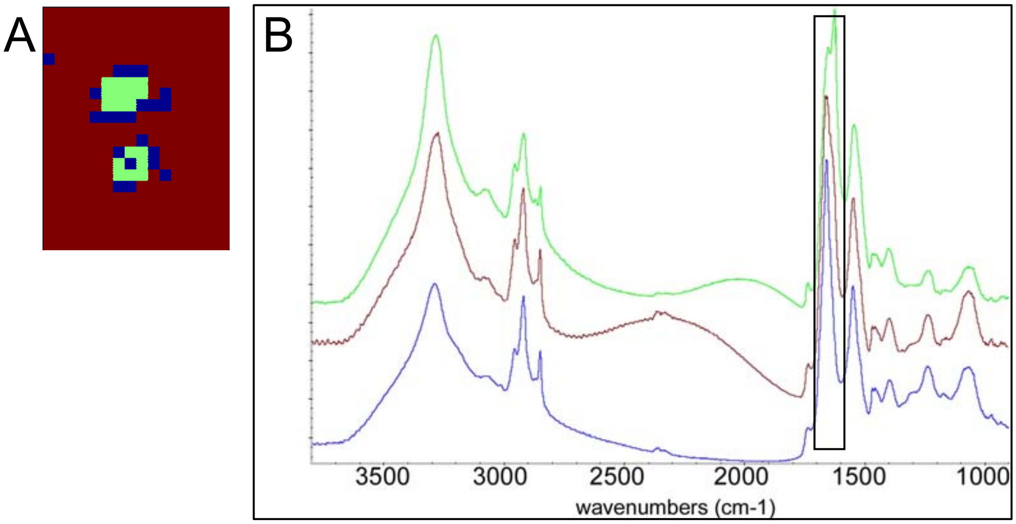

Figure 4.38. Cluster analysis on the amide I band. (A) Image and (B) corresponding average spectra created by hierarchical cluster analysis on the spectral region from 1700 to 1600 cm^{-1}.

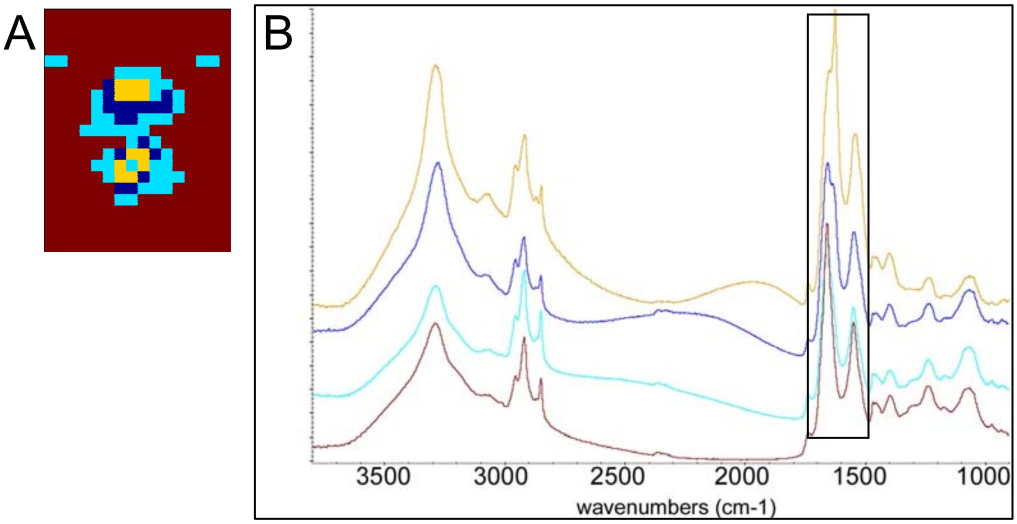

Figure 4.39. Cluster analysis on the amide I and II bands. (A) Image and (B) corresponding average spectra created by hierarchical cluster analysis on the spectral region from 1700 to 1500 cm^{-1}.

Clustering on the CH stretch region was successful in distinguishing the higher phospholipid levels around the plaque core (Figure 4.40). This method was also used to image white matter, neuropil and densely packed neurons in the hippocampus, as in Figures 4.11 and 4.21.

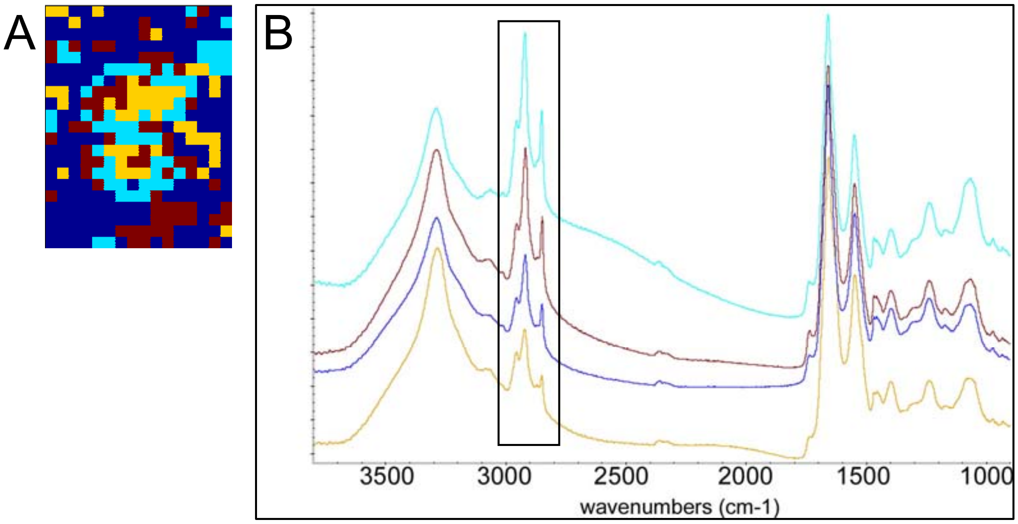

Figure 4.40. Cluster analysis on the CH stretch region. (A) Image and (B) corresponding average spectra created by hierarchical cluster analysis on the spectral region from 2998 to 2830 cm^{-1}.

Good results were also obtained by using both the CH stretch region and the amide I and II region (Figure 4.41).

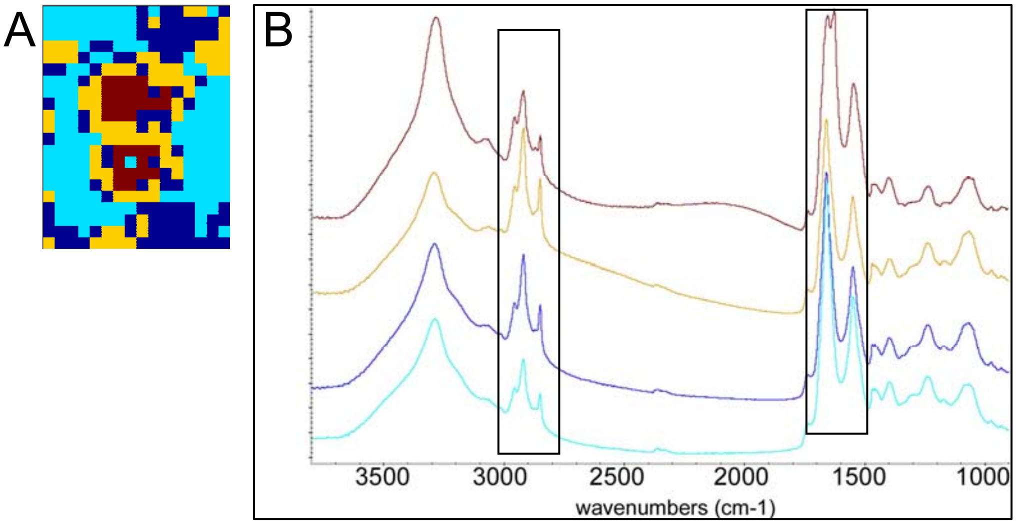

Figure 4.41. Cluster analysis on the amide I and II bands and the CH stretch region. (A) Image and (B) corresponding average spectra created by hierarchical cluster analysis on spectral regions from 1700 to 1500 cm^{-1} and 2998 to 2830 cm^{-1}.

Clustering on the region 1335 to 1010 cm^{-1}, which contains the phosphate stretches, the amide III and various sugar bands, was able to detect the elevation in phospholipids around plaque cores (Figure 4.42).

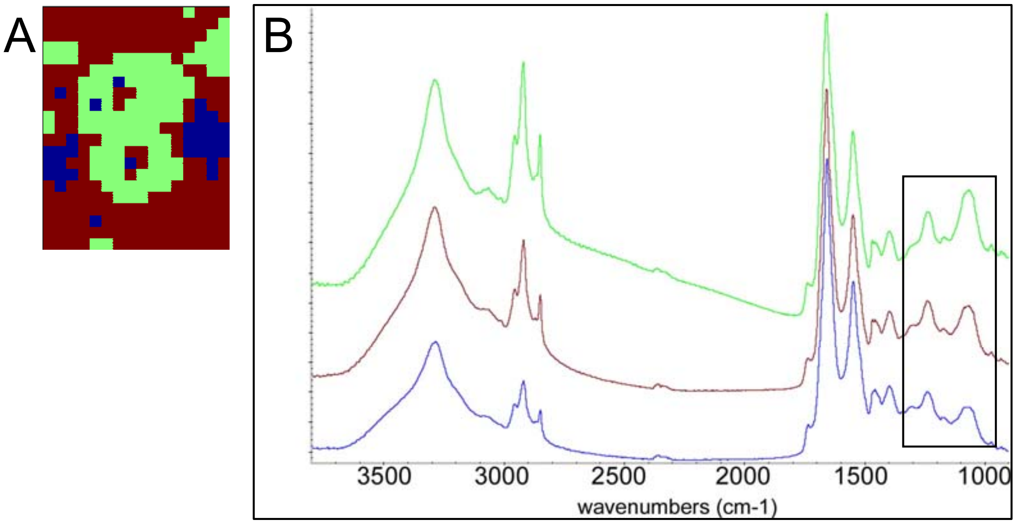

Figure 4.42. Cluster analysis on the phosphate stretch region. (A) Image and (B) corresponding average spectra created by hierarchical cluster analysis on the spectral region from 1335 to 1010 cm^{-1}.

The above results are in agreement with the results of the functional group analysis. The cores are composed of highly aggregated protein rich in β-sheet, with low amounts of other components. They are surrounded by elevated levels of phospholipids, indicated by increased intensity in the CH stretch peaks and the phosphate bands at 1230 and 1080 cm^{-1}. The spectra immediately around plaque cores often have a sinusoidal baseline that can distort the shape of the amide I band. Cluster analysis was applied to most of the maps collected. It was possible to distinguish between different tissue types in control and AD tissue, and to image the changes associated with dense-cored plaques. However, it was not successful in distinguishing the diffuse plaques from the surrounding tissue (see next section).

Many studies utilize second derivative spectra for multivariate analysis. Therefore, cluster analysis was also performed on second derivative spectra. This method was much less effective in imaging spectral differences than cluster analysis on the original spectra (data not shown). The main disadvantage of derivatization is the magnification of noise. The sharp peaks due to noise become much more prominent than the broad peaks due to tissue components. Therefore, a significant amount of smoothing was needed. A 9-point Savitzky-Golay algorithm (which uses a 9-point polynomial to smooth and derivatize the spectra) (Savitzky & Golay, 1964) was required to get second derivatives where noise did not swamp the peaks arising from the tissue components. This was the case even for spectra that did not appear to be noisy in their original form. However, the effect of this smoothing was to mask actual spectral differences. Cluster analysis of derivative spectra gave much poorer differentiation than cluster analysis of the original spectra.

4.4.4.7. Diffuse Plaques

In addition to dense-cored plaques, AD brains usually also have diffuse plaques. The two plaque types generally show different spatial and temporal distribution and their relative roles in the disease process are poorly understood (Armstrong, 1998; Dickson and Vickers, 2001; Selkoe, 2001; Wegiel et al, 2001). Diffuse plaques are also found in transgenic animal models such as the TgCRND8 mice. As diffuse plaques are invisible in unstained tissue, they were located though the examination of serial immunostained sections, and IR mapped in the corresponding region on the MirrIR slide. As discussed above, diffuse plaques were mapped predominantly in the caudate, where they are the principal plaque type and could be reliably identified. The caudate is composed of grey matter, with white matter fibres running throughout it. The white matter fibres can be easily distinguished visually in the stained and unstained tissue, and in the IR maps based on the lipid content. They are therefore very useful in locating corresponding regions in serial sections. Immunostaining showed that diffuse plaques were found only in the grey matter.

Representative data of diffuse plaques in the caudate of TgCRND8 mice at 11, 14, 16, 17, and 21-months-old are shown in Figures 4.43 to 4.47. The serial immunostained sections, and the mapped regions (both unstained and Congo red stained after mapping) are shown. Each IR map has been processed for β-sheet content, as well as for all other relevant bands. The amide I band showed exclusively the normal α-helical conformation throughout the diffuse plaque regions in all maps. This was confirmed by a lack of Congo red staining following IR mapping. An attempt was made to correlate diffuse plaque location with changes in the distribution of IR peaks due to other tissue components. Numerous data analysis protocols were evaluated in order to find differences between diffuse plaque and normal tissue spectra. These included univariate and bivariate analysis of spectral bands of interest, as well as hierarchical cluster analysis, which can objectively group spectra based on very subtle differences (Lasch et al, 2004). However, despite a broad range of strategies, it was not possible to differentiate between regions of diffuse Aβ immunostaining and normal tissue. The only differences observed were due to spectral differences between the white and grey matter of the caudate. The IR maps of diffuse plaques in TgCRND8 mice were indistinguishable from data of control caudate (Figure 4.48). Elevated levels of phospholipids always corresponded to white matter fibres. As in the corpus callosum white matter in the hippocampus, the amide I band of white matter in the caudate (both control and TgCRND8) showed a shift towards the lower wavenumbers, giving false positives in the β-sheet maps. However, as immunostaining demonstrated that diffuse Aβ plaques were never found in the white matter, these shifts could be ignored.

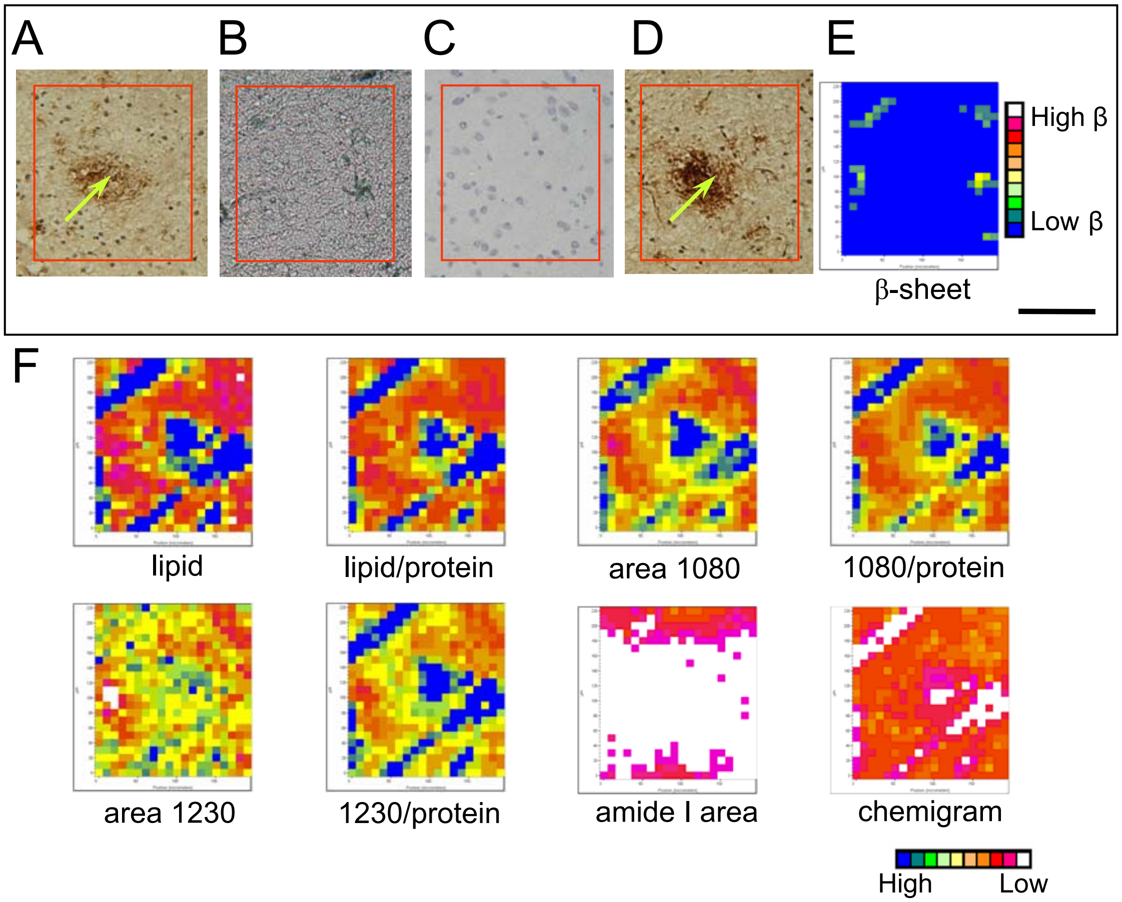

Figure 4.43. Diffuse plaque in the caudate of an 11-month-old TgCRND8 mouse. (A, D) Photomicrographs of sections serial to both sides of the IR mapped section, immunostained with anti-Aβ antibody 4G8 to show the presence of diffuse plaques. A diffuse plaque common to both serial immunostained sections (and therefore found in the mapped section between them) is indicated with arrows. Photomicrographs of the mapped region (B) unstained and (C) stained with Congo red after IR mapping. (E) The map processed to show elevated β-sheet proteins. No elevated β-sheet signal is detected throughout the IR map. (F) The map processed with the methods outlined in Table 3.1. Elevated phospholipids correspond to the white matter fibres. Scale bar = 100 μm.

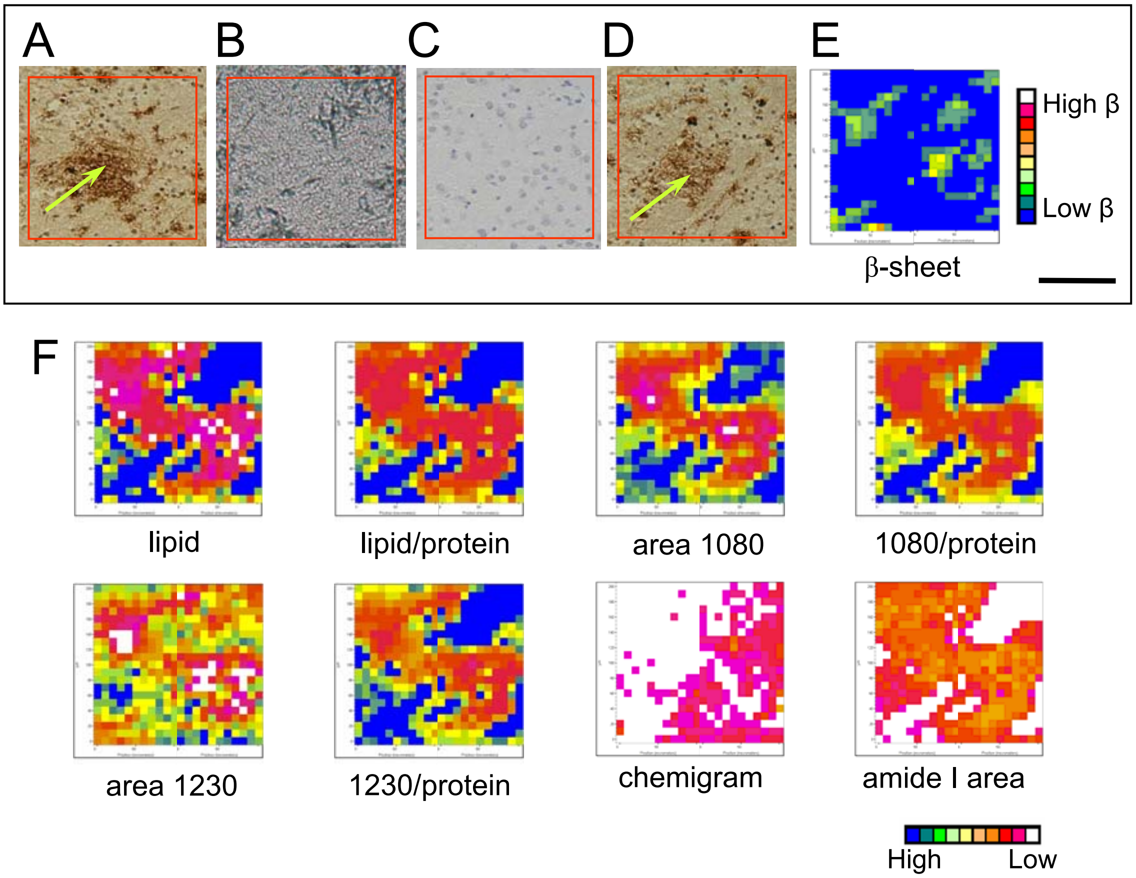

Figure 4.44. Diffuse plaque in the caudate of a 14-month-old TgCRND8 mouse. (A, D) Photomicrographs of sections serial to both sides of the IR mapped section, immunostained with anti-Aβ antibody 4G8 to show the presence of diffuse plaques. A large diffuse plaque common to both serial immunostained sections (and therefore found in the mapped section between them) is indicated with arrows. Photomicrographs of the mapped region (B) unstained and (C) stained with Congo red after IR mapping. (E) The map processed to show elevated β-sheet proteins. No elevated β-sheet signal is detected throughout the IR map. (F) The map processed with the methods outlined in Table 3.1. Elevated phospholipids correspond to the white matter fibres. Scale bar = 100 μm.

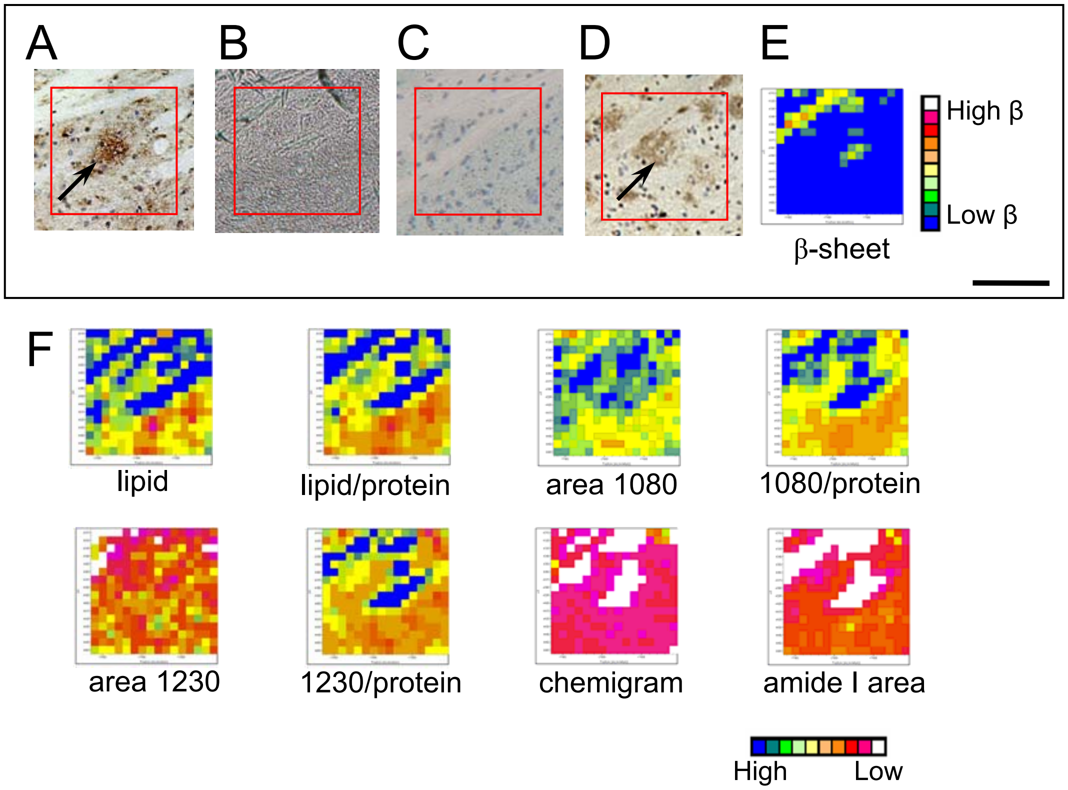

Figure 4.45. Diffuse plaque in the caudate of a 16-month-old TgCRND8 mouse. (A, D) Photomicrographs of sections serial to both sides of the IR mapped section, immunostained with anti-Aβ antibody 4G8 to show the presence of diffuse plaques. A diffuse plaque common to both serial immunostained sections (and therefore found in the mapped section between them) is indicated with arrows. Photomicrographs of the mapped region (B) unstained and (C) stained with Congo red after IR mapping. (E) The map processed to show elevated β-sheet proteins. No elevated β-sheet signal is detected throughout the IR map. (F) The map processed with the methods outlined in Table 3.1. Elevated phospholipids correspond to the white matter fibres. Scale bar = 100 μm.

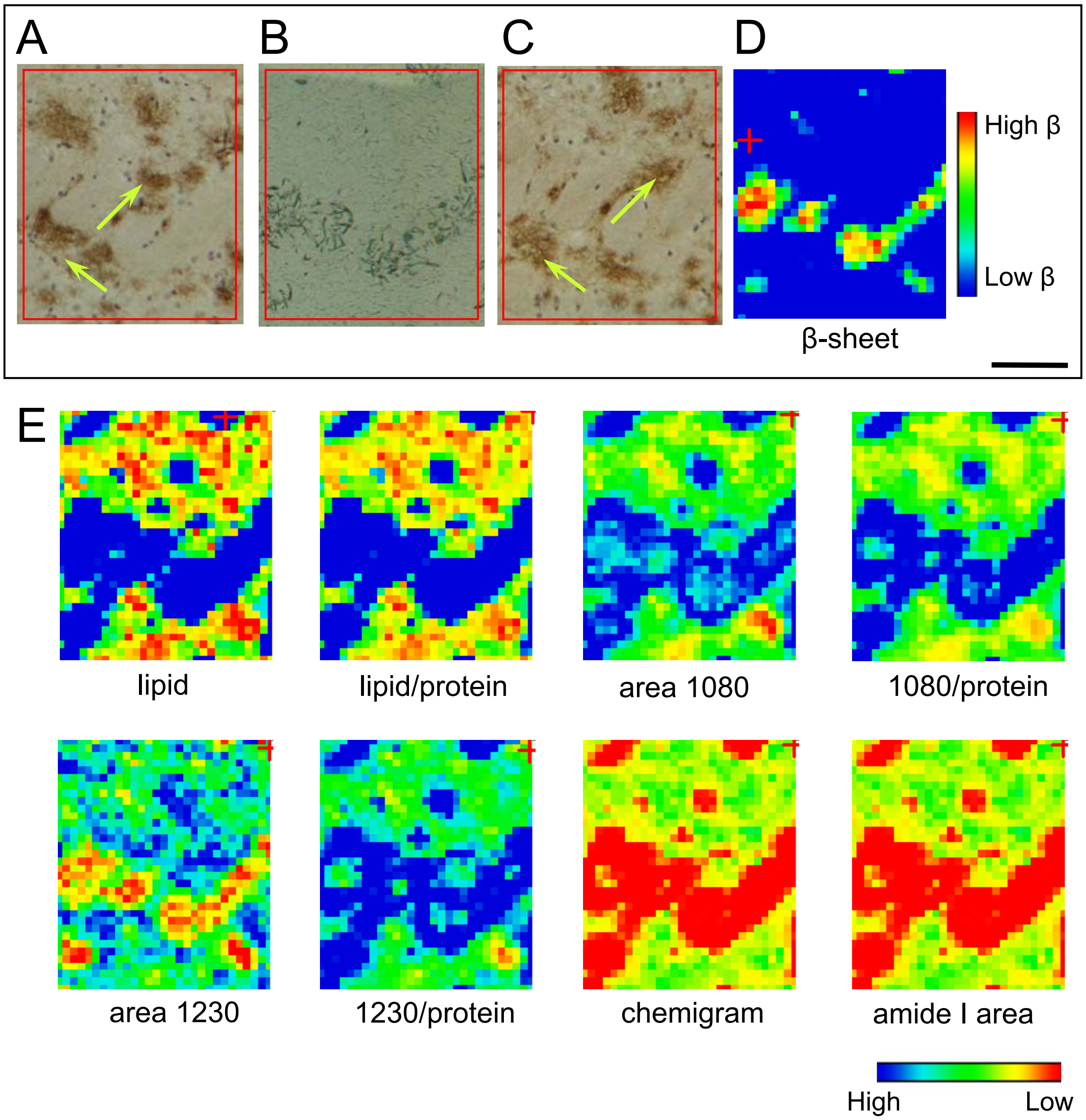

Figure 4.46. Diffuse plaques in the caudate of a 17-month-old TgCRND8 mouse. This map was collected with a new version of Atlµs which uses a different color-scale from the older version used for the remaining data. (A, C) Photomicrographs of sections serial to both sides of the IR mapped section, immunostained with anti-Aβ antibody 4G8 to show the presence of diffuse plaques. Two diffuse plaques common to both serial immunostained sections (and therefore found in the mapped section between them) are indicated with arrows. (B) A photomicrograph of the unstained mapped region. (D) The map processed to show elevated β-sheet proteins. As is often the case, the white matter gives a false-positive in the β-sheet map. (E) The map processed with the methods outlined in Table 3.1. Elevated phospholipids correspond to the white matter fibres. Scale bar = 100 µm.

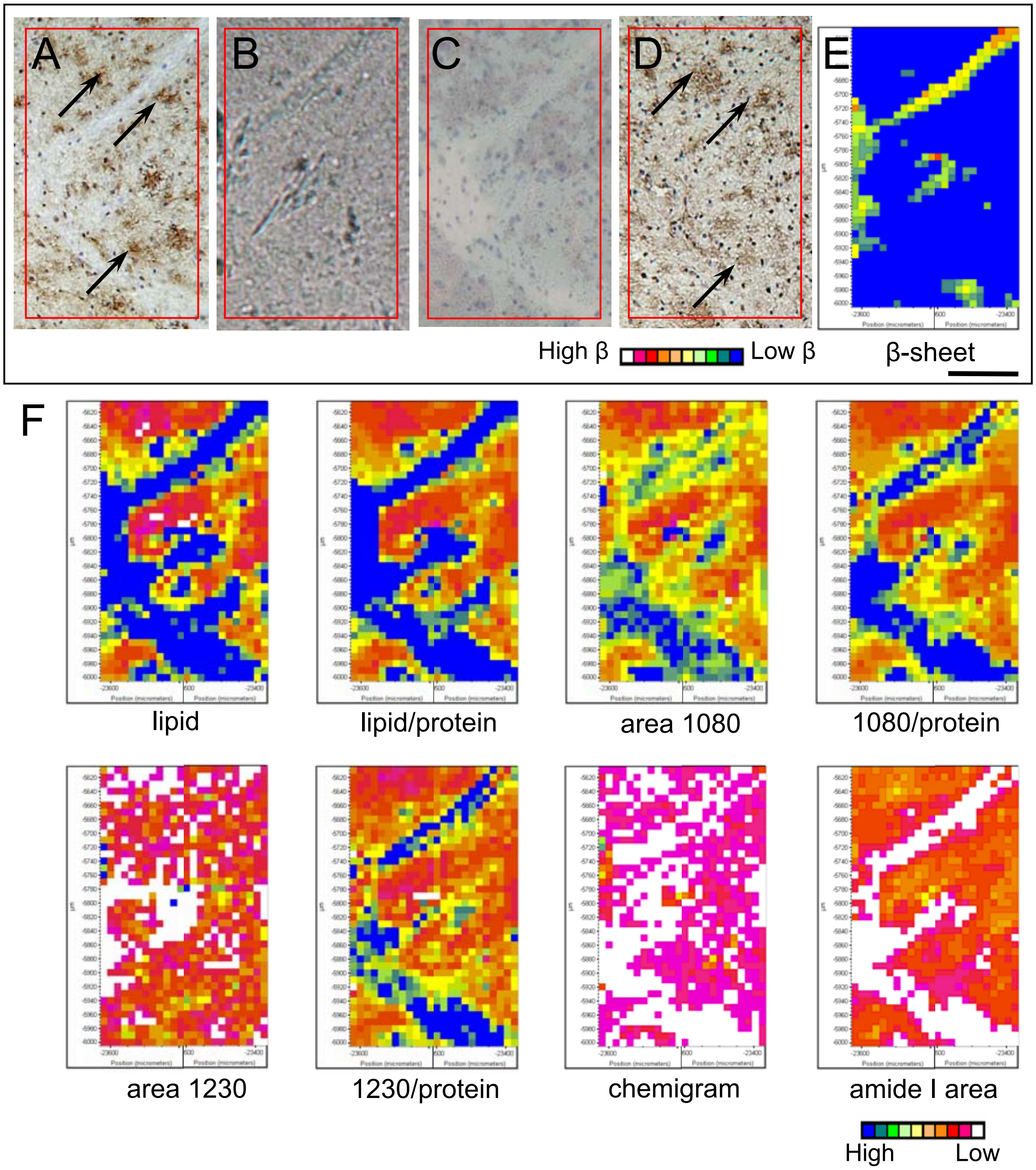

Figure 4.47. Diffuse plaques in the caudate of a 21-month-old TgCRND8 mouse. (A, D) Photomicrographs of sections serial to both sides of the IR mapped section, immunostained with anti-Aβ antibody 4G8 to show the presence of diffuse plaques. Several diffuse plaques common to both serial immunostained sections (and therefore found in the mapped section between them) are indicated with arrows. Photomicrographs of the mapped region (B) unstained and (C) stained with Congo red after IR mapping. (E) The map processed to show elevated β-sheet proteins. No elevated β-sheet signal is detected throughout the IR map. (F) The map processed with the methods outlined in Table 3.1. Elevated phospholipids correspond to the white matter fibres. Scale bar = 100 μm.

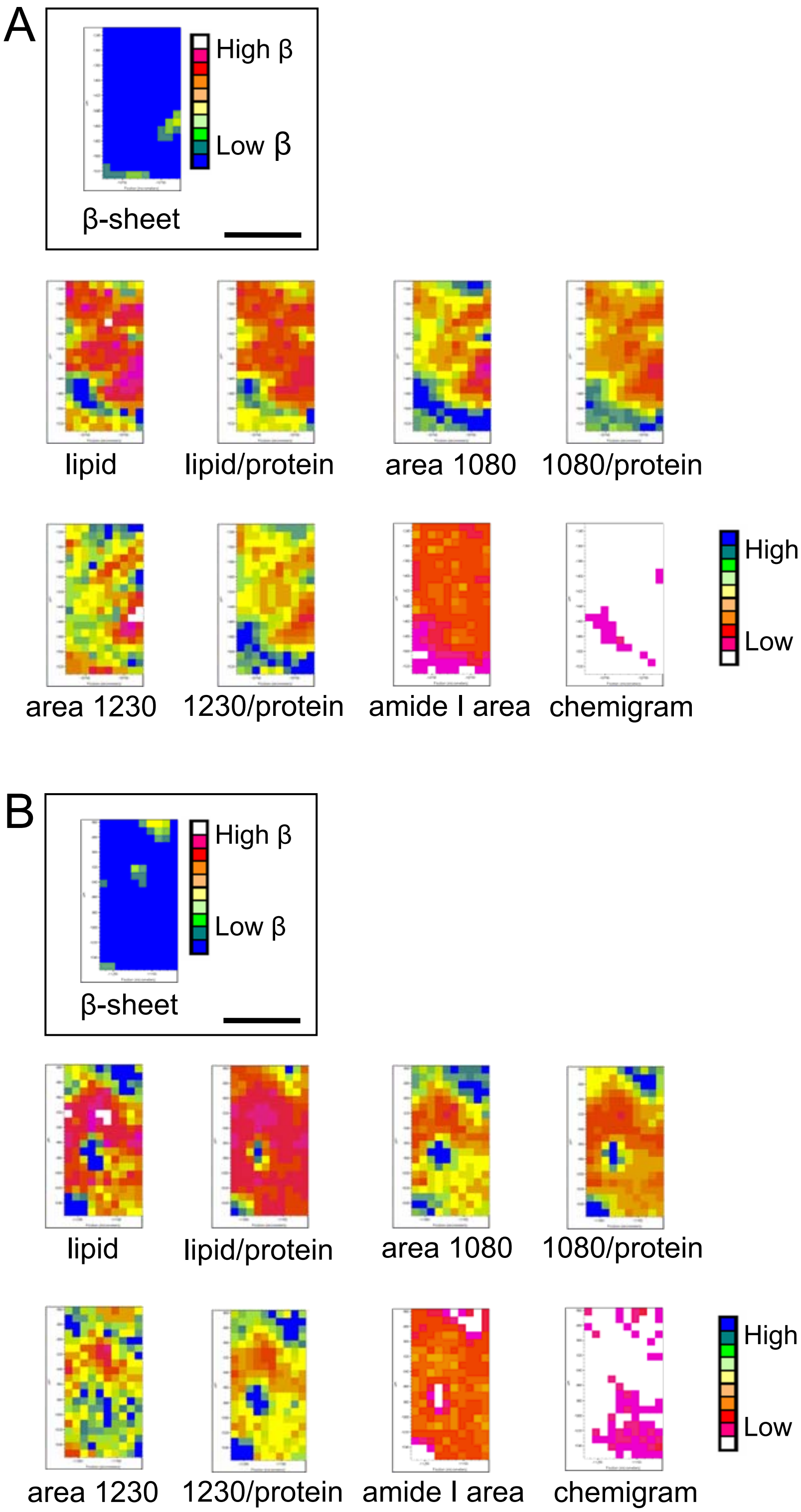

Figure 4.48. Control caudate maps. Representative IR maps in the caudate of 11-month-old control mouse. Scale bar = 100 μm. Figure continued on next two pages.

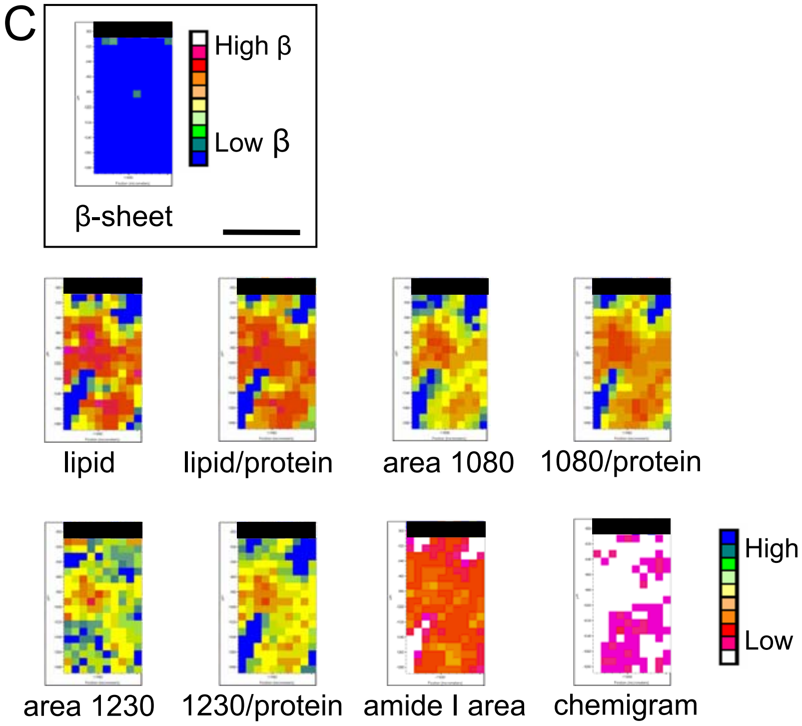
C
High β
Low β
β-sheet
lipid
lipid/protein
area 1080
1080/protein
area 1230
1230/protein
amide I area
chemigram
High
Low

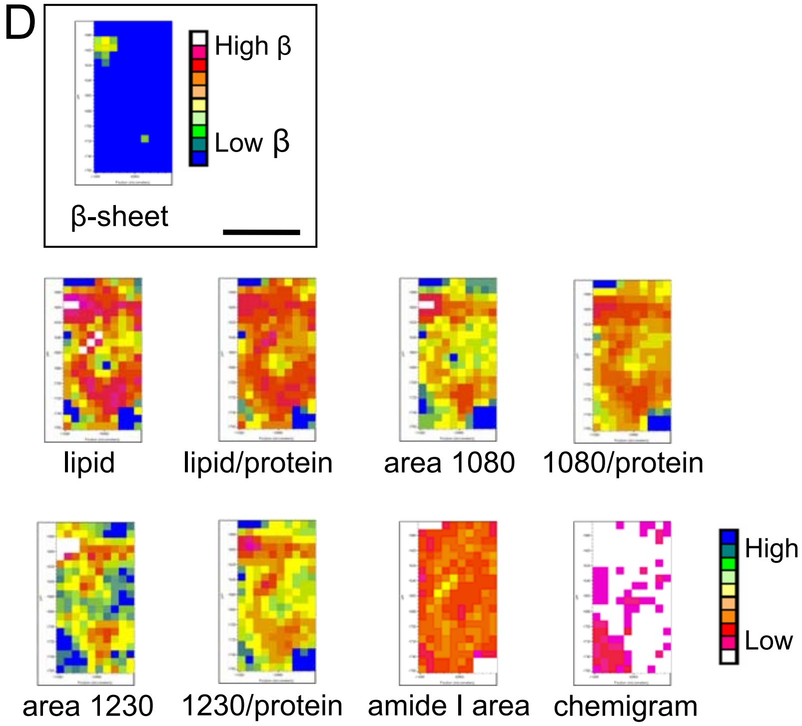
D
High β
Low β
β-sheet
lipid
lipid/protein
area 1080
1080/protein
area 1230
1230/protein
amide I area
chemigram
High
Low

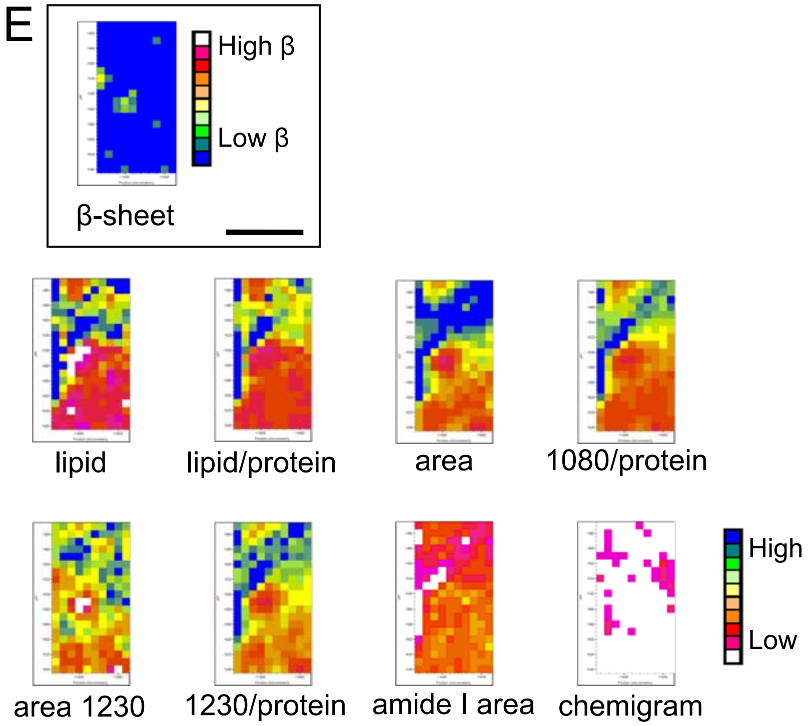
E
High β
Low β
β-sheet
lipid
lipid/protein
area
1080/protein
area 1230
1230/protein
amide I area
chemigram
High
Low

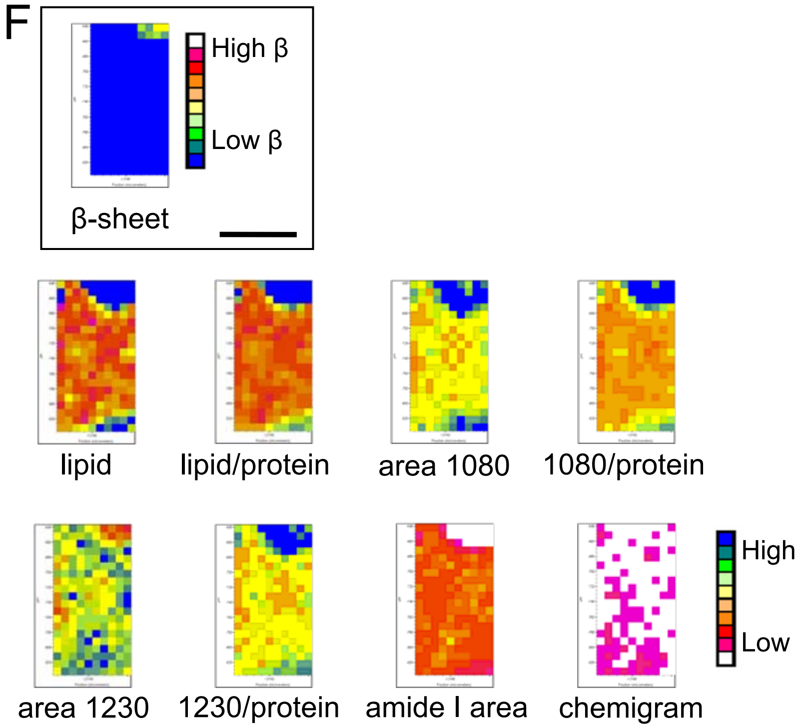
F
High β
Low β
β-sheet
lipid
lipid/protein
area 1080
1080/protein
area 1230
1230/protein
amide I area
chemigram
High
Low

Chapter 5. Alzheimer's Disease Study Discussion

5.1. IR Spectra Reflect Differences in Tissue Composition

The first part of this thesis involved mapping hippocampal neurons, as well as the neuropil and white matter, in the hippocampus of 5 and 11-month-old TgCRND8 and control mice. This was because IR mapping of human hippocampal neurons appeared to show an association between elevated β-sheet content and the presence of AD pathology in the brain (Ogg, 2002). The present data were analyzed using the ratio of the amide I band areas due to α-helix and β-sheet, to show the presence of elevated β-sheet in the tissue (Figures 4.17 to 4.20, maps labeled as a). The neurons, as well as the white matter, did show an increased absorbance in the spectral region attributed to β-sheet protein. However, this was found in both AD and control mice, at both ages. The neurons, neuropil and white matter had different Amide I band profiles (Figure 4.21F). This is due to differences in the secondary structure of the proteins in these different tissue types, and not the disease process. In fact, no pathological changes to the neurons, such as the accumulation of intraneuronal Aβ peptide that is seen in human AD, have been reported for this mouse model.

The data collected for this part of the project was however very useful, as the normal spectral variability of the tissue was established. As various tissue types have different molecular compositions, their spectra are also expected to be different. Brain tissue, in particular, is quite different from other tissue. Connective tissue rich in collagen is absent in the brain, while the content of lipids, especially phospholipids, is relatively high. Brain tissue can be divided into two main types, the white and grey matter. The white matter is composed of nerve cell fibers covered with a myelin sheath, produced by

Schwann cells, whose main component is a phospholipid known as sphingomyelin. The grey matter is composed of the neuronal bodies and their processes. It can be divided into the neuropil, a mixture of dendrites, axons and glial cell, and the neuronal bodies. The white and grey matter could be distinguished from each other based on the differences in lipid levels. In the grey matter, the densely-packed CA and dentate gyrus neurons were distinguishable from the neuropil as they were very low in lipid.

The different amide I band profiles of neurons, neuropil and white matter had to be considered when developing protocols to display the aggregated β-sheet of dense-cored plaques (Figure 4.27) in order to avoid false positives. When examined, the amide I profile of plaque cores (4.27) is different from the amide I bands of neurons or white matter, which are shifted to lower wavenumbers relative to the neuropil (Figure 4.21F). When the ratio of amide I band regions due to α-helix and β-sheet is used to visualize the changes in the amide I band, both the neurons, white matter and plaque cores show up as having elevated β-sheet. However, by choosing the right amide I regions for the analysis, most of the false-positives caused by white matter and neurons could be eliminated. Of course this is not an issue when more complex data analysis protocols, such as hierarchical cluster analysis (Section 4.4.4.6.), are used. Cluster analysis groups the data based on the shapes of the spectral bands, rather than on simple peak areas.

The normal tissue variability had to be distinguished from the pathological changes caused by the disease process. This is where the value of a transgenic animal model becomes most obvious. The transgenic mice and their littermate controls had been raised under exactly the same conditions, with the only difference being the transgene. Spectral differences that occurred in both groups were therefore due to the normal differences between tissue, such as those seen between the white matter, neurons and neuropil. Any differences found between control and transgenic animals, on the other hand, would have to be due to AD pathology.

.

5.2. Secondary Structure of Aβ in Plaque Cores

Plaques, the main pathological feature in TgCRND8 mice and human AD patients, play an important role in the pathogenesis of AD. Although it is still unclear whether plaques and/or NFTs are the cause or result of the disease process (Mudher and Lovestone, 2002; Smith et al, 2002), the most widely accepted hypothesis invokes deposition of Aβ in the brain (Selkoe, 2001; Uversky et al, 1999), since all variants of early-onset FAD are the result of mutations in the genes for APP, presenilins 1 or 2, that lead to increased levels of Aβ (Hardy and Gwinn-Hardy, 1998; Scheuner et al, 1996). The Aβ peptide is clearly neurotoxic. However, as it can form a number of different types of aggregates, the most toxic form is still unclear. The smaller pre-fibrillar intermediates may be more neurotoxic than the amyloid fibrils that make up dense-cored plaques (Lansbury, 1999; Watson et al, 2005). Aβ oligomers, ADDLs and fibrils are all toxic to cultured neurons, although the mechanisms by which they act may be different (Deshpande et al, 2006). As well, other processes such as oxidative stress, inflammation and energy disturbances may play key roles in AD pathogenesis (Beal, 1995; Butterfield et al, 2002; Gallant et al; 2005; Markesbery & Carney, 1999). However, in TgCRND8 mice, the onset of cognitive impairment coincides with plaque deposition, and becomes more severe with age, indicating that the plaques play a central role in the disease process (Belluci et al, 2006; Hyde et al, 2005).

IR microspectroscopy confirms that dense-core plaques in TgCRND8 mice are predominantly proteinaceous deposits with a highly aggregated β-sheet structure. The amide I maximum of TgCRND8 mouse plaque cores is found at 1623 cm^{-1}, which differs from a maximum of 1630-1632 cm^{-1} reported for human AD plaques (Choo et al, 1996;

Ogg, 2002). This could be due to biochemical or structural differences between human and TgCRND8 mouse plaques. Analysis of plaques in two other transgenic mouse models of AD (Kalback et al, 2002; Kuo et al, 2001) has shown that the post-translational modifications found in AD plaques are absent in the transgenic mice, whose plaques are much more soluble in detergent-containing buffers, compared to AD plaques. The post-translational modifications to the Aβ peptide would affect the structure of the Aβ fibrils, and hence would affect the Amide I band shape and position. The broad absorption still seen in the plaque core spectra between 1660-1640 cm^{-1} may be due to unordered structure, in agreement with solid state NMR work that indicates that the first 10 residues of the Aβ peptide fibrils are unstructured (Tycko , 2003). This could also be due to other proteins found in the plaque (Maury, 1995).

The general structure proposed for amyloid is a cross β-pleated sheet fibril (Glenner et al, 1974). *In vitro* IR spectra of Aβ fibrils typically show a splitting of the amide I band into a strong low frequency (1620-1630 cm^{-1}) and a weaker high frequency (1680-1690 cm^{-1}) component (Fabian et al, 1993; Lansbury, 1992), classic features of anti-parallel β-sheet (Krimm and Bandekar, 1986). It is important to keep in mind that amyloid fibrils formed *in vivo* aggregate under very different conditions than those *in vitro*, and may well be structurally different. By using the high spatial resolution of synchrotron IR microspectroscopy, the spectra of the aggregated Aβ in plaque cores can be analyzed *in situ*. There was no evidence of the splitting of the amide I band in mouse plaque core spectra (Figure 4.27), and it has not been reported for human AD plaques (Choo et al, 1996; Miller et al, 2006; Ogg, 2002). The high frequency region of the plaque amide I band shows only a broad, fairly intense absorbance, with no evidence of the split high frequency component. *In vitro*, both parallel and anti-parallel β-sheets are possible for the cross-β fibrils (Tycko, 2003). The IR spectra of dense-core plaques are however clearly indicative of β-sheet, in agreement with *in vitro* work on amyloid fibrils showing that aggregation is associated with an increase in β-sheet structure (Halverson et al, 1990).

Histological evaluation with the amyloid dye Congo red after IR mapping showed that the amide I band shape typical of aggregated β-sheet was always associated with Congo red staining. This was true of both plaque cores and blood vessels with congophilic angiopathy. The two methods were always in agreement, within the spatial resolution of IR microspectroscopy. This directly confirmed the specificity of Congo red for aggregated amyloid, *in situ*.

5.3. Dense-cored Plaques are Surrounded by Elevated Phospholipids

The chemical analysis of the plaque microenvironment, achieved by IR microspectroscopy, revealed a significant increase in phospholipids around dense-core plaques. This is most likely due to an increase in membranes or membrane fragments (the bulk of whose structure is composed of phospholipid bilayers) owing to dystrophic neurites and glial processes around the plaque core. Cored plaques in human AD, as well as transgenic AD mice, are typically surrounded by activated microglia, astrocytes and dystrophic neurites (Armstrong, 1998; Dickson & Vickers, 2001; Dodart et al, 2002; Masliah et al, 1996; Phinney et al, 2003). Dense-core plaques in another transgenic AD mouse appear to have a neurotrophic effect, which leads to aberrant axonal growth, dystrophic boutons and neurites (Phinney et al, 1999). In cultured neurons, Aβ induces neurite growth, which is associated with an increase in phospholipids (Wang et al, 2000). In the TgCRND8 mouse, Bielschowsky silver staining and various immunostains reveal the presence of dystrophic neurites around dense-core plaques in the TgCRND8 mice (Bell et al, 2003; Belluci et al, 2006; Chishti et at, 2001; this work), found as early as 4 months of age (Bell et al, 2003). The plaques are also associated with a focal inflammatory response accompanied by activated glia cells (Belluci et al, 2006; Chishti et at, 2001). The increase in phospholipid levels in the immediate vicinity of dense-core plaques is intriguing because, *in vitro*, phospholipids have been shown to induce a conformational change from random coil to β-sheet in the Aβ peptide (McLaurin and Chakrabartty, 1997; Terzi et al, 1994; Terzi et al, 1999). As, well, purified brain plasma, endosomal and lysosomal membranes have been shown to accelerate Aβ fibrillogenesis (Waschuk et al, 2001).

5.4. Diffuse Plaques Are Not Detectable by IR Spectroscopy

In contrast to dense-core plaques, IR microspectroscopy was unable to reveal any protein secondary structure or other compositional changes associated with diffuse amyloid deposits. As the amide I band of diffuse plaques *in situ* appears to be indistinguishable from normal tissue, this could be due to the peptide adopting an α-helical or random coil structure and/or of the concentration of the Aβ peptide in diffuse plaques being below the limit of detection with this technique. The fact that diffuse plaques do not stain with the amyloid markers Congo red or Thioflavin S suggests that they lack β-sheet structure. However, both fibrillar and amorphous morphologies have been reported for Aβ in diffuse plaques from electron microscopy studies (Davies and Mann, 1993; Yamaguchi et al, 2000). This is paralleled by *in vitro* work, which shows that Aβ can adopt a variety of secondary structures depending on experimental conditions, including β-sheet rich fibrils and protofibrils, and unstructured aggregates that do not have a regular secondary structure (Jackson Huang et al, 2000; Walsh et al, 1999).

Perhaps it is not surprising that diffuse plaques are not detectable by IR spectroscopy, given that they do not appear to disturb the tissue morphology. Unlike dense-core plaques, diffuse plaques do not disturb the structure of the neuropil and dendrites (Adlard and Vickers, 2002). In both human and transgenic mouse models, diffuse plaques are not associated with reactive glia (Stalder et al, 1999; Wegiel et al, 2001b; Wisniewski et al, 1998), dystrophic neurites (Argstrong, 1998; Brendza et al, 2003; Dickson and Vickers, 2001; Phinney et al, 1999), aberrant axonal sprouting (Phinney et al, 1999) and neurotoxicity (Urbanc et al, 2002). In human post-mortem tissue, diffuse plaques are found in both AD and normal aged brain, while dense-core plaques are associated with AD. Dense-core plaques are therefore believed to be the pathogenic species in AD, and separate processes are believed to be responsible for the formation of the dense-core and diffuse plaques (Armstrong, 1998; Dickson and Vickers, 2001; Van Groen et al, 2003; Wegiel et al, 2001).

Chapter 6. Alzheimer's Disease Study Conclusions

The following conclusions could be made:

- IR mapping analysis confirmed that dense-core plaques in TgCRND8 mice are composed of highly aggregated amyloid, while diffuse plaques, even in the oldest animals, did not have IR-detectable β-sheet structure.
- The aggregated amyloid is exclusively localized in the dense plaque cores; there is no evidence of Aβ aggregation in either the diffuse haloes that surround mature dense-core plaques or in the purely diffuse plaques found in the caudate.
- The amide I band maximum in the dense cores occurs at 1623 cm^{-1}, some 10 cm^{-1} lower than that reported in human plaque, but similar to that of Aβ fibrils grown *in vitro*.
- IR mapping provided unequivocal, physicochemical evidence that dense-core plaques are surrounded by significantly increased amounts of phospholipids. This increase could be the result of cellular reaction to aggregated amyloid (caused by dystrophic neurites and glial cells), but could also contribute to the development of aggregated amyloid through the interaction of newly secreted Aβ with phospholipids.
- The specificity of the Congo red stain for aggregated amyloid was confirmed directly *in situ*.
- There were no spectral differences found between hippocampal CA neurons of AD and control mice.
- In order to avoid false-positives, the spectral differences between different tissue types (such as neurons, neuropil and white matter) have to be considered.

Like all other techniques, IR microspectroscopy has its drawbacks. Although it is excellent for imaging dense-cored plaques, diffuse plaques cannot be located as their spectra are not different enough from those of normal tissue. As shown by this work, the specificity of Congo red staining and IR mapping for imaging dense-cored plaques is equivalent. Therefore, it is unlikely that IR mapping will replace conventional methods like Congo red staining and immunohistochemistry for diagnostic purposes. IR mapping however has several attributes that make it an excellent technique for research.

The combination of immunohistochemistry, Congo red staining and IR microspectroscopic mapping was a unique and powerful strategy to study plaques in a transgenic model of AD. Although staining methods are invaluable, they can usually only reveal one aspect of tissue composition at a time. The chemical information obtained from FTIR spectral analysis provides complementary information on the tissue composition in and around developing plaques. FTIR microspectroscopy permits the *in situ* study of both the secondary structure of proteins and the functional group content of tissue sections with minimal sample preparation, at the cellular level. The content of the sample is unaltered, with nothing added or taken away, providing information that cannot be gained with any other method. Additionally, as transgenic mice are often used to test potential treatments for AD (Chauhan et al, 2005; Janus et al, 2000; Schenk et al, 1999), FTIR microspectroscopic analysis could be a valuable complementary technique to analyzing tissue changes induced by these treatments.

Chapter 7. Creatine Deposits in AD Mouse Brain

7.1. Overview

This chapter describes the discovery of focally-elevated creatine (Cr) deposits in TgCRND8 mouse brain. The unusual spectral signature of these deposits was found in some of the IR plaque maps in the brains of transgenic mice recorded for this thesis. The spectra of these deposits were identical to those found previously by Mandy Ogg (M. Sc. student in Dr. K. Gough's laboratory) in human brain, although their identity was not known at the time (Ogg, 2002). The data presented will include IR maps of plaques which also contain the Cr deposits, as well as maps of large Cr streaks found in the cortex, caudate and hippocampus of aged TgCRND8 mice.

The creatine deposits were found in maps from the transgenic mice, never in the age-matched littermate controls. However, as that study involved mapping only regions of interest in AD, it was obvious that more systematic data collection was needed in order to draw conclusions about a possible relationship between the Cr deposits and AD. A related study, which involved mapping of the entire hippocampus in a series of transgenic and littermate control age-matched pairs, was therefore undertaken by Meghan Gallant (M. Sc. student in Dr. K. Gough's laboratory). This brain region was chosen because it is severely affected by AD pathology and the Cr deposits had often been found there. The mapping was performed by Meghan Gallant, aided by me and Dr. Robert Julian (SRC). In order to map a whole hippocampus, a large amount of data was required. The data collection was therefore shared by the people who could be at the synchrotron. The data included IR maps in transgenic animals and littermate controls. This set included six pairs of TgCRND8 mice and littermate controls (two 14-month-old pairs, and one each at 15, 16, 17 and 21 months). Two Tg(K670N/M671L+V717F)19959 mice and their littermate controls, (at 8 and 9 months old), were also analyzed. This mouse line was independently derived from the same transgene construct as TgCRND8 mice and expressed similar levels of APP holoprotein. Tg19959 mice had similar pathology to TgCRND8 mice but were maintained on a genetic background (129SvEv/Tac) different from the TgCRND8 mice (C3H/C57). The maps of the whole hippocampus will be presented in Meghan Gallant's thesis, but briefly mentioned in this chapter when relevant.

7.2. Introduction

7.2.1. The Cr/PCr System

The creatine-phosphocreatine (Cr/PCr) system plays a crucial role in the energy metabolism of tissues with high energy needs such as skeletal and cardiac muscle and the brain (see Wyss & Kaddurah-Daouk, 2000 for a review). ATP homeostasis is maintained by creatine kinase (CK), an enzyme that catalyzes the following reversible reaction:

$$\mathrm{Cr} + \mathrm{ATP} \leftrightarrow \mathrm{PCr} + \mathrm{ADP} + \mathrm{H}^+$$

ATP is synthesized in the mitochondrion, and its high energy phosphate is transferred to Cr by the mitochondrial isozyme of CK to form PCr (Figure 7.1A and B). Cytosolic CK then regenerates ATP from PCr and ADP in the cytosol, at the sites of energy usage. The Cr/PCr system thus acts as a shuttle of high energy phosphates, helping to maintain ATP homeostasis. Cr and PCr can diffuse in and out through the mitochondrial membrane as it is freely permeable to metabolites because of the large number of porin channels (Schlattner et al, 2006).

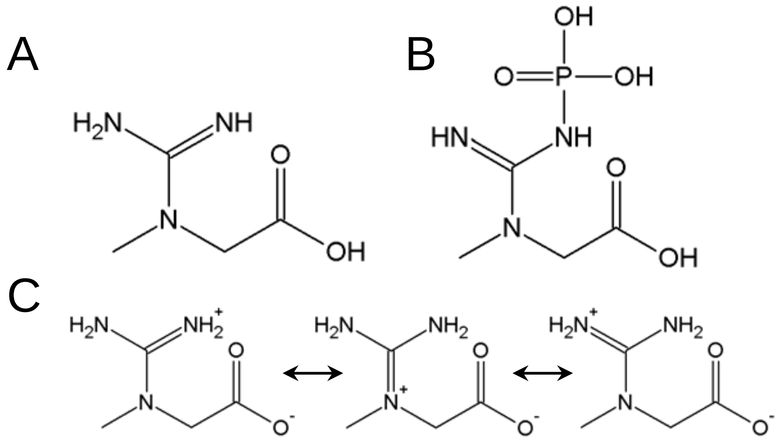

Figure 7.1. Creatine structure. (A) Cr and (B) PCr structure. (C) Cr exists as a zwitterion, its structure a hybrid of these three resonance structures.

Most of the body's Cr is synthesized in the liver and kidneys from arginine and glycine by the sequential action of L-arginine:glycine amidinotransferase (AGAT) and S-adenosyl-L-methionine:N-guanidinoacetate methyltransferase (GAMT) (Wyss & Kaddurah-Daouk, 2000). Cr-requiring cells use creatine transporters (CRT) in the plasma membrane to take it up from the blood (Wyss & Kaddurah-Daouk, 2000).

The Cr/PCr system appears to be highly regulated through the sub-cellular compartmentalization of the enzymes and substrates. It seems to not only buffer ATP levels, but to aid in the transport of high-energy phosphates in the form of PCr, which diffuses more easily than ATP from sites of generation to sites of usage (Hemmer & Wallimann, 1993). CRT is also localized in the mitochondrial membrane, which indicates that Cr and PCr are found in the mitochondria, in addition to the cytosol (Watzel et al, 2002). The mitochondria may therefore help to regulate the intracellular distribution of Cr (Watzel et al, 2002).

7.2.2. Cr/PCr System in the Brain

The brain requires large quantities of energy (Ames, 2000). The Cr/PCr system is therefore crucial to proper brain function. The two isozymes of CK found in brain are ubiquituous mitochondrial creatine kinase (uMtCK) and cytosolic brain-type creatine kinase (BB-CK). Mice lacking both brain isozymes of CK show severely impaired spatial learning and reduced body weight (Streijger et al, 2005). Patients with Cr deficiency syndromes, caused by deficits in the enzymes responsible for Cr synthesis or transport, show mental retardation and developmental delays, and a total absence of Cr and PCr in the brain (Schulze, 2003).

In normal mouse brain, the average concentration of Cr is 12 µM/g wet weight (Ipsiroglu et al, 2001). Isolated neural cells all contain Cr, with astrocytes having twice as much as neurons, and oligodedrocytes four times a much (Urenjak et al, 1993).

The source of Cr in the brain is still debatable as various studies give contradictory results. Cultured astroglial cells can synthesize Cr (Dringen et al, 1998). Studies in rat brain show that both AGAT and GAMT are expressed in neurons and glia (Braissant et al, 2001). CRT is expressed in neurons and oligodendrocytes, but not astrocytes, especially those of the blood-brain barrier (Braissant et al, 2001). This suggests that the brain is capable of de novo Cr synthesis and that Cr transport through the blood-brain barrier is difficult. Another study found preferential expression of GAMT in glia, which would suggest that Cr synthesized in the glia could be transported to the neurons (Tachikawa et al, 2004).

In contrast, other studies suggest that the brain gets most of its Cr by CRT-mediated transport through the blood-brain barrier (Ohtsuki et al, 2002). In Cr deficiency syndromes caused by malfunctioning GAMT or AGAT, oral Cr supplementation helps to ameliorate some symptoms and restore Cr levels in the brain. However, in Cr deficiency caused by CRT defects, supplementation does not restore Cr brain levels (Schulze, 2003). Cr appears to be able to cross the blood-brain barrier to a certain extent, as indicated by magnetic resonance spectroscopy (MRS) studies of Cr supplementation, which show increased brain levels of Cr by ^{1}H-MRS (Dechent, 1999; Lyoo, 2003) and marginal increases in brain PCr levels by ^{31}P-MRS (Lyoo, 2003). In conclusion, the source of the Cr used by the brain is still incompletely understood.

7.2.3. The Cr/PCr System and AD

Several studies point to an association of the Cr system with AD. CK is very sensitive to oxidative stress. It is one of the specific targets of post-translational oxidative modification in AD brain tissue (Aksenov et al, 2001; Castegna et al, 2002). The activity of CK is decreased in post-mortem AD brain compared to age-matched controls (David et al, 1998; Aksenov et al, 2000) and the decrease is negatively correlated with the formation of CK protein carbonyls, products of oxidative damage to proteins (Aksenova et al, 1999).

When cultured hippocampal neurons are exposed to Aβ, they undergo oxidative stress, including an increase in protein carbonyl formation and a decline in CK activity. (Aksenov et al, 1998) Also, ATP levels are reduced and mitochondrial function is disturbed (Mark et al, 1997; Casley et al, 2002). Reduced brain metabolism is almost always associated with AD and other forms of dementia (Beal, 1995; Blass et al, 2002). Oxidative stress and altered energy metabolism are believed to play a crucial role in

Alzheimer's pathology, however their respective roles are still unclear (Beal, 1995; Munch, 1998; Blass, 2001; Gibson, 2002).

In vitro, Cr has been shown to have protective effects on neurons exposed to glutamate and the Aβ peptide, by increasing the levels of PCr, which is used to regenerate ATP (Brewer & Wallimann, 2000). As an antioxidant with a crucial role in energy metabolism, Cr has been suggested as a potential therapy for AD and other neurodegenerative diseases (Tarnopolsky & Beal, 2001; Grundman & Delaney 2002; Wyss & Schulze 2002).

7.2.4. Measurement of Creatine in AD Brain

Cr levels in the brain can be measured with MRS. ^{1}H-MRS measures differences in proton resonance frequencies, *in vivo*, in specific volumes of tissue. It can be used to identify and measure the relative amounts of various proton-containing molecules. Cr is one of the molecules readily identified in a ^{1}H-MRS spectrum of brain tissue. The Cr peak is the sum of the Cr and PCr peaks. ^{31}P-MRS can be used to measure the levels of PCr alone based on the phosphate signal. The advantage of this technique is that *in vivo* measurements can be made on living subjects. However, the spatial resolution is quite low (1-8 cm^3 for ^{1}H-MRS, and 15-40 cm^3 for ^{31}P-MRS).

Many studies assume that the brain Cr levels are stable, and use it as an internal standard to normalize the levels of other metabolites in MRS spectra. (Firbank et al, 2002). However, this is generally not true and may lead to incorrect conclusions (Schirmer & Auer, 2000; Li et al, 2003).

Attempts have been made to measure the levels of Cr, as well as other metabolites, in AD and other neurological disorders. Most *in vivo* ^{1}H-MRS studies, in which the total Cr levels (PCr and Cr) were measured have reported no changes in total Cr between AD subjects and age-matched controls (Pfefferbaum et al, 1999; Parnetti et al, 1997; Rose et al, 1999; Stoppe et al, 2000; Schuff et al, 1997; Schuff et al, 2002; Dixon et al, 2002). Of these, only a few examined the hippocampus (Schuff et al, 1997; Schuff et al, 2002; Dixon et al, 2002). One study found a correlation between higher Cr levels in the gray matter of AD patients and lower word-recognition scores (Pfefferbaum et al, 1999). Increases in total Cr (Huang et al, 2001) and slight decreases in some brain regions (Chantal et al, 2002) have also been recorded. No changes were reported in Cr and PCr levels in perchlorate extracts of control and AD brain by ^{1}H-MRS and ^{31}P-MRS (Klunk et al, 1996).

^{31}P-MRS studies have shown decreases in PCr in mild AD, followed by increases with worsening dementia (Pettegrew et al, 1994; Pettegrew et al, 1997), as well as no significant differences between AD patients and normal controls (Bottomley et al, 1992).

The contradictory results of the MRS studies (see Valenzuela 2001 for a review) are most likely due to small sample sizes, examination of different regions of the brain, and the difficulty of confirming AD in living subjects. Differences in MRS technique may also play a part (Bottomley, 1992). As well, little is yet known about the distribution of Cr in normal brain and the changes that take place with age. Total Cr appears to be higher in gray matter than in white matter, and is increased with age (Pfefferbaum et al, 1999; Schuff et al, 2001).

7.3. Methods

Focally-elevated Cr deposits were discovered in many of the maps that were collected for the plaque study (see Chapter 3) in the TgCRND8 brain. See Sections 3.2.1. for information on sample preparation. Additional maps of regions suspected of having Cr deposits were collected, in regions of the brain including the hippocampus, cortex, and caudate. These samples were mostly mounted on gold-coated silicon chips, as in certain instances the larger Cr deposits were visible when viewed in reflectance mode with a light microscope.

Data collection was the same as for the plaque data (see Section 3.2.5.). The data were collected at both the SRC and NSLS synchrotrons, with an aperture size of 12 x 12 μm^2, and a step size of 10 µm. A few higher resolution maps were collected at the NSLS with an aperture of 8 x 8 μm^2 and step size of 6 µm. In order to map large areas, a number of smaller, adjacent maps were collected, processed for Cr and the resulting spectral images were joined together. IR spectra of pure Cr monohydrate (Sigma) were collected in reflectance mode on a benchtop Bruker Tensor 27 FTIR with a Bruker Hyperion Microscope.

The presence of Cr deposits in the IR maps was visualized using the area of the Cr peak at 1304 cm^{-1}, as it is less overlapped with tissue bands than other Cr peaks. The maps collected at the SRC and NSLS were processed using the Atlus/Omnic software. A peak area from 1311 to 1300 cm^{-1}, with a baseline from 1322 to 1289 cm^{-1}, was used.

7.4. Results

7.4.1. Identification of the Creatine Deposits

An unusual spectral signature was initially found in several maps from 11-month-old TgCRND8 mice and one map in the 5-month-old mice (Figure 7.2A and B, red spectrum), recorded from the first set of 5 and 11-month-old animals. This spectrum was identical to spectra observed in IR maps of human AD brain (Ogg, 2002). A spectral library search identified it as Cr, a normal component of brain tissue. The identity was confirmed by comparing a spectrum of a deposit (following subtraction of tissue bands) to a spectrum of pure Cr monohydrated (Figure 7.2A and B, green spectrum). The Cr deposits were also found in a second set of older TgCRND8 mice and littermate controls (two 14-month-old pairs, and one each at 15, 16, 17 and 21 months) studied at a later time.

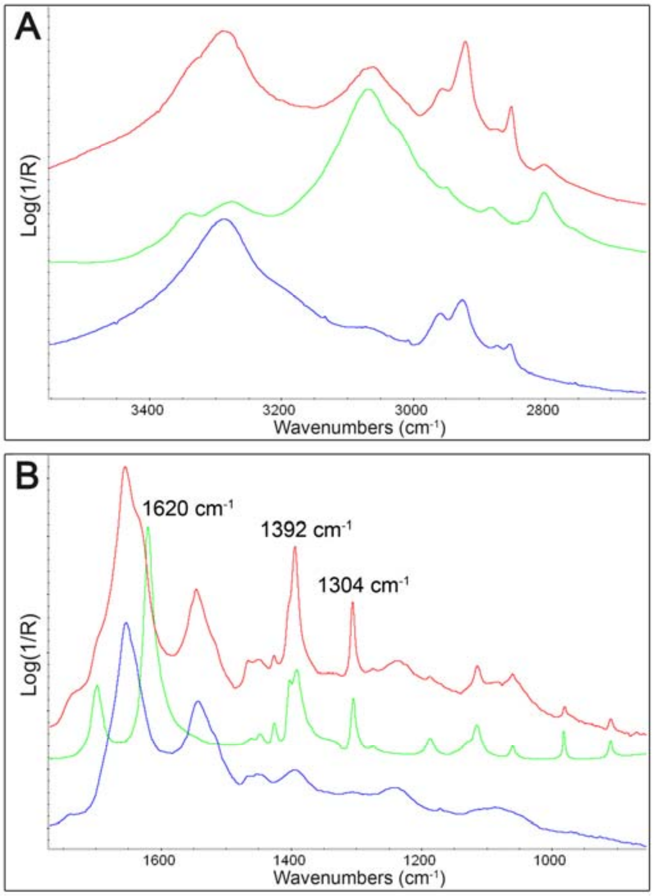

Figure 7.2. IR spectra of creatine deposits. IR spectra in the (A) NH and CH stretch region and (B) the fingerprint region. Spectra of normal tissue (blue), pure Cr (green) and a Cr deposit in the brain of a TgCRND8 mouse (red).

The spectra of Cr deposits exhibit several sharp, narrow bands, including two prominent ones at 1304 and 1392 cm^{-1}, that are unlike the broad bands of tissue components. The area of the band at 1304 cm^{-1} (Figure 7.2B) was used to image the Cr deposits in IR maps. This peak was chosen as that region of the spectrum was relatively free of tissue bands. Spectra of the Cr deposits have a shoulder in the amide I band reminiscent of the β-sheet found in plaques. However, this is due to the superimposition of the strong Cr band at 1620 cm^{-1} with the amide I band profile.

Generally, the Cr deposits are invisible in the unstained tissue. However, some of the larger deposits in sections mounted on gold are visible as a slight change in the texture of the tissue when viewed in reflectance mode under a light microscope (Figure 7.3). However, in many instances, similarly textured regions do not correspond to Cr.

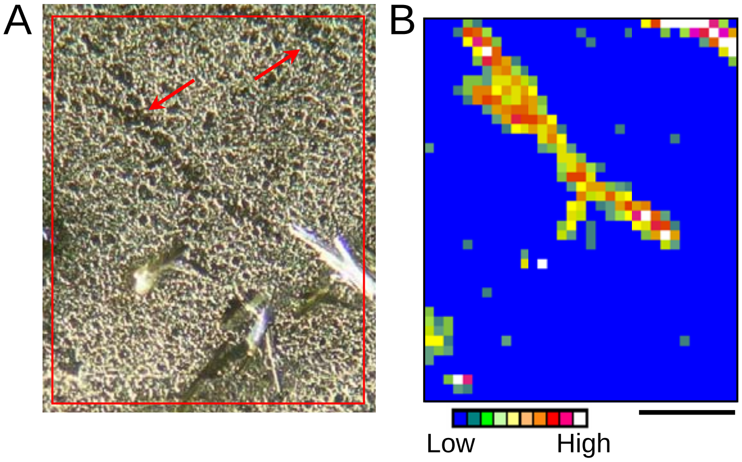

Figure 7.3. Creatine deposit in the caudate. (A) The caudate of a 14-month-old TgCRND8 mouse, mounted on a gold-coated slide, photographed at x10 magnification in reflectance mode. (B) The IR map of the same region, processed for Cr. Note a slight change in the appearance of tissue that closely matches the shape of the Cr deposits (the objects in the lower right corner are white matter fibres). Scale bar = 100 µm.

The Cr deposits were not visible in sections mounted on MirrIR. Some Cr deposits had been found in sections on MirrIR that had serial sections immunostained with anti-Aβ antibodies (these were the samples for plaque mapping). The MirrIR sections had then been stained with Congo red and hematoxylin so that the tissue morphology could be examined (Figure 7.4). No obvious disturbances in the tissue morphology were seen in the regions with the Cr deposits.

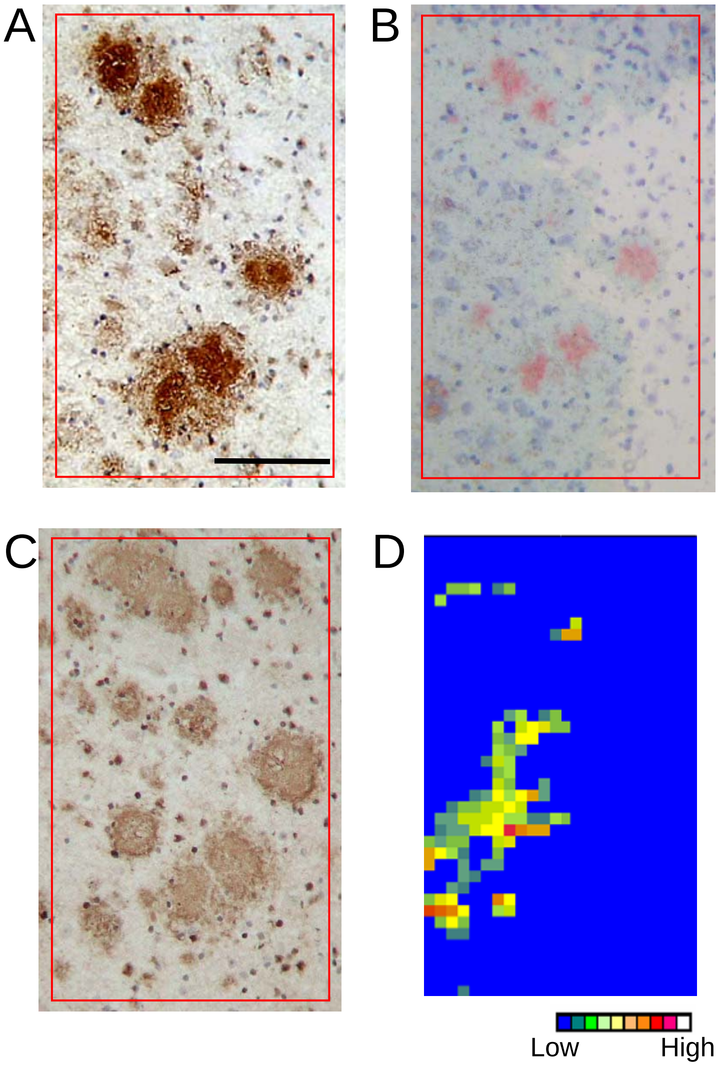

Figure 7.4. Cr deposits are not associated with obvious disturbances in the tissue morphology. A set of serial sections, in the hippocampus of a 17-month-old TgCRND8 mouse, stained with anti-Aβ antibodies (A) BAM-10 and (C) 4G8, and (B) the mapped section on MirrIR, stained with Congo red after mapping. The map contains several dense-cored plaques, and the right-side of the map (lighter colored in the Congo red image) corresponds to the white matter of the corpus callosum. (D) The map processed for the presence of creatine. Scale bar = 100 µm.

7.4.2. Distribution of the Creatine Deposits

The Cr deposits have been located in all the brain regions examined so far, including the hippocampus, cortex and caudate. These are the regions with prominent plaque pathology. Some of the Cr deposits were closely associated with dense-cored plaques (Figure 7.5D and G). The others were found away from plaques, but of course they could be associated with the edges of plaques found in adjacent sections (Figure 7.5A and J). However, as the deposits were discovered in the process of mapping plaques, this association was not unexpected, as most IR maps in the AD mice were of plaques. The Cr deposits were never found in the white matter.

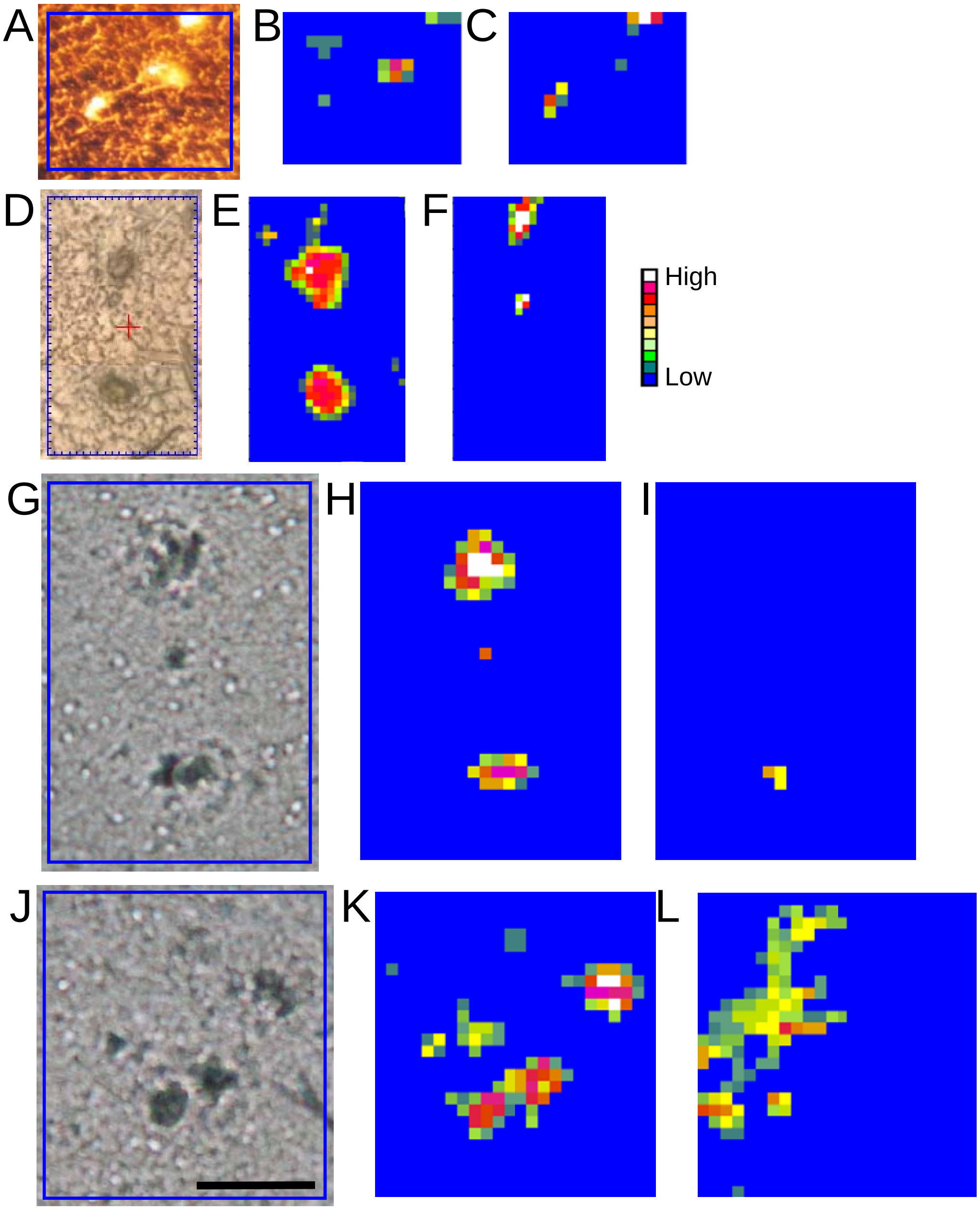

Figure 7.5. Creatine deposits near dense-cored plaques. Micrograph of unstained plaques in (A) 5-month-old mouse brain on gold, (D) 11-month-old mouse brain on MirrIR, (G) 16-month-old mouse brain on MirrIR, and (J) 17-month-old mouse brain on MirrIR. The corresponding IR maps processed for (B, E, H, K) protein secondary structure, where the plaque cores, high in aggregated β-sheet, show up as red, and (C, F, I, L) for the presence of Cr deposits. Scale bar = 100 μm.

The number and size of Cr deposits appear to increase with age. Only very few, isolated pixels were found in 5-month-old TgCRND8 mice. Semi-quantitatively, the deposits were more common in 11-month-old mice, but were generally just a few pixels across. In the mice 14 months and older, the deposits were more common and much larger. The larger deposits are usually in the shape of streaks. This was seen in both the maps that I took in various regions of the caudate and cortex, and the whole hippocampus maps (Gallant et al, 2006). Some of these streak-shaped deposits were several hundred microns long (Figures 7.3 and 7.6). These larger deposits were not usually associated with plaques. The Cr deposits are sometimes found in the most aged control mice, but are much smaller and sparser.

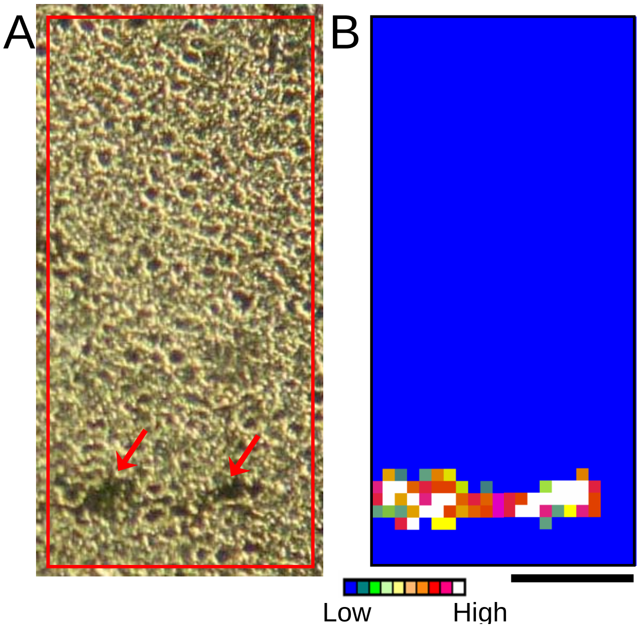

Figure 7.6. Creatine deposit in the cortex. (A) The caudate of a 14-month-old TgCRND8 mouse, mounted on a gold-coated slide, photographed at x10 magnification in reflectance mode. Arrows point to a change in tissue texture that corresponds to the CR streak (B) The IR map of the same region, processed for Cr. Note a slight change in the appearance of tissue that closely matches the shape of the Cr deposits (the objects in the lower right corner are white matter fibres). Scale bar = 100 μm.

Most of the mapping of the Cr deposits had been done in sections mounted on gold-coated slides, which made examination of the tissue morphology more difficult as these sections could not be stained after mapping. However, some Cr deposits had been found in sections on MirrIR slides that were stained with Congo red and hematoxylin after mapping, and that had serial sections immunostained with anti-Aβ antibodies. The tissue morphology could be examined in those cases. It may be significant that in several instances, the Cr deposits have been found in the vicinity of blood vessels (Figure 7.7). Unfortunately, the slow pace of data collection and the amount of synchrotron beamtime available limited the amount of data that could be collected. This made statistical analysis difficult and beyond the scope of this thesis.

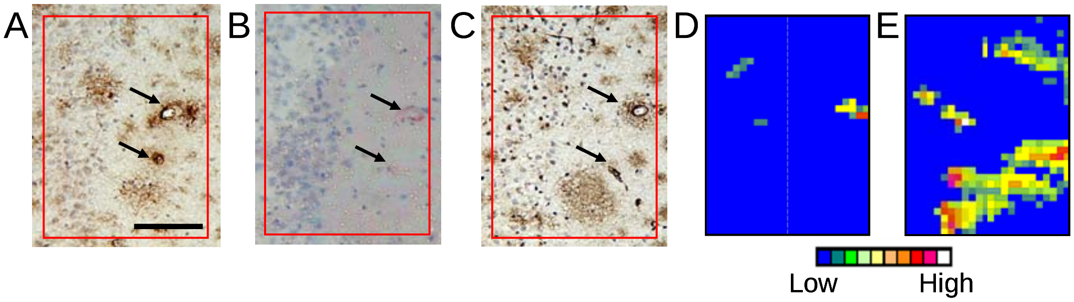

Figure 7.7. Association of creatine deposits with blood-vessels and plaque edges. A set of serial sections, in the hippocampus of a 21-month-old TgCRND8 mouse, stained with anti-Aβ antibodies (A) BAM-10 and (C) 4G8, and (B) the IR mapped section on MirrIR, stained with Congo red after data collection. The arrows point to a larger blood-vessel in the middle, right part of the map, and a smaller blood vessel below it. The antibodies indicate the presence of Aβ, part of the halo of a dense-cored plaque found further in the tissue (not shown). Amyloid is seen around the larger blood vessel, with both the antibodies and Congo red. (D) The map processed for secondary protein structure based on the Amide I band shows that the larger blood-vessel is surrounded by elevated beta sheet (red). (E) The map processed for the presence of creatine.

There does not seem to be any co-localization of the Cr deposits with other tissue components. When maps with large deposits are processed for the distribution of tissue peaks (lipid, protein, phosphates), the region containing the deposit is identical to the adjacent tissue. This could be due to the relatively low spatial resolution of IR microspectroscopy, which causes some normal tissue to be included in spectra of the deposit. However, even the centers of large deposits still contain prominent tissue bands.

7.5. Discussion

The focally-elevated Cr deposits had not been previously reported. Staining methods commonly used to study tissue sections involve numerous solvent treatments that would wash away small, soluble molecules like Cr. Sample preparation for IR, on the other hand, involves freezing, cryosectioning and desiccating the sections. Water is the only component removed. The control and AD brains were processed simultaneously, with identical tools and protocols. Therefore, the results could not be due to contamination. It is possible that upon thawing, the Cr found in the section crystallized out into localized deposits. However this is unlikely, as other small molecules found in the brain (some at concentrations higher than Cr) do not form similar localized deposits. This strongly points to the Cr deposits being the result of specific physiological processes, especially as they have not been found in young controls and their numbers seem to increase with age.

The form and location of the Cr deposits *in vivo* is unknown. The sharp Cr IR bands point to a crystalline structure, but as the tissue is desiccated, the crystallization could be an artifact. Nothing is known yet about the state of the deposits *in vivo*. In the living brain, they may be crystalline or soluble but sequestered. The deposits may be extra- or intracellular. If they are located inside cells, then they may be compartmentalized in subcellular organelles, such as vesicles or mitochondria. However, their large size makes this unlikely. The Cr deposits may be associated with a particular cell type, such as neurons, astrocytes, microglia or oligodendrocytes. So far, the deposits have never been found in the white matter, which could be due to the lower Cr levels there (Pfefferbaum et al, 1999; Schuff et al, 2001). The spatial resolution of synchrotron

IR microspectroscopy is generally 10 microns. Even when the creatine deposits are very large, the spectra still contain strong tissue bands. This would point to small deposits scattered throughout the tissue, but localized in groups. Alternatively, if the excess Cr is found in the extracellular space, it could have been deposited between the neuronal and glial processes. It should be noted that, in tissue where Cr deposits were found, no significant disturbances in tissue morphology are seen upon staining with hematoxylin after mapping (Figure 7.4). No disturbances are seen in sections from the mice stained with more sensitive stains, such as the Bielschowsky silver stain for neuronal processes.

Almost all of the larger deposits, found in the older mice, have the form of streaks (Figure 7.3 and 7.6). This would point to an association with axons or blood vessels, the only linear structures in the brain. Several of the Cr deposits have in fact been found in the vicinity of blood vessels (Figure 7.7). The deposits were first found near plaques, which would be expected as these were the regions of interest in the transgenic mice. Further mapping did not indicate any specific association with plaques. However, it is hard to tell as the plaque load (both dense-cored and diffuse) becomes very high in the older mice. To study whether there is a statistical association of the Cr deposits with blood vessels or plaques would require more animals and a much greater amount of data, which would be outside the scope of this thesis.

The deposits of Cr in brain tissue have previously escaped attention. However, many pathological states are associated with crystalline or amorphous deposits of various metabolites in tissues. The aggregating molecules may be small and fairly soluble, similar to Cr. In a condition known as cystinosis, crystals of the amino acid cystine form inside cells, especially of the kidneys and eyes (Gahl et al, 2002). In gout, crystals of sodium urate, a small molecule, are formed in the cartilage tissue of joints (Martinon & Glimcher, 2006). Crystals of calcium oxalate, calcium pyrophosphate dihydrate, apatite, cholesterol, and xanthine are also known to accumulate in tissues as a result of pathological conditions (Reginato et al, 1999). A number of proteins can form amyloids in various organs (Glenner et al, 1974), while polysaccharides can form aggregates known as corpora amylacea in brain and other tissues (Cavanagh, 1999). Thus, although the focally elevated Cr deposits may seem physiologically unlikely to form, the prevalence of various other deposits shows that this possibility should not be ruled out.

No clear reason for the existence of the Cr deposits exists at this time but several facts about AD and the Cr/PCr systems may be relevant to their formation. Cr deposits are found only in transgenic mice with advanced AD pathology and in much smaller amounts in the most aged controls. The deposits have also been found in human AD brain (Ogg, 2002; Gallant et al, 2006). Therefore, they must be the result of a process associated with both aging and AD, whether sporadic or caused by Aβ overexpression in the transgenic mice. Inflammation and the associated oxidative stress occur with normal aging in both humans (Floyd & Hensley, 2002) and mice (Lee et al, 2000). Protein oxidation increases with age and the activity of enzymes vulnerable to oxidation, such as CK, is decreased (Smith et al, 1991). The inflammatory response is even greater in AD compared to age-matched controls (Neuroinflammation Working Group, 2000). Inflammation also occurs in the TgCRND8 mice as indicated by activated microglia and hypertrophic astrocytes found around dense-cored plaques (Chishti et al, 2001; Belluci et al, 2006).

There appears to be a complex, but still poorly understood, relationship between Aβ overproduction, inflammation, oxidative stress, reduced energy metabolism and AD. The increased oxidative stress seen in AD brain could be due directly to the Aβ peptide (Varadarajan et al, 2000). Exposure of cells to Aβ results in oxidative stress, a reduction in ATP levels and mitochondrial dysfunction (Aksenov et al, 1998; Mark et al, 1997; Casley et al, 2002). However, the increase in inflammation with age may make the brain more susceptible to neurodegenerative diseases like AD. (Blasko et al, 2004). Defective mitochondrial metabolism has been proposed as a cause of sporadic AD (Castellani et al, 2002). The overproduction of reactive oxygen species by mitochondria may trigger the cell to make Aβ as a compensatory event (Swerdlow and Khan, 2004). Regardless of what is the initiating cause, reduced brain metabolism and oxidative stress are always found in AD and other types of dementia (Blass et al, 2002; Gibson, 2002; Lucas et al, 2006).

The oxidative stress associated with ageing and AD affects CK. It is a specific target of post-translational oxidative modification in AD brain tissue (Castegna et al, 2002), and the activity of CK is decreased in post-mortem AD brain compared to age-matched controls (David et al, 1998; Aksenov et al, 2000). Given the crucial role of the Cr/PCr system in the brain's energy metabolism, this could have a deleterious effect on the brain's energy supply and lead to the formation of the Cr deposits. The inactivation of CK by oxidation could limit the formation of PCr, causing an increase in the levels of Cr, which may then form the deposits (Burklen et al, 2006). Alternatively, if neurons are energetically stressed, the uptake of Cr from glia to neurons could be reduced, leading to excess Cr in the extracellular space (Burklen et al, 2006). There is no clear evidence for elevated bulk levels of Cr in AD brain (see section 7.2.4. in Introduction). The deposits therefore may not be the result of increased synthesis of Cr. Rather, some disturbance in the PCr/Cr system may cause the Cr in the tissue to be localized.

It is important to note that the Cr deposits had been found in Tg19959 mice, which carry the same APP gene (see Meghan Gallant's thesis), human AD tissue (Ogg, 2002), and, to a much smaller extent, aged control mice (14 months and older). The Cr deposits may be a general disease marker, as inflammation, and the resulting oxidative stress, are found in AD, epilepsy, ALS, MS, and Parkinson's disease (Lucas et al, 2006). For example, the activity of CK is reduced in the spinal cord, but not the cortex, from amyotrophic lateral sclerosis (ALS) mice compared to wild type controls, while the total amounts of CK stay the same. These mice are known to have increased free radical activity in the spinal cord, but not in the cortex (Wendt et al, 2002). In aged brain, CK activity is also reduced, and protein carbonyl content increased, compared to young controls (Smith et al, 1991). Now that the identity of the deposits found in AD tissue is known, studies in other neurodegenerative conditions are also needed.

7.6. Conclusions

The discovery of focally-elevated Cr deposits in brain tissue is a novel finding. The cause of the deposits, their state *in vivo* and their association with neural structures is still unknown. Most of the larger Cr deposits are in the form of streaks, which could suggest an association with blood vessels or axons. No specific association with plaques was found. However, it is clear that the deposits are associated with the disease process and, to a much smaller extend, normal ageing. This could indicate a relationship with oxidative stress and inflammation, which increase with normal aging, and to a much greater extent, with AD. Enzymes of the Cr system, such as CK, are known to be damaged by oxidation, in both aging and AD.

The discovery of focally-elevated Cr deposits in the brains of mice expressing human Aβ raises important questions about the role of energy metabolism in the disease process. The deposits may be a previously undiscovered marker of AD, oxidative stress or dysfunctional energy metabolism. This discovery obviously raises more questions than can be answered in the scope of this thesis. Further studies, employing both spectroscopic and biochemical methods, are required.

Part 2. Infrared Microspectroscopy of Scar Tissue

Chapter 8. Introduction to the Scar Tissue Study

8.1. Overview

The work described in this chapter is part of a larger Natural Sciences and Engineering Research Council Collaborative Health Research Project (NSERC CHRP). Excessive scar tissue formation, or fibrosis, is the main cause of failed back surgery syndrome (FBSS), a disorder characterized by chronic pain following back surgery. Oxidative stress and the associated inflammation are believed to be one of the main causes of fibrosis. This study is therefore designed to evaluate the effect of two anti-oxidant compounds, L-2-oxo-thiazolidine-4-carboxylate (OTC) and quercetin, on scar tissue formed after laminectomy in rats. The hypothesis is that the administration of these compounds will reduce oxidative stress and inflammation, and therefore decrease peridural scarring following surgery. The tissue is being analyzed with a variety of methods by three collaborating groups, including histochemistry and immunohistochemistry (Dr. B. Juurlink, Department of Anatomy and Cell Biology, University of Saskatchewan), *in situ* hybridization (Dr. W. Kulyk, Department of Anatomy and Cell Biology, University of Saskatchewan) and synchrotron IR microspectroscopy (Dr. K. Gough, Department of Chemistry, University of Manitoba). The animals were sacrificed at 3, 21 and 63 days following surgery, in order to monitor the development of the scar tissue. The final goal of this research is to determine whether OTC and quercetin can be used in clinical trials on human patients undergoing back surgery. However, the goals of the preliminary work presented in this thesis were to identify the spectral differences associated with scar tissue development and to utilize the available software to highlight these differences.

The scope and extent of this research required contributions by many individuals. Thus, it is important to first mention the various people involved and to clarify my role in this study. Dr. Elizabeth Schultke (Juurlink group) performed surgeries, animal care, and tissue preparation on a preliminary group of animals. Nicky Cox (M. Sc. student, Juurlink group) carried out the remainder of the animal work, and is performing histochemistry and immunostaining. Suraj Abraham (Ph. D. student, Kulyk group) is generating cDNA probes against mRNAs of interest and will use them to analyze gene expression in the scar tissue. He also performed picrosirius red staining on tissue sections serial to those analyzed by IR in order to study collagen orientation.

The IR mapping has been performed by a number of people in Dr. Gough's group. Prior to the CHRP funding, some preliminary data were collected by Dr. Gough and Dr. Elizabeth Schultke. However, due to problems with tissue preparation, this data was not usable. In the summer of 2003, just after CHRP funding was awarded, the sample preparation protocols were finally perfected. Good synchrotron IR data were obtained by Dr. Gough and two summer students (Meghan Gallant and Vincent Okoli). This initial data set included 3-day-old scar tissue from animals treated with saline, OTC, and quercetin, 21-day-old scar tissue treated with saline only, with two animals per group. Tissue from two healthy controls, which did not undergo the surgery, was analyzed as well. In the fall of 2003, I obtained data on 21-day-old scar tissue treated with OTC and quercetin, with two animals per group. At that point, a total of 12 treated animals (n = 2 per group), plus the two healthy controls, were analyzed. In the summer of 2004, tissue from 3 more animals per treatment group was analyzed with synchrotron IR microspectroscopy by me and Richard Wiens (Ph. D. student, Gough group). In the fall of 2004, Richard Wiens took the scar tissue project over, as I was concentrating on the work involving Alzheimer's disease tissue. The data presented in this thesis will therefore be from the 3 and 21-day-old scar tissue, as I was involved in the data collection and analysis of these. Analysis of tissue from the 63-day-old scar tissue is currently in progress, being performed wholly by Richard Wiens. He will also correlate the results of the IR mapping with the results of the remaining techniques once the work is finished.

A goal of the NSERC CHRP program is for graduate students to acquire interdisciplinary experience. This involved the graduate students visiting each others laboratories. I spent a week at the Synchrotron Radiation Center with Nicky Cox, where I taught her about synchrotron IR microspectroscopy data collection and analysis. Richard Wiens and I also visited the University of Saskatchewan campus. Suraj Abraham showed us how to synthesize cDNA probes, and perform gel electrophoresis and Western blots. Nicky Cox explained to us the basics of animal care, tissue preparation, and the analysis of histochemistry data.

8.2. Failed Back Surgery Syndrome

Failed back syndrome or failed back surgery syndrome is a serious complication of spinal cord surgery. It is a heterogeneous group of disorders with many possible etiologies; different authors may use different criteria to diagnose FBSS (Slipman et al, 2002; Onesti, 2004). However, FBSS generally involves an unsatisfactory outcome following one or more laminectomies or discectomies, usually performed for a herniated or degenerative disc (Robertson, 1996; Onesti, 2004). A laminectomy is a surgery performed to trim or remove the lamina (Figure 8.1A) of the vertebrae, while a discectomy is surgery to remove the extruding portion of a herniated disc (Figure 8.1B). Patients with lower back pain who do not improve after surgery are said to have FBSS (Slipman et al, 2002). The patients suffer from chronic pain in the lower back, hip, thigh or leg (Robertson, 1996). The pain may either be mechanical (associated with activity) or neuropathic (constant) (Onesti, 2004). An unsatisfactory outcome following surgery occurs in 10 to 30% of back-surgery patients, with many needing additional surgeries (Fritsch et al, 1996). The social, economic, and psychological costs are severe (Onesti, 2004). Treatment of FBSS generally involves medication to manage the pain (Kumar et al, 2002; Onesti, 2004), as well as additional surgery, epidural steroid injections, radiofrequency neurolysis, spinal cord stimulation with implanted electrodes, and physiotherapy (Hazard, 2006).

The diagnosis of FBSS is ambiguous and subjective, as psychological and financial factors play a role in the reporting of symptoms (Burton et al, 1981). However, fibrosis, or the formation of excess fibrous tissue after spinal surgery is believed to be the main cause (Robertson, 1996; Coskun et al, 2000). The peridural scarring surrounds the nerve roots and the dura, resulting in pain (Robertson, 1996). Magnetic resonance imaging has shown a significant association between peridural fibrosis following back surgery and chronic pain (Ross et al, 1996). Prevention of peridural fibrosis may therefore decrease pain (Robertson, 1996).

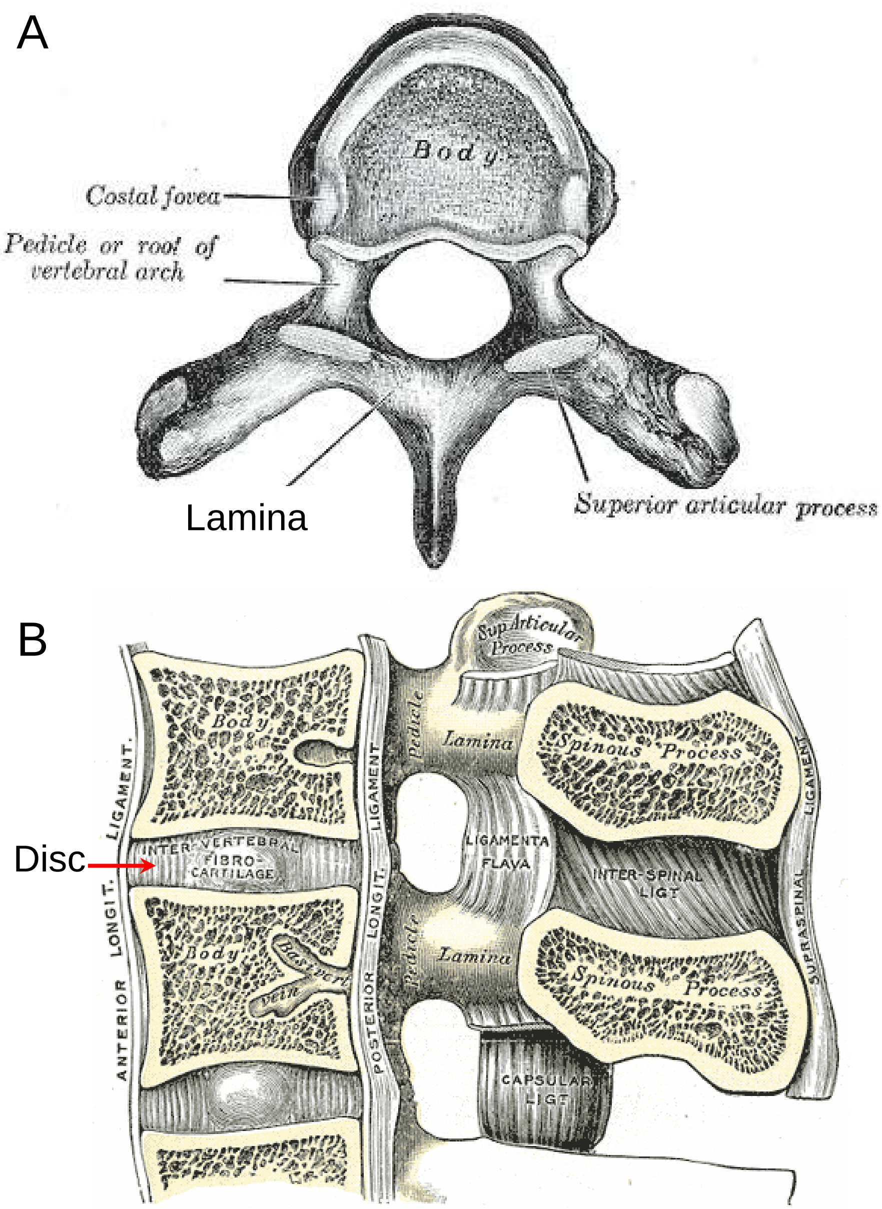

Figure 8.1. The lamina and discs of the spinal cord vertebrae. (A) A human vertebra, viewed from above. (B) A sagittal section through two human lumbar vertebrae. A label for an intervertebral disc has been added. (Images from Gray, H. (1918) Anatomy of the Human Body. Lea & Febiger: Philadelphia. Public Domain.)

8.3. Wound Healing

In order to understand the excess scar tissue formation or fibrosis that may occur following injury, it is important to first describe the process of normal wound healing. Immediately following injury, the wound needs to be sealed off to prevent infection and loss of blood. Therefore, the platelet cells begin hemostasis, or blood clot formation. The platelets synthesize an initial wound matrix, composed of proteins like fibrin and fibronectin, and proteoglycans like dermatan sulfate and hyaluronan (Monaco & Lawrence, 2003; Diegelmann & Evans, 2004). The process of wound healing can then begin. In mammals, it involves three overlapping, highly-regulated stages, called the inflammatory, granulation, and remodeling phases (O'Leary et al, 2002).

The inflammatory phase, lasting from 1 to 3 days after injury, starts when inflammatory cells enter the wound (O'Leary et al, 2002). They remove bacteria, damaged tissue and foreign matter (Diegelmann & Evans, 2004). The inflammatory cells also release signaling molecules needed for healing, such as growth factors, cytokines and lymphokines (Park & Barbul 2004). Transforming growth factor (TGF-β) is one of the most important, as it signals to macrophages to enter the wound and helps to regulate collagen synthesis (Varga & Jimenez, 1995; Diegelmann & Evans, 2004). The mast cells release signalling molecules like histamine that cause the symptoms of inflammation (Diegelmann & Evans, 2004). Neutrophils enter the wound within 24 hours of injury and clean it through phagocytosis (Park & Barbul 2004). Macrophages, which arrive 48 to 96 hours after injury, carry out phagocytosis, generate free radicals and secrete a variety of regulatory molecules (Park & Barbul 2004). Lymphocytes migrate into the wound 5 to 7 days after injury, but their role is poorly understood (Park & Barbul 2004).

The granulation phase, which occurs 2 to 6 days after injury, usually overlaps with the inflammatory phase (O'Leary et al, 2002). Initially, the inflammatory cells dominate the wound, but eventually fibroblasts become the predominant cell type (Monaco & Lawrence, 2003). The role of the fibroblasts is to deposit a new extracellular matrix. At this stage, the wound tissue is called granulation tissue because of its granular appearance. It is composed predominantly of collagen, but also includes other proteins and proteoglycans (Diegelmann & Evans, 2004). Initially, the fibroblasts secrete type III collagen, but type I collagen starts to be synthesized at the end of this phase (O'Leary et al, 2002).

The final stage of wound healing is the remodeling phase, which involves the replacement of the granulation tissue with mature scar (O'Leary et al, 2002). This stage can last 3 to 4 weeks or longer (O'Leary et al, 2002). The number of cells in the wound is reduced by apoptosis; the final scar is largely acellular (Monaco & Lawrence, 2003). The collagen matrix is cross-linked and large bundles of collagen are formed, arranged in a parallel pattern (O'Leary et al, 2002; Diegelmann & Evans, 2004). The changes in scar tissue composition are needed to increase its strength (Monaco & Lawrence, 2003).

These wound healing stages are observed in animal laminectomy models. A hematoma forms first, 1 or 2 days after the surgery (Lee & Alexander, 1984; Songer et al, 1995). By 2 weeks, it is replaced by granulation tissue, and fibrous tissue fills the wound by 4 weeks (Songer et al, 1995). The fibrous tissue starts to be transformed into bone, starting 2 weeks after surgery, to form new laminae (Lee & Alexander, 1984). In a rat laminectomy model, the number of inflammatory cells and fibroblasts peaks at 8 days post-surgery, and starts to decrease 15 days after surgery (He et al, 1995).

8.3.1 Scar Tissue Composition

Collagen, an extracellular matrix protein (discussed in the section below), is the main component of scar tissue. It makes up 50 % of the protein in mature scar (Monaco & Lawrence, 2003). The other major components are the proteoglycans (Monaco & Lawrence, 2003). Like collagen, they are also a normal component of the extracellular matrix. Proteoglycans are large molecules, composed of glycosaminoglycans (GAGs) covalently bound to protein cores. The GAGs are repeating disaccharide units that have a hexosamine residue (Hascall & Kimura, 1982). They include hyaluronic acid, the chondroitin sulfates, keratin sulfates, and heparin sulfates. Early in wound healing, hyaluronic acid is the main proteoglycan found in scar, while the sulfated proteoglycans increase in the later stages (Longas & Garg, 1992).

8.3.2. Collagen

Collagen is a fibrous protein found in the skin, bones, tendons, and cartilage of vertebrate animals. It is the body's major structural protein. As a component of the extracellular matrix of connective tissues, it helps to hold cells together (Woodhead-Galloway, 1980). A number of collagen types exist in different tissues, including Type I, II, III, IV and V, (Miller & Gay, 1982).

Unlike most proteins, collagen has a repetitive primary structure and a high percentage of a few amino acids. It is composed of 35% glycine, 11% alanine and 21% proline and hydroxyproline, the latter a modified amino acid. Collagens have the sequence Gly-X-Y through at least 90% of their length, where X is often proline and Y hydroxyproline (Miller & Gay, 1982). Collagen undergoes a number of posttranslational modifications, which include proline and lysine hydroxylation to form hydroxyproline and hydroxylysine, crosslinking through the formation of disulfide bonds, and glycosylation (Davidson & Berg, 1981). Collagen undergoes O-glycosylation of hydroxylysine and N-glycosylation of asparagines residues (Davidson & Berg, 1981).

The secondary structure of collagen is a triple-helix. This structure is different from the α-helix found in globular proteins. The triple-helix is left-handed, with three amino acids per turn. Three of these helices, known as α-chains, are twisted about each other in a right-handed way to form the tropocollagen molecule. Glycine, the smallest amino acid, allows for tight contact between the respective α-chains, while proline forces the helix to twist sharply. The tropocollagen molecules associate to form larger fibrils. Cross-linking between lysine, hydroxylysine or histidine holds the fibrils and α-chains together (Lehninger et al, 1993). The cross-linking is responsible for the tensile strength of collagen. Collagen is often closely associated with other components of the extracellular matrix such as calcium phosphate salts and glycoproteins (Miller & Gay, 1982).

8.4. Oxidative Stress and Inflammation

Reactive oxygen species (ROS), such as free radicals and other oxidants, are generated during normal cellular processes, including mitochondrial respiration and cellular signaling. Inflammatory cells also release free radicals during wound healing (Park & Barbul, 2004). The free radicals formed in tissues include the superoxide anion, hydroxyl radical and nitric oxide radical; other reactive species include singlet oxygen, hydrogen peroxide, peroxynitrite anion, and hypochlorite anion (Juurlink & Paterson, 1998). These molecules are highly reactive and can damage tissue components, resulting in lipid peroxidation, protein carbonyls, advanced glycation endproducts and DNA damage. Free radicals are especially dangerous, as they can start chain reactions. When a free radical reacts with a biological molecule, it is damaged and a new reactive free radical is formed.

Cells have therefore developed a number of mechanisms to scavenge free radicals and other reactive species. The enzyme glutathione peroxidase plays a crucial role in protecting cells from oxidative stress. This enzyme requires the anti-oxidant glutathione (GSH) as an electron donor (Juurlink & Paterson, 1998). GSH is a tripeptide composed of glutamate, cysteine, and glycine (γ-Glu-Cys-Gly). It has several important roles, including reducing oxidized ascorbic acid, regenerating vitamin E, preventing lipid peroxidation, and neutralizing ROS and peroxides (Anderson, 1998).

A complex relationship exists between oxidative stress, inflammation and numerous pathological states. Oxidative stress refers to a state of imbalance in the cell; too many ROS are produced and cannot be effectively scavenged by the cell’s antioxidant defenses. The levels of free radicals and oxidative stress increase in various diseases and pathological states, including atherosclerosis, Alzheimer's disease, Parkinson's disease, diabetes, and brain and spinal cord injury (Juurlink, 2001). Trauma to the spinal cord, for example, is associated with oxidative stress and inflammation, followed by necrosis and loss of function; the tissue deterioration appears to be the result of free radical damage (Anderson & Hall, 1993). Oxidative stress may lead to inflammation by upregulating a transcriptional factor, known as NFκB, which causes pro-inflammatory genes to be expressed (Juurlink, 2001). Inflammation may therefore be reduced by scavenging oxidants, such as by increasing the levels of the anti-oxidant GSH.

8.4.1. The Role of Inflammation in Fibrosis

Fibrosis is the excessive deposition of scar tissue. There is increased deposition and decreased removal of the extracellular matrix (Diegelmann & Evans, 2004). A relationship appears to exist between inflammation and fibrosis. A number of conditions associated with chronic inflammation also involve fibrosis (Gutierres-Ruiz et al, 2002; Ardies, 2003). Embryos lack an inflammatory response following injury and normally exhibit scarless healing (Redd et al, 2004). However, when fetal wounds are treated with hydrogen peroxide, scars tissue is formed (Wilgus et al, 2005). As hydrogen peroxide is an oxidant produced by inflammatory cells during wound healing, the scar tissue may be formed as a direct result of the inflammatory response (Wilgus et al, 2005). In PU.1 null mice (which are incapable of an inflammatory response as they lack macrophages and neutrophils) wound healing proceeds at a rate similar to wild type mice but scar tissue is not formed (Martin et al, 2003). This suggests that as long as infection is controlled (in that study with antibiotics), the inflammatory response is not essential to wound healing, but is involved in scar tissue formation (Martin et al, 2003).

A number of studies have attempted to evaluate treatments to reduce fibrosis following laminectomy. A resorbable gel composed of gelatin and carbohydrate (ADCON-L) was successful in reducing peridural fibrosis when placed into the surgical site in a dog model, by preventing fibroblast migration into the wound (Einhaus et al, 1997). Application of hyaluronan to the wound in a rat laminectomy model decreased the number of monocytes and macrophages in the inflammatory wound healing phase (Schimizzi et al, 2006). This led to decreased inflammation and therefore decreased scar formation (Schimizzi et al, 2006). Administration of an anti-inflammatory corticosteroid decreased the density of scar tissue in a rat laminectomy model (Hinton et al, 1995); local administration of mitomycin C, which may prevent fibroblast proliferation, also reduced fibrosis in a surgical rat mode (Lee et al, 2004).

Inflammation appears to be a factor in fibrosis (Varga & Jimenez, 1995). As the inflammatory response is driven by excessive oxidative stress, it is likely that reducing oxidative stress will reduce the inflammatory response (Juurlink, 2001), and this will lead to reduction of scarring. Therefore, there appears to be potential for the use of the anti-oxidants quercetin and OTC in the prevention of fibrosis following laminectomy.

8.5. Quercetin

Quercetin (Figure 8.2) belongs to a group of plant compounds known as flavonoids. They consist of 2 benzene rings connected by an oxygen-containing pyrene ring. Quercetin is the most common flavonoid in the diet, found in onions, tea, wine, apples and berries (Erlund, 2004). It has several physiological effects on animal cells. Quercetin has been shown to have antioxidant, anti-carcinogenic, anti-inflammatory and vasodilating properties (Erlund, 2004).

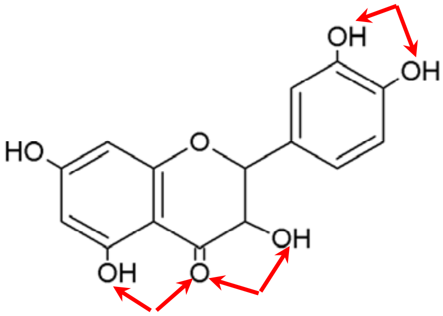

Figure 8.2. Quercetin. The three bidentate sites that appear to be important in iron chelation are indicated by arrows (Schultke et al, 2003).

Quercetin has many anti-oxidant functions, including the scavenging of radicals, the chelation of iron, and inhibition of lipid peroxidation (Juurlink & Paterson, 1998). Administration of quercetin following spinal cord damage can prevent secondary injury, most likely by chelating free iron released from hemoglobin and thus preventing oxidative damage to the tissue (Schultke et al, 2003). *In vitro*, quercetin blocks the TGF-β and IGF pathways (associated with fibrosis) and collagen expression in keloid fibroblasts (Phan et al, 2003; Phan et al, 2004). As well, quercetin administration has been shown to elevate intracellular GSH levels by around 50% *in vitro*, by increasing expression of the enzyme γ-glutamylcysteine synthase, involved in the synthesis of GSH (Myhrstad et al, 2002).

8.6. OTC

L-2-oxothiazolidine-4-carboxylate (OTC) (Figure 8.3A) can increase the intracellular levels of the anti-oxidant GSH (Figure 8.3B) in tissue (Mesina et al, 1989). It does this by increasing the levels of the amino acid cysteine (Figure 8.3C), as the incorporation of cysteine is the rate-limiting step in the synthesis of GSH (Anderson, 1998). OTC is transported into cells, where the enzyme 5-oxyprolinase converts it to cysteine (Anderson & Meister, 1989). OTC administration can increase intracellular cysteine in rodent brains much more effectively than the direct administration of cysteine (Anderson & Meister, 1989). As well, cysteine administration is generally not feasible as it can cause neurological damage and it readily forms a dimer, cystine (Mesina et al, 1989), while GSH itself is not readily transported into cells (Lucas et al, 1998).

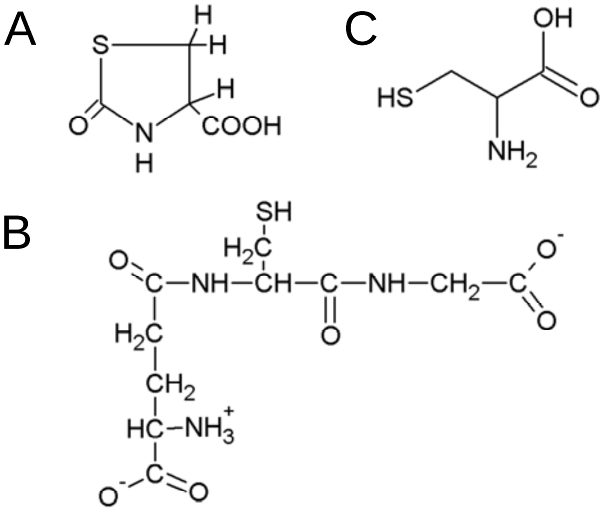

Figure 8.3. OTC. (A) L-2-oxothiazolidine-4-carboxylate (OTC), (B) cysteine and (C) glutathione.

OTC administration has been shown to have beneficial effects following various types of injury. *In vitro*, OTC can increase the survival of neuronal cells following injury to axons by increasing GSH levels (Lucas et al, 1998). Administration of OTC to a surgical rat model of spinal cord trauma resulted in a reduction of oxidative stress by increasing the levels of GSH in spinal cord (Kamenic et al, 2001). By decreasing oxidative stress, OTC administration decreased the associated secondary tissue destruction and helped to preserve mobility in the treated animals (Kamenic et al, 2001).

8.7. IR Spectroscopy of Collagen

IR spectroscopy has been used for a long time to study the structure of collagen (Frazer, 1950; Ambrose & Elliott, 1951; Seeds, 1953). IR spectroscopy has been used to study the assembly of collagen fibrils *in vitro* (Jakobsen et al, 1983), collagen fibril denaturation (Payne & Veis, 1988), and collagen cross-linking in bone (Paschalis et al, 2001).

The IR spectra of collagen, whether in aqueous solution, or in dried films or KBr pellets, are dominated by the amide band, found at around 1650 cm^{-1}, and the amide II band at around 1560 cm^{-1} (Figure 8.4A). The amide III band is part of a complex profile centered at 1245 cm^{-1} (Payne & Veis, 1988). It is more intense than the amide III peaks of other proteins. The IR spectrum of collagen shows a characteristic series of peaks at around 1202, 1240, 1283, 1315 and 1338 cm^{-1} (Figure 8.4B) due to the amide III mode with contributions from CH_2 wagging from the glycine backbone and the proline side chains. Collagen also has two peaks at 1032 and 1082 cm^{-1}, due to C-O stretching of the carbohydrate residues associated with collagen (Jackson et al, 1995).

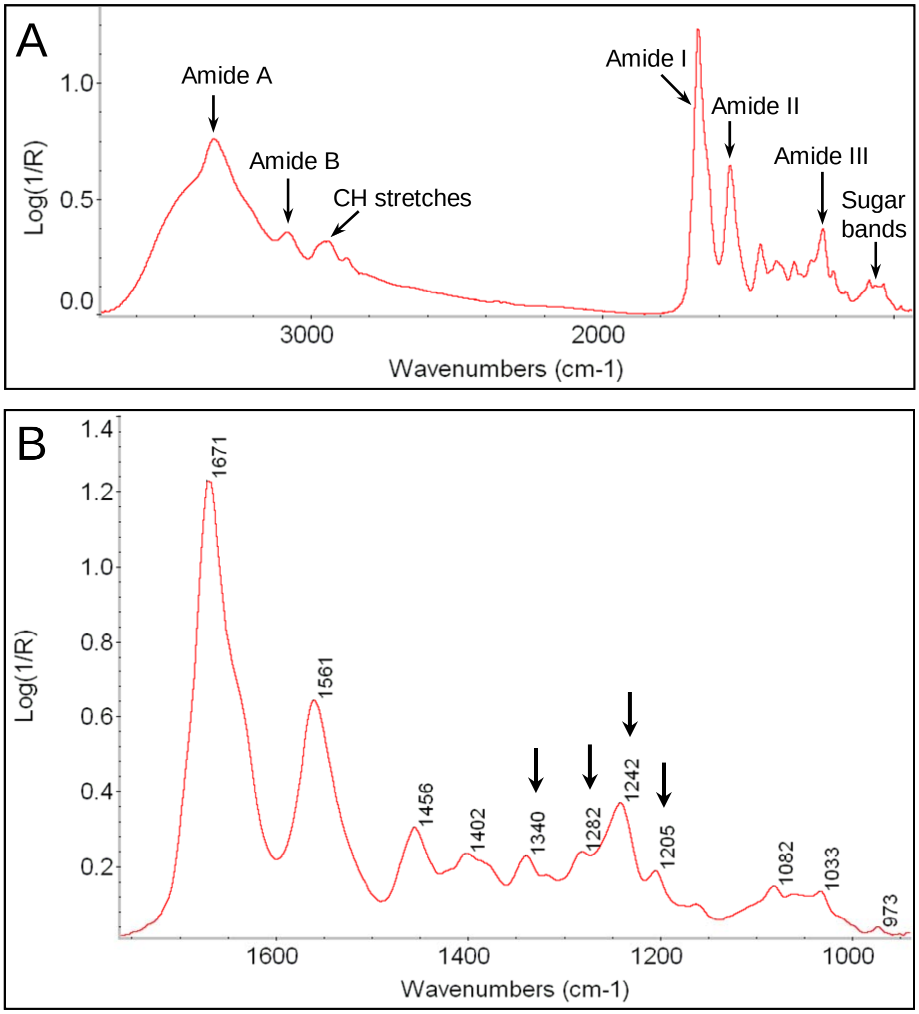

Figure 8.4. The IR spectrum of collagen. (A) An IR spectrum of a thin film of dried rat tail collagen. (B) A close-up of the fingerprint region, with the positions of the major collagen bands marked. The series of specific collagen bands in the amide III regions is marked with arrows.

The amide I of collagen appears to have several components. Fourier-self deconvolution is often used to track the changes in the amide I profile. Deconvoluted spectra of the amide I band of rat skin collagen in solution show three pseudo-bands at 1633, 1643 and 1660 cm^{-1} (Payne & Veis, 1988). Their relative intensities depend on the collagen conformation (Payne & Veis, 1988). Their positions and intensities vary when the assembly of collagen is studied over a temperature range (George & Veis, 1991). In the native collagen configuration, the peak at 1660 cm^{-1} is most prominent, and drops in intensity upon denaturation (Payne & Veis, 1988). Other authors have reported that the amide I band of rat-skin collagen in aqueous solution has shoulders at 1630 and 1670, and a central peak at 1656 cm^{-1} (Lazarev et al, 1985). The low-frequency shoulder and the central peak are strongly dependent on the amino-acid composition of the collagen, while the high frequency peak does not appear to be so (Lazarev et al, 1985). From studies of model polytripeptides, this is believed to be due to heterogeneity of the peptide C=O groups in the triple helix (Lazarev et al, 1985). Each of the carbonyl groups of the collagen triple helix region Gly-X-Y repeat exists in a different environment, giving rise to the three sub-bands of the amide I peak (George & Veis, 1991). There may however be overlapping or unresolved components (Lazarev et al, 1985; Payne & Veis, 1988). As the overlapped collagen amide I has to be resolution-enhanced with Fourier self-deconvolution or derivative spectroscopy, the results are likely an oversimplification (Surewicz et al, 1993). The exact shape of the amide I depends on the sample, and is affected by factors such as humidity, aggregation state and amino acid composition.

8.7.1. IR Spectroscopy of Collagen-containing Tissues

Collagen makes up approximately a third of the body’s protein (Woodhead-Galloway, 1980). It will therefore dominate the IR spectra of many tissues. IR microspectroscopic studies of several collagen containing tissues have been done. IR microspectroscopy has been used to study collagen in bone (Mendelsohn et al, 1999), the distribution of collagen and proteoglycans in cartilage (Camacho et al, 2001) and to image localized focal microscopic scarring in cardiomyopathic hamster heart (Gough et al, 2003). As the amide III region of collagen shows a series of bands not seen in other proteins, it is especially useful in studies of collagen-containing tissues (Gough et al, 2003).

8.7.2. Polarized IR Spectroscopy of Collagen

Polarized infrared spectroscopy can be used to obtain additional spectral information about oriented molecules (Campbell & Dwek, 1984). Electromagnetic radiation is composed of an electric and magnetic component, propagated in the same direction, but perpendicular to each other. When the light is not polarized, these components oscillate in all directions perpendicular to the direction of propagation. When the light oscillates in only one direction or plane, it is said to be plane-polarized. During molecular vibrations, the transition dipole moment of the absorbing molecule will oscillate when it absorbs IR light. Only the components of the electromagnetic radiation that are in the same direction as the transition dipole moments of the vibrating bonds will give rise to IR absorptions. When the absorbing molecules are randomly oriented, the polarization of the light will not have an effect on the intensity of IR bands. However, if the sample is oriented, or anisotropic, light of different polarizations will be absorbed to different extents. This gives rise to dichroism, or the differential absorption of polarized radiation. Plane-polarized IR light can be used to measure the changes in the intensity of absorption bands as a function of the angle of polarization. The spectra then provide information on the direction of the transition dipole moments, which can be correlated to structure. The intensity of IR bands is dependent on the degree of coincidence between the direction of the transition dipole moment of the molecular vibration causing the band and the direction of polarization (electric field vector) of the incident radiation.

This technique is very useful for studying oriented samples such as polymers and fibrous proteins. Polarized IR spectroscopy has therefore been used to provide additional information about the structure of collagen (Frazer, 1950; Ambrose and Elliott, 1951). Collagen orientation in calcified turkey leg tendon has been studied by polarized IR microspectroscopy (Gadaleta et al, 1996). The amide I band of collagen (as well as the amide A and B bands) have transition moments perpendicular to those of the amide II and III bands. The amide II and III bands therefore show dichroism opposite to that of the amide I band. A ratio of the amide I to the amide II band has been used to image the collagen orientation in the cartilage, as these bands have perpendicular transition dipole moments (Camacho et al, 2001).

Chapter 9. Scar Tissue Study Methods

The surgery, treatment, tissue harvesting and preparation were performed by Nicky Cox and Dr. Elizabeth Schultke in the laboratory of Dr. Juurlink at the University of Saskatchewan.

9.1. Surgery and Treatment

Male Wistar rats weighing an average of 250 g were purchased from Charles River (Laval, PQ, Canada). Spinal laminectomies were performed on the animals over two levels (L4-L5), in accordance with the guidelines set by the Canadian Council on Animal Care and the Animal Resources Center at the University of Saskatchewan. A laminectomy involves cutting through the skin, peeling back the muscle, and trimming the lamina of the vertebrae.

The rats were divided into three treatment groups. Animals from each group were sacrificed at both 3 and 21 days after surgery, in order to study the development of scar tissue with time (animals sacrificed 63 days after surgery will not be discussed in this thesis). The first treatment group received 1 mmol/kg of OTC starting 30 minutes after surgery. This was repeated every 12 hours for 36 hours for the animals sacrificed 3 days after surgery and every 12 hours for 120 hours for the animals sacrificed 21 days after surgery. The other treatment group received 0.025 mmol/kg of quercetin started 1 hour after surgery. For the animals sacrificed 3 days after surgery, this was repeated every 12 hours for 36 hours, while for the animals sacrificed 21 days after surgery this was repeated every 12 hours for 240 hours. The control group received 3 ml of normal saline, started 30 minutes after surgery. For the animals sacrificed 3 days after surgery, this was repeated every 12 hours for a total of 36 hours. For the animals sacrificed 21 days after surgery, this was repeated every 12 hours for a total of 120 hours. The treatments were delivered as intra-peritoneal injections. The number of animals assigned to each of the treatment groups and sacrifice times was 5, for a total of 30 animals (More animals had been operated on since, but they will not be discussed in this thesis). Tissue from two healthy, untreated rats was harvested in the same way as an additional control.

9.2. Tissue Harvesting and Preparation

The rats were anesthetized by halothane gas and sacrificed by perfusion. The scar tissue was dissected from the bone and surrounding musculature. The scar was placed in a mold filled with OCT compound (Sakura, Tokyo, Japan), and flash frozen in liquid nitrogen-cooled isopentane. The scar tissue was cryotomed at 10 μm thickness. Forty slides (labeled 1 to 40), were prepared from each animal, with two sections per slide. Every tenth slide in the series was a reflective MirrIR slide (Kevley Technologies, Chesterland, OH) for FTIR analysis. The others were Superfrost Plus micro slides (VWR Scientific, West Chester, PA) for histochemical or immunocytochemical staining. For some of the samples, hematoxylin and eosin (H&E) staining was done on sections cut about 200 μm away from the mapped sections (staining performed by Nicky Cox using standard protocols).

Achilles tendon was harvested from a few anaesthetized rats preceding sacrifice and frozen as for the scar tissue samples. Tendons are composed of highly oriented collagen and were therefore used as a control for polarized light IR spectroscopy of collagen fibrils. The same protocol used to freeze the scar tissue was used for the tendons. They were stored at -80° C until sectioned length-wise in the direction of the collagen fibers and mounted onto MirrIR slides for FTIR microspectroscopy. Sections were placed on the slide in both the vertical and horizontal direction.

9.3. FTIR Microspectroscopy Data Collection

Data collection was performed at the Synchrotron Radiation Centre (SRC, the University of Wisconsin) and at the National Synchrotron Light Source (NSLS, Brookhaven National Laboratories). IR maps were recorded on a Nicolet Magna 500 FTIR with Nicolet Nic-Plan IR microscope (SRC) or a Nicolet Magna 860 FTIR with Spectra Tech Continuum IR microscope (NSLS). The areas for IR mapping were selected based on a visual examination of the sample. The better of the two sections on the MirrIR slide labeled as 10 was analyzed. In the 3-day post-surgery tissue sections, mapped areas included developing scar tissue, some of it next to necrotic and healthy muscle fibers, as well as maps of the skin and fat tissue folded into the wound. In the 21-day post-surgery tissue sections, the mapped areas included fibrous scar tissue, granulation tissue, and areas of developing scar tissue around necrotic and healthy muscle fibers. About 6 to 10 maps were collected per sample.

All spectra were collected in reflectance mode from 4000 to 800 cm^{-1} at 4 cm^{-1} spectral resolution, using Happ-Genzel apodization. From 16 to 32 spectra were coadded, depending on the operating conditions, to achieve acceptable signal-to-noise ratio. Spectral maps were collected by raster scanning across the area of interest, using a step size of 10 μm and aperture of 12x12 μm. The spectra were saved in log(1/R) format.

Point spectra of the tendons, placed both vertically and horizontally on the MirrIR slide, were collected at both the SRC and NSLS. Spectra of the tendon were also collected on a Bruker Tensor 27 FTIR with Bruker Hyperion microscope. As that instrument used a standard glowbar source, the aperture size was increased to 25 μm. The spectra were taken with linearly polarized light, oriented in two orthogonal directions, referred to as 0 and 90 degree polarized light, obtained by placing a polarizer in the path of the light. Several orientations of light between these were also tested (22, 45 and 66 degrees).

9.4. IR Data Analysis

As with the maps acquired for the AD study, data analysis was performed on the original spectra. Smoothing, derivatization and Fourier self-deconvolution were not employed, in order to avoid the introduction of artifacts. In this section, the methods used to process the scar tissue data will be discussed briefly. The data analysis was based on the same principles as for the brain tissue (see Sections 1.3.6, 3.2.5.2, and 4.4.1). However, the exact parameters were optimized for the scar tissue (see Table 9.1 and 9.2 below).

9.4.1. Univariate and Bivariate Analysis

A variety of univariate and bivariate data processing methods, shown in Table 9.1, were used to analyze the data. IR maps were processed with OMNIC/Atlμs software (ThermoNicolet).

Table 9.1. Processing parameters used for scar tissue IR maps

Function	Peak 1 (cm^{-1})	Baseline (cm^{-1})	Peak 2 (cm^{-1})	Baseline (cm^{-1})	Display limits
Lipid					
CH stretch peak area	2940-2915	2998-2760			2-8
CH_2/CH_3 peak area ratio	2940-2915	2998-2760	2977-2952	2760-2998	1.3 to 2.5
Protein					
Amide I peak area	1700-1600	1806-900			50-150
Collagen 1204 cm^{-1} peak area	1211-1198	1214-1188			0.025-0.45
Other Peaks					
1230 cm^{-1} peak area	1300-1184	1307-1147			5-15
1080 cm^{-1} peak area	1130-1014	1145-900			4-11
Total peak area or chemigram	3999-900	3999-900			300-1500

Compared to brain (see Chapter 4), the scar tissue was generally low in lipid. Using the CH stretch peak area did not generally work well, as this was affected by the density of the tissue and the amount of other components, such as proteins, present in the sample. The CH_2/CH_3 ratio generally served better to distinguish regions with very low lipid (and therefore a lower ratio of CH_2 to CH_3) and those where more lipid was present (a higher ratio of CH_2 to CH_3).

The amide I peak area was used to image the relative amounts of protein in the tissue. The area of the peak at 1204 cm^{-1}, which occurs in collagen but not other proteins, was used to image the presence of collagen in the tissue.

The intensity of the peak at 1080 cm^{-1} was imaged based on its area. This overlapped peak is assigned to the phosphate symmetric stretching modes of phospholipids and nucleic acids, as well as carbohydrate C-O stretching bands. The exact maximum of this peak is variable, but for convenience, it will be referred to as the 1080 cm^{-1} peak. The area of the peak at 1230 cm^{-1}, due to phosphate asymmetric stretching and protein amide III modes, was imaged as well. Similarly for reasons of convenience, this band will be called the 1230 cm^{-1} peak. The Chemigram (see section 3.2.5.2.3) was also calculated, to permit an appreciation of the tissue density.

9.4.2. Hierarchical Cluster Analysis

Hierarchical cluster analysis was performed with CytoSpec software (Lasch et al, 2004) using D-values distance matrix calculations and Ward's hierarchical clustering algorithm. Clustering was performed on several regions (Table 9.2). The amide I and amide II region (1700-1500 cm^{-1}), the fingerprint region (1700-1010 cm^{-1}), and the phosphate stretch region (1300-1010 cm^{-1}) were found to be most useful for distinguishing differences in the tissue spectra.

Table 9.2. Spectral regions used for hierarchical cluster analysis of scar tissue

Region	**Wavelength Range (cm^{-1})**
Amide I	1700-1600
Amide I and II	1700-1500
Fingerprint region	1700-1010
Phosphate stretch region	1300-1010
Amide III/ asymmetric phosphate stretch	1300-1180
Sugars/phosphate symmetric stretch	1140-1010
CH stretch region	2998-2830

Chapter 10. Scar Tissue Study Results

The work on scar tissue presented in the second part of this thesis includes preliminary data from a much larger study. A major objective of this project was to analyze scar tissue development with IR microspectroscopy. It should be noted that the tissue in the 3-day-postsurgery animals cannot be considered scar in the biomedical sense. It is actually a combination of inflammatory tissue, granulation tissue, and developing scar. However, the tissue will be referred to as scar tissue or wound tissue, for convenience.

10.1. Tissue Samples

Generally, in studies analyzing post-laminectomy tissue in small animals, the scar tissue is removed with the spine attached, decalcified with formic acid and then sectioned (Lee et al, 2004). This approach was tried before the CHRP research commenced, but it altered the content of the tissue, and therefore the IR spectra, and was avoided in this study. The scar tissue was therefore dissected from the bone and surrounding musculature, before being frozen and sectioned in the transverse direction. The samples contained scar tissue in the centre and some muscle tissue to either side. As the scar had to be dissected from the rat, the samples were morphologically variable. The amount of muscle tissue, and even scar, was different from sample to sample. However, in most instances it was still possible to identify the major features of the tissue.

As a control, back muscle tissue from two healthy animals that had not previously undergone laminectomy was removed, in the same way as the scar tissue from the animals that had the surgery. Visually, this tissue was composed mostly of muscle fibers that had been sectioned transversally in the fiber direction and some tendon from the skin side of the sample (Figure 10.1, red arrow). There were also regions of smooth connective tissue in the sides adjacent to the spine and skin.

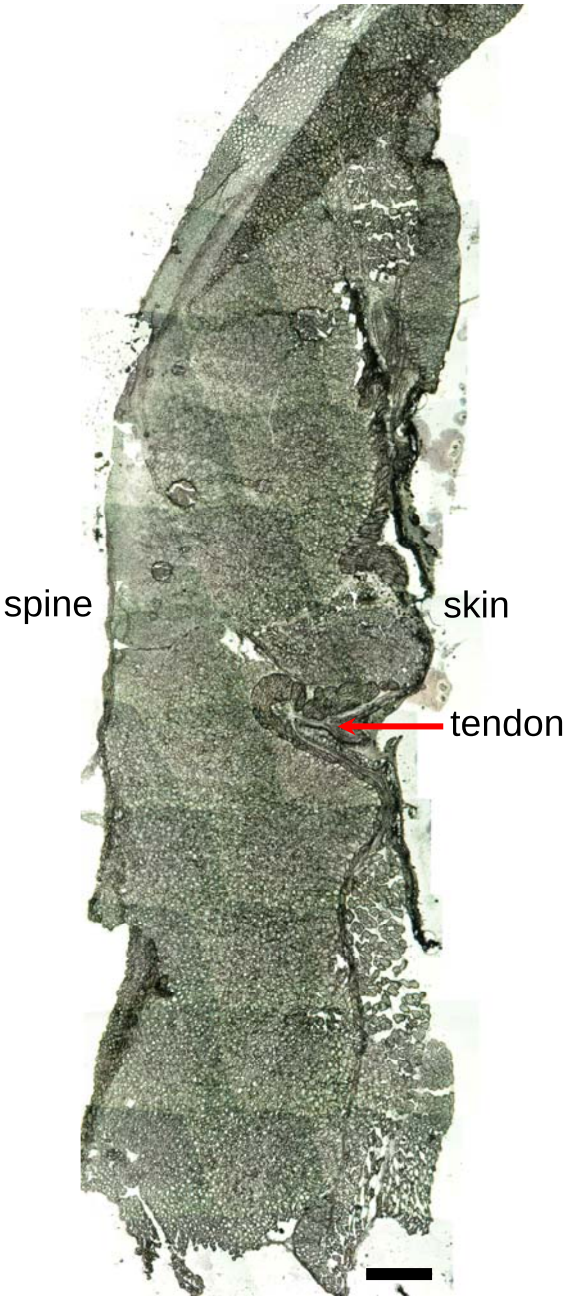

Figure 10.1. Tissue section from rat which did not undergo laminectomy. A photomicrograph of an unstained muscle tissue section. The left-hand side of the tissue was dissected away from the spine while the skin side is to the right. The sample is composed mostly of muscle fibers. Scale bar = 1000 µm.

The 3-day post-surgery samples are composed mostly of muscle tissue (Figure 10.2A). The area of developing scar is quite small (Figure 10.2A, red box). After the surgery, the skin tissue was folded over into the scar before being sectioned. This was a procedural flaw that was corrected in later experiments not included in this thesis. Therefore, the skin tissue and the attached tendon are found in the developing scar. There are also regions containing fat deposits, in the form of lipid droplets. The scar tissue generally looked smooth, and just slightly granular.

The 21-day post-surgery samples contain a large amount of scar, with just a small amount of muscle tissue to either side (Figure 10.2B, red box defines the scar area). The scar tissue seemed to spread beyond the initial site of injury and contained regions of necrotic muscle fibers being replaced by scar, as well as regions of granular-looking and fibrous scar tissue. The 21-day post-surgery tissue therefore contained scar tissue at various stages of development.

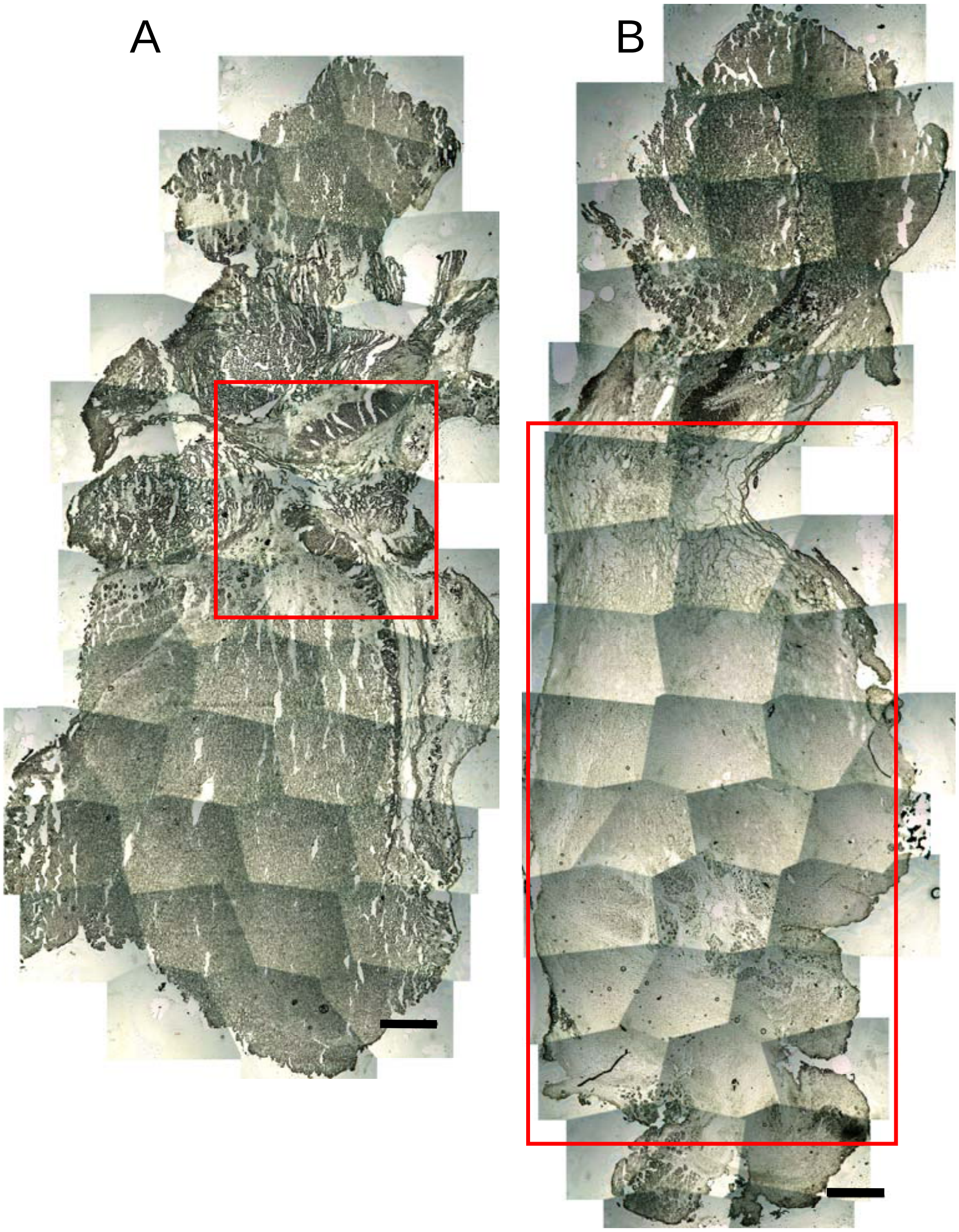

Figure 10.2. Typical unstained scar tissue sections. (A) Scar tissue harvested 3 days post-surgery from a saline-treated rat. The region of developing scar is relatively small (red box, light grey areas) and most of the section is composed of muscle fibers (dark grey areas). (B) Scar tissue harvested 21 days post-surgery from a saline-treated rat. The region of scar is now much larger (red box, light grey areas), and only a small amount of muscle tissue is found to either side of it (top and bottom, dark grey areas). For both sections, the left-hand side has been dissected away from the spine while the skin side is to the right. Scale bars = 1000 µm.

10.1.1. H & E Stained Scar Tissue

Examination of H&E stained scar tissue sections revealed morphological differences between the 3 and 21-day-old scar tissue. The wound tissue in the 3-day post-surgery samples was relatively homogenous (Figure 10.3A). The scar was infiltrating the muscle tissue; degenerating muscle fibers were found in some regions of the wound (large dark pink bodies in Figure 10.3A). There were a large number of nuclei (stained blue with hematoxylin) throughout all regions of the wound, indicating high cellularity, due to large numbers of inflammatory cells infiltrating the wound.

The wound tissue in the 21-day post-surgery sections was much larger and morphologically heterogeneous. There were regions next to the muscle tissue that resembled the 3-day post-surgery tissue (Figure 10.3B). Other types of tissue included granular-looking scar tissue (Figure 10.3C). This tissue still contained large numbers of cells, indicated by hematoxylin-stained nuclei, but also cell-free regions that were starting to look fibrous. The 21-day post-surgery sections also had fibrous regions with few cells (Figure 10.3D) that corresponded to maturing scar.

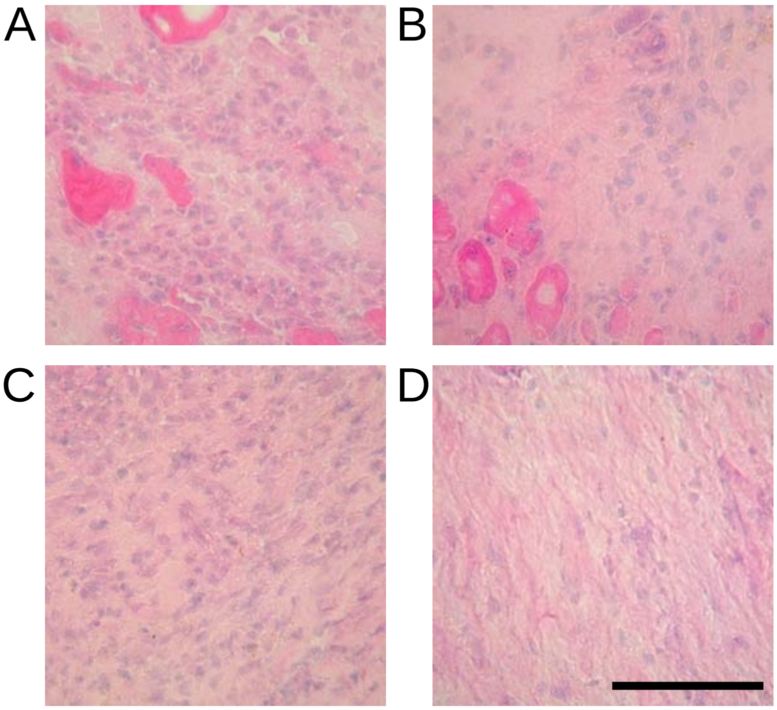

Figure 10.3. H&E stained scar tissue. Wound tissue next to degenerating muscles fibers (A) 3 and (B) 21 days post-surgery. (C) Granular looking wound tissue, 21 days post-surgery. (D) Fibrous-looking wound tissue, 21 days post-surgery. (Images of tissue stained by Nicky Cox, University of Saskatchewan). ×40 magnification. Scale bar = 100 μm.

10.2. IR Mapping of Scar Tissue

The development of scar tissue varied between the animals, and the resulting samples were heterogeneous. Representative IR maps were collected of each sample, with 6 to 10 maps per animal.

10.2.1 Normal Muscle Tissue IR Data

The muscle fibers did not yield good IR spectra due to their density. The spectra were oversaturated and often had sinusoidal baselines which distorted peak shapes and intensities. The smoother connective tissue gave much better spectra. As would be expected, the tissue appeared to be composed mostly of collagen (as indicated by the typical collagen amide III bands at 1337, 1281, 1236 and 1204 cm^{-1}), and was very low in other components such as lipid.

10.2.2. IR Mapping of Saline-treated 3-Day Post-surgery Scar Tissue

The mapped regions included developing scar tissue, some of it next to muscle tissue. As well, maps were taken in regions of skin and fat deposits folded over into the wound during the surgery. As expected, the regions of skin were high in collagen and those of the fat deposits were high in lipids. However, as these non-wound tissue regions are an artifact of post-surgical suturing, they will not be discussed in detail.

The spectra of 3-day-old wound tissue were generally similar to each other. A typical IR map is shown in Figure 10.4. The map was taken at a region of developing scar tissue next to muscle fibers (Figure 10.4A). H&E staining of the corresponding region in a section about 200 μm from the IR mapped section indicates that the mapped region is highly cellular (Figure 10.4B). A typical spectrum is shown in Figure 10.4C. Lipids were present, but low. The amide I band was the most intense band in the spectrum. Analysis of the amide III region showed that collagen was low or absent, as indicated by the absence or very low intensity of collagen-specific bands at 1338, 1281 and 1204 cm^{-1}. The sugar/symmetric phosphate stretch band is broad and has a prominent maximum at 1084 cm^{-1}. As the CH stretch peaks were generally low and the carbonyl stretch band barely noticeable, this band could not be attributed to phospholipids. The two bands that showed the most variability across the map are indicated with arrows in Figure 10.4C. The amide I peak position ranged from 1657 to 1648 cm^{-1}, and the sugar/symmetric phosphate stretch band (called the 1080 cm^{-1} band for convenience) changed in intensity across the map. Figure 10.4D shows the IR map processed for the intensities of various peaks, as outlined in Table 9.2. The intensities of most components are generally homogenous. The 1080 cm^{-1} peak is the only one to show significant variation in intensity.

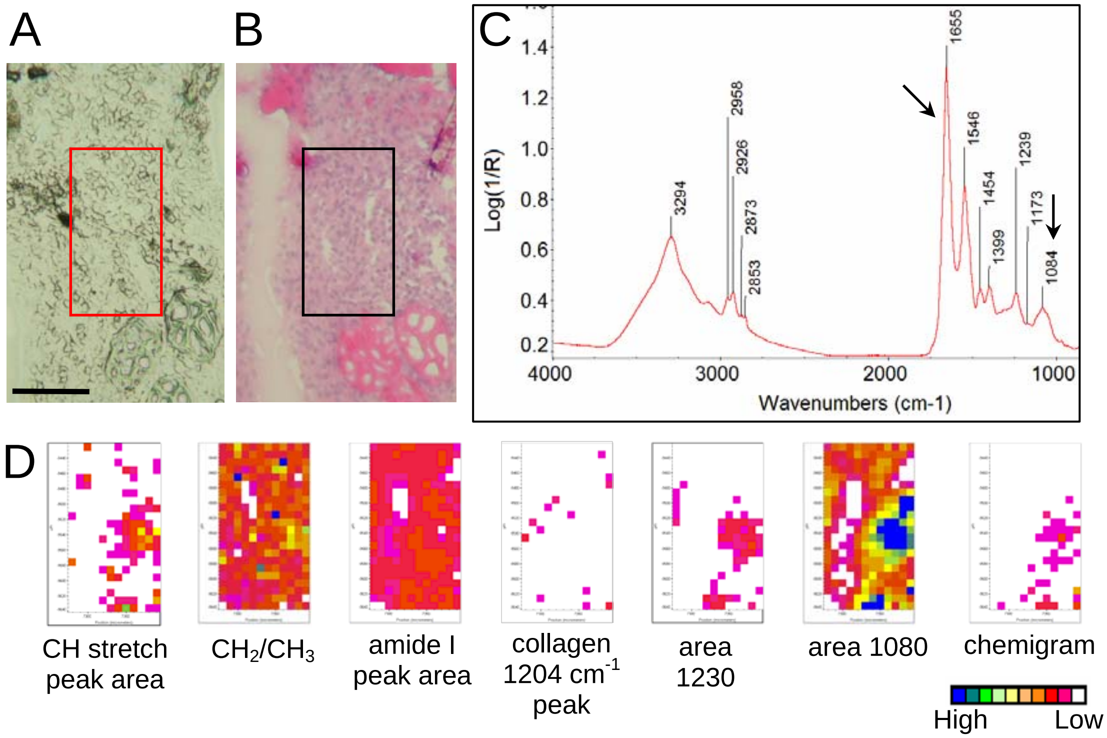

Figure 10.4. Wound tissue in saline treated rat, 3 days after surgery. The wound tissue is found next to degenerating muscle fibres (bright pink in H&E section). (A) The IR mapped region and (B) the corresponding area in an H&E stained section. This section is about 200 µm from the IR mapped section. (C) A typical IR spectrum of 3-day-old wound tissue; the bands showing the most variability in intensity across the map are indicated with arrows. (D) The IR map processed with the methods outlined in Table 9.1. Scale bar = 100 µm.

In addition to simple univariate and bivariate analysis, the IR maps were processed with hierarchical cluster analysis. Several spectral regions, shown in Table 9.2, were used for the analysis. The most interesting results were obtained with the spectral regions from 1700-1500 cm^{-1} (the amide I and II bands), 1300-1010 cm^{-1} (the phosphate stretch region, overlapped with the amide III band and various sugar vibrations), and 1700-1010 cm^{-1} (the fingerprint region). The results of cluster analysis based on these regions, for the representative map from Figure 10.4, are shown below in Figures 10.5, 10.6, and 10.7.

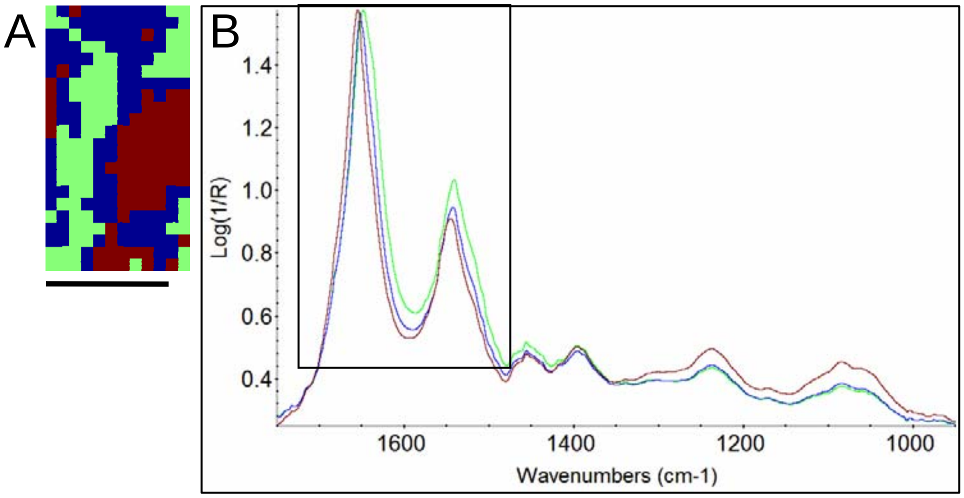

Figure 10.5. Cluster analysis of 3-day-old wound tissue on the amide I and II bands. (A) Image and (B) corresponding average spectra created by hierarchical cluster analysis on the spectral region from 1700 to 1500 cm^{-1}. Scale bar = 100 µm.

Figure 10.5 shows (A) the cluster image, and (B) the corresponding average spectra, obtained from hierarchical cluster analysis on the amide I and II bands. The results of this cluster analysis bear a striking resemblance to the spectral map obtained by imaging the area of the symmetric phosphate stretch/sugar band (Figure 10.4D, area 1080). The regions in the IR map where the absorbance of this band is elevated correspond to the brown regions of the cluster image (Figure 10.5 A). Examination of the corresponding average spectrum (Figure 10.5B, brown spectrum), shows that it has a higher absorbance of the 1080 cm^{-1} band (and to a smaller extent the band at 1230 cm^{-1}) than the other average spectra. These results appear to be quite interesting, as the cluster analysis was performed on the amide I and II bands. The amide I bands of the average spectra in Figure 10.5 are indeed distinct. The average spectrum with the highest absorbance of the 1080 cm^{-1} band has an amide I maximum of 1656 cm^{-1} (Figure 10.5B, brown spectrum). The average spectra where that absorbance is lower have amide I maxima at either 1652 cm^{-1} (Figure 10.5B, blue spectrum) or 1648 cm^{-1} with a shoulder at 1637 cm^{-1} (Figure 10.5B, green spectrum).

Figure 10.6 shows (A) the cluster image, and (B) the corresponding average spectra, obtained from hierarchical cluster analysis on the phosphate stretch region. Although clustering on that region gives four major clusters, the results are very similar to those of Figure 10.5. The cluster image (Figure 10.6A) resembles the cluster image from Figure 10.5A and the spectral map obtained by imaging the area of the 1080 cm^{-1} band (Figure 10.4D, area 1080). The average spectra (Figure 10.6B) show a relationship between the shape of the amide I band and the intensity of the bands in the phosphate stretch region. The spectra with the highest absorbances of the 1080 cm^{-1} band have amide I maxima at 1656 cm^{-1} (Figure 10.6B, blue and brown spectra, however the brown spectrum has baseline problems). The spectrum with the medium absorbance of that band has an amide I maximum of 1653 cm^{-1} (Figure 10.6B, cyan spectrum), while the spectrum with the lowest absorbance of the 1080 cm^{-1} peak, has an amide I maximum of 1652 cm^{-1}, with a shoulder at 1637 cm^{-1} (Figure 10.6B, yellow spectrum).

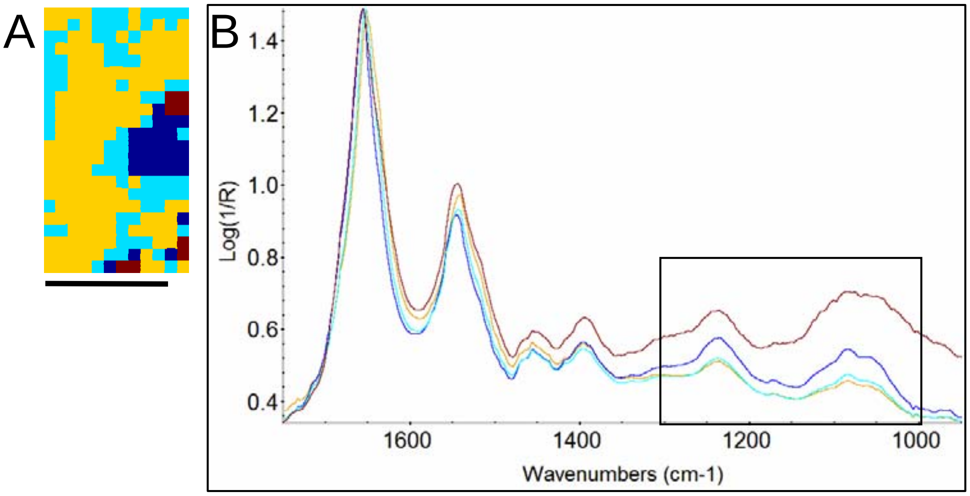

Figure 10.6. Cluster analysis of 3-day-old wound tissue on the phosphate stretch region. (A) Image and (B) corresponding average spectra created by hierarchical cluster analysis on the spectral region from 1300 to 1010 cm^{-1}. Scale bar = 100 µm.

When cluster analysis is performed on the fingerprint region (Figure 10.7), very similar results to Figures 10.5 and 10.6 are observed, for both the cluster image (Figure 10.7A) and average spectra (Figure 10.7B). The average spectra with the highest absorbances of the phosphate stretch bands, such as the brown and cyan spectra, have amide I maxima at 1657 and 1654 cm^{-1}, respectively. The spectra with the lower absorbances in these bands, such as the blue and yellow spectra, have amide I maxima at 1652 cm^{-1} and 1649 cm^{-1} with at shoulder at 1637 cm^{-1}, respectively.

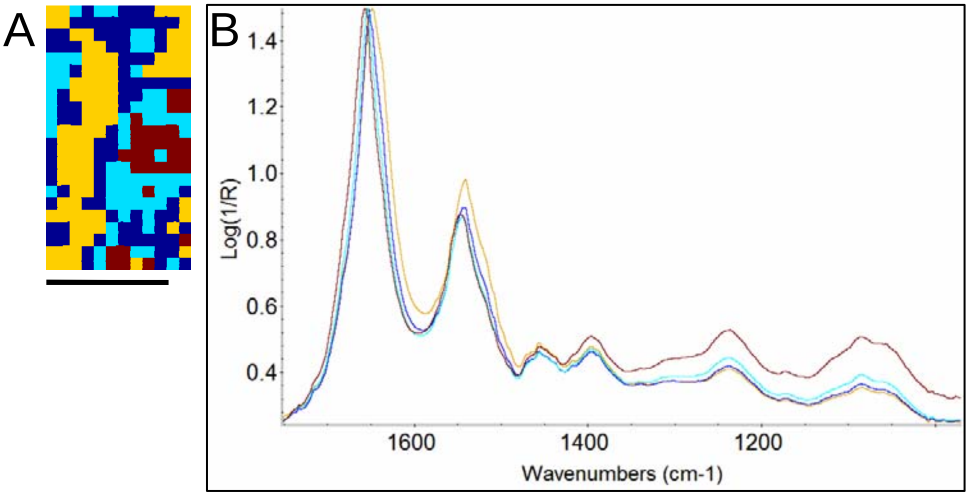

Figure 10.7. Cluster analysis of 3-day-old wound tissue on the fingerprint region. (A) Image and (B) corresponding average spectra created by hierarchical cluster analysis on the spectral region from 1700 to 1010 cm^{-1}. Scale bar = 100 µm.

Similar results are obtained when the cluster analysis is performed on the amide I and II bands (Figure 10.5), the phosphate stretch bands (Figure 10.6), or the fingerprint region (Figure 10.7), which includes both of the above regions. The cluster analysis shows that changes to the amide I and II region of the spectra are correlated with changes to the phosphate stretch region.

10.2.3. IR Mapping of Saline-treated 21-Day Post-surgery Scar Tissue

The tissue morphology and IR data from the tissue 21 days post-surgery were significantly more heterogeneous than those from the 3-day post-surgery tissue. Based on the morphology and IR data, they could be classified into three groups. They included developing scar tissue (also called granulation tissue), fibrous scar tissue, and wound tissue next to degenerating muscles, which seemed to be in the early stages of scar development (See Figure 10.3B, C, and, D).

10.2.3.1. Developing Scar Tissue

Figure 10.8 shows a typical IR map from developing scar tissue. Morphologically, the regions classified as developing scar tissue looked granular and irregular (Figure 10.8A and B). The IR spectra of this type of tissue generally showed the characteristic series of peaks in the amide III region (1338, 1283, and 1204 cm^{-1}) due to collagen (Figure 10.8C). The spectral maps (Figure 10.8D) show regions where the relative intensities of the bands at 1080, 1230 cm^{-1}, and 1204 cm^{-1} are both high and low, and they all show similar distributions. However, much more information can be obtained from cluster analysis, as this method considers not only the total absorbance of the bands but also their shapes.

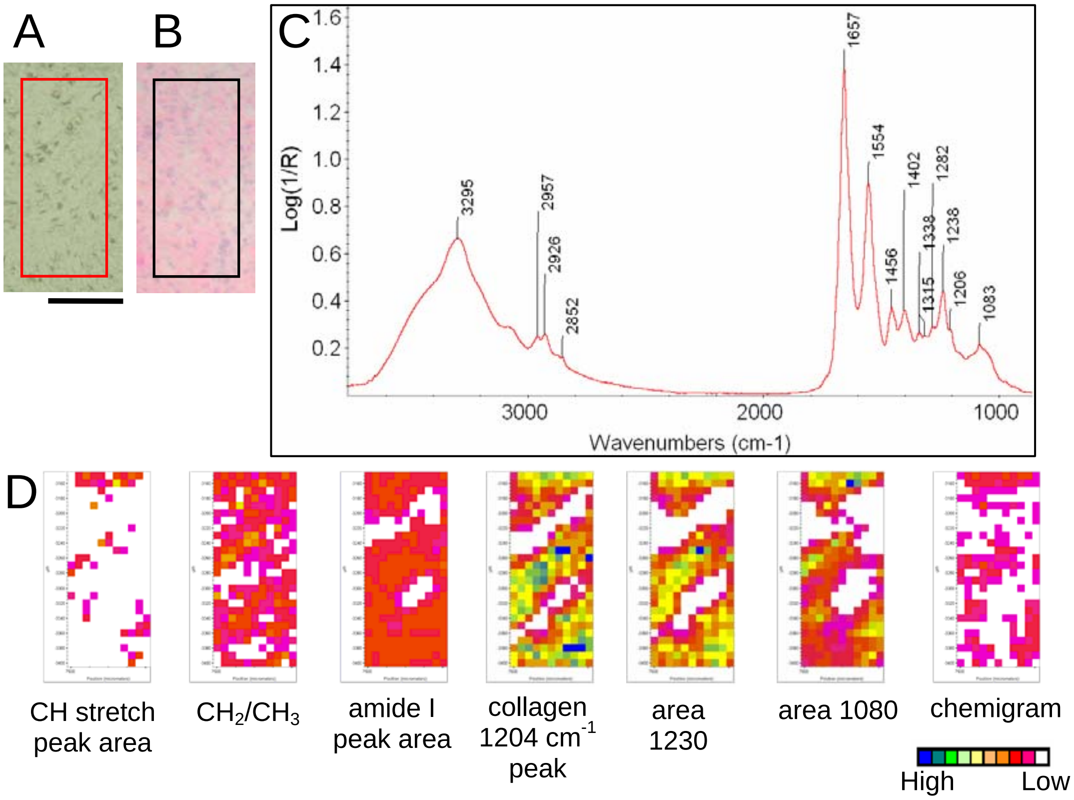

Figure 10.8. Developing scar tissue in saline treated rat, 21 days after surgery. (A) The unstained, granular-looking developing scar tissue, with the mapped region outlined in red. (B) The corresponding area in an H&E stained section. This section is about 200 µm from the IR mapped section. (C) A typical IR spectrum of 21-day-old developing scar tissue. (D) The IR map processed with the methods outlined in Table 9.1. Scale bar = 100 µm.

Figure 10.9 shows the cluster image (A) and average spectra (B) obtained from performing hierarchical cluster analysis on the above map, on the spectral region from 1700 to 1500 cm^{-1}. The cluster image resembles the spectral images based on the areas of the bands at 1230 and 1080 cm^{-1}, as well as the collagen peak at 1204 cm^{-1} (Figure 10.8D). The average spectra show the series of collagen band at 1338, 1282, and 1204 cm^{-1} in the amide III region. The symmetric phosphate/sugar peak has a maximum at 1083 cm^{-1}. The three average spectra have different amide I maxima. The average spectrum with the highest absorbance in the phosphate stretch region (brown) has an amide I maximum at 1657 cm^{-1}. The spectra with the lower absorbances in that region (blue and green) have amide I maxima at 1652 cm^{-1} and 1650 cm^{-1} with a shoulder at 1637 cm^{-1}, respectively.

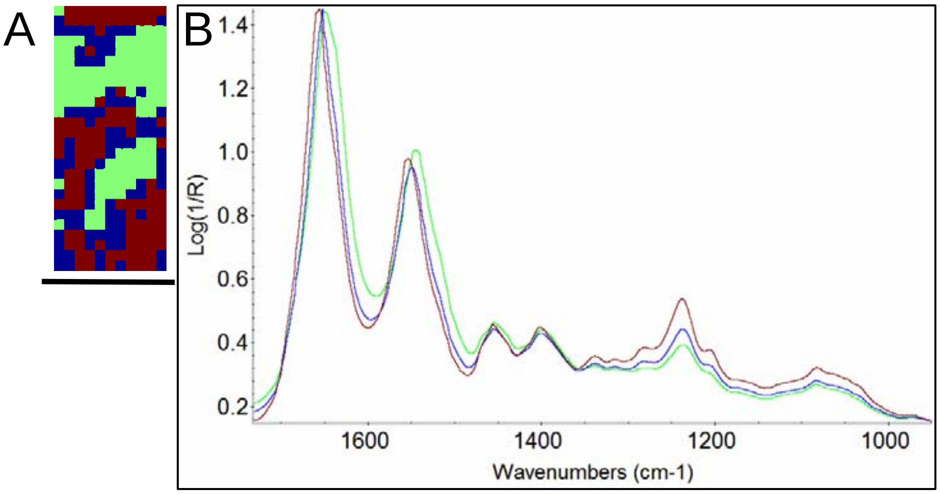

Figure 10.9. Cluster analysis of 21-day-old wound tissue on the amide I and II bands. (A) Image and (B) corresponding average spectra created by hierarchical cluster analysis on the spectral region from 1700 to 1500 cm^{-1}. Scale bar = 100 µm.

Figure 10.10 shows the (A) cluster image and (B) corresponding average spectra created on the phosphate stretch region from 1300 to 1010 cm^{-1}. There are four main clusters. The cluster image (Figure 10.10A) seems to correspond best with the peak area image based on the 1204 cm^{-1} band (Figure 10.8C, collagen 1204 cm^{-1} peak). The blue and brown average spectra are low in collagen (collagen peaks at 1338, 1282 and 1204 cm^{-1} are barely visible), while the cyan and yellow spectra appear to be high in collagen. Once again there is a relationship between the phosphate stretch region and the amide I band profile. The cyan spectrum has an amide I maximum at 1657 cm^{-1}, the yellow and brown at 1653 cm^{-1}, and the blue at 1652 cm^{-1} with a shoulder at 1637 cm^{-1}.

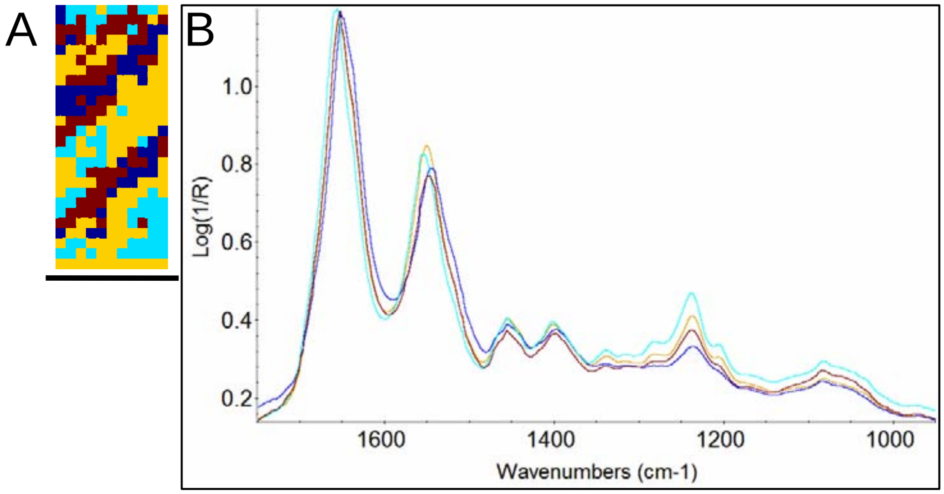

Figure 10.10. Cluster analysis of 21-day-old wound tissue on the phosphate stretch region. (A) Image and (B) corresponding average spectra created by hierarchical cluster analysis on the spectral region from 1300 to 1010 cm^{-1}. Scale bar = 100 μm.

Figure 10.11 shows the (A) cluster image and (B) corresponding average spectra for the fingerprint region. The cluster image (Figure 10.11A) resembles the amide I and II cluster image from Figure 10.9A.

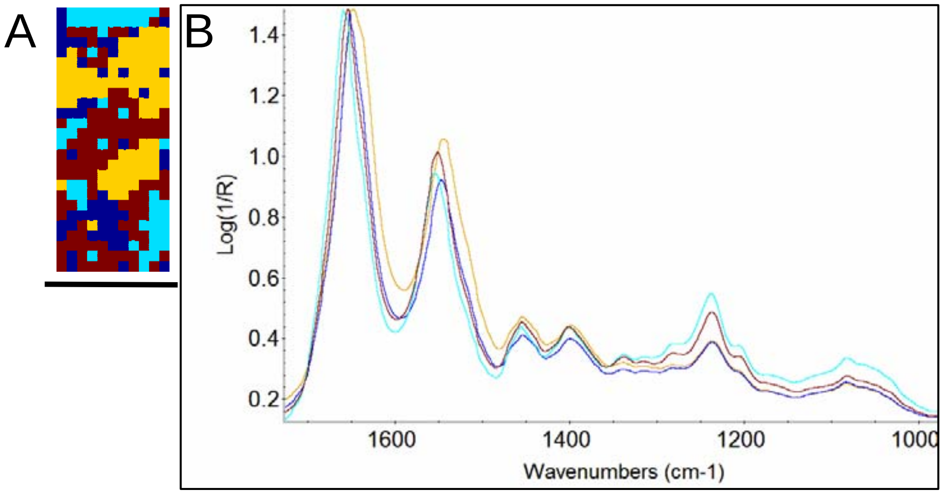

Figure 10.11. Cluster analysis of 21-day-old wound tissue on the fingerprint region. (A) Image and (B) corresponding average spectra created by hierarchical cluster analysis on the spectral region from 1700 to 1010 cm^{-1}. Scale bar = 100 µm.

10.2.3.2. Fibrous Scar Tissue

Figure 10.12 shows a typical IR map of fibrous scar tissue (Figure 10.12A and B) from a 21-day post-surgery sample. The IR spectra (Figure 10.12C) of this type of tissue have strong collagen bands at 1338, 1284, and 1204 cm^{-1}, and the band at 1080 cm^{-1} has two maxima at around 1082 and 1032 cm^{-1}. The IR maps (Figure 10.12D) of fibrous scar show high intensity of the bands at 1080 and 1230 cm^{-1}, as well as the small band at 1204 cm^{-1} attributable to collagen, throughout the map.

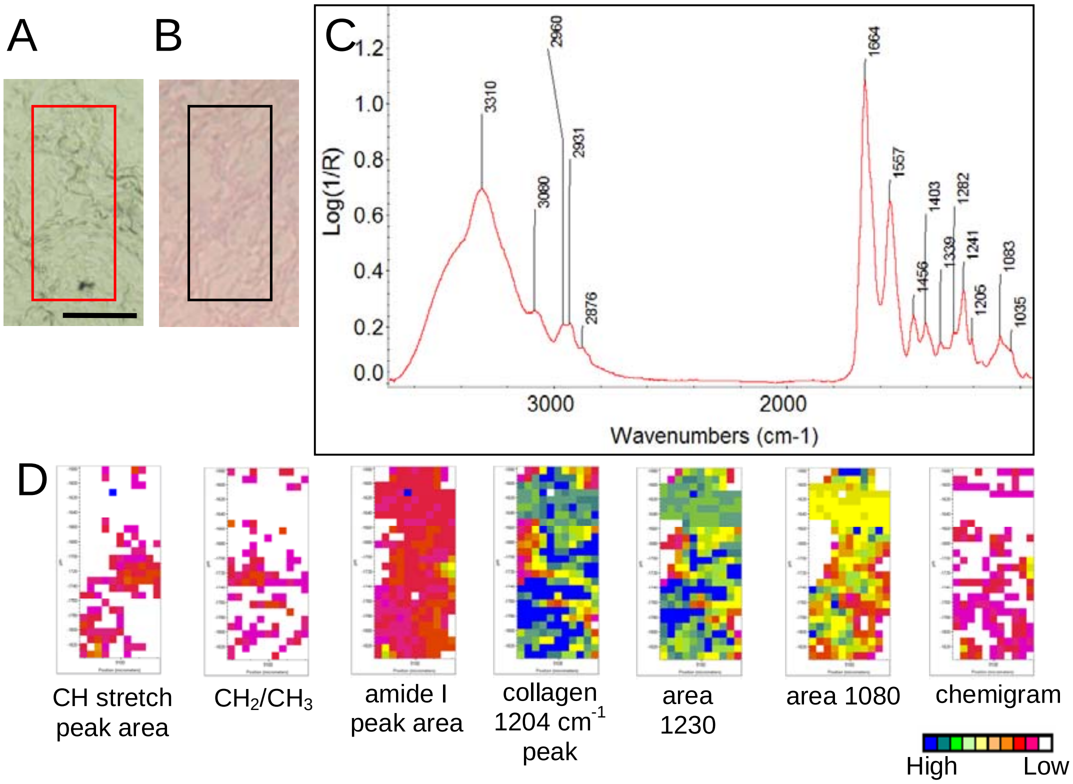

CH stretch peak area

CH_2/CH_3

amide I peak area

collagen 1204 cm^{-1} peak

area 1230

area 1080

chemigram

Figure 10.12. Fibrous scar tissue in saline treated rat, 21 days after surgery. (A) The IR mapped region and (B) the corresponding area in an H&E stained section. This section is about 200 µm from the IR mapped section. (C) A typical IR spectrum of 21-day post-surgery fibrous scar tissue. (D) The IR map processed with the methods outlined in Table 9.1. Scale bar = 100 µm.

Figure 10.13 shows the results of cluster analyses performed on the spectral regions from 1700-1500 cm^{-1} (A and B), 1300-1010 cm^{-1} (C and D), and 1700-1010 cm^{-1} (E and F). The cluster images (Figure 10.13A, C, and E) resemble the IR maps created on the peak areas of the bands at 1230, 1080, and 1204 cm^{-1} (Figure 10.12D). The amide I bands of the average spectra where these bands are most intense (Figure 10.13B green spectrum, D green and blue spectra, and F green spectrum) have maxima at 1664 cm^{-1} with a slight shoulder at 1637 cm^{-1}. The other amide I bands are shifted to lower wavenumbers.

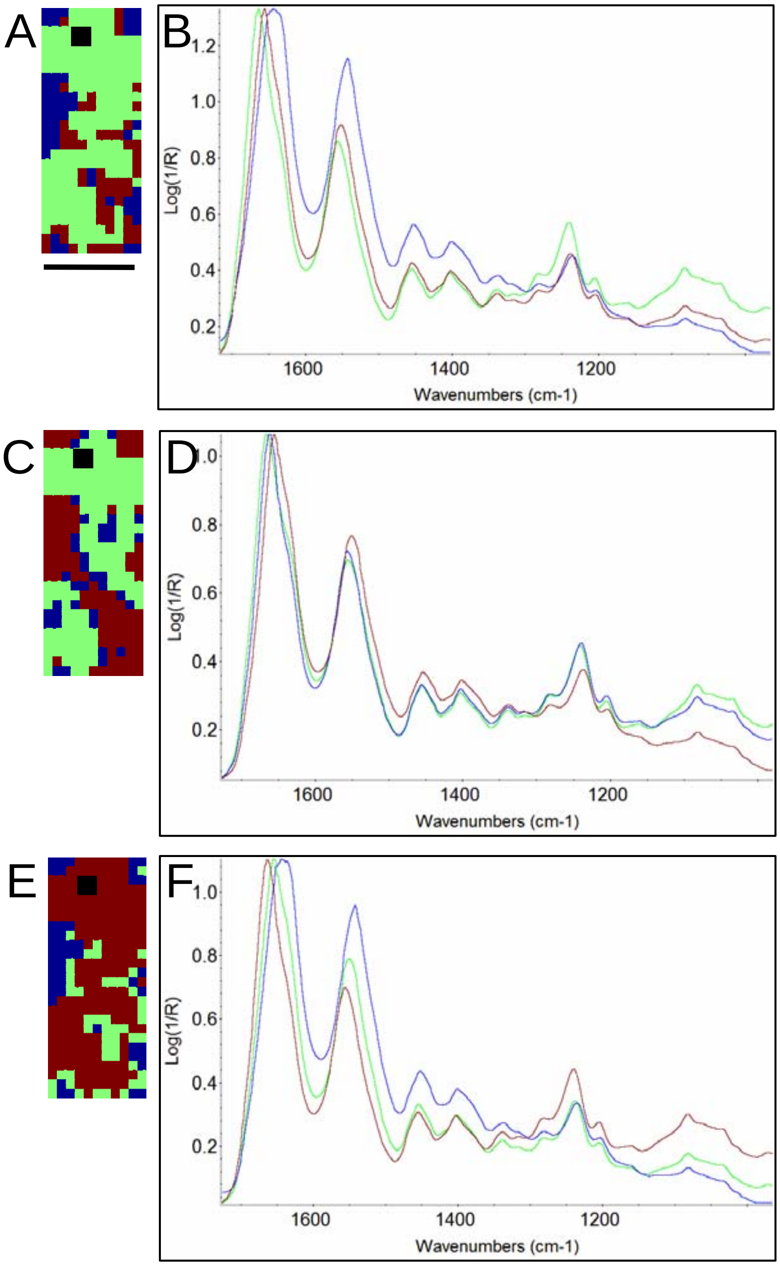

Figure 10.13. Cluster analysis of 21-day-old fibrous wound tissue. (A) Image and (B) corresponding average spectra created by hierarchical cluster analysis on the spectral region from 1700 to 1500 cm^{-1}. (C) Image and (D) corresponding average spectra created by hierarchical cluster analysis on the spectral region from 1300 to 1010 cm^{-1}. (E) Image and (F) corresponding average spectra created by hierarchical cluster analysis on the spectral region from 1700 to 1010 cm^{-1}. Black regions in cluster maps are noisy spectra not included in the analysis. Scale bar = 100 μm.

10.2.3.3. Wound Tissue Next to Degenerating Muscles

The 21-day post-surgery saline-treated samples also contain regions of smooth-looking wound tissue that seem to be infiltrating the muscle tissue (Figure 10.14A and B). A typical spectrum of this type of tissue is shown in Figure 10.14C. The peaks due to collagen (1338, 1282 and 1204 cm^{-1}) are absent or of very low intensity, while the band at 1080 cm^{-1} has a distinct maximum at around 1084 cm^{-1}. The spectra of this tissue resemble those of the 3-day post-surgery tissue. The two most variable bands were the amide I and the sugar/symmetric phosphate stretch band (the 1080 band). The amide I maxima and 1080 cm^{-1} peak intensities varied in the maps from this type of tissue. The relative intensities of most components in the IR maps (Figure 10.14D) are generally homogeneous. The 1080 cm^{-1} peak is the only one to show significant variation in intensity throughout the map.

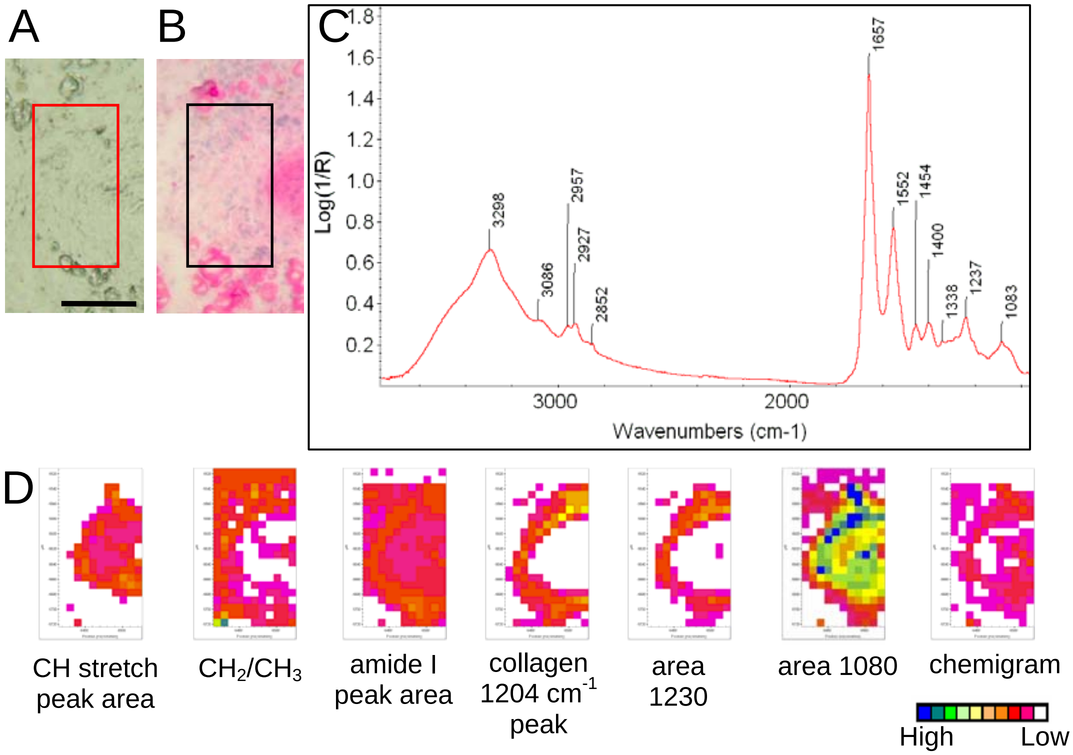

Figure 10.14. Wound tissue next to degenerating muscle, 21 days post-surgery. The wound tissue is found next to degenerating muscle fibres. (A) The IR mapped region and (B) the corresponding area in an H&E stained section. This section is about 200 µm from the IR mapped section. (C) A typical IR spectrum of 21-day-old wound tissue. (D) The IR map processed with the methods outlined in Table 9.1. Scale bar = 100 µm.

Figure 10.15 shows the results of cluster analysis performed on the spectral regions from 1700-1500 cm^{-1} (A and B), 1300-1010 cm^{-1} (C and D), and 1700-1010 cm^{-1} (E and F) for the above map. All the cluster images (Figure 10.15A, C, and E) resemble the IR map based on the 1080 cm^{-1} peak areas (Figure 10.14D, area 1080). Similar results are obtained when the cluster analysis is performed on the amide I and II bands (Figure 10.15A and B), the phosphate stretch bands (Figure 10.15C and D), and the fingerprint region (Figure 10.15E and F), which shows that changes to the amide I and II region of the spectra are associated with changes to the phosphate stretch region. For all the average spectra with the highest intensity in the phosphate stretch bands, the amide I maximum was located at 1663 cm^{-1} (Figure 10.15B yellow spectrum, D green spectrum, F blue spectrum) and for the lowest intensity at 1652 cm^{-1} with a shoulder at 1637 cm^{-1} (Figure 10.15B brown spectrum, D brown spectrum , F green spectrum). The average spectra with intermediate intensities in these bands had amide I maxima located at around 1657 cm^{-1} (Figure 10.15B cyan and blue spectra, D blue spectrum, F brown spectrum).

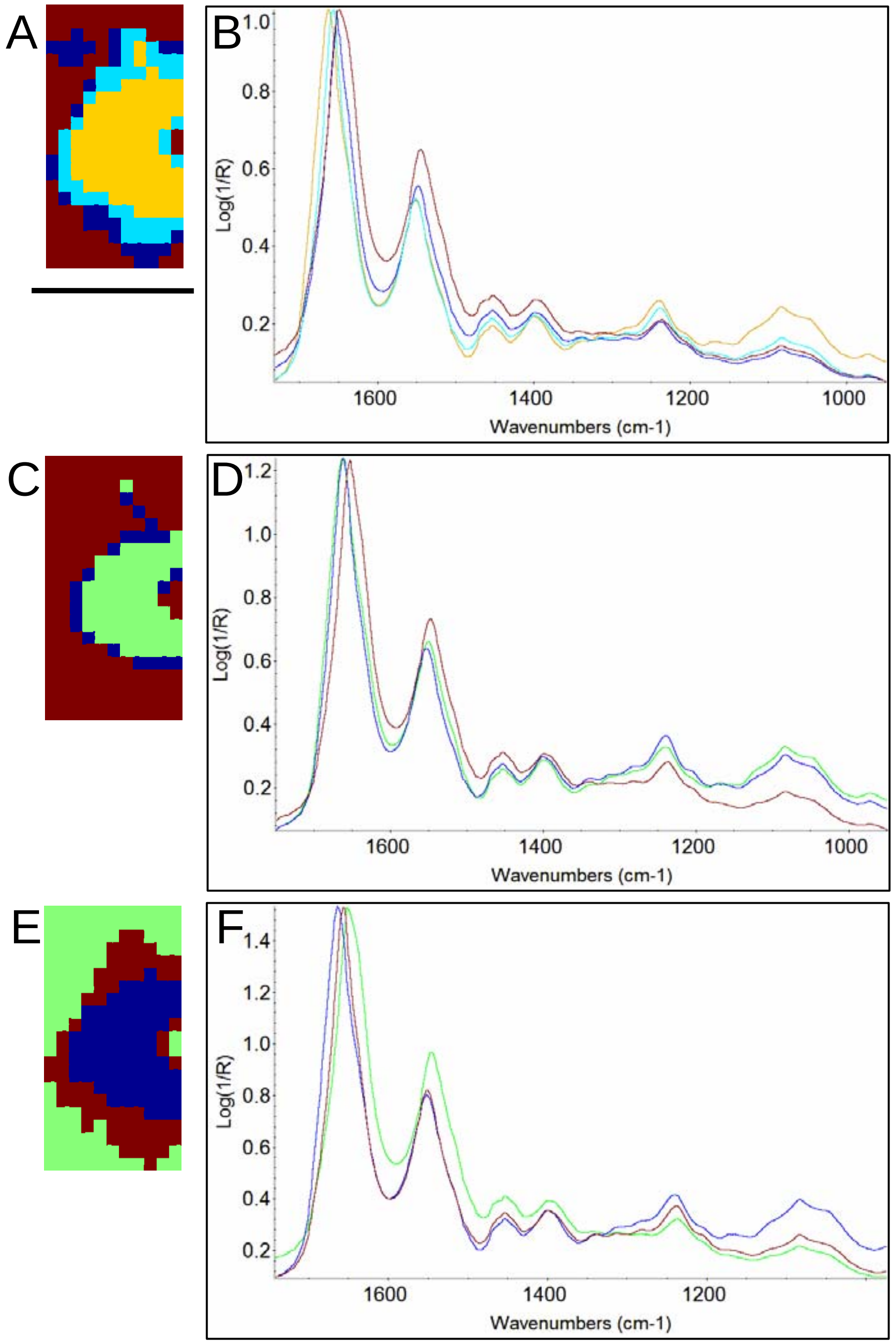

Figure 10.15. Cluster analysis of 21-day-old wound tissue next to degenerating muscle. (A) Image and (B) corresponding average spectra created by hierarchical cluster analysis on the spectral region from 1700 to 1500 cm^{-1}. (C) Image and (D) corresponding average spectra created by hierarchical cluster analysis on the spectral region from 1300 to 1010 cm^{-1}. (E) Image and (F) corresponding average spectra created by hierarchical cluster analysis on the spectral region from 1700 to 1010 cm^{-1}. Scale bar = 100 µm.

10.2.4. IR Mapping of Scar Tissue from Treated Rats

The tissue sections from both the OTC and quercetin-treated animals, 3 days post-surgery, were similar to those from the saline-treated control rats. The main difference noted between both the OTC and quercetin-treated samples and the saline-treated controls, 21 days post-surgery, was that the area of scar tissue in the treated samples was smaller. However, a final conclusion about this cannot be reached until analysis of stained sections (histochemistry, immunohistochemistry and *in situ* hybridization) is completed by our collaborators at the University of Saskatchewan. An initial analysis of tissue morphology and IR data from the 21-day post-surgery OTC and quercetin-treated samples showed that there were again three categories of scar tissue. The tissue could be divided into granular-looking developing scar tissue, fibrous, mature scar tissue, and regions of newly-formed wound tissue near degenerating muscles. Representative data, processed and presented in the same way as the data for the saline treated samples, is shown in the sections below. One example map is shown for each of the treatment groups, 3 days after surgery. As the 21-day post-surgery tissue was more morphologically variable, 3 maps are shown per treatment group. They include maps from developing, granular scar tissue, fibrous scar tissue, and newly formed wound tissue next to degenerating muscles. Figures 10.16 and 10.17 show data for OTC-treated tissue, 3 days after surgery. Figures 10.18 to 10.23 show data for OTC-treated tissue, 21 days after surgery. Figures 10.24 and 10.25 show data for quercetin-treated tissue, 3 days after surgery. The data presented in Figures 10.26 to 10.31 is from quercetin-treated rats, 21 days after surgery. As can be clearly seen, the maps are very similar to those of saline-treated scar tissue.

10.2.4.1. IR Mapping of OTC-treated 3-Day Post-surgery Scar Tissue

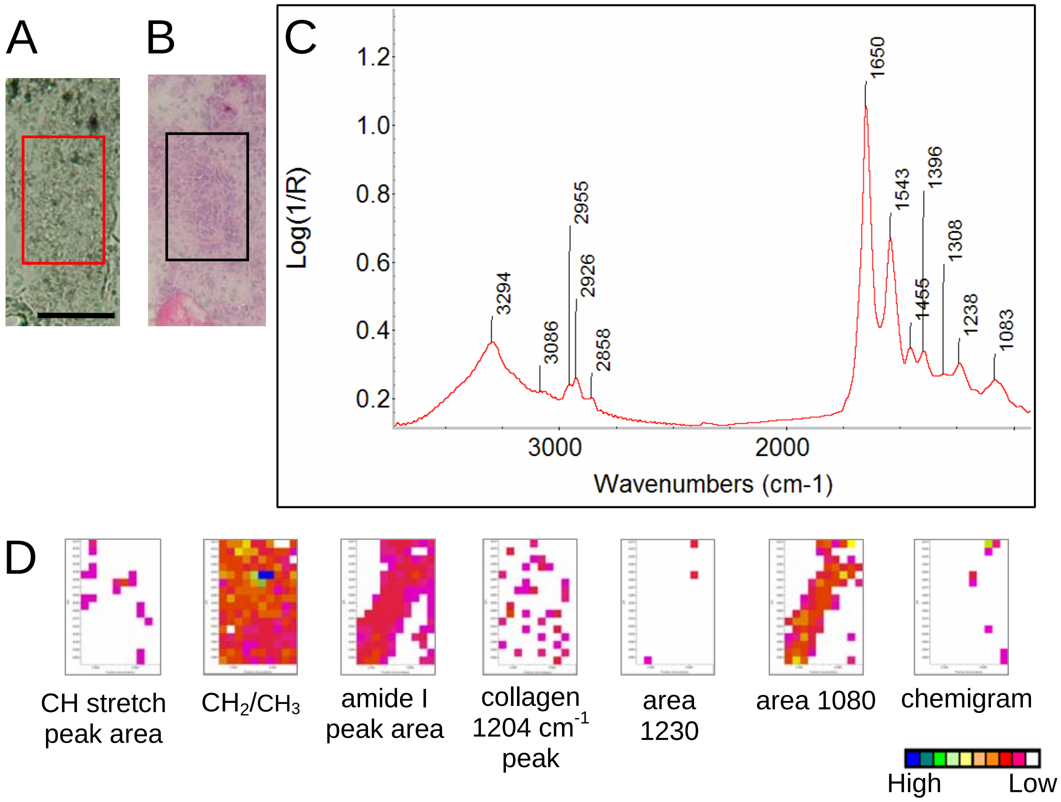

Figure 10.16. Wound tissue in OTC-treated rat, 3 days after surgery. The wound tissue is found next to degenerating muscle fibres (bright pink in H&E section). (A) The IR mapped region and (B) the corresponding area in an H&E stained section. This section is about 200 µm from the IR mapped section. (C) A typical IR spectrum of 3-day-old wound tissue; the most variable regions are indicated with arrows. (D) The IR map processed with the methods outlined in Table 9.1. Scale bar = 100 µm.

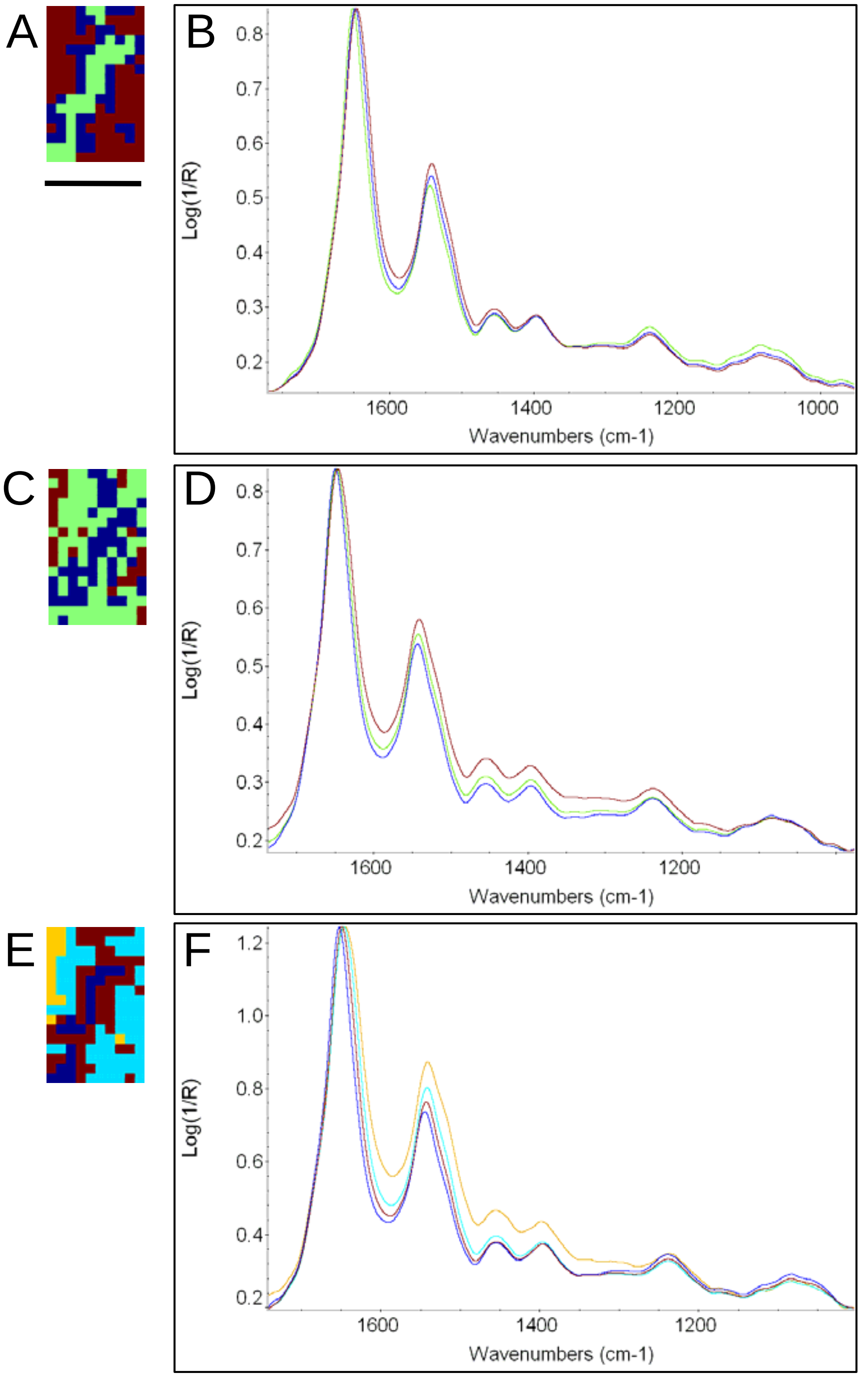

Figure 10.17. Cluster analysis of OTC-treated tissue, 3 days after surgery. (A) Image and (B) corresponding average spectra created by hierarchical cluster analysis on the spectral region from 1700 to 1500 cm^{-1}. (C) Image and (D) corresponding average spectra created by hierarchical cluster analysis on the spectral region from 1300 to 1010 cm^{-1}. (E) Image and (F) corresponding average spectra created by hierarchical cluster analysis on the spectral region from 1700 to 1010 cm^{-1}. Scale bar = 100 µm.

10.2.4.2. IR Mapping of OTC-treated 21-Day Post-surgery Scar Tissue

10.2.4.2.1. Developing Scar Tissue

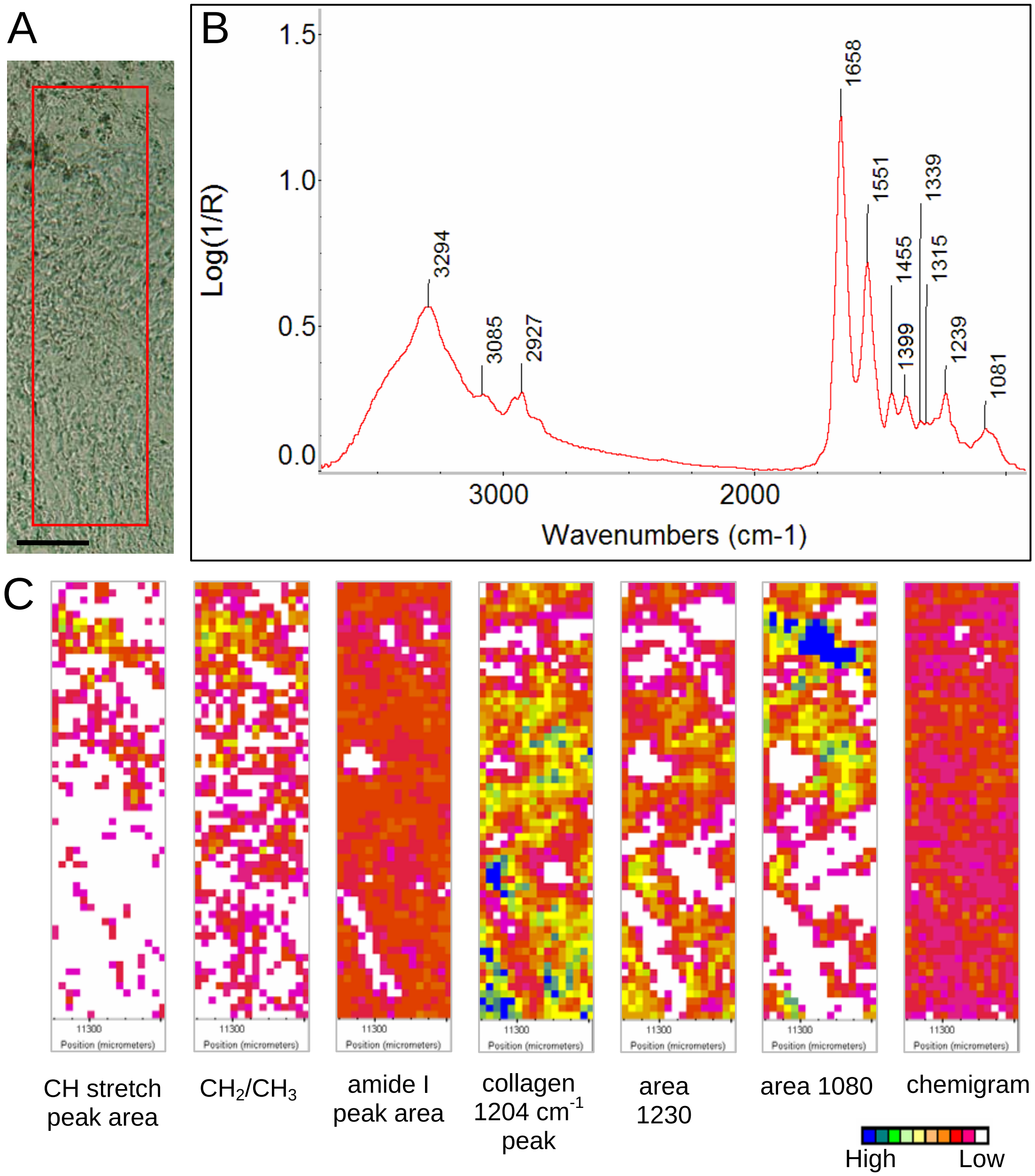

Figure 10.18. Developing scar tissue in OTC-treated rat, 21 days after surgery. (A) The unstained, granular-looking developing scar tissue, with the mapped region outlined in red. (B) A typical IR spectrum of 21-day-old developing scar tissue. (C) The IR map processed with the methods outlined in Table 9.1. Scale bar = 100 μm.

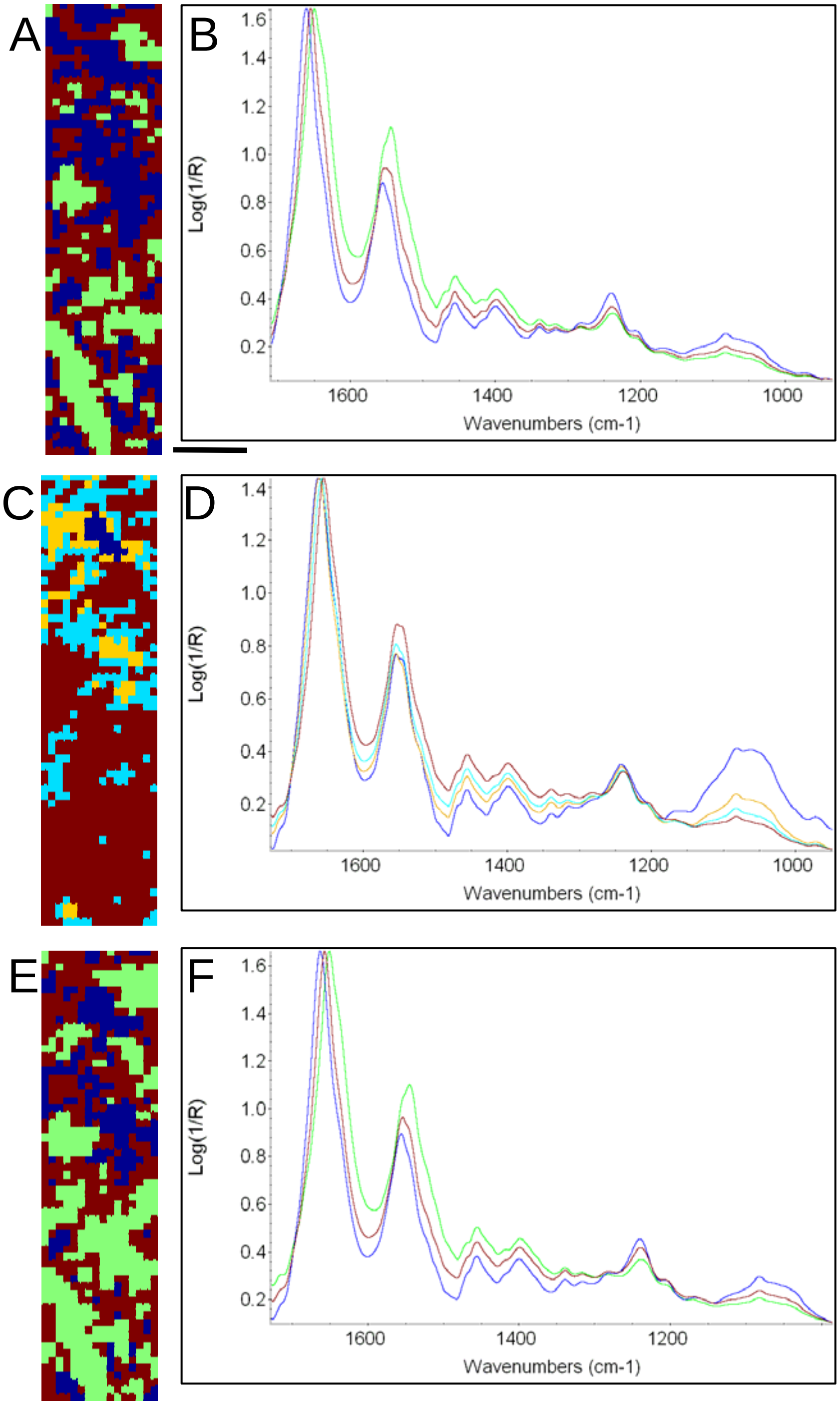

Figure 10.19. Cluster analysis of OTC-treated developing scar tissue, 21 days after surgery. (A) Image and (B) corresponding average spectra created by hierarchical cluster analysis on the spectral region from 1700 to 1500 cm^{-1}. (C) Image and (D) corresponding average spectra created by hierarchical cluster analysis on the spectral region from 1300 to 1010 cm^{-1}. (E) Image and (F) corresponding average spectra created by hierarchical cluster analysis on the spectral region from 1700 to 1010 cm^{-1}. Scale bar = 100 µm.

10.2.4.2.2. Fibrous Scar Tissue

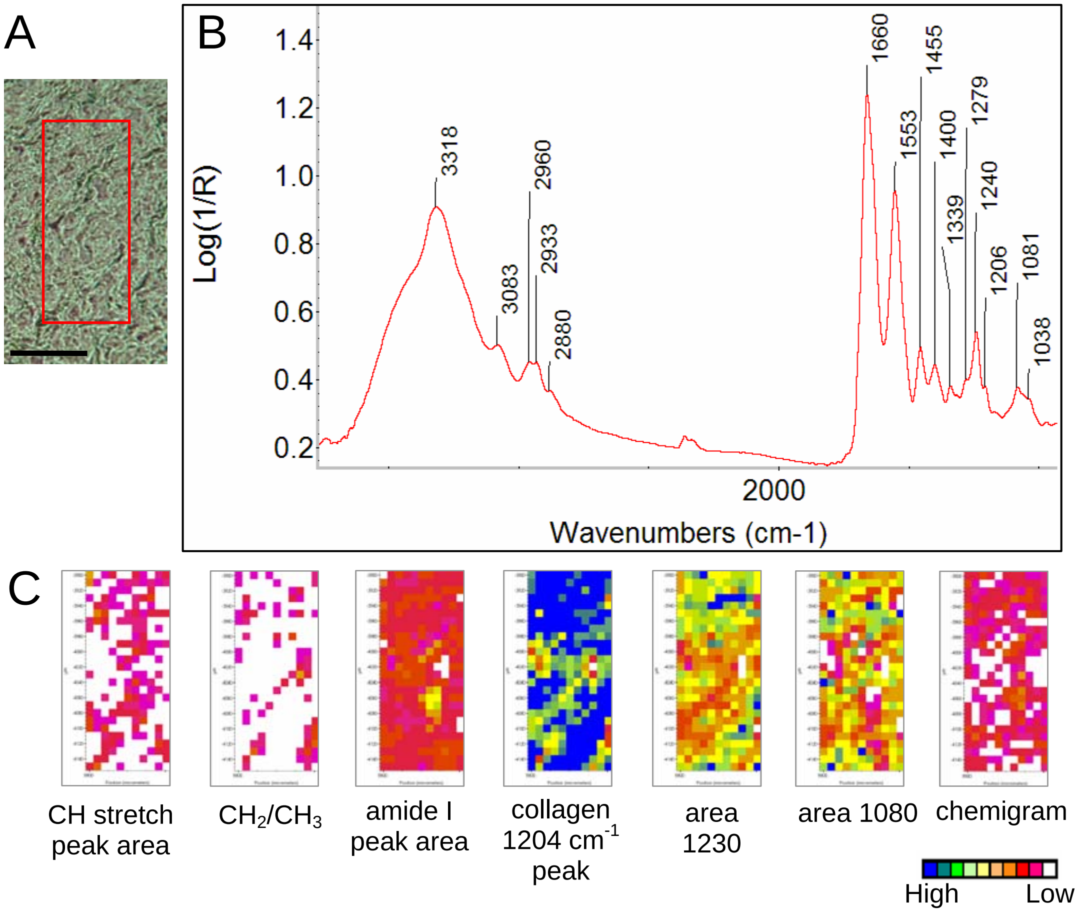

Figure 10.20. Fibrous scar tissue in OTC-treated rat, 21 days after surgery. (A) The IR mapped region. (B) A typical IR spectrum of 21-day post-surgery fibrous scar tissue. (C) The IR map processed with the methods outlined in Table 9.1. Scale bar = 100 µm.

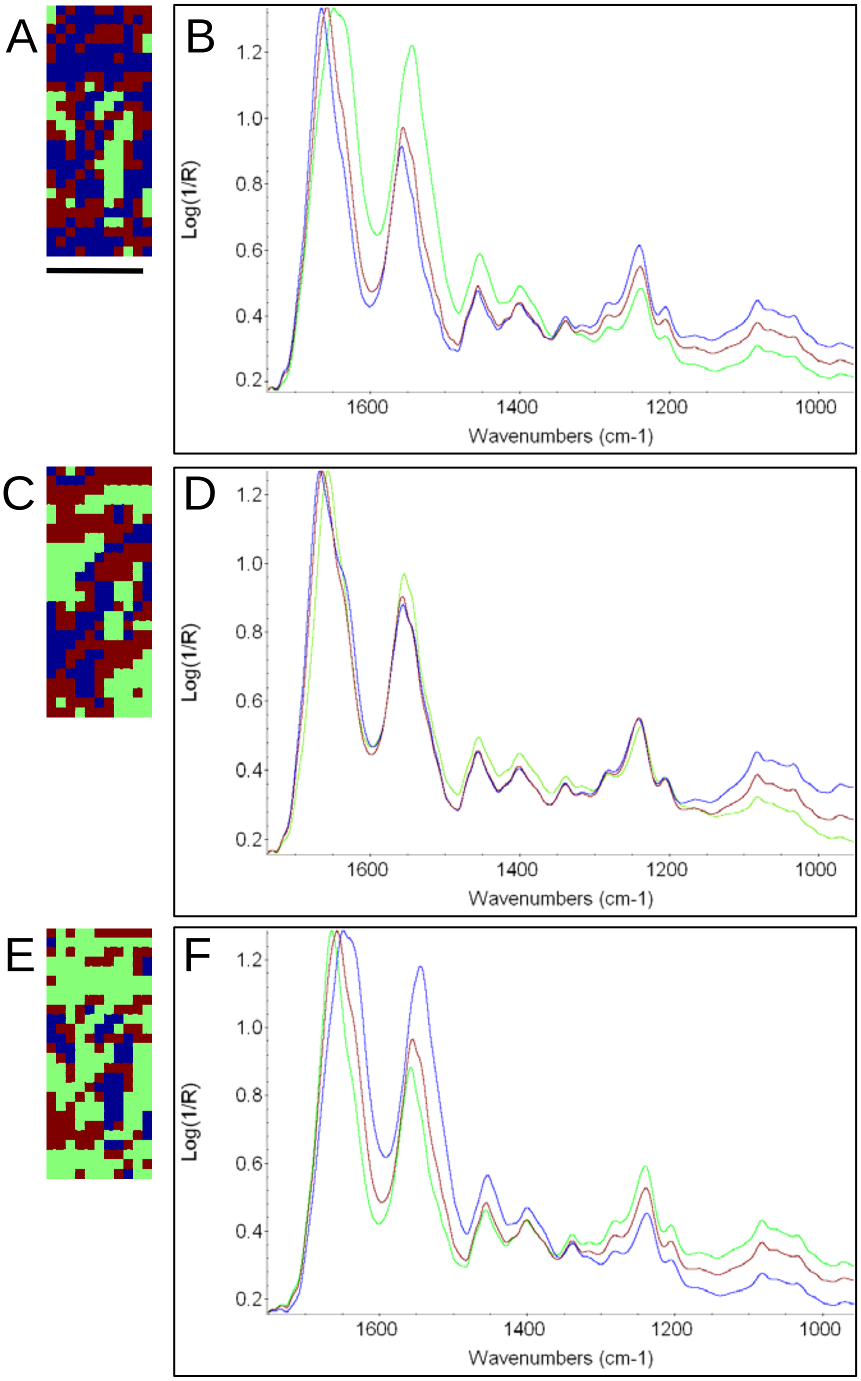

Figure 10.21. Cluster analysis of OTC-treated fibrous scar tissue, 21 days after surgery. (A) Image and (B) corresponding average spectra created by hierarchical cluster analysis on the spectral region from 1700 to 1500 cm^{-1}. (C) Image and (D) corresponding average spectra created by hierarchical cluster analysis on the spectral region from 1300 to 1010 cm^{-1}. (E) Image and (F) corresponding average spectra created by hierarchical cluster analysis on the spectral region from 1700 to 1010 cm^{-1}. Scale bar = 100 µm.

10.2.4.2.3. Wound Tissue Next to Degenerating Muscles

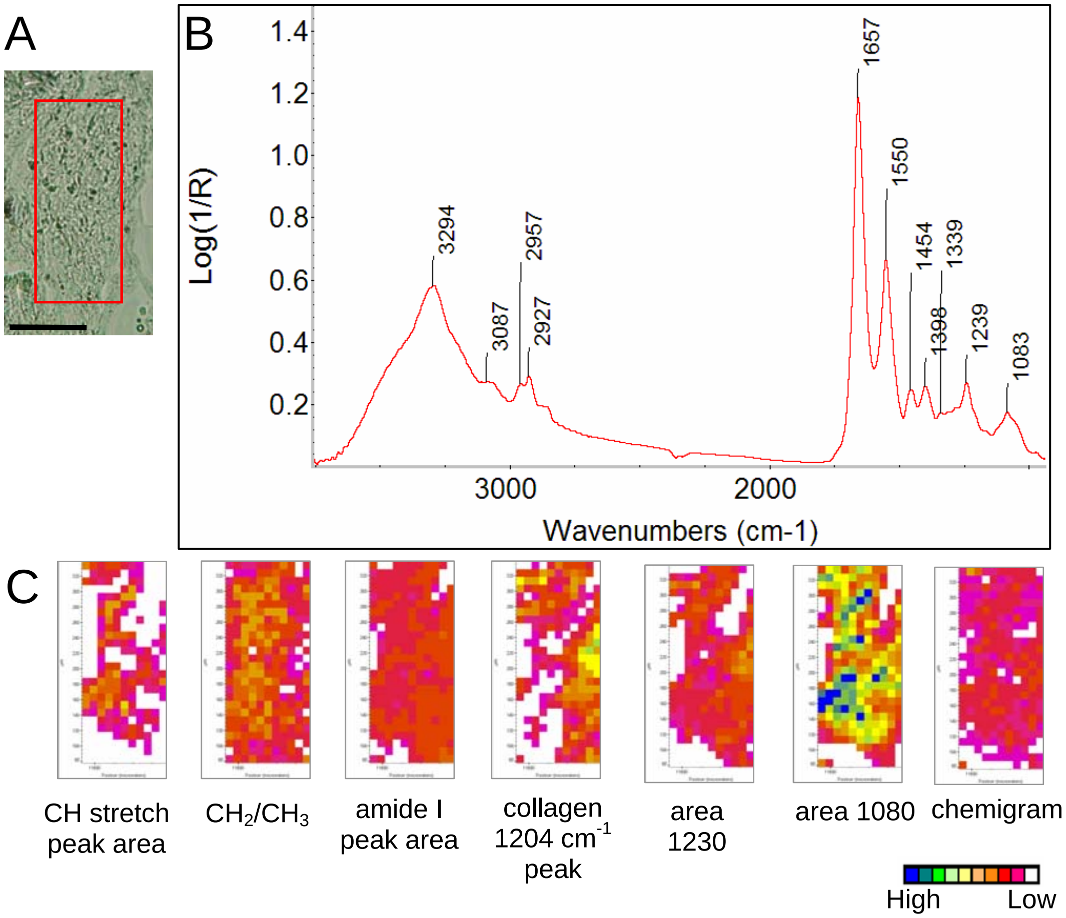

Figure 10.22. Wound tissue next to degenerating muscle in OTC-treated rat, 21 days post-surgery. The wound tissue is found next to degenerating muscle fibres. (A) The IR mapped region. (B) A typical IR spectrum of 21-day-old wound tissue. (C) The IR map processed with the methods outlined in Table 9.1. Scale bar = 100 µm.

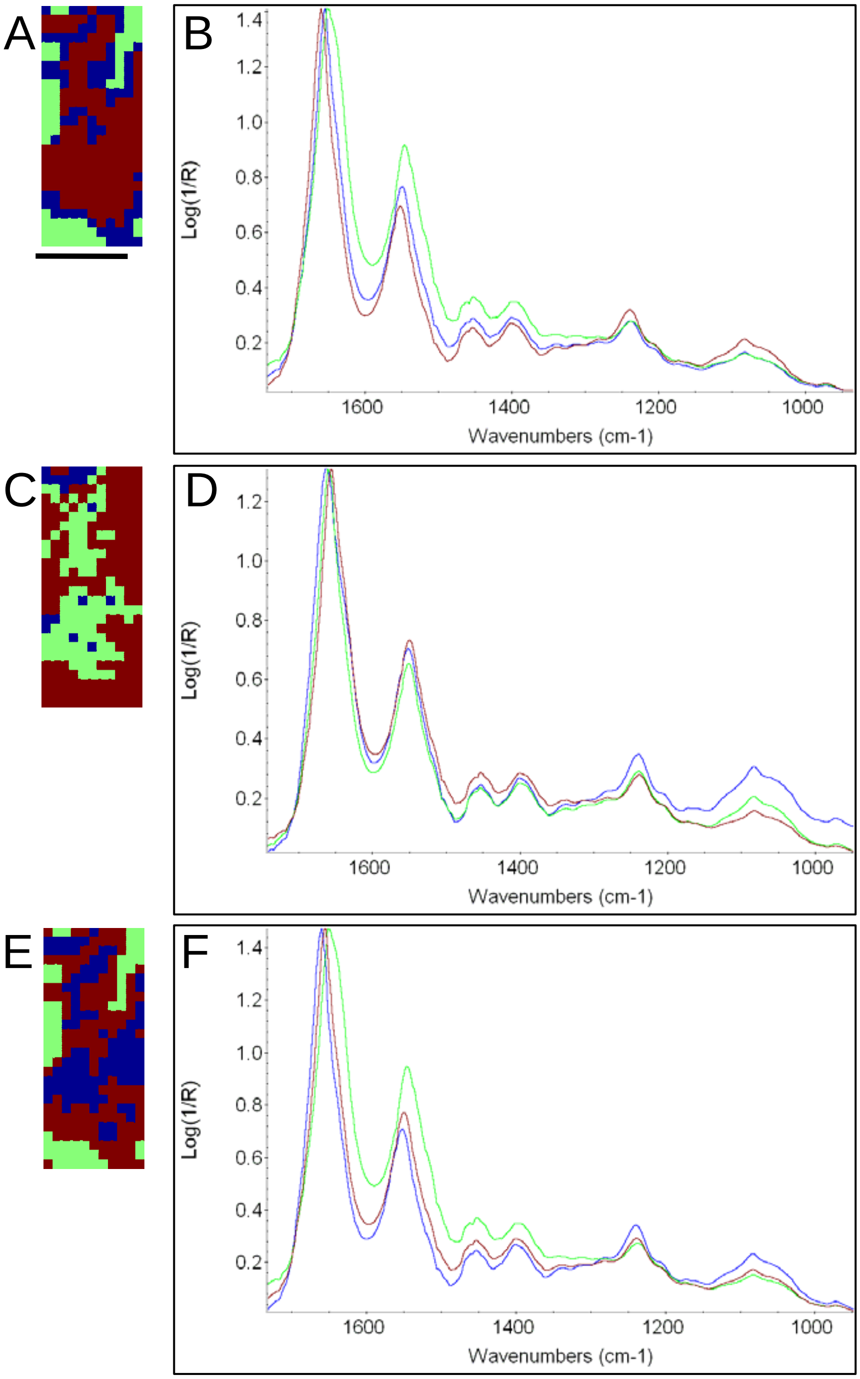

Figure 10.23. Cluster analysis of OTC-treated wound tissue next to degenerating muscle, 21 days after surgery. (A) Image and (B) corresponding average spectra created by hierarchical cluster analysis on the spectral region from 1700 to 1500 cm^{-1}. (C) Image and (D) corresponding average spectra created by hierarchical cluster analysis on the spectral region from 1300 to 1010 cm^{-1}. (E) Image and (F) corresponding average spectra created by hierarchical cluster analysis on the spectral region from 1700 to 1010 cm^{-1}. Scale bar = 100 μm.

10.2.4.3. IR Mapping of Quercetin-treated 3-Day Post-surgery Scar Tissue

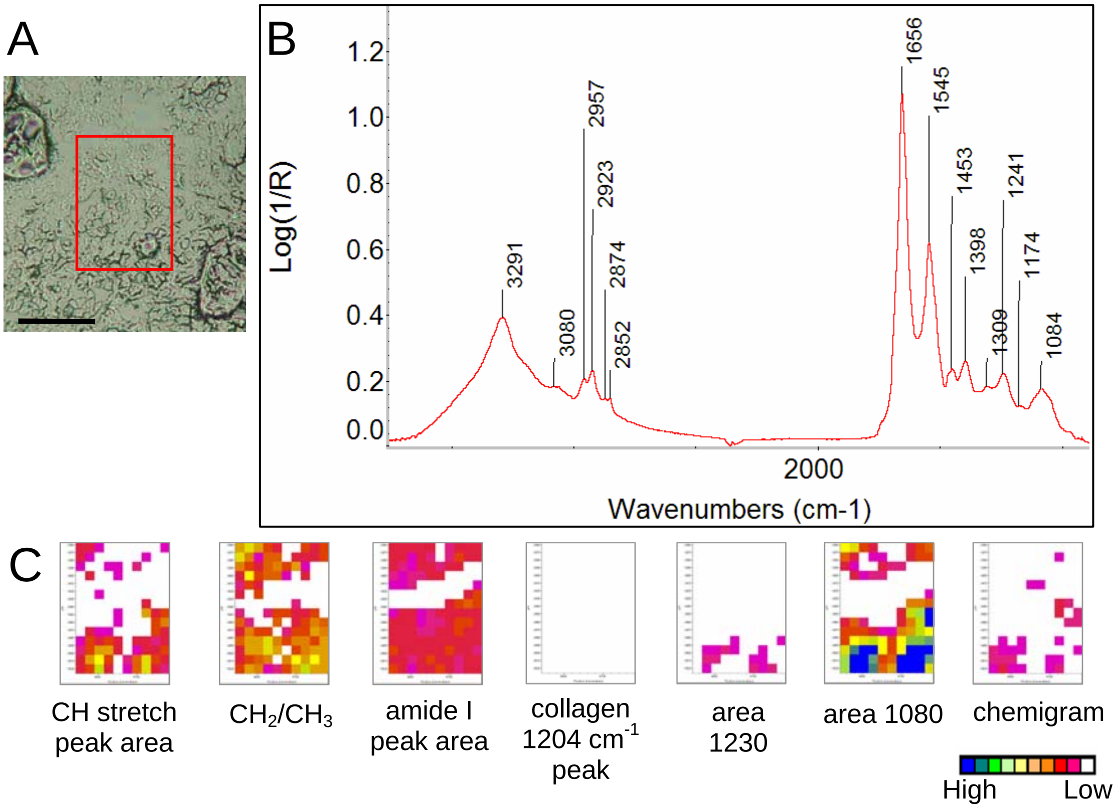

Figure 10.24. Wound tissue in quercetin-treated rat, 3 days after surgery. The wound tissue is found next to degenerating muscle fibres (A) The IR mapped region. (B) A typical IR spectrum of 3-day-old wound tissue. (C) The IR map processed with the methods outlined in Table 9.1. Scale bar = 100 µm.

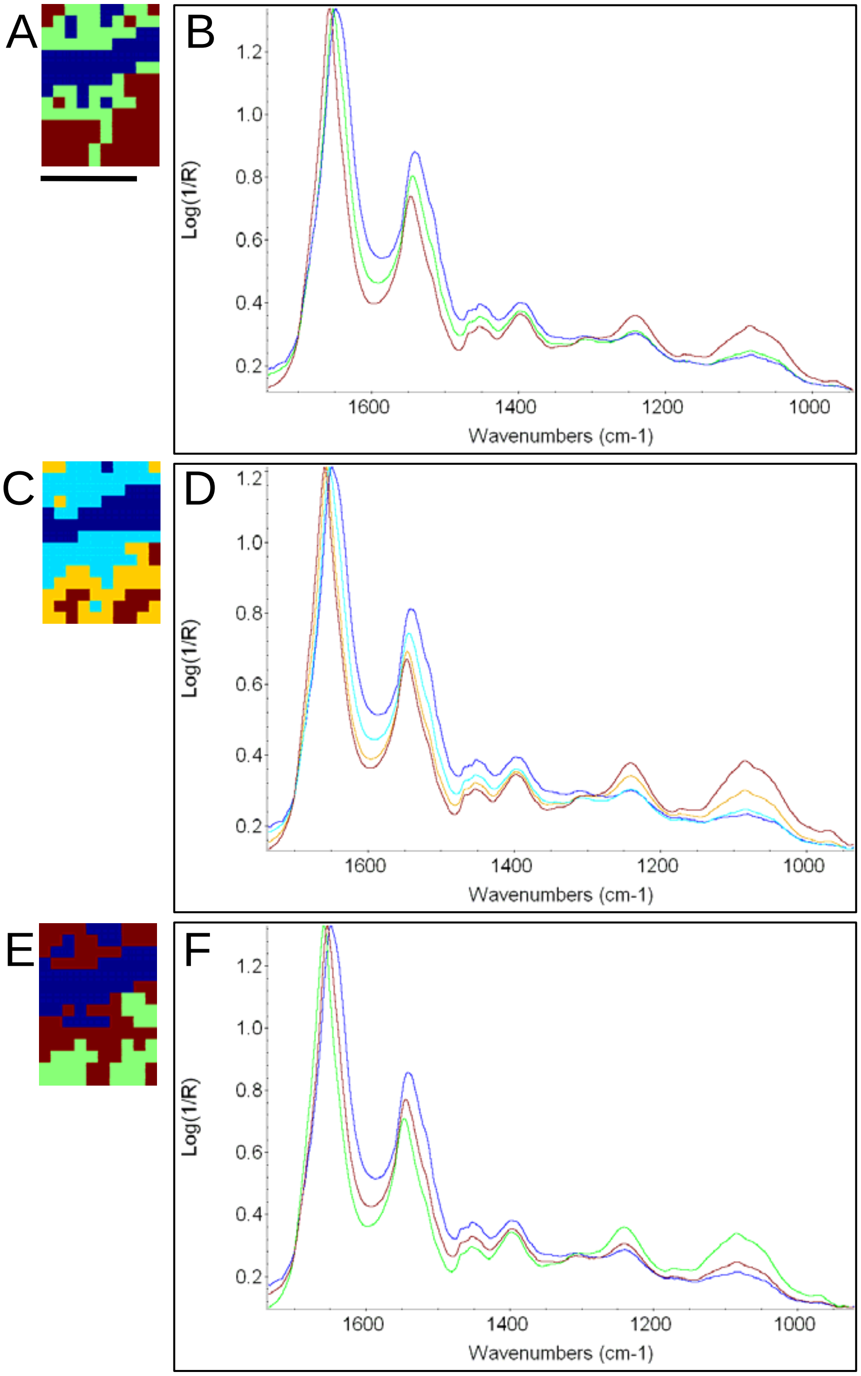

Figure 10.25. Cluster analysis of quercetin-treated tissue, 3 days after surgery. (A) Image and (B) corresponding average spectra created by hierarchical cluster analysis on the spectral region from 1700 to 1500 cm^{-1}. (C) Image and (D) corresponding average spectra created by hierarchical cluster analysis on the spectral region from 1300 to 1010 cm^{-1}. (E) Image and (F) corresponding average spectra created by hierarchical cluster analysis on the spectral region from 1700 to 1010 cm^{-1}. Scale bar = 100 µm.

10.2.4.4. IR Mapping of Quercetin-treated 21-Day Post-surgery Scar Tissue

10.2.4.4.1. Developing Scar Tissue

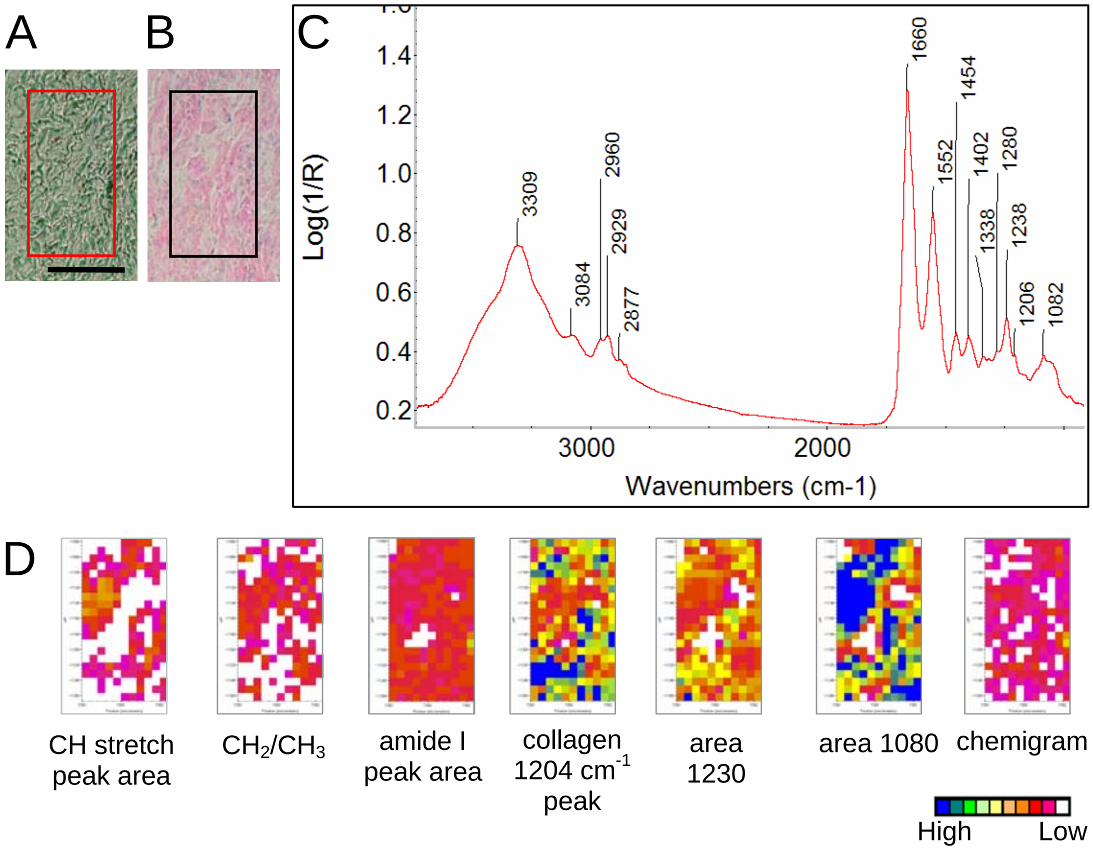

Figure 10.26. Developing scar tissue in quercetin-treated rat, 21 days after surgery. (A) The unstained, granular-looking developing scar tissue, with the mapped region outlined in red. (B) The corresponding area in an H&E stained section. This section is about 200 µm from the IR mapped section. (C) A typical IR spectrum of 21-day-old developing scar tissue. (D) The IR map processed with the methods outlined in Table 9.1. Scale bar = 100 µm.

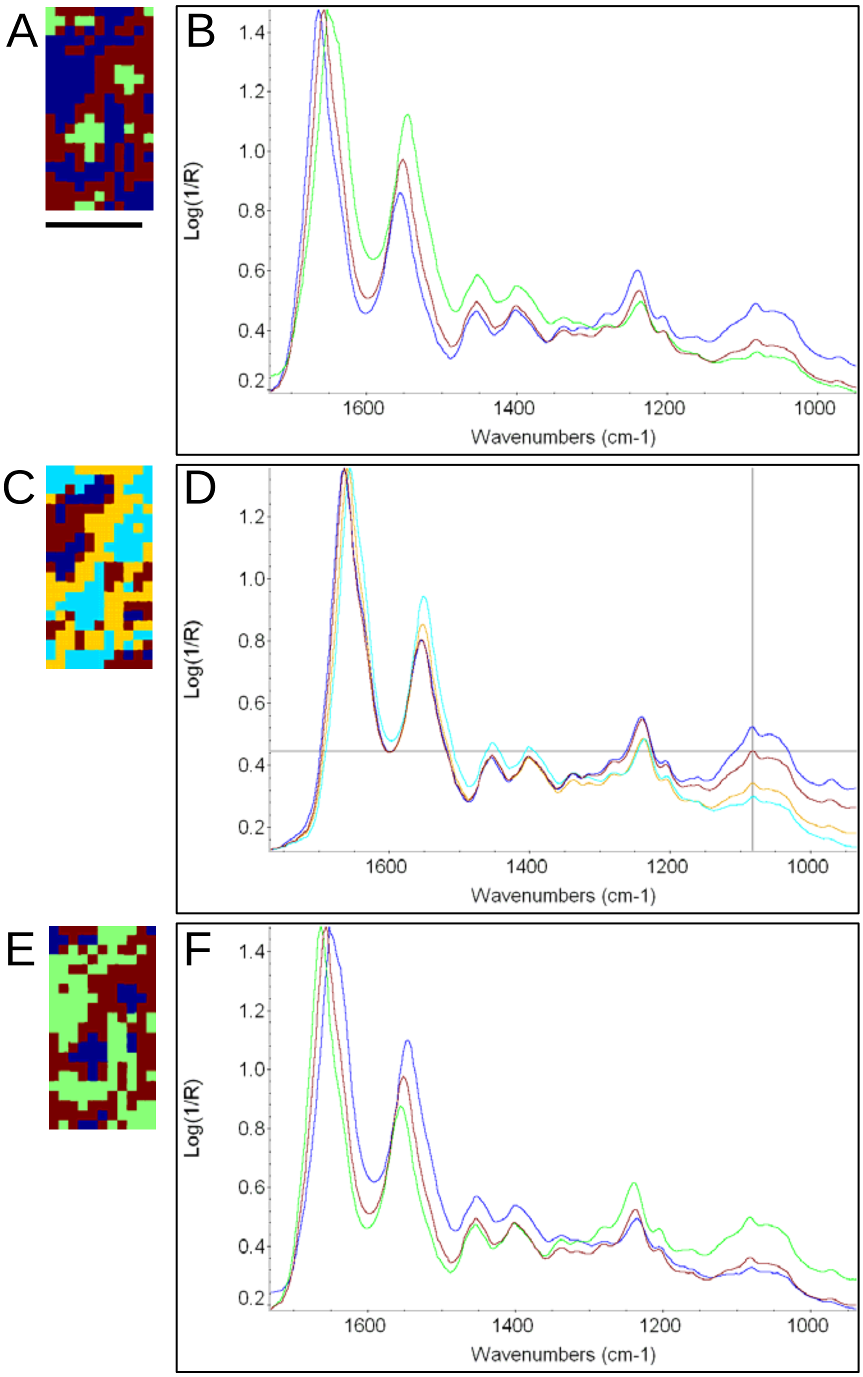

Figure 10.27. Cluster analysis of quercetin-treated developing scar tissue, 21 days after surgery. (A) Image and (B) corresponding average spectra created by hierarchical cluster analysis on the spectral region from 1700 to 1500 cm^{-1}. (C) Image and (D) corresponding average spectra created by hierarchical cluster analysis on the spectral region from 1300 to 1010 cm^{-1}. (E) Image and (F) corresponding average spectra created by hierarchical cluster analysis on the spectral region from 1700 to 1010 cm^{-1}. Scale bar = 100 μm.

10.2.4.4.2. Fibrous Scar Tissue

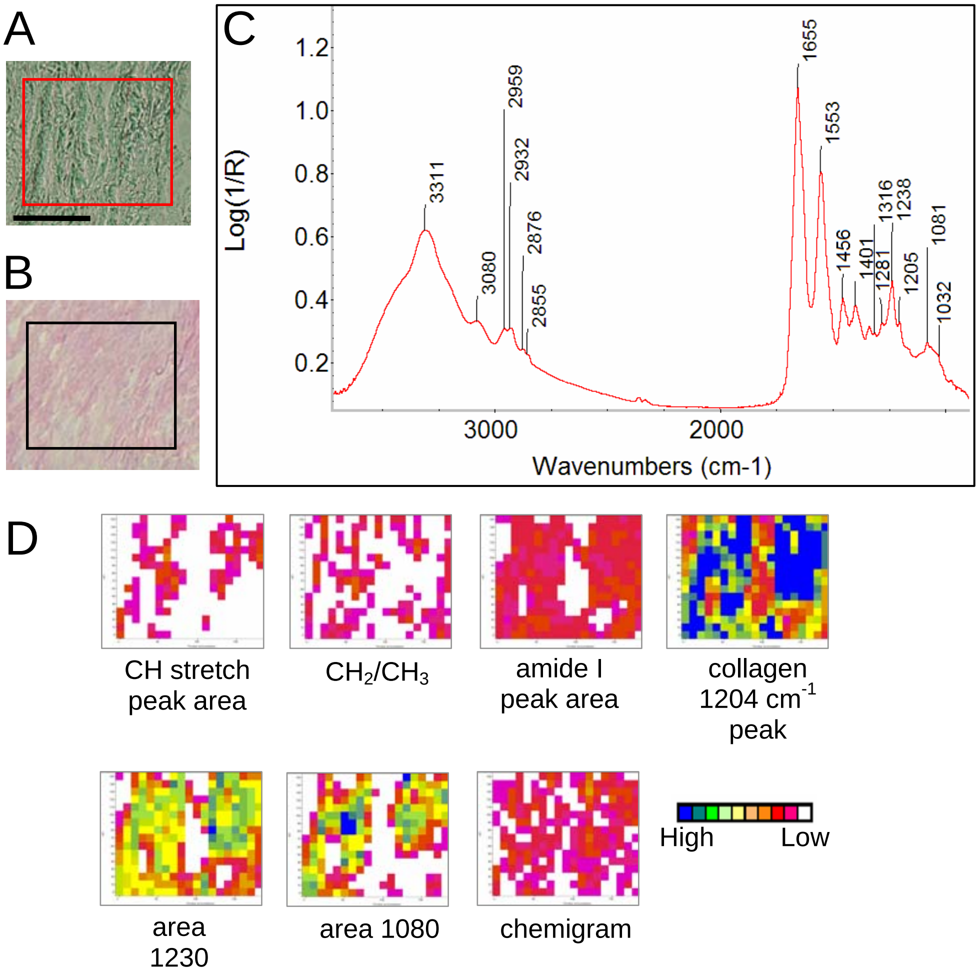

Figure 10.28. Fibrous scar tissue in quercetin-treated rat, 21 days after surgery. (A) The IR mapped region and (B) the corresponding area in an H&E stained section. This section is about 200 μm from the IR mapped section (C) A typical IR spectrum of 21-day post-surgery fibrous scar tissue. (D) The IR map processed with the methods outlined in Table 9.1. Scale bar = 100 μm.

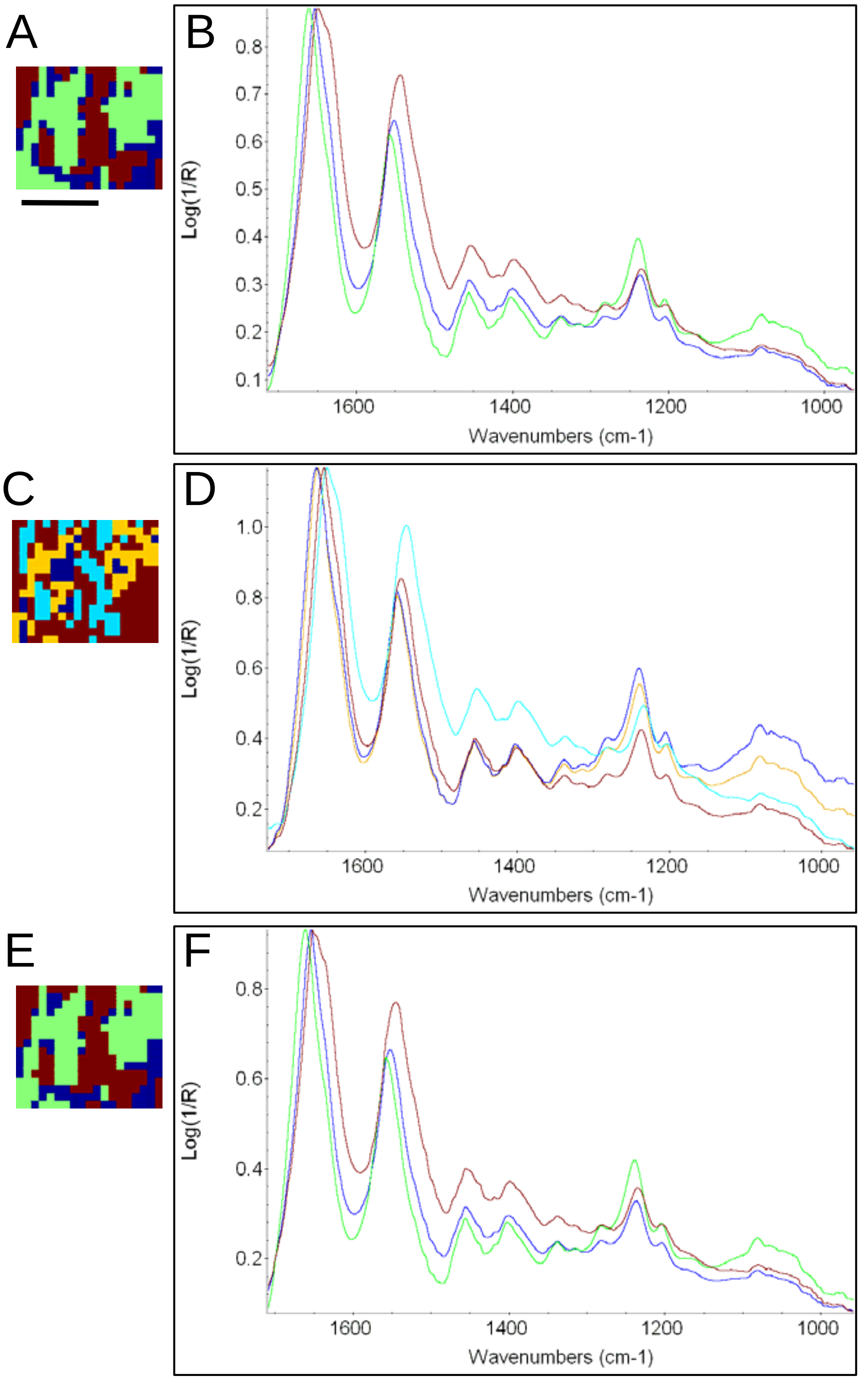

Figure 10.29. Cluster analysis of quercetin-treated fibrous scar tissue, 21 days after surgery. (A) Image and (B) corresponding average spectra created by hierarchical cluster analysis on the spectral region from 1700 to 1500 cm^{-1}. (C) Image and (D) corresponding average spectra created by hierarchical cluster analysis on the spectral region from 1300 to 1010 cm^{-1}. (E) Image and (F) corresponding average spectra created by hierarchical cluster analysis on the spectral region from 1700 to 1010 cm^{-1}. Scale bar = 100 µm.

10.2.4.4.3. Wound Tissue Next to Degenerating Muscles

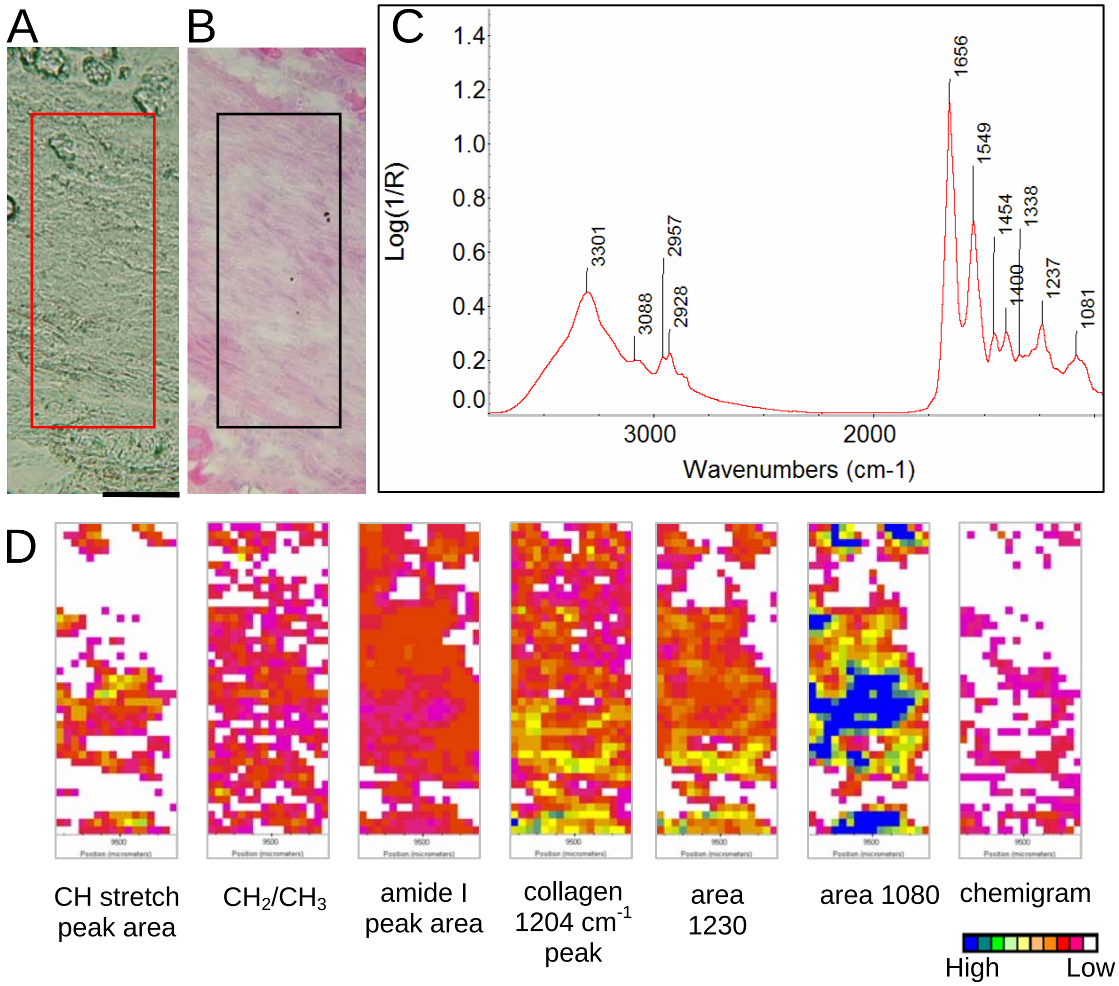

Figure 10.30. Wound tissue next to degenerating muscle in quercetin-treated rat, 21 days post-surgery. The wound tissue is found next to degenerating muscle fibres. (A) The IR mapped region and (B) the corresponding area in an H&E stained section. This section is about 200 µm from the IR mapped section. (C) A typical IR spectrum of 21-day-old wound tissue. (D) The IR map processed with the methods outlined in Table 9.1. Scale bar = 100 µm.

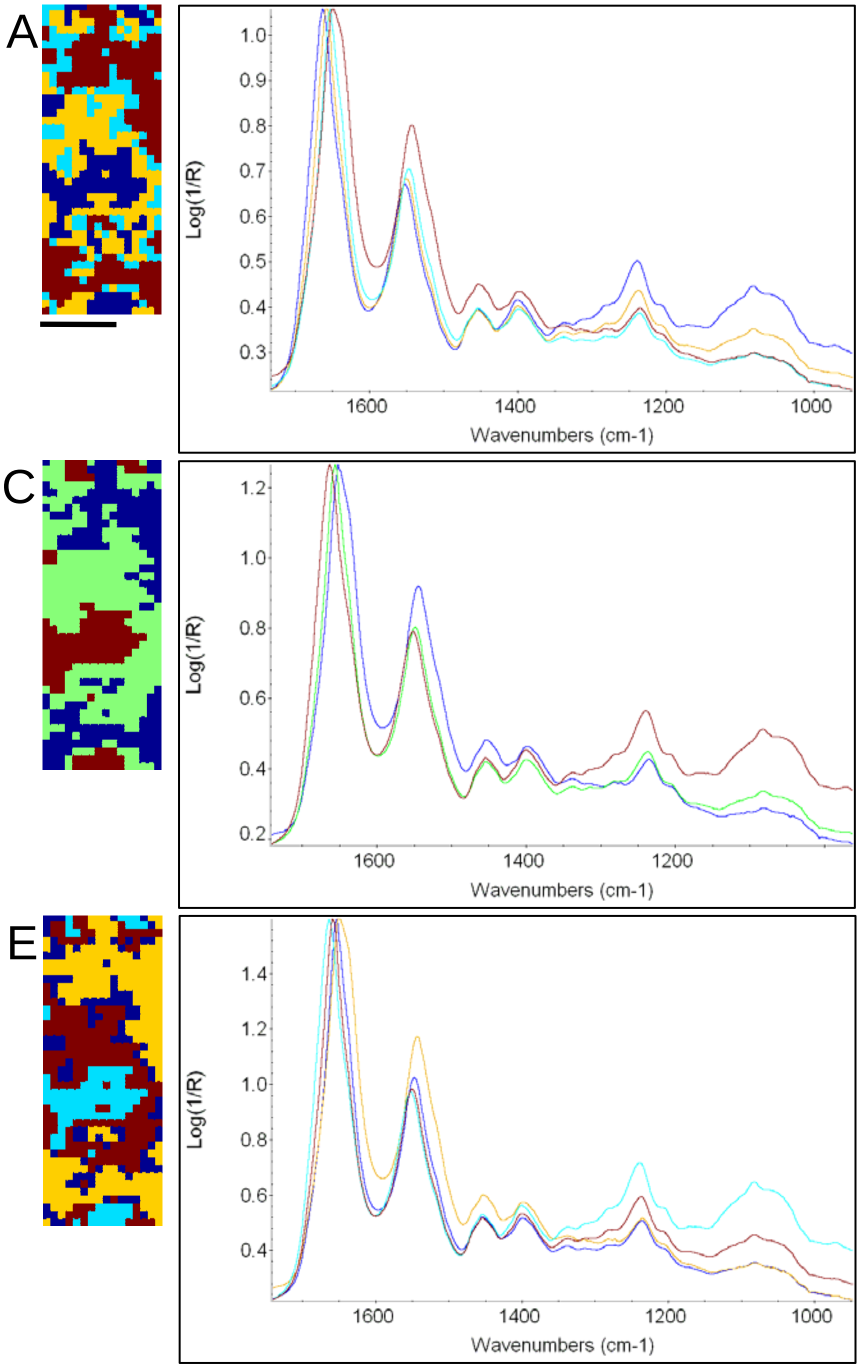

Figure 10.31. Cluster analysis of quercetin-treated wound tissue next to degenerating muscle, 21 days after surgery. (A) Image and (B) corresponding average spectra created by hierarchical cluster analysis on the spectral region from 1700 to 1500 cm^{-1}. (C) Image and (D) corresponding average spectra created by hierarchical cluster analysis on the spectral region from 1300 to 1010 cm^{-1}. (E) Image and (F) corresponding average spectra created by hierarchical cluster analysis on the spectral region from 1700 to 1010 cm^{-1}. Scale bar = 100 μm.

10.3. The Effect of Polarized Synchrotron Light on Scar Tissue Spectra

Unusual looking spectra appeared in some of the synchrotron IR maps from 21-day-old scar tissue. The intensities of the amide II and III bands were increased relative to the amide I band intensity. Figure 10.32 shows a spectrum where this effect is especially strong (top spectrum). The amide II band is almost as intense as the amide I, and the amide III is significantly stronger than normal. This effect was only seen in the spectra of fibrous scar. However, the extent of this effect was variable and it was not seen in all spectra from fibrous scar tissue. The bottom spectrum in Figure 10.32 is also of fibrous collagen-rich scar, but the relative amide band intensities appear normal.

This effect was interpreted as arising from the interaction of the highly-oriented collagen fibrils in fibrous scar tissue with plane-polarized light. Synchrotron light is known to be intrinsically polarized (Wiedemann, 2003), and this can affect the band intensities in oriented samples. Scar development involves the synthesis of collagen. During the remodelling phase of wound healing, this collagen becomes re-organized into oriented fibrils (O’Leary et al, 2002; Diegelmann & Evans, 2004). This orientation will affect the relative intensities of the amide bands when the spectra are collected with polarized synchrotron light. The extent of this effect is a function of the relative orientations of the collagen fibrils and the plane of the light. This dependence therefore presented an opportunity for monitoring the development of fibrous collagen in the scar.

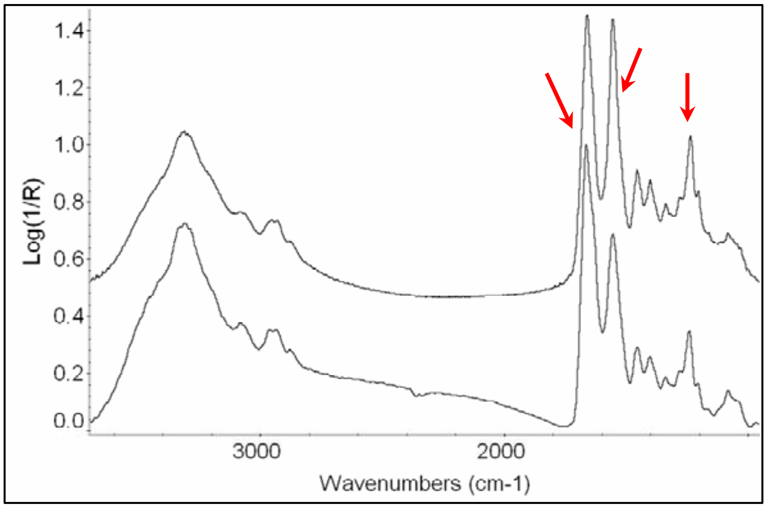

Figure 10.32. Effect of polarized synchrotron IR light on 21-day post-surgery scar tissue spectrum. Spectra of fibrous, collagen-rich scar tissue collected at SRC. The relative intensities of the amide I, II and III bands in the top spectrum (arrows) were affected by polarized light.

10.3.1. Polarized IR Spectra of Achilles Tendon

Optics are known to alter the polarization of light. A sample with high molecular orientation was therefore needed, in order to test the polarization of the synchrotron IR light at the NSLS and SRC. Achilles tendons are composed mostly of fibrillar, highly oriented type I collagen, and small quantities of proteoglycans. They are therefore a very good model system for studying collagen orientation. The rat Achilles tendon was sectioned and placed in orthogonal directions (vertically and horizontally) on the MirrIR substrate.

Spectra were first taken with light of known polarization on a benchtop instrument. When the polarization of the light was varied, the intensities of the amide bands, as well as their shapes, changed (Figure 10.33).

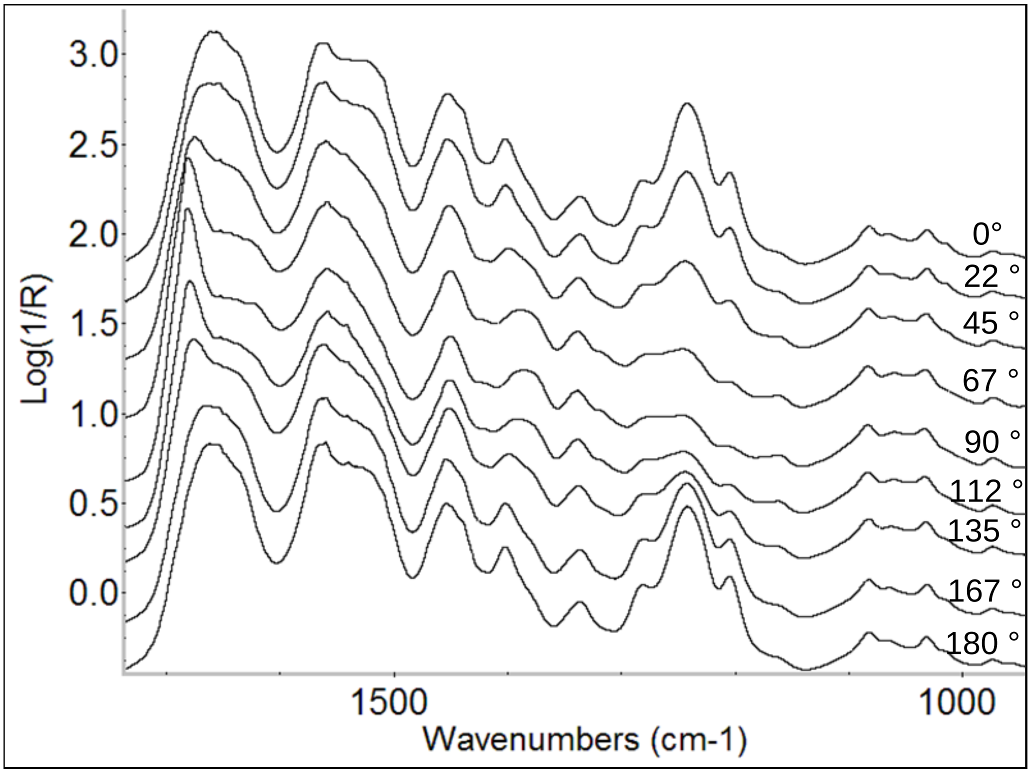

Figure 10.33. IR spectra of Achilles tendon taken with linearly polarized light. The tendon was placed vertically on the slide and the direction of the plane-polarized light relative to the sample was changed at regular intervals.

Figure 10.34 shows the spectra of both vertically and horizontally oriented tendon, taken with light plane-polarized in orthogonal directions (0 and 90 degrees). The IR spectrum of tendon placed horizontally on the slide taken with light at 0° polarization is identical to the spectrum of tendon placed vertically on the slide taken with 90° plane-polarized light. The same is true of the spectrum of horizontally-placed tendon with 90° polarized light and the spectrum of vertically-placed tendon taken with 0° plane-polarized light. This shows that changing either the orientation of the sample or the light is equivalent. As expected, the amide I, A, and B bands of collagen show opposite dichroism to those of the amide II and III bands; if the amide I, A, and B bands are more intense at a particular degree of polarization, than the amide II and III bands are less intense, and vice versa (Frazer, 1950). This is because the transition dipole moments of these groups of bands are perpendicular in the collagen fibril.

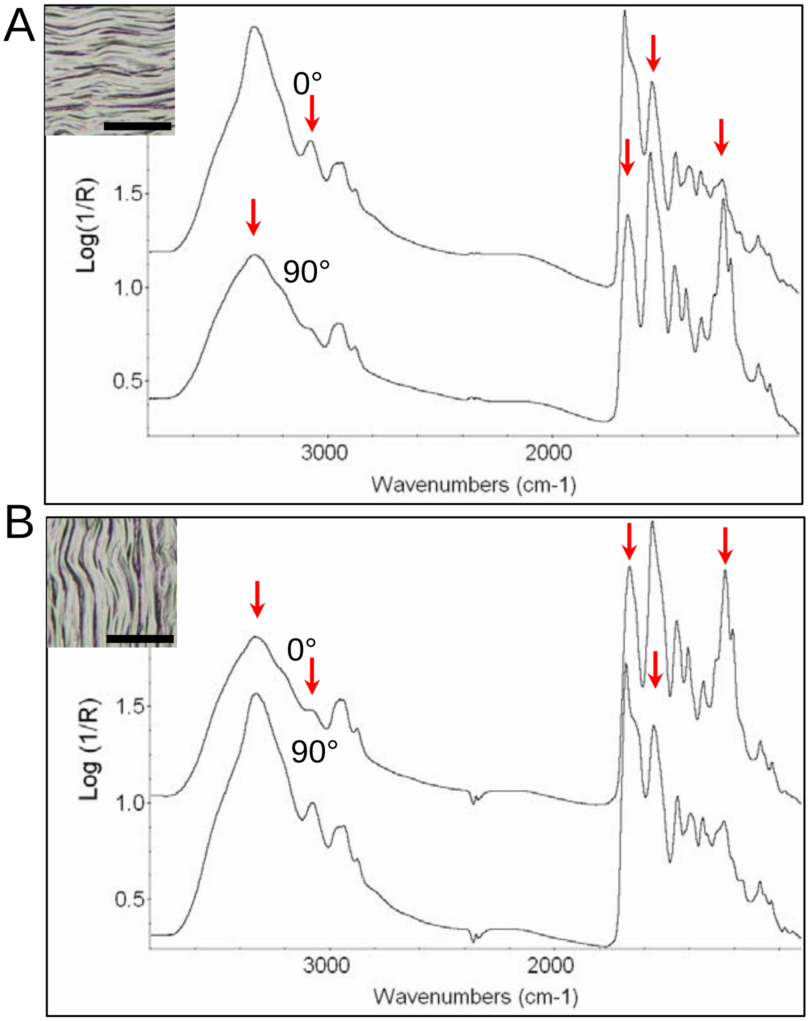

Figure 10.34. Tendon spectra taken with orthogonally plane-polarized light. (A) Spectra of horizontally placed tendons (inset), taken with 0° and 90° polarized light. (B) Spectra of vertically placed tendons (inset), taken with 0° and 90° polarized light. Arrows point to dichroic amide bands. Scale bar = 100 μm.

IR spectra of the tendons in both orientations were then collected at both the NSLS and SRC synchrotrons, without the use of polarizers (Figure 10.35). The results demonstrated that light at both synchrotrons was highly polarized. The light at the two synchrotrons was however polarized in opposite directions, due to the arrangement of the optics.

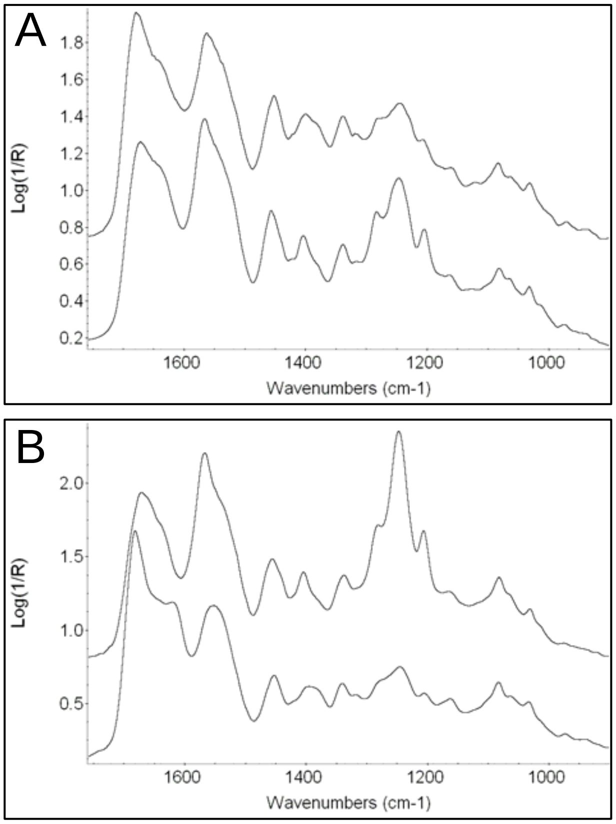

Figure 10.35. Synchrotron IR spectra of Achilles tendon. (A) Spectra from the NSLS, taken of horizontally (top spectrum) and vertically (bottom spectrum) oriented tendons. (B) Spectra from the SRC, taken of horizontally (top spectrum) and vertically (bottom spectrum) oriented tendons. The spectra indicate that the light is polarized, but in the opposite direction, at each synchrotron.

The IR maps collected with the synchrotron light could therefore be re-analyzed to show the relative collagen orientation in the map. The ratio of the amide I to the amide II band had been used to map the collagen orientation in cartilage (Camacho et al, 2001). Our group applied the same method to the fibrous scar tissue in post-laminectomy rat tissue (Wiens et al, 2007).

These data demonstrate that the plane-polarized nature of synchrotron light allows useful information about sample orientation to be obtained. However, the changes to the relative intensities of dichroic bands need to be considered during data analysis, especially when peak heights or areas are considered.

Chapter 11. Scar Tissue Study Discussion

The overall hypothesis for this project was that one or both of the anti-oxidants administered after surgery would result in less scarring in the long term. Since the project is not yet completed, this hypothesis cannot be tested with the present data. The primary objective for the work presented in this thesis was to examine the spectra from the first set of animals in order to determine what spectral differences are present, how to best utilize the available software to highlight these differences, and where possible, to provide some interpretation for their origin. The dataset has since been extended to 6 animals per group, sacrificed 3, 21, and 63 days post-surgery.

11.1. Comparison of 3-Day and 21-Day Data

Typical spectra of 3-day and 21-day post-surgery wound tissue are presented in the sections below. The set is comprised of one spectrum from the 3-day post-surgery tissue, three from the 21-day post-surgery tissue, including one each from wound tissue next to degenerating muscle, developing scar, and more mature fibrous scar. A spectrum of type I collagen, the main component of mature scar, is also shown. Spectral regions of interest, including the phosphate stretch, the amide I and II, and the CH stretch regions are discussed. The spectra show significant differences between both the 3 and 21-day post-surgery wound tissue, and the different stages of scar development in the 21-day post-surgery tissue.

11.1.1. Phosphate Stretch Region

The spectral region from 1300 to 1010 cm^{-1} contains several overlapped bands, making interpretation difficult. The 1230 cm^{-1} band includes contributions from asymmetric phosphate stretching, the amide III band and sulfate stretching of sulfated glucosaminoglycans. The band at 1080 cm^{-1} contains contributions from symmetric phosphate stretching and various sugar ring modes. The phosphate stretch bands arise from phospholipids and nucleic acids. Therefore interpretation of this region is complicated by the overlap between the various bands.

In the 3-day post-surgery wound tissue, the distinct collagen amide III profile (which includes bands at 1338, 1282 and 1204 cm^{-1}) is absent or very weak and the symmetric phosphate stretching/sugar band has a distinct peak maximum at 1084 cm^{-1} (Figure 11.1, pink spectrum). The spectra of regions near degenerating muscle of 21-day post-surgery tissue are similar to those of the 3-day post-surgery tissue (Figure 11.1, red spectrum). IR spectra of 21-day post-surgery developing scar tissue (which has a grainy or granular appearance) show the collagen amide III profile, while the symmetric phosphate stretching/sugar band still has a distinct maximum at 1084 cm^{-1} (Figure 11.1, green spectrum). Fibrous-looking scar in the 21-day post-surgery samples display the collagen amide III profile, and there are now two maxima, at 1082 and 1032 cm^{-1}, in the symmetric phosphate stretch/sugar band (Figure 11.1, blue spectrum). This spectrum resembles the spectrum of isolated collagen (Figure 11.1, black spectrum).

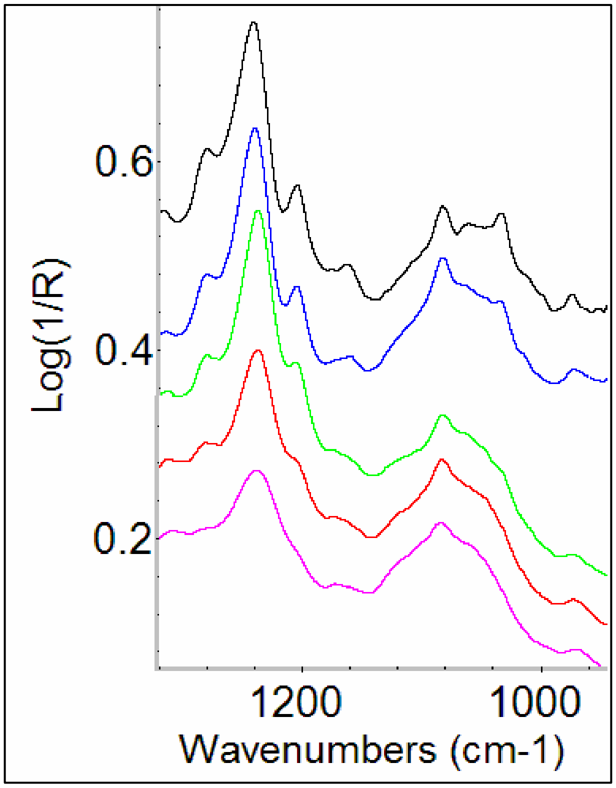

Figure 11.1. The phosphate stretch region of scar tissue IR spectra. The IR spectrum of 3-day post-surgery wound tissue (pink). Spectra of tissue next to degenerating muscle (red), developing scar tissue (green), and fibrous scar tissue (blue) of 21-day post-surgery scar tissue. The spectrum of isolated type I collagen (black).

11.1.2. Amide I Band

There are also differences in the shape of the amide I bands for the scar tissue at different stages of development. Examples are shown in Figure 11.2, however the amide I peak maximum varies by as much as 20 cm^{-1} in each group. In 3-day post-surgery tissue, 21-day post-surgery tissue next to degenerating muscle fibers and 21-day post-surgery developing scar tissue, the amide I band maximum ranged from 1662 to 1649 cm^{-1}. Generally, the more intense the bands at 1080 cm^{-1} and 1239 cm^{-1}, the further the amide I maximum was shifted to higher wavenumbers. The spectra with the lowest absorbance in these bands showed a distinct profile with a maximum of 1652 to 1649 cm^{-1} and a shoulder at 1637 cm^{-1}. The amide I band of fibrous scar often had an amide I maximum at 1666 to 1662 cm^{-1}, with a shoulder at 1637 cm^{-1} (Figure 11.2, blue spectrum), very similar to the amide I of isolated collagen fibrils (Figure 11.2, black spectrum). This indicates that changes in the average protein secondary structure take place during scar tissue developments. This may be due to the replacement of the initial hematoma, composed of fibrin and fibronectin, by the scar tissue composed of collagen. Post-translational modifications to the collagen may also be responsible for changes to average protein secondary structure. The changes in the protein composition may be associated with changes in other tissue components, such as proteoglycans or nucleic acids that have absorptions in the phosphate stretch region. Both nucleic acids and proteoglycans also have IR bands in the region of the amide I band, which could affect its shape.

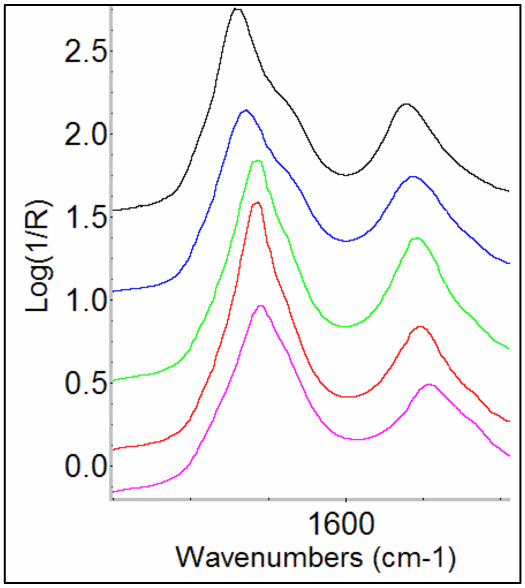

Figure 11.2. The amide I and II bands of scar tissue IR spectra. The IR spectrum of 3-day post-surgery wound tissue (pink). Spectra of tissue next to degenerating muscle (red), developing scar tissue (green), and fibrous scar tissue (blue) of 21-day post-surgery scar tissue. The spectrum of isolated type I collagen (black).

11.1.3. CH Stretch Region

The wound tissue was generally low in lipids, marked by fairly low intensity of the CH stretch bands. The main difference in this region was found between the fibrous scar tissue and all the other tissue types. The CH stretch region contains contributions from the long acyl chains of lipids, as well as the various CH groups found in proteins, sugars and nucleic acids. Only the lipids contain long acyl chains, with a high ratio of CH_2 to CH_3 groups. This is reflected in the IR spectra. When the tissue contains significant amounts of lipids, the asymmetric CH_2 stretch peak at 2922 cm^{-1} is more intense than the asymmetric CH_3 stretch peak at 2956 cm^{-1}. This is seen in the IR spectra of 3-day post-surgery tissue (Figure 11.3, pink spectrum), 21-day post-surgery tissue near necrotic muscle (Figure 11.3, red spectrum) and 21-day post-surgery granular-looking wound tissue (Figure 11.3, green spectrum). The CH stretch profile of 21-day post-surgery fibrous scar suggests low lipid levels (Figure 11.3, blue spectrum), as the intensity of the CH_2 and CH_3 bands is very similar. The CH stretch region of fibrous scar most closely resembles the profile of pure collagen (Figure 11.3, black spectrum).

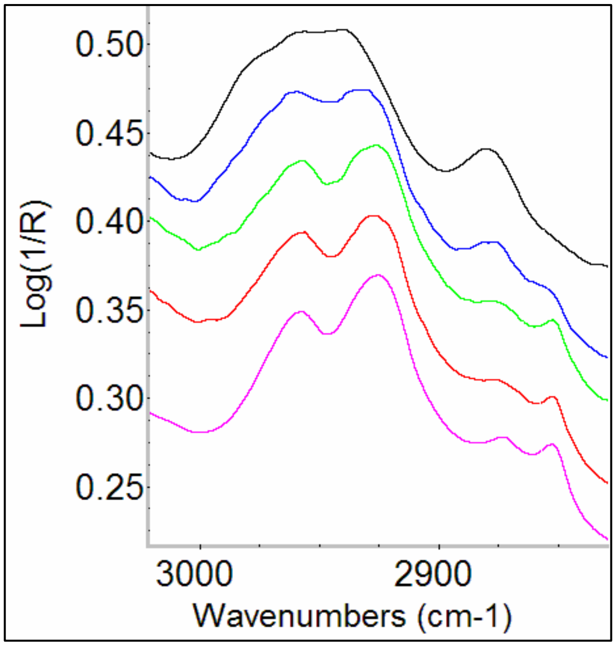

Figure 11.3. The CH stretch region of scar tissue IR spectra. The IR spectrum of 3-day post-surgery wound tissue (pink). Spectra of tissue next to degenerating muscle (red), developing scar tissue (green), and fibrous scar tissue (blue) of 21-day post-surgery scar tissue. The spectrum of isolated type I collagen (black).

11.2. IR Spectra Reflect the Molecular Composition of Scar Tissue

The IR spectra of scar tissue at all ages are dominated by the absorptions of proteins. The amide I band is usually the strongest absorption, followed by the amide II. The levels of lipids in wound tissue are also low, indicated by the low absorbance in the CH stretch region and an extremely weak C=O band at 1740 cm^{-1}. The main function of lipids in wound tissue is as cellular membranes; therefore the higher the lipid levels, the higher the cellularity of the wound tissue. Other bands of interest include the amide III/asymmetric phosphate stretch band at 1239 cm^{-1} and the sugar/symmetric phosphate stretch band at 1084 cm^{-1}. Because these bands arise from the overlap of different components, they can be difficult to interpret.

The IR spectra of 3-day post-surgery wound tissue (Figures 10.4) show that it is rich in proteins. However, the series of peaks at 1318, 1282 and 1204 cm^{-1} specific for collagen is absent or very weak, indicating that collagen is not a major component of scar at this time-point. The symmetric phosphate stretch/sugar band is broad, with a prominent maximum at 1084 cm^{-1}. The interpretation of this band is difficult, as many molecules have absorbances in this region. As the intensity of the asymmetric phosphate stretch band at 1239 cm^{-1} increases with the 1084 cm^{-1} band (for example, see Figure 10.5), the amount of phosphate-containing molecules must be increasing. Phosphate-containing molecules include phospholipids that make up the cell membranes, as well as nucleotides like DNA and RNA. As the lipid levels of wound tissue are low (indicted by the low absorbance in the CH stretch region and the extremely weak C=O band at 1740 cm^{-1}), most of this intensity can be attributed to the nucleic acids and/or proteoglycans. The profile of the symmetric phosphate stretch band, with the characteristic maximum at 1084 cm^{-1} above the broad band resembles that of RNA (Boydston-White et al, 1999). The development of scar tissue is associated with high levels of protein synthesis and therefore transcription; RNA levels are expected to be high. The increased intensity in these bands is also due to proteoglycans, as the ring modes of sugars absorb between 1200 to 900 cm^{-1} (and will therefore overlap with the symmetric phosphate stretch band), while the sulfate groups of the sulfated proteoglycans absorb at around 1245 cm^{-1} (and will overlap with the asymmetric phosphate stretch and amide III band) (Donoff et al, 1984; Longas & Garg, 1992).

The spectra of 21-day post-surgery wound tissue are more variable than those of the 3-day post-surgery wound tissue, in agreement with the greater morphological variability of the older scar tissue. There are regions next to degenerating muscle fibers whose spectra are very similar to those of the 3-day post-surgery scar tissue (Figure 10.14), indicating an early stage of scar tissue development. The IR spectra of these regions indicate that collagen is absent or very low.

The 21-day post-surgery tissue also contains grainy-looking regions of scar, which appear to correspond to granulation tissue, an intermediate stage in scar development (Figure 10.8). The IR spectra of granulation tissue are marked by the presence of the series of bands in the amide III region attributable to collagen. The intensity of the amide III band centered at 1238 cm^{-1} is increased, as the amide III of collagen is more intense than the amide III of other proteins, for which it is usually very weak. The symmetric phosphate stretch/sugar band is broad, but has a prominent maximum at 1084 cm^{-1}. This can again be interpreted as high levels of sugars and/or nucleic acids, as the levels of protein synthesis and the amount of proteoglycans in the wound are expected to be high. The levels of lipids (as indicated by the shape of the CH stretch peaks) are low, but still detectable, as the developing scar tissue is still highly cellular due to the presence of collagen-secreting fibroblasts and other cells associated with the wound healing process.

21-day post-surgery wound tissue also contains fibrous looking regions that correspond to the most mature scar tissue (Figure 10.12). The IR spectra of the fibrous scar tissue indicate that it is composed of high levels of collagen. The shape of the amide I band is very similar to the amide I band of isolated type 1 collagen, with a maximum at 1664 cm^{-1} and a shoulder between 1640 and 1630 cm^{-1}. The amide III region shows prominent absorptions at 1318, 1282 and 1204 cm^{-1}, typical of collagen. The symmetric phosphate stretch/sugar band has two maxima, at 1082 and 1032 cm^{-1}. These bands are observed in isolated type I collagen, and are most likely due to collagen glycosylation. Examination of the CH stretch region indicates that lipids, and therefore cell membranes, are very low. This is in agreement with the low cellularity of mature scar tissue.

Hierarchical cluster analysis revealed that the shape of the amide I band changes with the intensity of the bands at 1080 and 1239 cm^{-1}. Generally, the more intense these bands, the more the amide I band is shifted to higher wavenumbers (Figure 10.17). However, it is extremely difficult to interpret changes in the amide I band for such complex samples like wound tissue. The changes to the amide I band could reflect changes in the secondary structure of the protein with changes in the proteoglycan or nucleic acid levels, as well as increasing amounts of collagen in the scar tissue. However, both proteoglycans and nucleic acids have absorptions in the amide I band region, so that changes in the concentration of these components could alter the shape of the amide I band.

Hierarchical cluster analysis was found to be very useful for processing this data. The results of this study show that a variety of approaches are needed to analyze the IR microspectroscopy data from complex biological samples. Univariate analysis, employing either peak heights or areas, can be affected by changes in the thickness or density of samples. Bivariate analysis does not suffer from this problem, but when spectral regions are due to the overlap of bands from several different components, analysis of the data is difficult. Hierarchical cluster analysis can take differences in the shapes of bands into account. It can also simplify the data and reveal relationships between bands.

11.3. IR Spectra Can be Related to the Stages of Wound Healing

The differences between IR spectra from 3 and 21-day post-surgery tissue can be interpreted in terms of the changes in composition of wound tissue that take place during healing. At 3 days post-surgery, the scar is in the inflammatory phase, although the granulation phase is just beginning. At this stage, the wound tissue is composed of proteins like fibrin and fibronectin, and proteoglycans like dermatan sulfate and hyaluronan; collagen synthesis is starting (Monaco & Lawrence, 2003; Diegelmann & Evans, 2004). The IR spectra indicate that the wound at this stage is protein rich, but collagen is low or absent. The cellularity of the wound is expected to be high, as inflammatory cells and fibroblasts are found throughout the wound matrix (O’Leary et al, 2002). High cellularity is associated with high levels of phospholipid cell membranes, reflected in the CH stretch region of the spectrum.

The 21-day post-surgery sections are composed of tissue at the granulation and remodeling phases. The spectra of this tissue indicated the presence of collagen. Granulation tissue is composed predominantly of type III collagen, but also includes other proteins and proteoglycans (Diegelmann & Evans, 2004).

During the remodeling phase, the granulation tissue is replaced with mature scar, as the collagen matrix is cross-linked and rearranged into large bundles, arranged in a parallel pattern (O'Leary et al, 2002; Diegelmann & Evans, 2004). The spectra of fibrous scar tissue have prominent collagen absorptions, which would be expected as collagen makes up 50 % of the protein in mature scar (Monaco & Lawrence, 2003). The mature scar is very low in lipid. As the scar tissue matures, the number of cells is reduced by apoptosis during the remodeling phase (Monaco & Lawrence, 2003). The levels of lipids, and therefore cell membranes, in the mature scar tissue are therefore very low. In a rat laminectomy model similar to the one in this study, the number of inflammatory cells and fibroblasts peaks at 8 days post-surgery, and starts to decrease 15 days after surgery (He et al, 1995).

11.4 OTC and Quercetin-treated Scar Tissue

The spectra of both 3-day and 21-day post-surgery tissue treated with OTC and quercetin are very similar to those of control tissue. Generally, collagen is absent in the 3-day post-surgery tissue and present in the 21-day post-surgery tissue. The differences to the scar tissue caused by these compounds may be too subtle to be visible by IR microspectroscopy. The morphological, and therefore spectral, heterogeneity of the 21-day post-surgery scar tissue makes statistical analysis impractical. Although every attempt was made to sample similar regions in each sample, this was difficult as the majority of the staining and immunohistochemistry had not yet been performed by our colleagues at the time of data collection. Any statistical results obtained from the IR data (such as the number of pixels with high collagen) will be affected by the exact areas sampled. The slow pace of IR data collection limits the amount of data that can be collected, and just a small percentage of each scar tissue section is mapped. Examination of 63-day post-surgery tissue (not part of this thesis) may reveal differences between the treatment groups that become more obvious at the later time-point. However, examination of the tissue sections in the treated animals seems to suggest that the area of scar tissue 21 days post-surgery is smaller in both the quercetin and OTC-treated rats than in the saline treated controls, where the scar spreads significantly beyond the early site of injury. This suggests that the anti-oxidants may alter the extent, but not the composition of the scar tissue. Before conclusions can be made about the efficacy of OTC and quercetin in the prevention of fibrosis, the tissue at the last time point (63 days post-surgery) needs to be analyzed and the IR data correlated with the results of histochemistry, immunostaining and *in situ* hybridization. However this is beyond the scope of the initial analysis presented in this thesis.

11.5. Effect of Polarized Synchrotron Light on Oriented Samples

The main advantage of synchrotron IR light is that, due to its very high brightness, diffraction-limited spatial resolution can be reached (Carr et al, 1995). A much less well-known feature of synchrotron IR light is that it is plane-polarized. This is not an issue when the samples are randomly oriented. However, if the plane-polarized light interacts with oriented samples, the band intensities will be a function of the relative orientation between the oriented molecules in the sample and the plane of the light.

The development of scar tissue is associated with the formation of large bundles of collagen, arranged in a parallel pattern (O'Leary et al, 2002). Therefore, when spectra of mature scar are collected with IR light, polarization effects become important, and intensities of dichroic bands will change depending on their orientation with respect to the plane of the light. The potential advantage of this is that additional structural information can be obtained about the sample. However, with complex biological samples like scar tissue, the fibril orientation will depend on the way in which the sample is sectioned and placed on the slide relative to the synchrotron light, which makes comparison between different samples difficult. When the intensities of bands are altered because of their interactions with plane-polarized light, the results of spectral images created using peak heights or areas of dichroic bands cannot be trusted. Therefore, if the samples are highly oriented and quantitation is required, non-dichroic bands should be used or the data should be collected with non-polarized light from a globar source.

Collagen is the main structural protein in animal tissues, where it is often highly oriented. Thus, when collagen-containing tissues are studied with synchrotron light, the effect of polarization cannot be ignored, especially when peak heights or areas are used to image the relative distribution of tissue components. If changes to the relative intensities of amide bands are seen in spectra from scar tissue or other collagen-containing samples, then the oriented nature of collagen in the sample can be revealed.

Chapter 12. Scar Tissue Study Conclusions

The analysis of the initial scar tissue data presented in this thesis shows that synchrotron IR microspectroscopy can be used to monitor changes in the composition of scar tissue sections that take place during wound healing. The molecular changes detected by IR spectroscopy correspond well with what is known about scar tissue development. The main difference between the 3 and 21-day post-surgery tissue was in the presence of collagen in the latter. Collagen was absent or barely detectable in the 3-day post-surgery wound tissue. This tissue was rich in nucleic acids, as scar tissue development is accompanied by a high rate of protein synthesis and therefore transcription. Sugar levels were also elevated as the wound healing matrix contains high levels of proteoglycans. The 21-day post-surgery scar tissue contained wound healing tissue at various stages of development. Some regions, especially those close to degenerating muscle, had IR spectra similar to those of 3-day post-surgery wound tissue, indicating that they were in an early stage of scar tissue development. Other regions were at an intermediate stage, containing significant levels of collagen, sugars and nucleic acids. There were also regions of developed scar tissue. The IR spectra of this tissue indicated the high percentage of collagen. Unlike the other types of tissue, which contained low but detectable lipid levels, fibrous scar tissue was practically free of lipids. This was interpreted as being due to decreased cellularity of the developing scar, as scar maturation is accompanied by apoptosis of the inflammatory cells and fibroblasts that are found in large numbers in wound tissue.

The analysis of IR data at the two earliest time points (3 and 21 days post-surgery) is not enough to tell whether OTC and quercetin are affecting the scar tissue composition. The results of further studies (IR analysis of 63-day post-surgery tissue, histochemistry, immunostaining, and *in situ* hybridization) need to be completed first.

Synchrotron light is intrinsically plane-polarized. This can affect the relative intensities of dichroic bands in highly oriented the samples. This was found for the fibrous scar from 21-day post-surgery scar tissue that contained significant amounts of oriented, highly fibrillar collagen. The changes in the relative intensities of the amide bands of fibrillar collagen may be used to monitor the relative collagen orientation in the tissue section. However, as the intensities of the amide bands are affected by the relative orientation between the sample and plane-polarized synchrotron light, care must be taken when interpreting the data from tissue samples with large amounts of fibrillar collagen.

Chapter 13. Summary and Future Work

13.1. Summary

In this thesis, synchrotron IR microspectroscopy was used to study biological tissues. The presented research demonstrates that the molecular and conformational information available from IR microspectroscopy can provide new insights into pathological processes such as Alzheimer's disease and scar tissue formation.

The samples studied included brain tissue from a transgenic mouse model of AD and scar tissue at various stages of development from a rat laminectomy model. The function and therefore composition of these tissues is very different, and this is reflected in their spectra. Nervous system tissue, such as brain, is composed of neurons and glial cells and their processes. Many of these neuronal processes are myelinated. Brain tissue is therefore very rich in lipid. Scar tissue, on the other hand, is lipid-poor, but has a high content of the structural protein collagen.

IR spectra contain a large amount of chemical and conformational information. However, the composition of tissue samples is very complex and there is significant overlap between spectral features arising from the proteins, lipids, nucleic acids, and carbohydrates that make up the sample. Several approaches were used in order to display the information available in the spectral maps as false-color images that could be correlated with tissue morphology. They included univariate and bivariate methods, based on peak heights or areas, and theirs ratios. A multivariate method, hierarchical cluster analysis, was used as well.

The same approach was used for analyzing the data from both projects. The first step in data analysis was to view each of the spectra in the IR maps. This allowed bad data and spectral artifacts to be identified. Spectral maps based on the heights or areas of peaks of interest (whose assignments were known from the literature) were then created. The exact peak regions selected for each analysis were found through trial and error in order to best represent the spectral variability of the map. For this reason, the precise methods used for the brain tissue (Table 3.1) and the scar tissue (Table 9.1) were different. The display limits or the numerical values of the peak height, area, or their ratio, represented by a particular color in the map, were selected so that the range would work well for each of the maps. However, at times, the display limits had to be adjusted for a particular map. IR microspectroscopy is a semi-quantitative method, as the exact sample thickness is not known. The data was collected at two different synchrotrons, which operate at different energies. As well, the signal at the synchrotron decays with time following the injection of electrons into the ring (generally performed several times a day). These factors will all affect the data. Therefore, the color scale for each map represents the relative differences in band intensities across the map. Any comparison between different maps is only semi-quantitative. However, the chemical information about the sample is very useful.

Hierarchical cluster analysis was found to be the most useful multivariate method of all the methods available in the Atlμs and Cytospec software, which included principal components analysis, k-means clustering, and fuzzy c-means clustering. This method was not only the most straight forward, but also seemed to give the best differentiation of the data into groups that corresponded to sample morphology. Cluster analysis was found to be a very useful method of analyzing the data from both brain and scar tissue. In this method, the user selects the region (or regions) of the spectrum, and the software organizes the data into hierarchical clusters, based on the similarity in that spectral region. The user then decides how many clusters to use, and the map pixels with spectra belonging to the same group are represented with the same color. An average spectrum for each cluster is also generated. The main disadvantage is that the method is applied to one map at a time and the user has to decide how many clusters to use for each map, thus it is a subjective process. This makes direct comparison between different maps difficult. As well, the exact spectral region selected will affect the results. The advantage of cluster analysis is that it is objective and does not require any previous knowledge about the assignment of the spectral peaks, aside from the choice of spectral region used in the classification. The software can find patterns in the data, such as spectral features that tend to co-localize. The data is greatly simplified by hierarchical cluster analysis, as generally between 3 and 5 clusters were found to be sufficient to display the main features of the IR maps in this study. The resulting average spectra can then be examined and interpreted in more detail. This is therefore a very good method for exploratory data analysis.

IR microspectroscopy provides spatially resolved molecular information from thin tissue sections. It is therefore very complementary to histochemistry and immunostaining. These methods use a chemical or biological probe in order to study tissue composition and morphology. As both techniques require thin tissue sections, both can be applied to either serial sections or, in some instances, the sample can be stained following IR analysis. The false-color maps that visualize some aspect of the IR data can be correlated with the results of staining. For example, in both of the studies in this thesis, H&E staining was used to visualize sample morphology. In the AD study, plaques were visualized with anti-Aβ antibodies, which revealed the presence of Aβ peptide in the tissue regardless of its conformation, and with Congo red staining, which revealed the presence of aggregated amyloid. The results were then correlated with the IR data. In the scar tissue study, sections serial to those that were IR mapped will be stained with various stains, antibodies, and cDNA probes by our collaborators in order to help with the interpretation of the IR data (not discussed in this thesis).

Although the IR spectra of tissue samples look quite simple, they result from the contributions of all the molecules found in the sample. Each peak is the result of the overlap of many different components. For example, the spectral region from 1300 to 1000 cm^{-1} can be quite difficult to interpret. This region contains the asymmetric and symmetric phosphate stretch bands, which arise from the phosphate groups of phospholipids and nucleic acids (as well as any other phosphorylated molecules). The asymmetric phosphate stretch is found at approximately 1230 cm^{-1}, and is overlapped with the amide III band of proteins and sulfate stretching of sulfated glycosaminoglycans. The symmetric phosphate stretch band is found at around 1080 cm^{-1} and is overlapped with various sugar ring modes, due to the sugar residues of nucleic acids, glycosaminoglycans, and glycosylated proteins. Interpreting spectral changes in this region is therefore very difficult. However, spectral changes in this highly-overlapped region can be interpreted by examining the whole spectrum and looking for associated changes in other bands. In brain, an increase in intensity of the bands at 1230 and 1080 cm^{-1} was always associated with an increase in the CH stretch bands (3000 to 2800 cm^{-1}), as well as the C=O stretch band (1740 cm^{-1}), and the CH deformation band at 1466 cm^{-1}. All of these bands arise from phospholipids. The increase in the intensity of the 1230 and

1080 cm^{-1} bands found around plaque cores was therefore clearly due to increased levels of phospholipids. In the scar tissue, the intensities of the CH stretch, C=O stretch, and CH deformation bands were low, but the bands at 1230 and 1080 cm^{-1} had increased intensity in many mapped regions. The increased intensity of these bands is not due to phospholipids, as other phospholipids bands were low. In the developing scar tissue, the increased intensity arose from the proteoglycans that form the wound healing matrix and the phosphate stretching modes of nucleic acids. In the mature fibrous scar tissue, the 1230 cm^{-1} band often had high intensity, while the 1080 cm^{-1} band had two maxima at 1082 and 1032 cm^{-1}. This was always found in spectra that also had a series of peaks at 1338, 1282 and 1204 cm^{-1}, which are specific for collagen. The increased intensity of the 1230 cm^{-1} band was also due to collagen, as its amide III band is more intense than the amide III of other proteins.

Although IR microspectroscopy is a semi-quantitative methods and the interpretation of IR spectra is complicated by the overlap between peaks from different components, significant and useful information about biological samples can be obtained. IR microspectroscopy allows information about the functional group composition and average protein conformation to be obtained *in situ* from unstained tissue sections. IR microspectroscopy of brain tissue from the TgCRND8 mouse confirmed that dense-cored plaques are composed of highly aggregated β-sheet, while no IR-detectable compositional or conformational changes are associated with diffuse plaques. IR microspectroscopy provided direct physical evidence of elevated phospholipids around plaque cores. IR microspectroscopy was central to the discovery of the focally-elevated deposits in transgenic mouse brain. As the sample preparation is minimal, these deposits were not removed and the identity of creatine could be unambiguously confirmed by its characteristic IR spectrum. IR microspectroscopy was also useful for monitoring the molecular changes that take place during scar tissue development. The polarized nature of synchrotron light was shown to affect the spectra from oriented samples such as collagen fibrils in maturing scar tissue.

13.2. Future Work

13.2.1. Alzheimer's Disease Project

It would be useful to extend the work done on plaques in the TgCRND8 mouse model to human AD tissue. Some *in situ* IR data on human dense-cored plaques has been presented in the literature (Choo et al, 1996; Ogg, 2002; Miller et al, 2006). However, in all of these studies data analysis was restricted to the amide bands, which provide information about protein secondary structure. It would be interesting to see whether there is an elevation of phospholipids associated with human dense-cored plaques, similar to that seen in the TgCRND8 mouse. As well, there are no reported IR studies of diffuse plaques in human brain. IR map data could therefore be collected on diffuse plaques in human AD brain, using the anti-Aβ serial staining protocol developed in this thesis. As diffuse plaques are often found in cognitively-normal aged individuals (Selkoe, 2001), as well as in AD patients, a comparison of IR data from the two groups could be interesting.

In this thesis, the IR mapped plaques were mostly present in the grey matter. However, TgCRND8 mice also have dense-cored plaques in the white matter (Belluci et al, 2006). These plaques are accompanied by demyelination, a loss of the lipid-rich myelin sheet (Belluci et al, 2006). As lipids have distinct peaks in IR spectra, IR mapping could be used to study this process.

The presence of focally-elevated Cr deposits in AD tissue was a novel and unexpected discovery. Very little is currently known about these deposits, and they will continue to be investigated in Dr. Gough's research group with a variety of techniques. For example, I proposed IR mapping of corresponding regions in several serial sections of TgCRND8 mouse brain, in order to study the three-dimensional distribution of Cr deposits. This project was undertaken by Meghan Gallant (M. Sc. student in Dr. Gough's laboratory). Other individuals in the group will continue to investigate Cr deposits, in both transgenic AD mice and human brain tissue, with IR microspectroscopy and other methods such as Raman spectroscopy, scanning electron microscopy, and x-ray fluorescence. A combination of technique will hopefully provide further information about the physical nature of the Cr deposits, which may lead to insight into their role in Alzheimer's disease, ageing, and neurodegeneration.

13.2.2. Scar Tissue Project

The scar tissue research presented in this thesis was part of a much larger NSERC CHRP project that has since been taken over by another student in the group (Richard Wiens, Ph. D. student). The data set has since been extended to 63 day post-surgery tissue. The research presented in this thesis demonstrated that changes that take place with scar tissue development may be monitored with IR microspectroscopy, and that the heterogeneity of scar tissue at 21 days post-surgery is responsible for much of the spectral variability seen at that time point. However, there were no spectral differences noted between scar tissue from the OTC, quercetin, and saline-treated rats. Hopefully, the analysis of the 63-day-post-surgery scar tissue may reveal some differences that will indicate the effectiveness of quercetin or OTC in reducing excessive scar tissue development.

Chapter 14. Appendix 1. IR Maps of Dense-cored Plaques

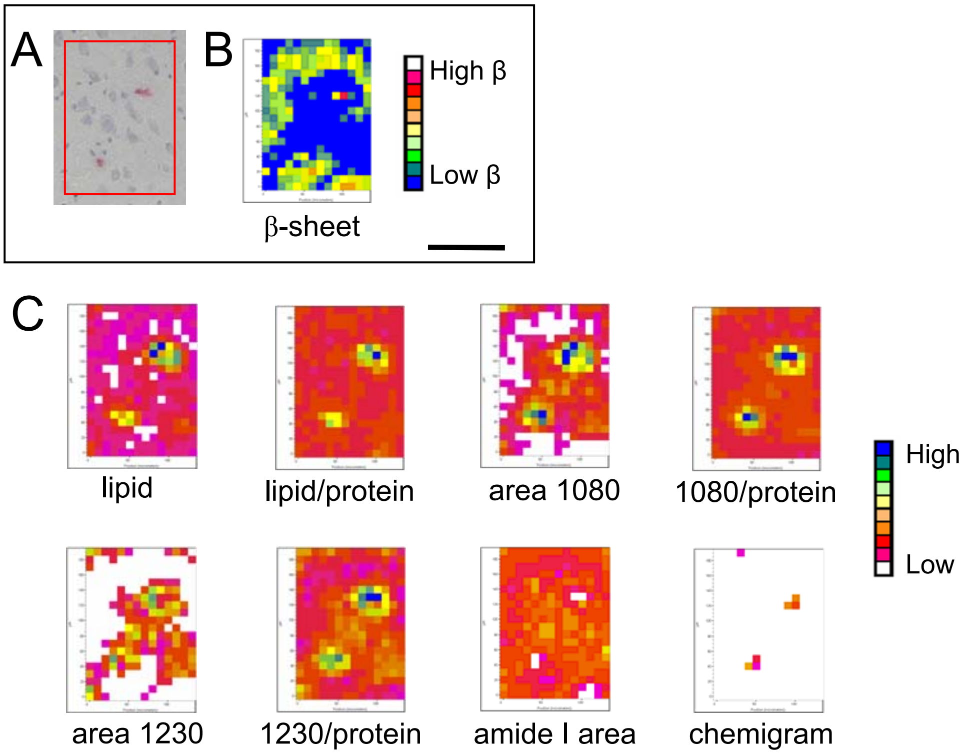

Figure 14.1. Dense-cored plaques from a 5-month-old TgCRND8 mouse. (A) A photomicrograph of the mapped region, stained with Congo red after IR mapping. The two small plaques are located in the hippocampus. (B) The map processed to show elevated β-sheet proteins. (C) The map processed with the methods outlined in Table 3.1. In spite of their small size and the early stage of the disease progress, the plaques are surrounded by elevated phospholipids. Scale bar = 100 μm.

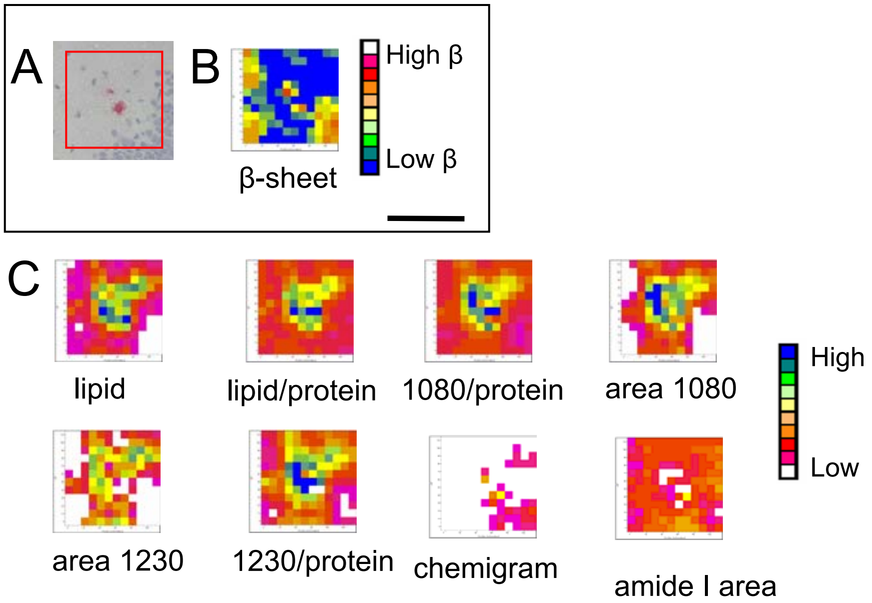

Figure 14.2. Dense-cored plaque from a 5-month-old TgCRND8 mouse. (A) A photomicrograph of the mapped region, stained with Congo red after IR mapping. The plaque is located in the hippocampus, near the dentate gyrus. (B) The map processed to show elevated β-sheet proteins. (C) The map processed with the methods outlined in Table 3.1. Scale bar = 100 μm.

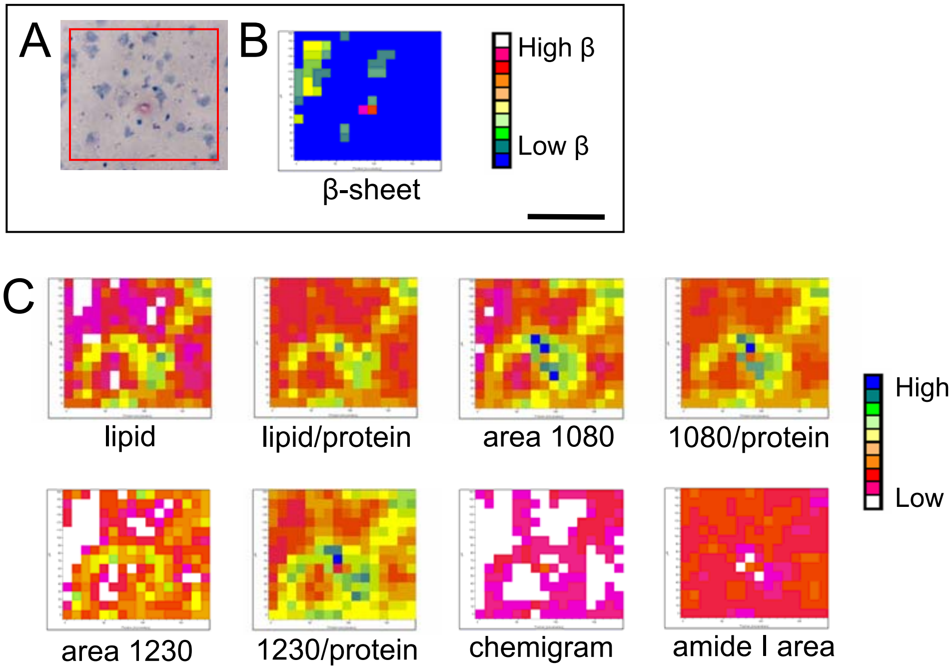

Figure 14.3. Dense-cored plaque from a 5-month-old TgCRND8 mouse. (A) A photomicrograph of the mapped region, stained with Congo red after IR mapping. The mapped region is located in the cortex. (B) The map processed to show elevated β-sheet proteins. (C) The map processed with the methods outlined in Table 3.1. Even though the map has variable phospholipid levels, it is obvious that the plaque is surrounded by elevated phospholipids. Scale bar = 100 μm.

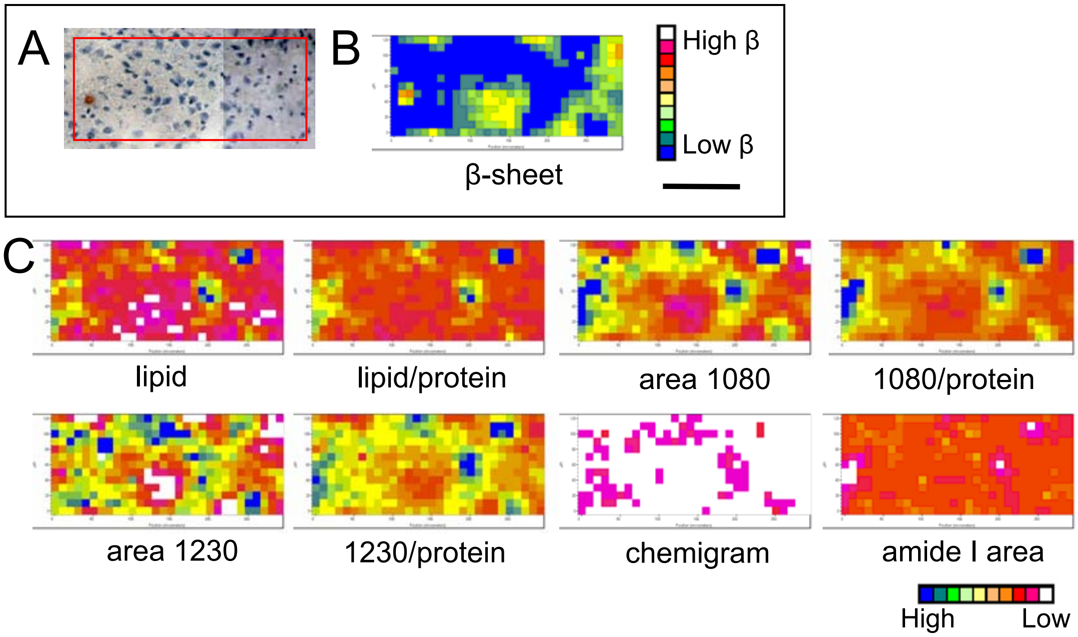

Figure 14.4. Dense-cored plaque from a 5-month-old TgCRND8 mouse. (A) A photomicrograph of the mapped region, stained with Congo red after IR mapping, showing a small plaque in the cortex. (B) The map processed to show elevated β-sheet proteins. (C) The map processed with the methods outlined in Table 3.1. Even though the mapped region has variable levels of phospholipid, the tiny plaque is still surrounded by elevated phospholipids. Scale bar = 100 µm.

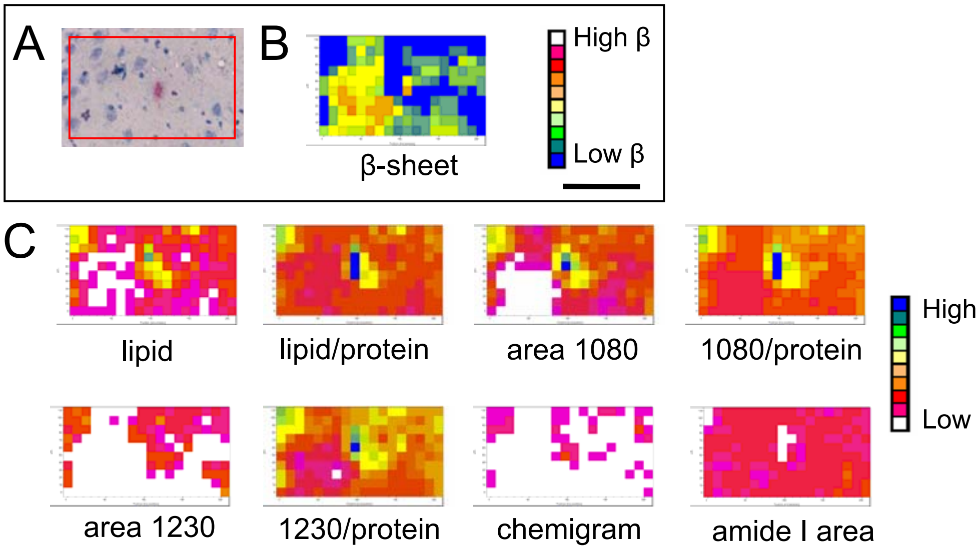

Figure 14.5. Dense-cored plaque from a 5-month-old TgCRND8 mouse. (A) A photomicrograph of the mapped region, stained with Congo red after IR mapping. The plaque is located in the cortex. (B) The map processed to show elevated β-sheet proteins. (C) The map processed with the methods outlined in Table 3.1. Scale bar = 100 µm.

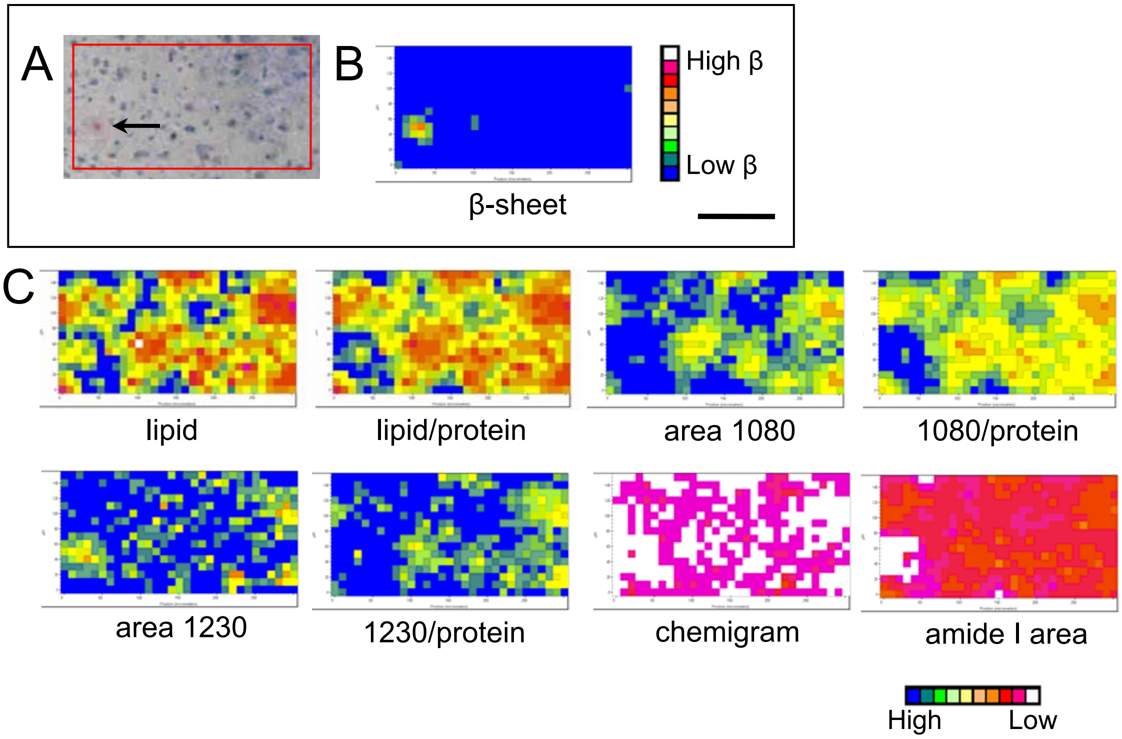

Figure 14.6. Dense-cored plaque from a 5-month-old TgCRND8 mouse. (A) A photomicrograph of the mapped region, stained with Congo red after IR mapping. The mapped region is in the cortex, and contains one small plaque (arrow). (B) The map processed to show elevated β-sheet proteins. (C) The map processed with the methods outlined in Table 3.1. Due to the tiny size of the plaque and the high and variable levels of phospholipids in the map, the elevation of phospholipids around the plaque core is hard to see. Scale bar = 100 μm.

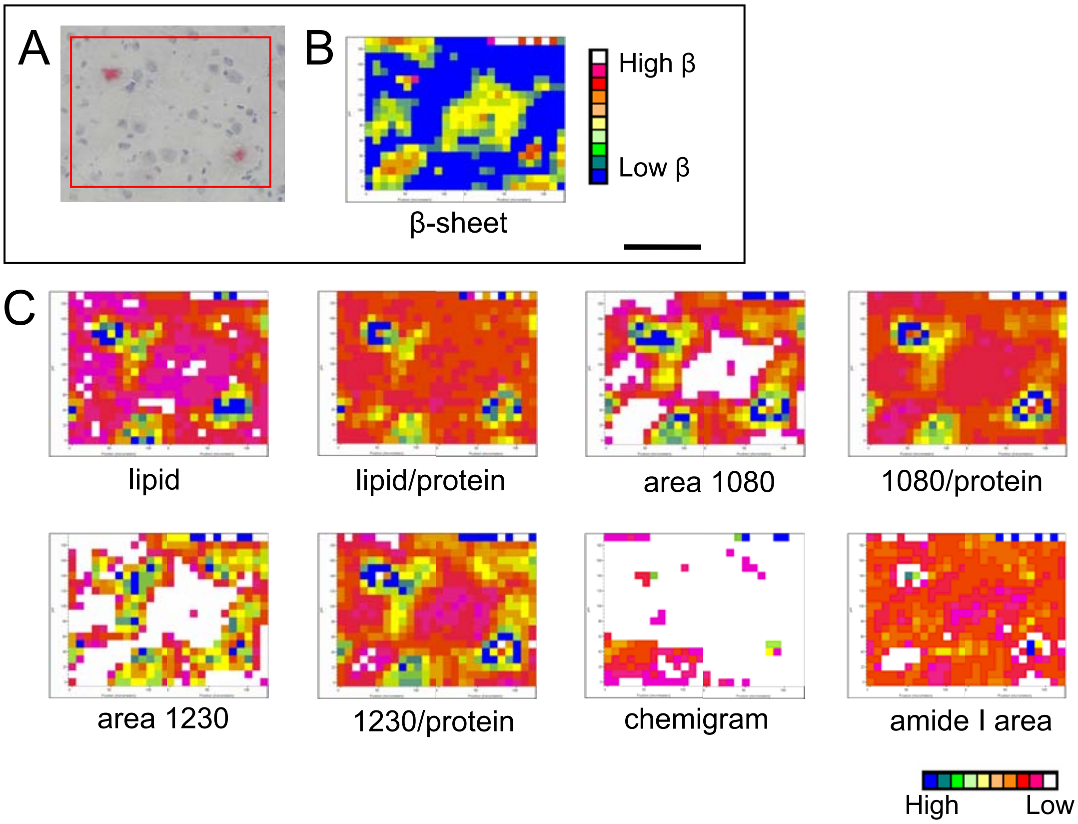

Figure 14.7. Dense-cored plaques from a 5-month-old TgCRND8 mouse. (A) A photomicrograph of the mapped region, stained with Congo red after IR mapping. The two plaques are located in the cortex. (B) The map processed to show elevated β-sheet proteins. There are some non-plaque regions that show up as elevated β-sheet, but examination of the spectra reveals that this is due to a shift to lower wavenumbers of the amide I band rather than to actual aggregated β-sheet indicative of amyloid. (C) The map processed with the methods outlined in Table 3.1. Scale bar = 100 μm.

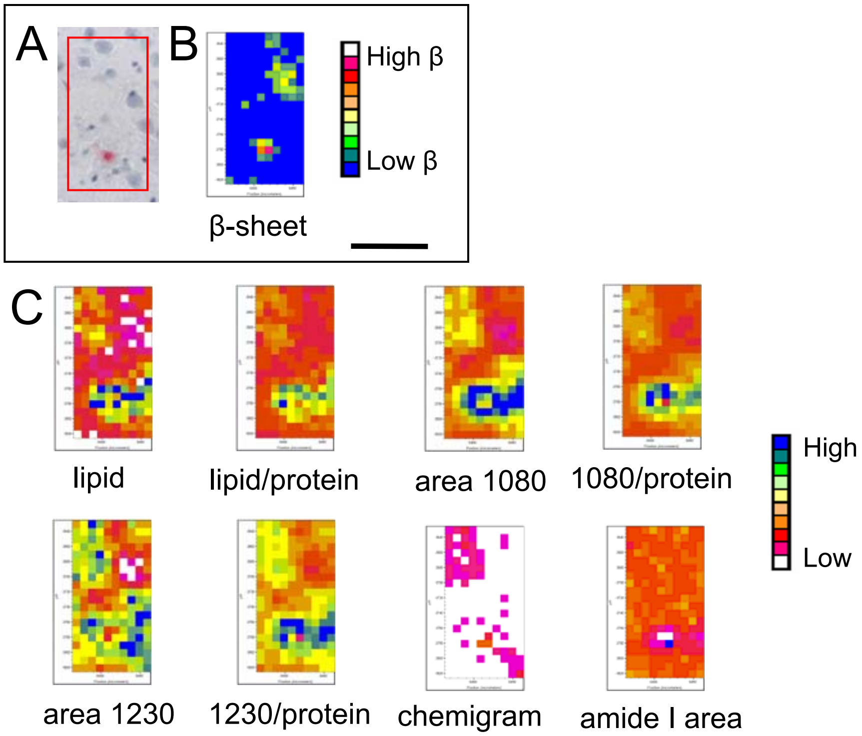

Figure 14.8. Dense-cored plaque from a 5-month-old TgCRND8 mouse. (A) A photomicrograph of the mapped region, stained with Congo red after IR mapping, showing a small plaque in the cortex. (B) The map processed to show elevated β-sheet proteins. (C) The map processed with the methods outlined in Table 3.1. The plaque is surrounded by elevated phospholipids in an uneven pattern. Scale bar = 100 µm.

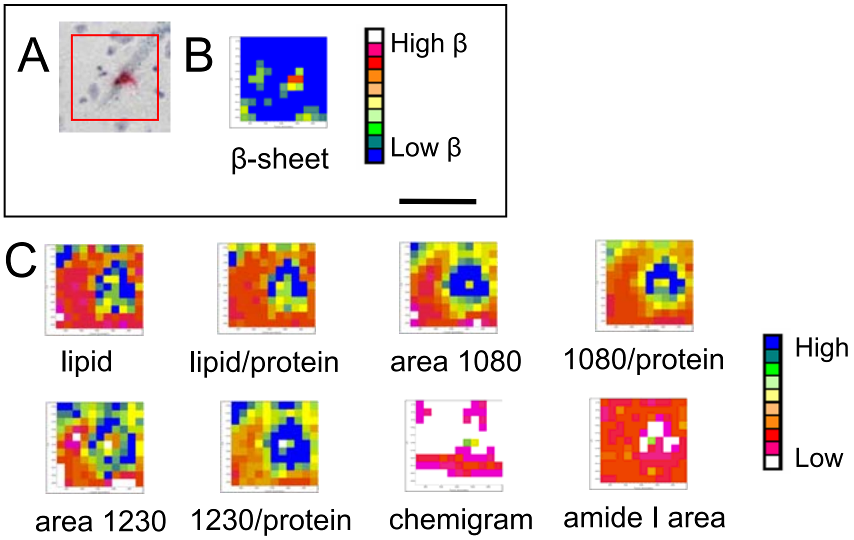

Figure 14.9. Dense-cored plaque from a 5-month-old TgCRND8 mouse. (A) A photomicrograph of the mapped region, stained with Congo red after IR mapping. The plaque is located in the cortex. (B) The map processed to show elevated β-sheet proteins. (C) The map processed with the methods outlined in Table 3.1. Scale bar = 100 µm.

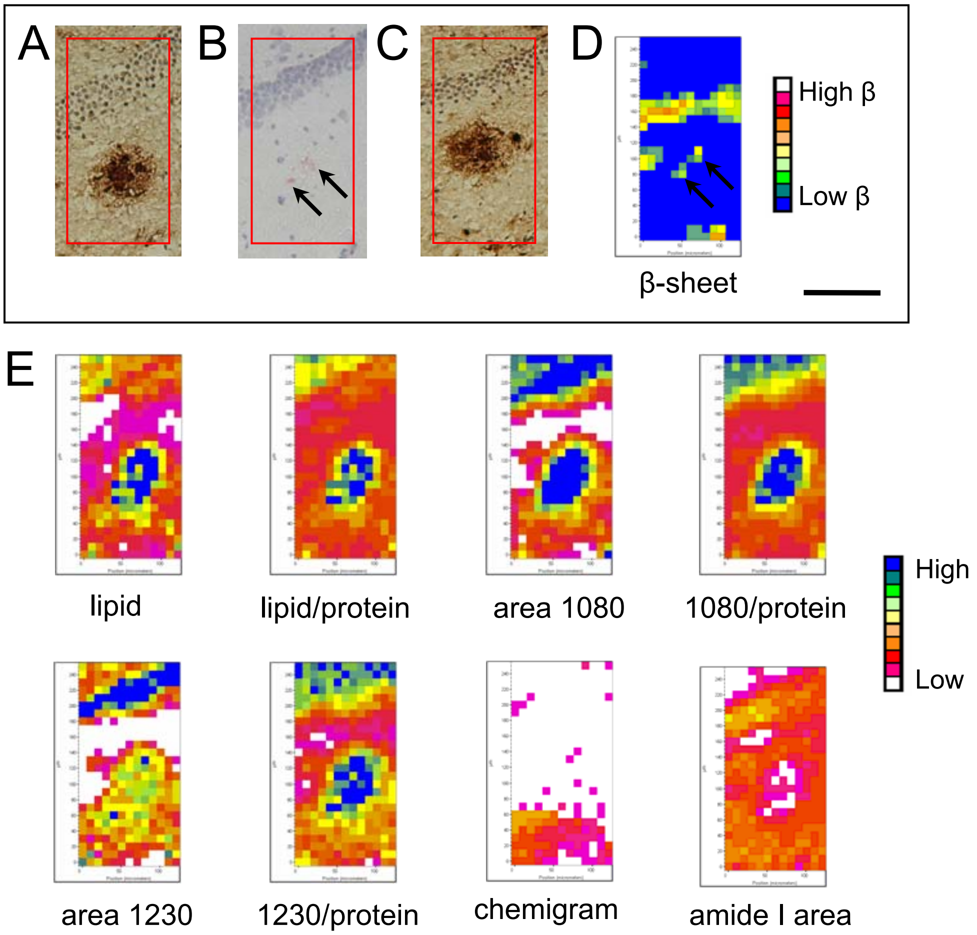

Figure 14.10. Dense-cored plaque from an 11-month-old TgCRND8 mouse. Photomicrographs of (A, C) serial sections immunostained with antibodies against the Aβ-peptide and (B) the mapped region, stained with Congo red after IR mapping. The plaque is found in the hippocampus, near the dentate gyrus. The closely-spaced dentate gyrus neurons are found in the top of the map. The amyloid core is small (arrows in Congo red stained micrograph), but the serial anti-Aβ immunostaining shows a large halo of diffuse amyloid surrounding the core. (D) The map processed to show elevated β-sheet proteins. Aggregated β-sheet (arrows in the β-sheet map) corresponds to the plaque core. The other regions showing elevated β-sheet are just due to a shift in the amide I band. (E) The map processed with the methods outlined in Table 3.1. The plaque core is surrounded by elevated phospholipids in an oval pattern. Scale bar = 100 μm.

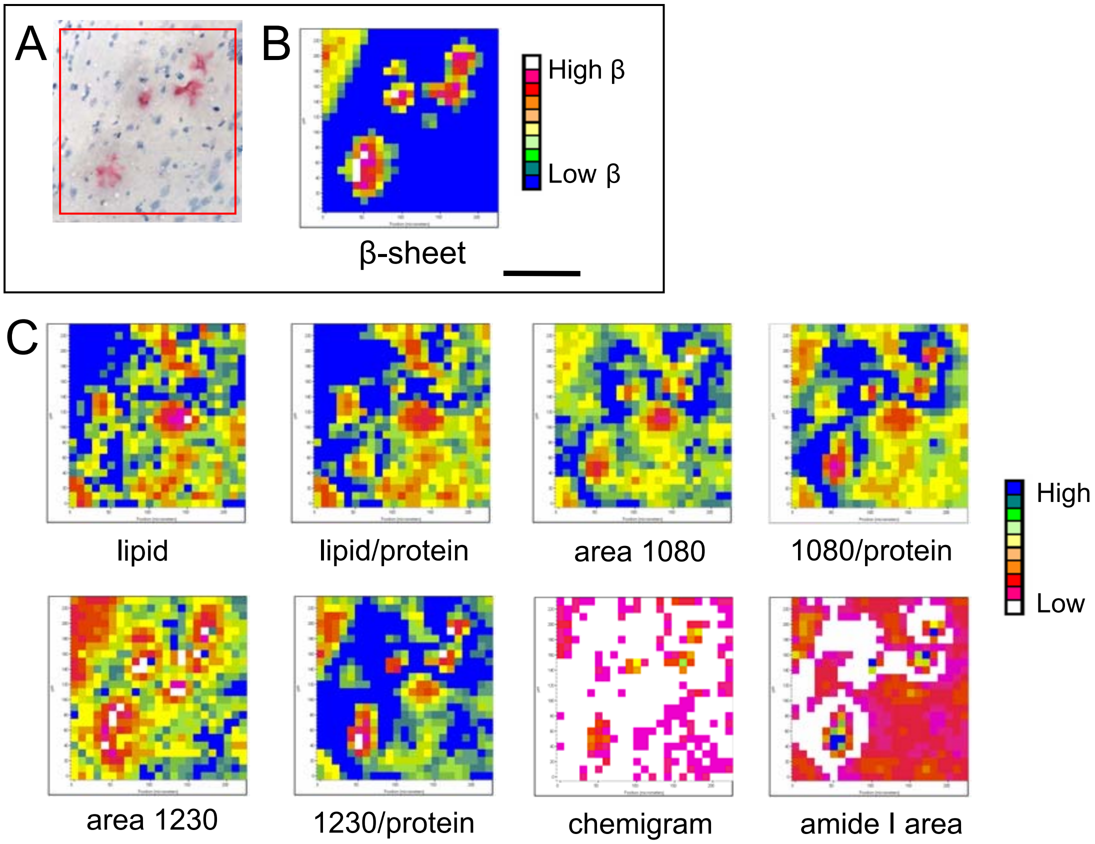

Figure 14.11. Several dense-cored plaques from an 11-month-old TgCRND8 mouse. (A) A photomicrograph of the mapped region, stained with Congo red after IR mapping. The mapped region is in the hippocampus, near the corpus callosum white matter (top left corner). (B) The map processed to show elevated β-sheet proteins. The white matter shows up as having elevated β-sheet, as the amide I bands of white matter are always broader than those of neuropil, and shifted to lower wavenumbers. (C) The map processed with the methods outlined in Table 3.1. The map is high in phospholipids, but they still appear higher around the plaque cores, and low in the cores. Scale bar = 100 µm.

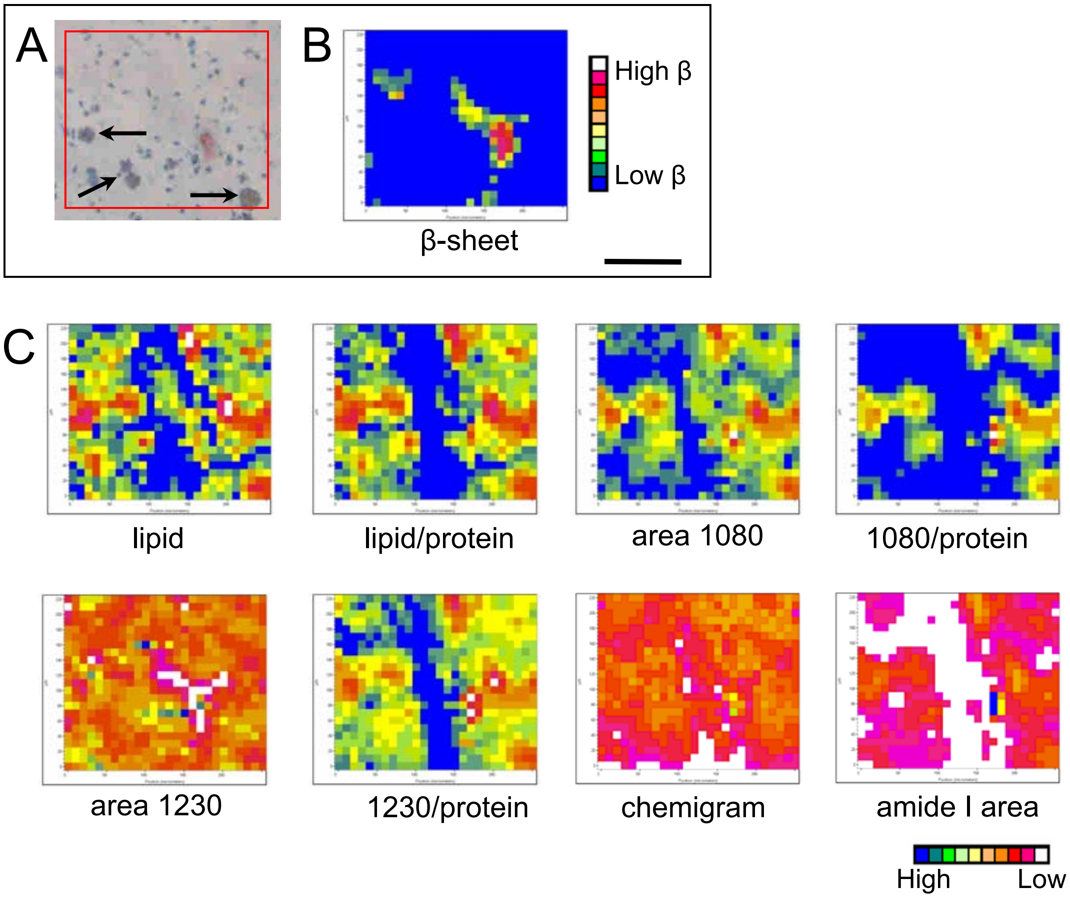

Figure 14.12. A dense-cored plaque from an 11-month-old TgCRND8 mouse. (A) A photomicrograph of the mapped region, stained with Congo red after IR mapping. The plaque is located in the hippocampus, near the molecular layer of the dentate gyrus. (B) The map processed to show elevated β-sheet proteins. (C) The map processed with the methods outlined in Table 3.1. The map is high in phospholipids so no elevation is seen around the plaque core. The objects indicated by arrows are imperfections in the MirrIR slide that occur after staining. Scale bar = 100 μm.

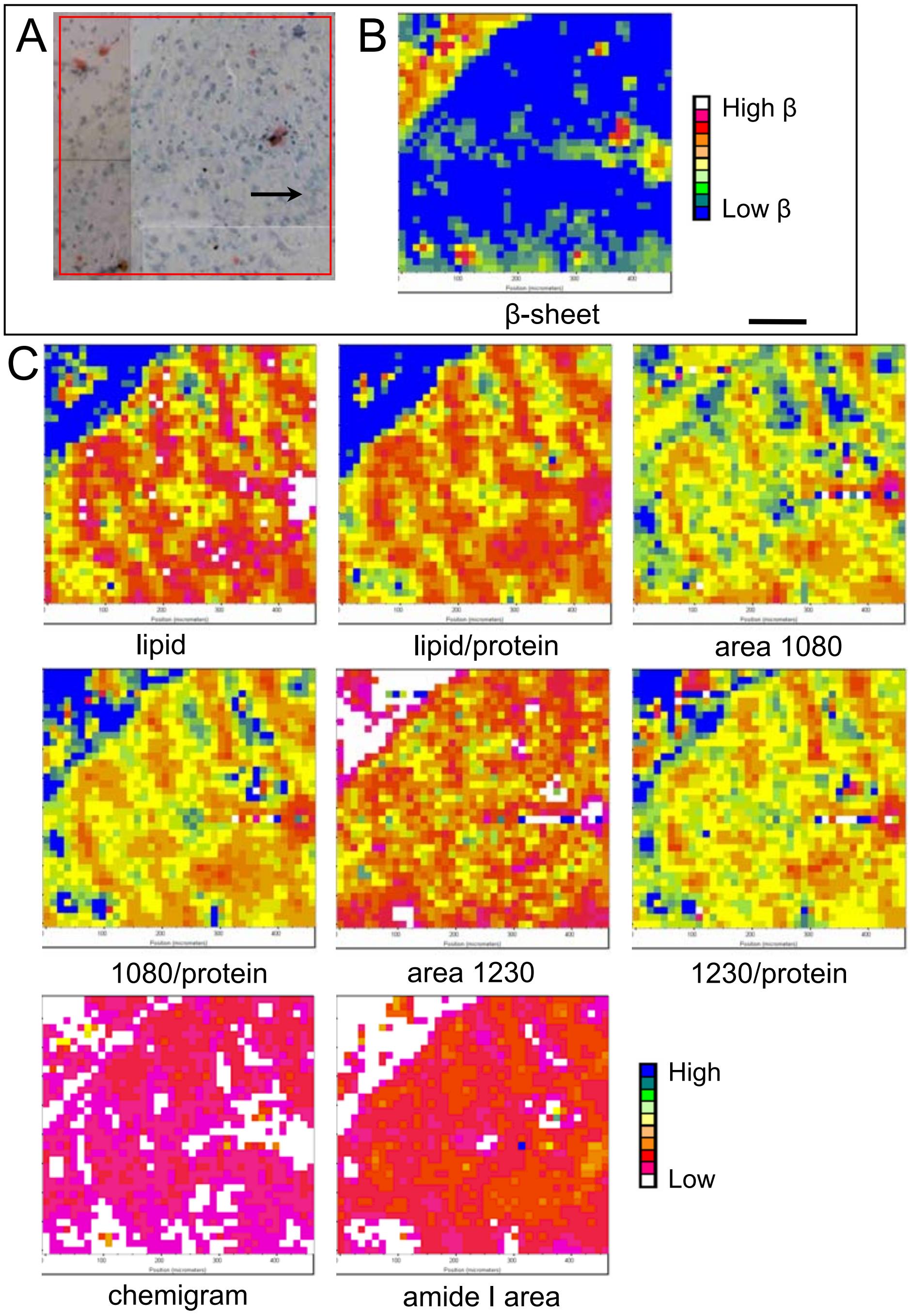

Figure 14.13. Several small dense-cored plaques from an 11-month-old TgCRND8 mouse. (A) A photomicrograph of the mapped region, stained with Congo red after IR mapping. The large map is located in the hippocampus and includes corpus callosum white matter (top left corner) and CA neurons (red arrow), as well as several dense-cored plaques. (B) The map processed to show elevated β-sheet proteins. (C) The map processed with the methods outlined in Table 3.1. The phospholipids levels are variable, but slightly elevated around the plaque cores. Scale bar = 100 μm.

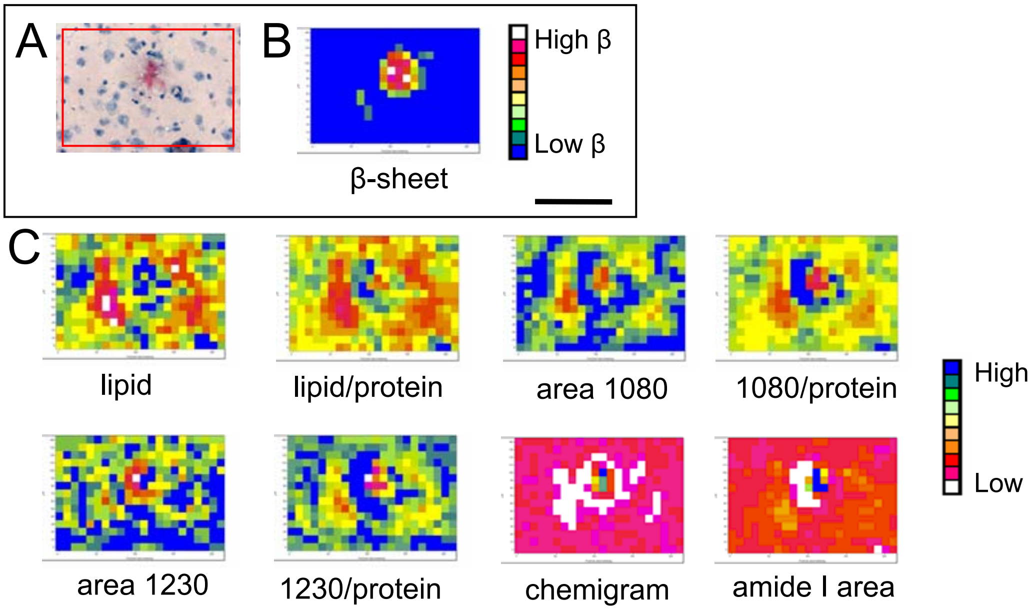

Figure 14.14. A dense-cored plaque from an 11-month-old TgCRND8 mouse. (A) A photomicrograph of the mapped region, stained with Congo red after IR mapping, showing a large single-cored plaque in the cortex. (B) The map processed to show elevated β-sheet proteins. (C) The map processed with the methods outlined in Table 3.1. Scale bar = 100 µm.

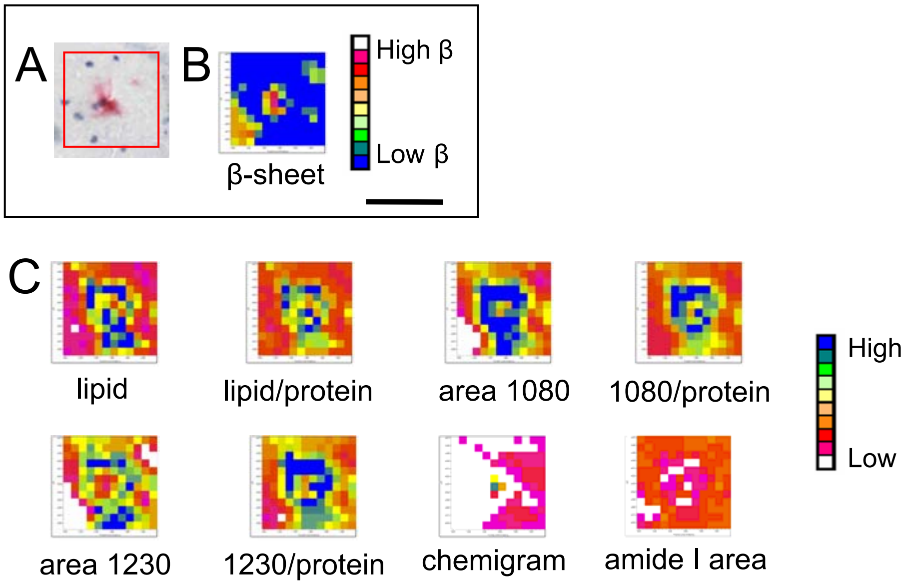

Figure 14.15. A dense-cored plaque from an 11-month-old TgCRND8 mouse. (A) A photomicrograph of the mapped cortex region, stained with Congo red after IR mapping. (B) The map processed to show elevated β-sheet proteins. (C) The map processed with the methods outlined in Table 3.1. The plaque is surrounded by elevated phospholipid levels in an irregular oval pattern. Scale bar = 100 µm.

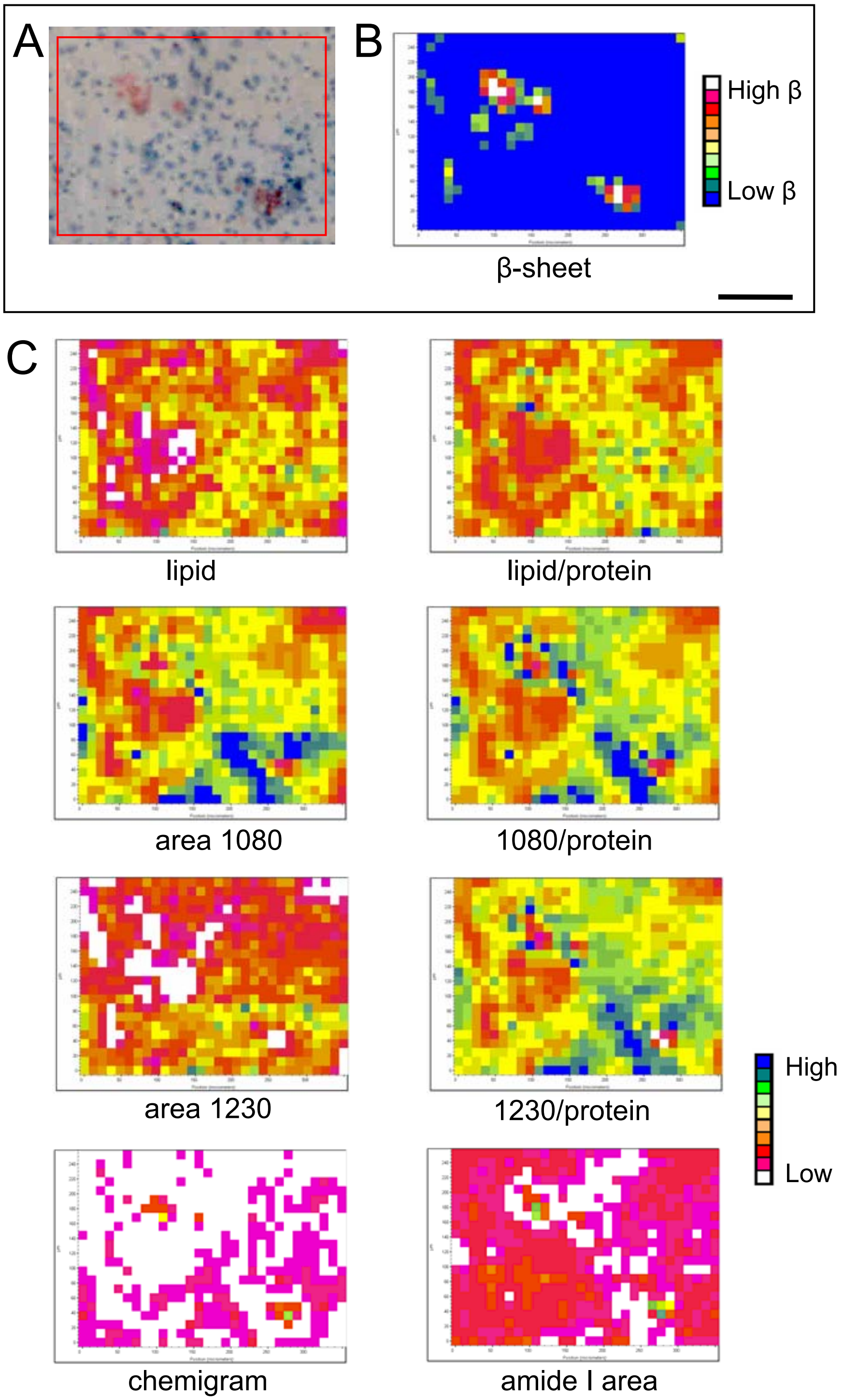

Figure 14.16. Two dense-cored plaques from an 11-month-old TgCRND8 mouse. (A) A photomicrograph of the mapped region, stained with Congo red after IR mapping. The two large plaques are located in the cortex. (B) The map processed to show elevated β-sheet proteins. (C) The map processed with the methods outlined in Table 3.1. Scale bar = 100 μm.

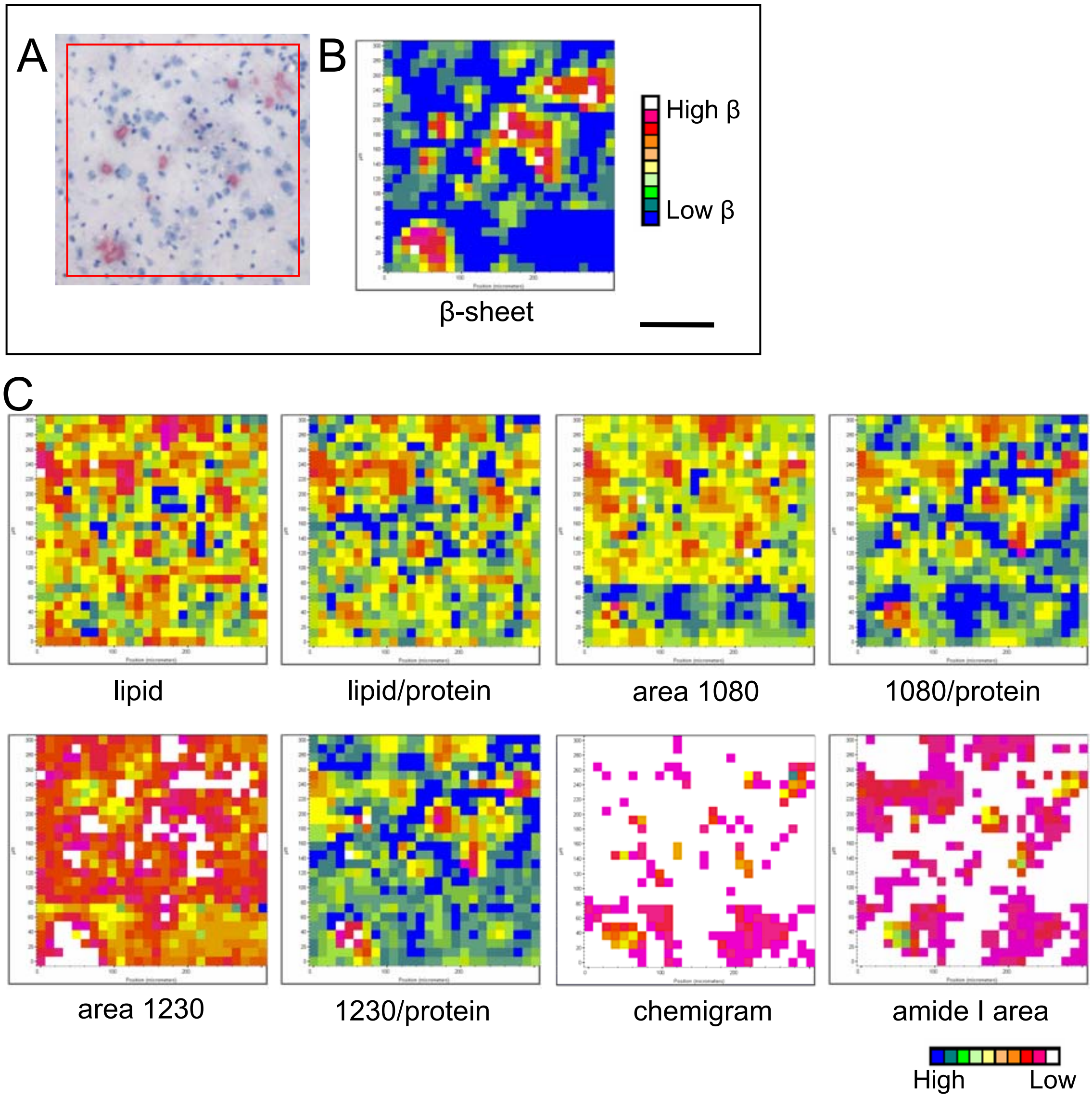

Figure 14.17. Several large multicored plaques from an 11-month-old TgCRND8 mouse. (A) A photomicrograph of the mapped region, stained with Congo red after IR mapping. The plaques are located in the cortex. (B) The map processed to show elevated β-sheet proteins. (C) The map processed with the methods outlined in Table 3.1. The map is high in phospholipids, but it is still possible to see the elevation of phospholipids around the plaque cores. Scale bar = 100 µm.

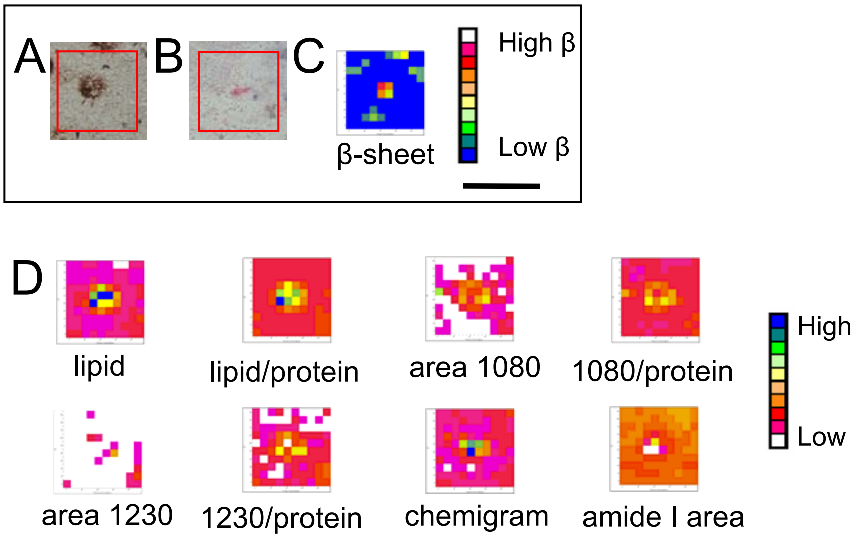

Figure 14.18. Dense-cored plaque from a 14-month-old TgCRND8 mouse. Photomicrographs of (A) a serial section immunostained with antibodies against the Aβ-peptide and (B) the mapped region, stained with Congo red after IR mapping, showing a small plaque in the hippocampus. (C) The map processed to show elevated β-sheet proteins. (D) The map processed with the methods outlined in Table 3.1. The plaque, despites its small size, is surrounded by elevated phospholipids. Scale bar = 100 µm.

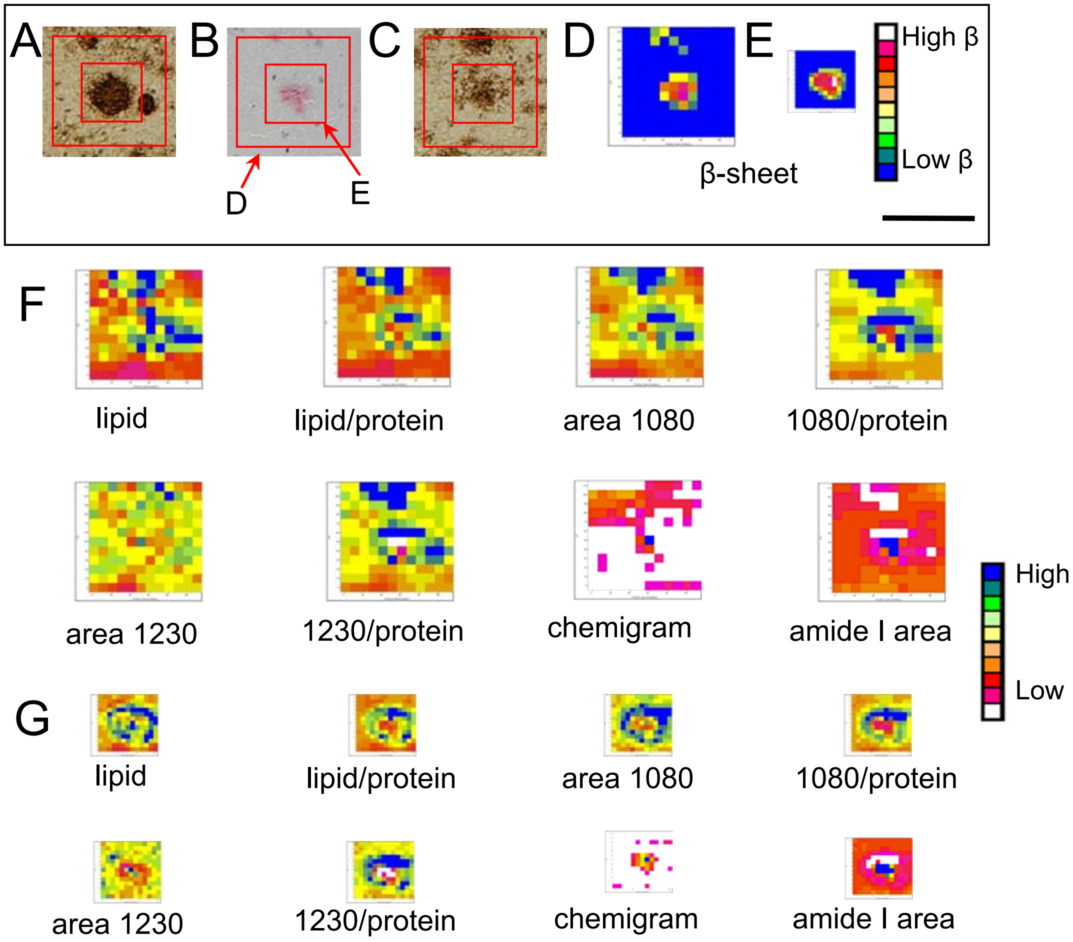

Figure 14.19. Dense-cored plaque from a 14-month-old TgCRND8 mouse. Photomicrographs of (A, C) serial sections immunostained with antibodies against the Aβ-peptide and (B) the mapped region, stained with Congo red after IR mapping. The plaque is located in hippocampus. (D) The plaque mapped with an aperture and step size of 10 μm, and (E) with an aperture of 10 μm and a step size of 5 μm (oversampled), processed to show elevated β-sheet proteins. Oversampling gives slightly more spatial detail, although it does not really increase the spatial resolution of the map. (F) The map from D, processed with the methods outlined in Table 3.1. (G) The map from E, processed with the methods outlined in Table 3.1. Elevated phospholipids around the plaque are seen in both maps. Scale bar = 100 μm.

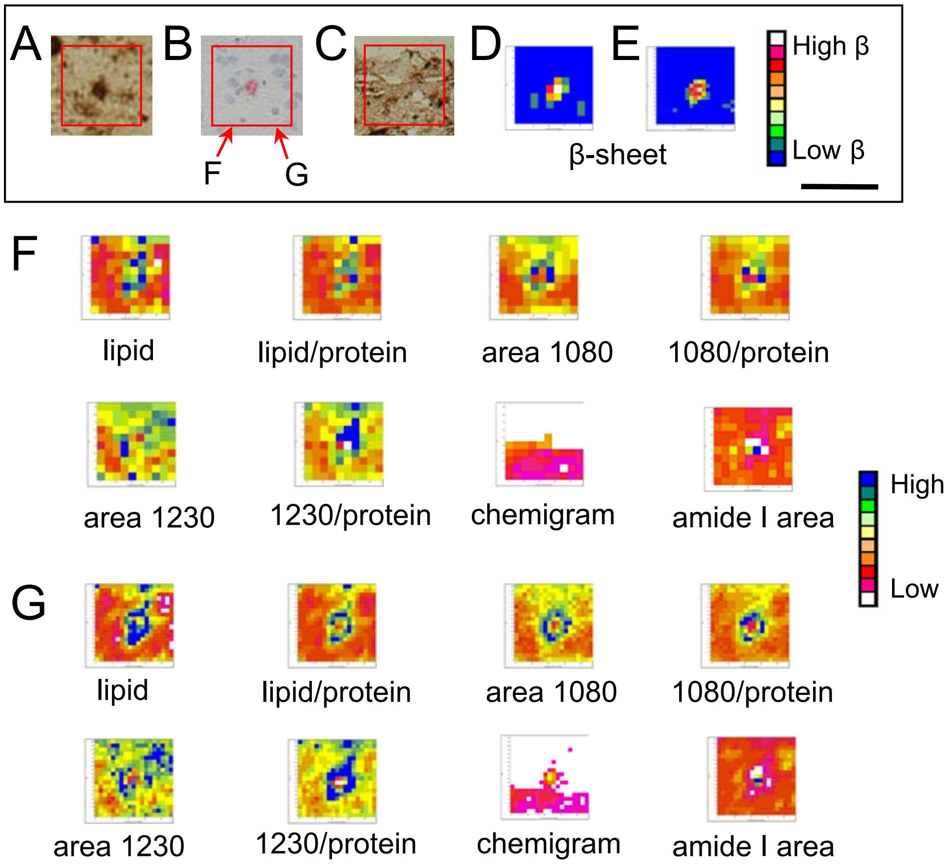

Figure 14.20. Dense-cored plaque from a 14-month-old TgCRND8 mouse. Photomicrographs of (A, C) serial sections immunostained with antibodies against the Aβ-peptide and (B) the mapped region, stained with Congo red after IR mapping. The mapped region is in the cortex. (D) The plaque mapped with an aperture and step size of 10 μm, and (E) with an aperture of 10 μm and a step size of 5 μm (oversampled), processed to show elevated β-sheet proteins. Oversampling gives slightly more spatial detail, although it does not really increase the spatial resolution of the map. (F) The map from D, processed with the methods outlined in Table 3.1. (G) The map from E, processed with the methods outlined in Table 3.1. Elevated phospholipids around the plaque are seen in both maps, but show up especially nicely in the oversampled map. Scale bar = 100 μm.

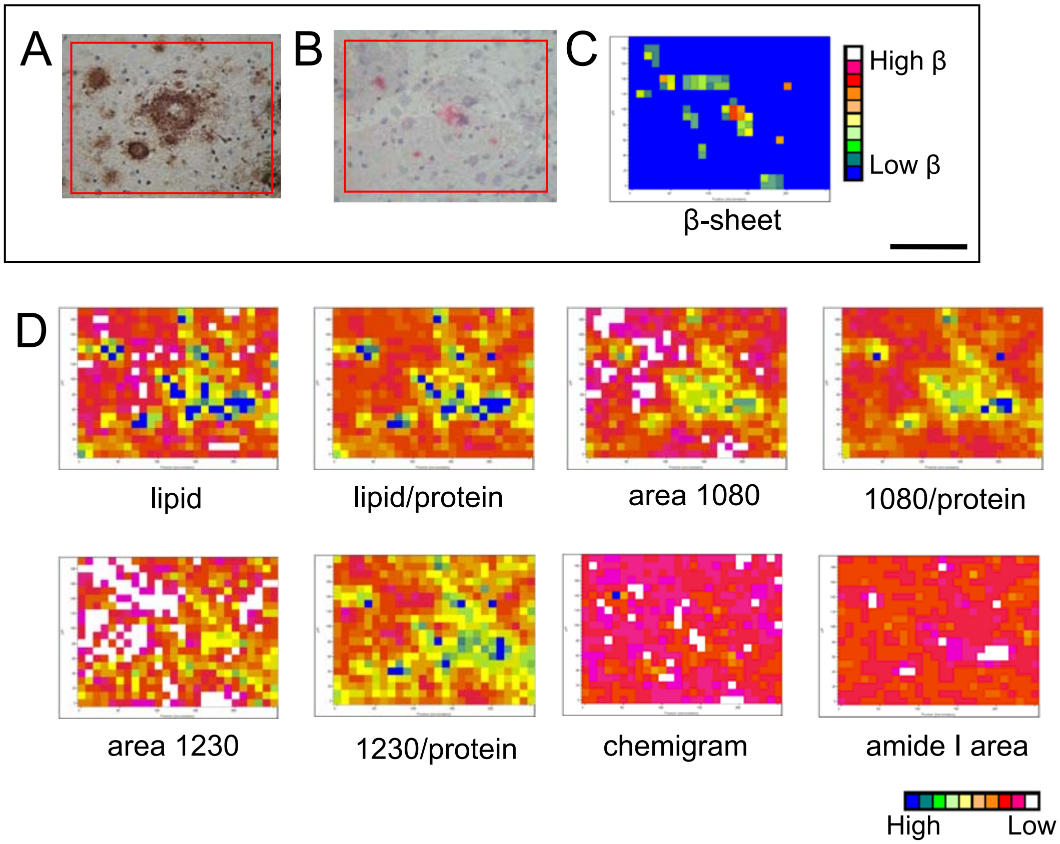

Figure 14.21. Dense cored plaques from a 14-month-old TgCRND8 mouse. Photomicrographs of (A) a serial section immunostained with antibodies against the Aβ-peptide and (B) the mapped region, stained with Congo red after IR mapping. The plaques are located in the cortex. (C) The map processed to show elevated β-sheet proteins. (D) The map processed with the methods outlined in Table 3.1. The plaques and surrounded by elevated phospholipids. Scale bar = 100 µm.

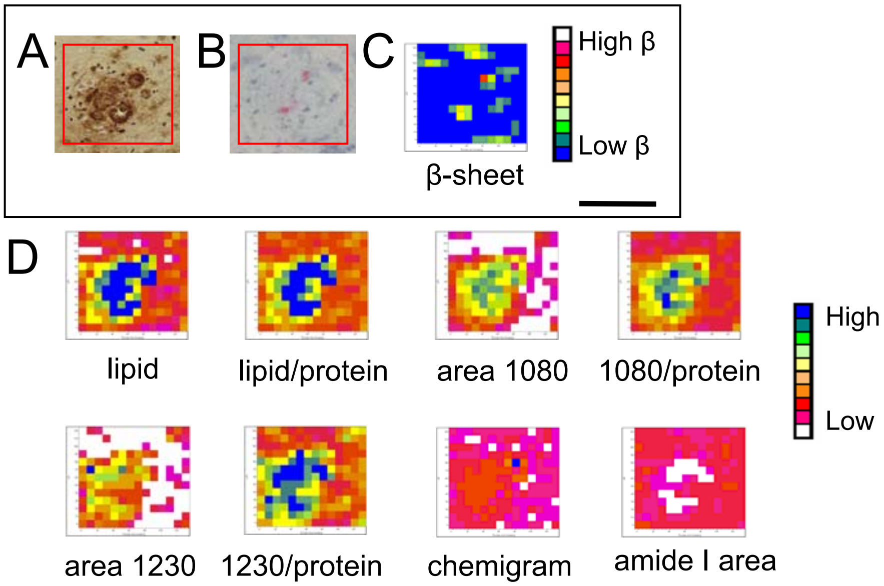

Figure 14.22. Dense-cored plaque from a 14-month-old TgCRND8 mouse. Photomicrographs of (A) a serial section immunostained with antibodies against the Aβ-peptide and (B) the mapped region, stained with Congo red after IR mapping, showing a multicored plaque in the hippocampus. (C) The map processed to show elevated β-sheet proteins. (D) The map processed with the methods outlined in Table 3.1. The two amyloid cores are very small but surrounded by a fairly large area of elevated phospholipids. Scale bar = 100 µm.

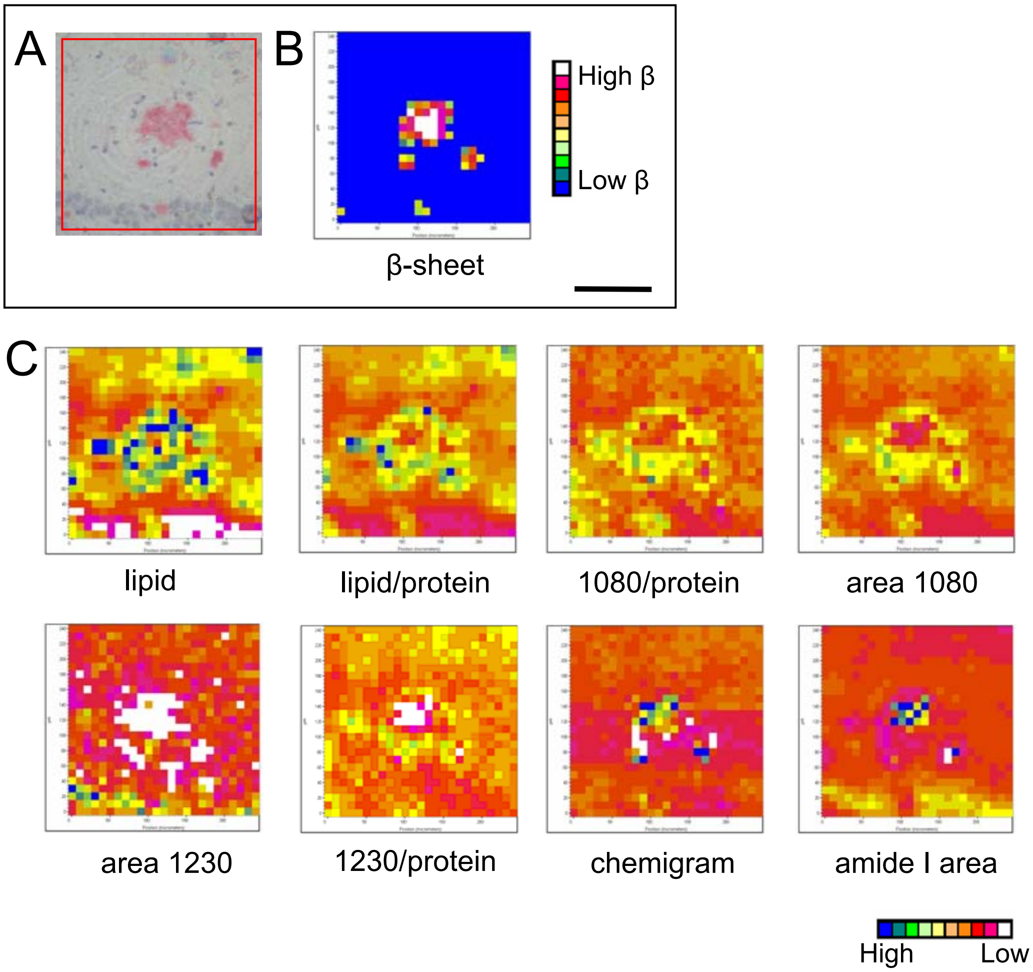

Figure 14.23. Dense-cored plaques from a 16-month-old TgCRND8 mouse. (A) A photomicrograph of the mapped region, stained with Congo red after IR mapping. A multicored plaque in the hippocampus, and a tiny plaque (arrow) next to the CA neurons, visible in the lower part of the Congo red stained photomicrograph. (B) The map processed to show elevated β-sheet proteins. (C) The map processed with the methods outlined in Table 3.1. Scale bar = 100 µm.

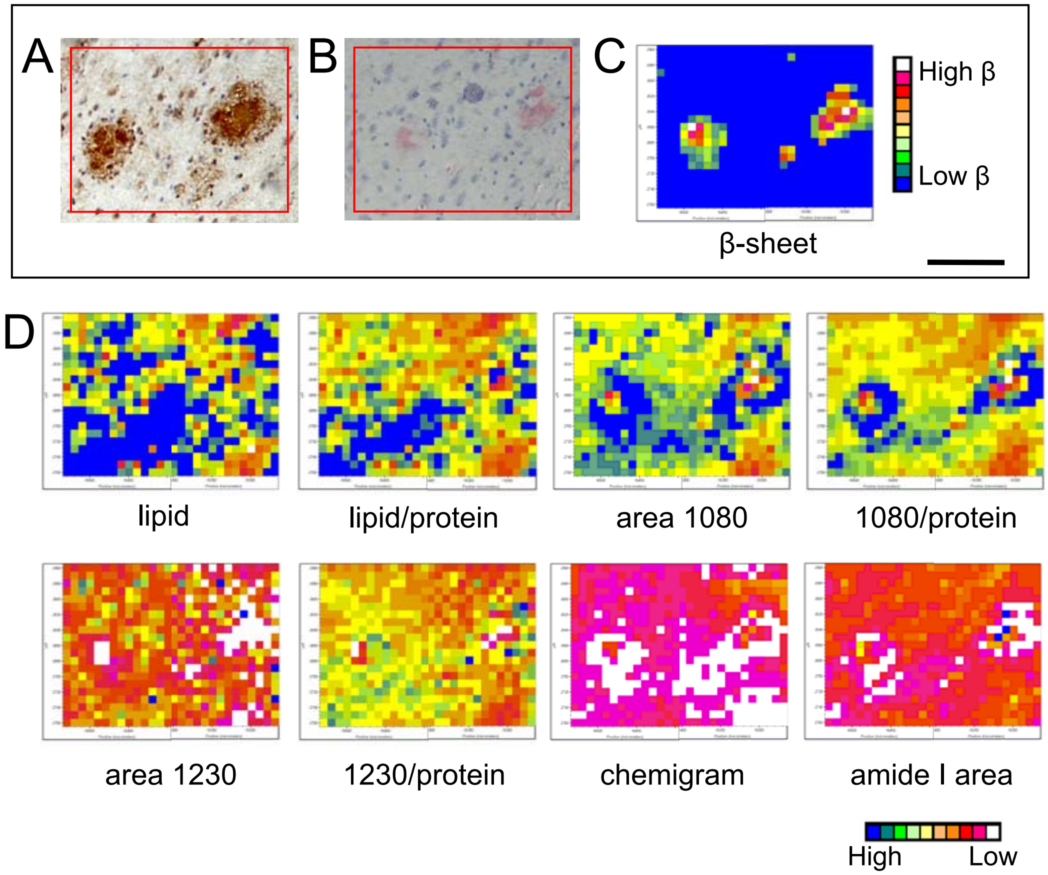

Figure 14.24. Two-dense cored plaques from a 16-month-old TgCRND8 mouse. Photomicrographs of (A) a serial section immunostained with antibodies against the Aβ-peptide and (B) the mapped region, stained with Congo red after IR mapping. The plaques are found in the cortex. (C) The map processed to show elevated β-sheet proteins. (D) The map processed with the methods outlined in Table 3.1. The mapped region is high in lipid, so it is difficult to see the elevated phospholipids around the plaque cores. Scale bar = 100 μm.

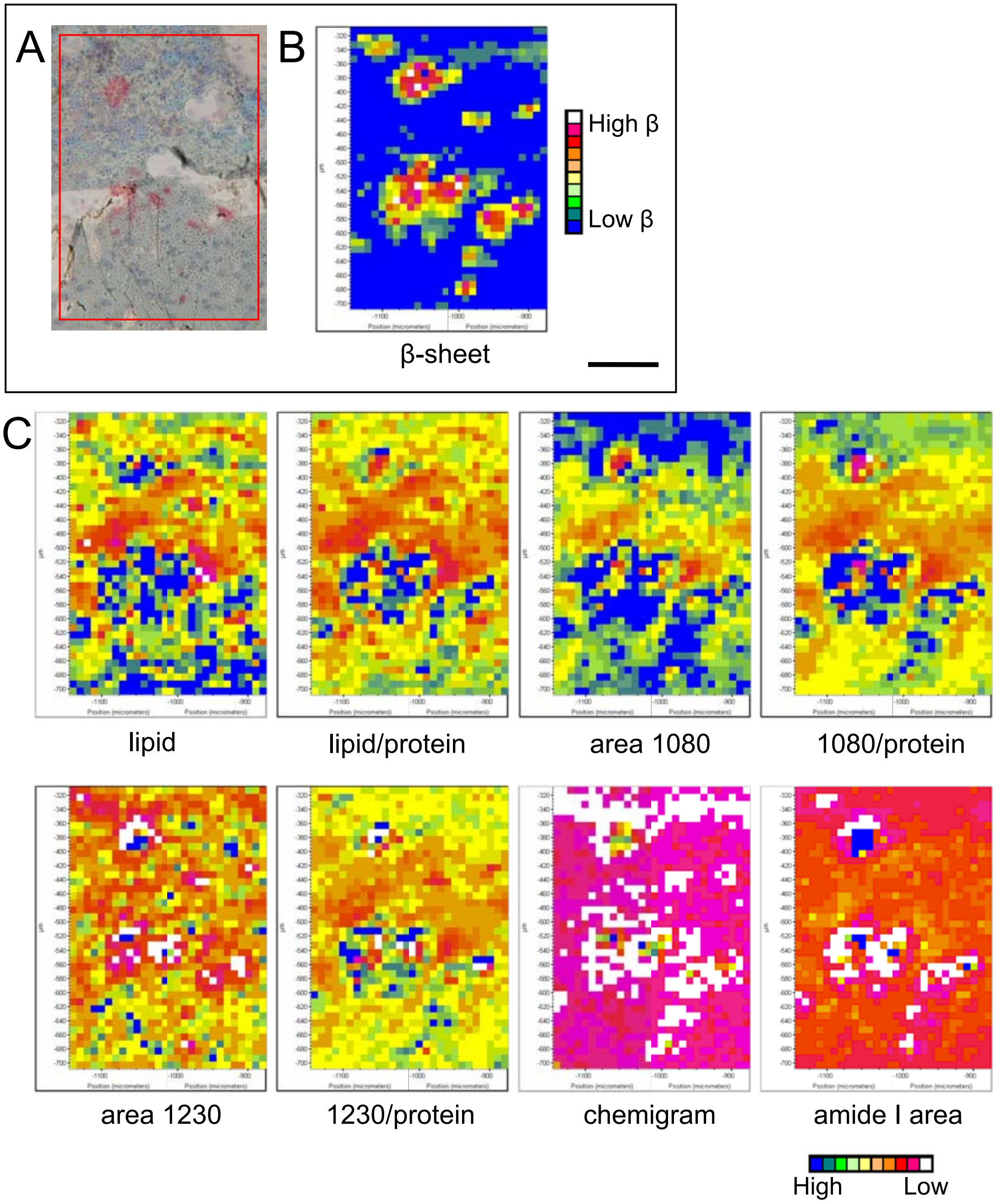

Figure 14.25. Dense-cored plaques from a 16-month-old TgCRND8 mouse. (A) A photomicrograph of the mapped region, stained with Congo red after IR mapping, showing several plaques in the cortex. The tissue was slightly damaged during Congo red staining, but most of the congophilic plaque cores are still visible in the micrograph. (B) The map processed to show elevated β-sheet proteins. (C) The map processed with the methods outlined in Table 3.1. Scale bar = 100 µm.

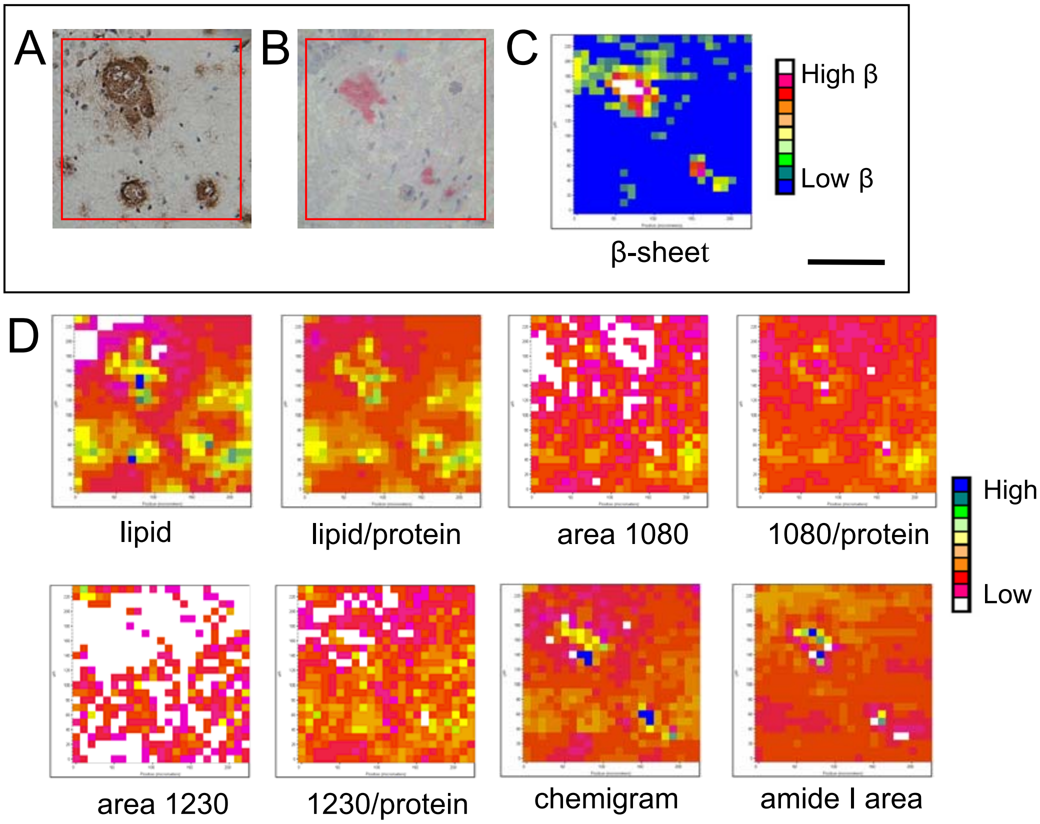

Figure 14.26. Dense-cored plaques from a 17-month-old TgCRND8 mouse. Photomicrographs of (A) a serial section immunostained with antibodies against the Aβ-peptide and (B) the mapped region, stained with Congo red after IR mapping. The plaques are in the central part of the hippocampus. (C) The map processed to show elevated β-sheet proteins. (D) The map processed with the methods outlined in Table 3.1. Scale bar = 100 µm.

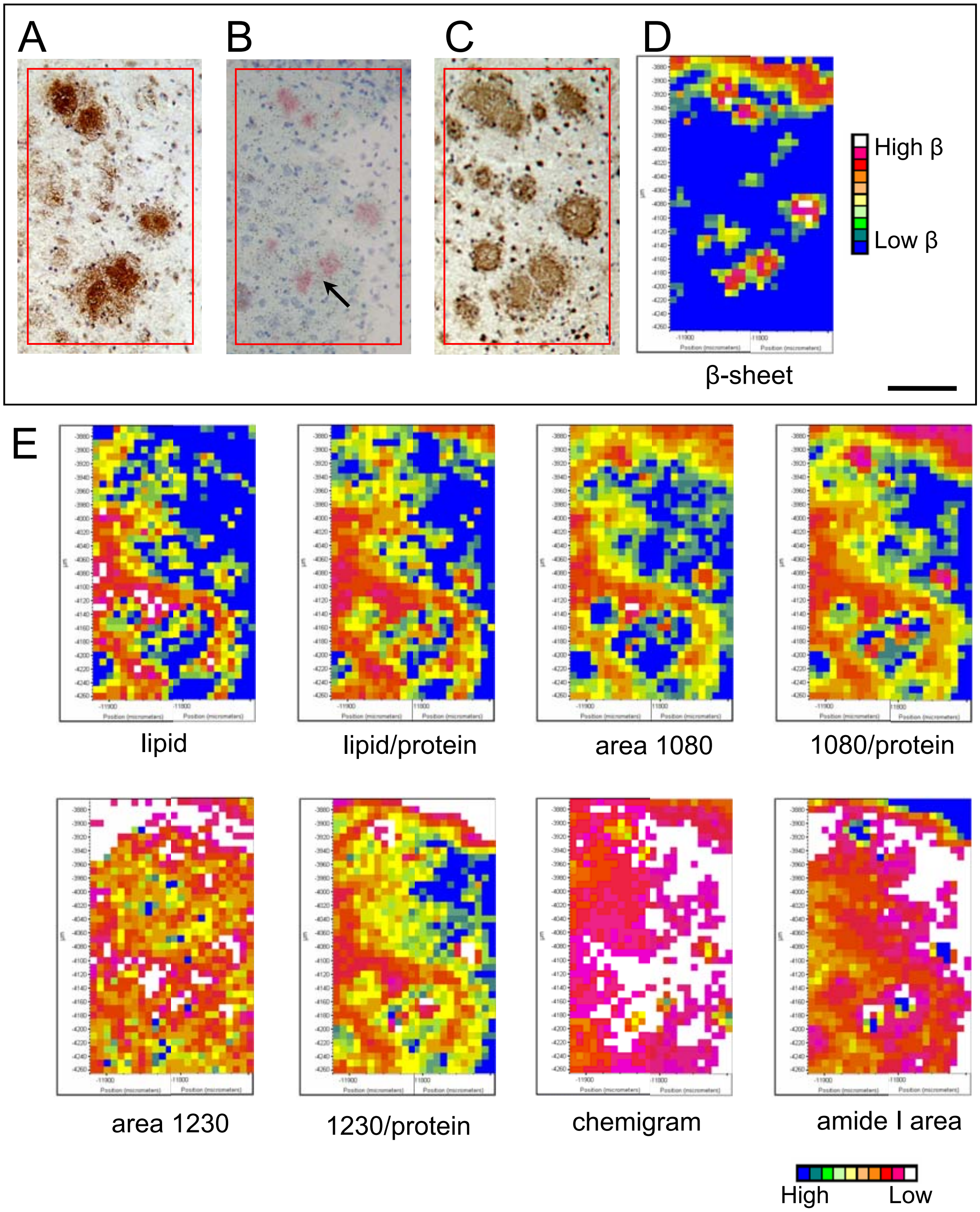

Figure 14.27. Dense-cored plaques from a 17-month-old TgCRND8 mouse. Photomicrographs of (A, C) serial sections immunostained with antibodies against the Aβ-peptide and (B) the mapped region, stained with Congo red after IR mapping. The mapped region is in the hippocampus, and includes corpus callosum on the right-hand side. (D) The map processed to show elevated β-sheet proteins. A fold in the tissue along the top shows up as having elevated β-sheet due to distorted spectra. (E) The map processed with the methods outlined in Table 3.1. The white matter is high in phospholipid. Elevated phospholipids are seen around the plaques in the grey matter, such as the double plaque in the lower part of the map (arrow). Scale bar = 100 μm.

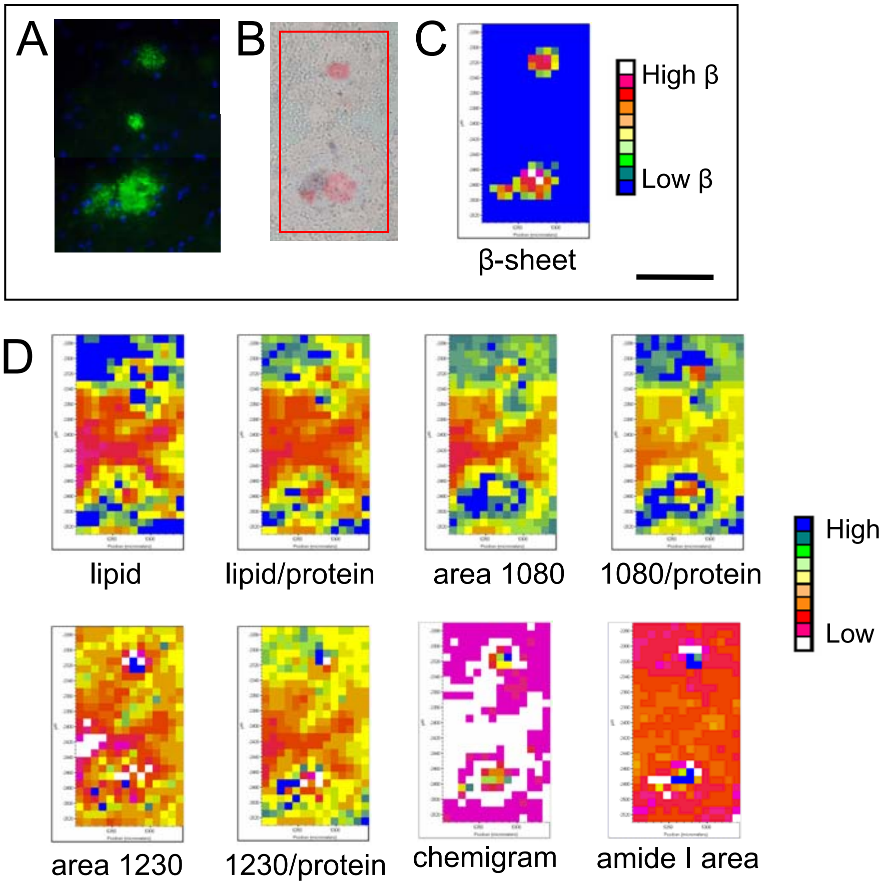

Figure 14.28. Dense-cored plaques from a 17-month-old TgCRND8 mouse. Photomicrographs of (A) a serial section immunostained with antibodies against the Aβ-peptide and (B) the mapped region, stained with Congo red after IR mapping. The plaques are in the hippocampus. (C) The map processed to show elevated β-sheet proteins. (D) The map processed with the methods outlined in Table 3.1. Scale bar = 100 μm.

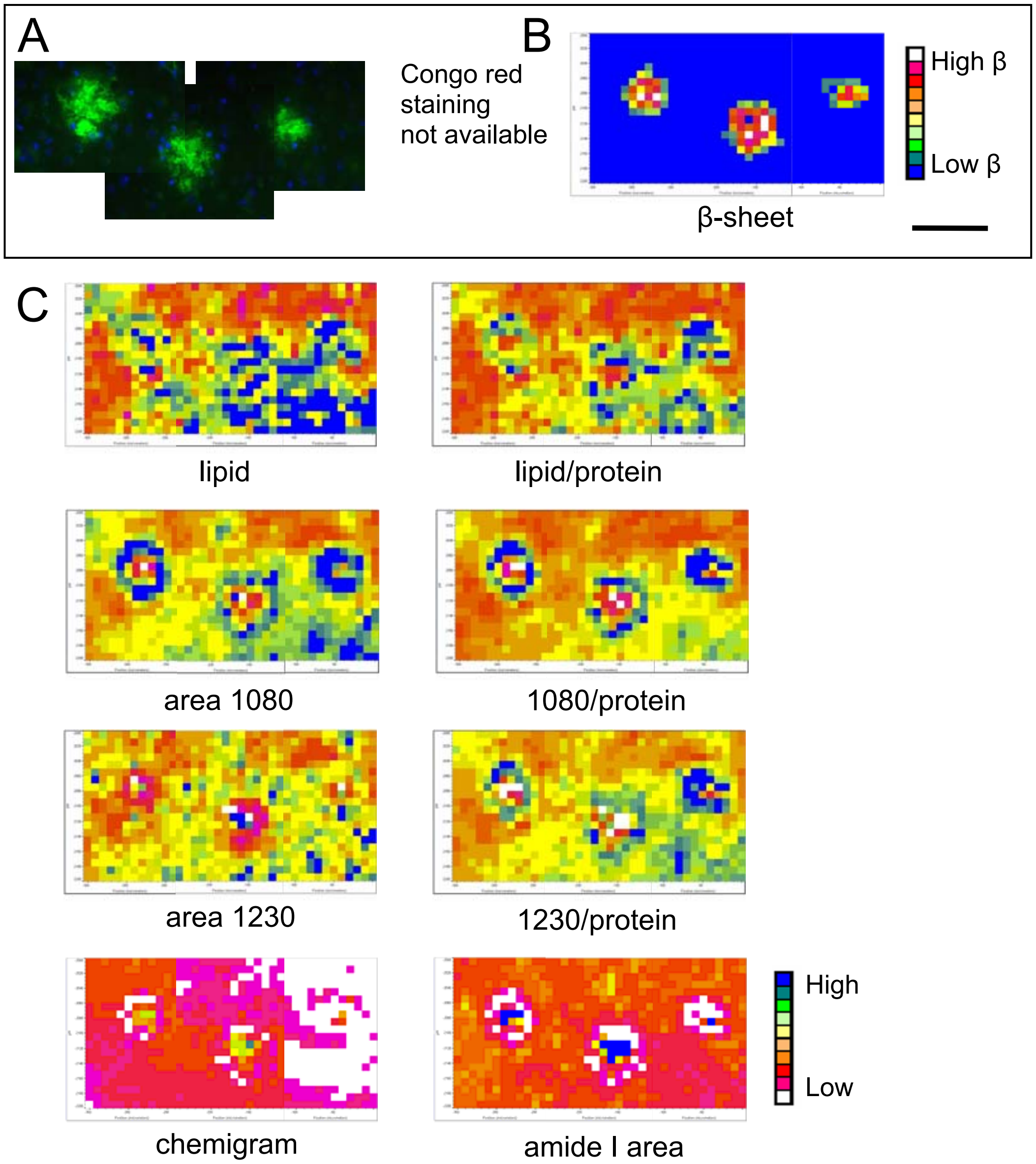

Figure 14.29. Dense-cored plaques from a 17-month-old TgCRND8 mouse. (A) A photomicrograph of a section serial to the IR mapped section, immunostained with antibodies against the Aβ-peptide. The plaques are located in the cortex. (B) The map processed to show elevated β-sheet proteins. (C) The map processed with the methods outlined in Table 3.1. The plaques are surrounded by an irregular distribution of elevated phospholipids. Scale bar = 100 μm.

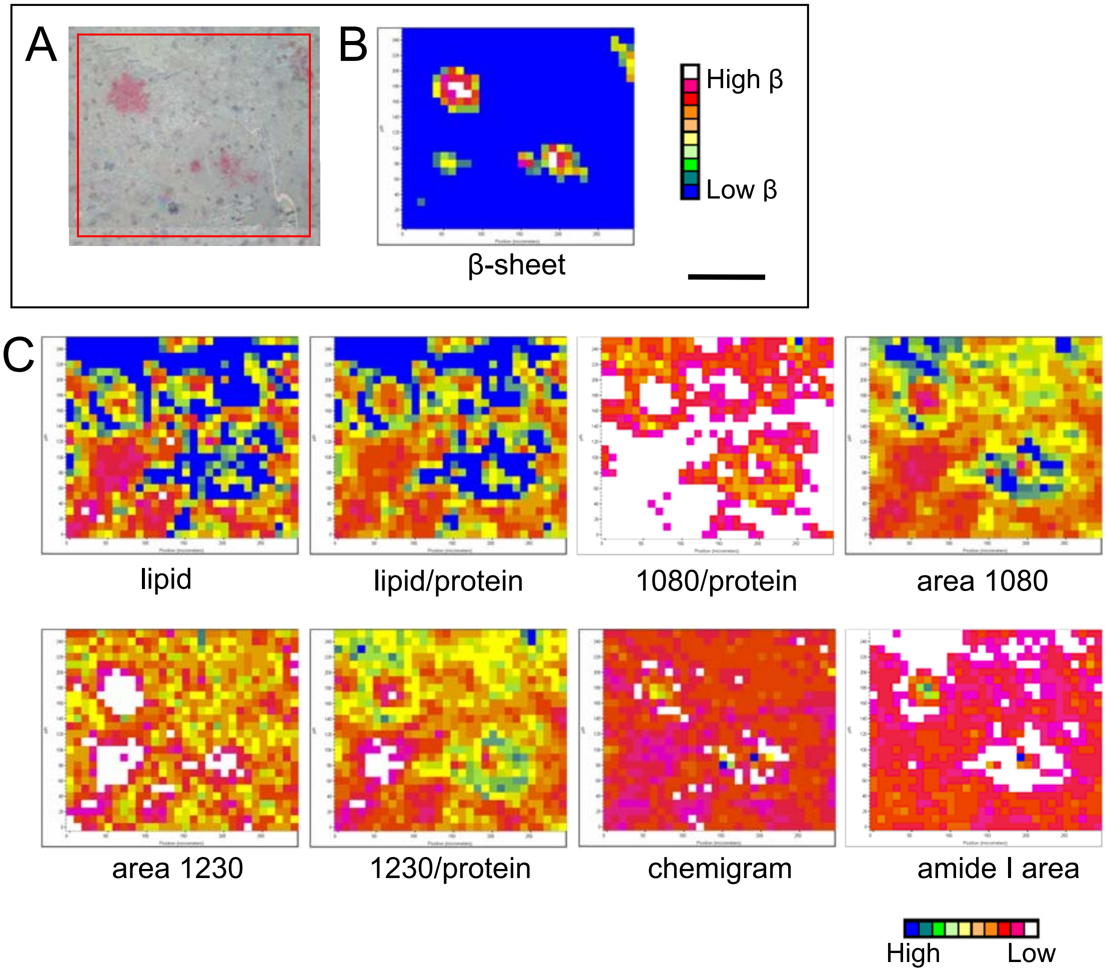

Figure 14.30. Dense-cored plaques from a 21-month-old TgCRND8 mouse. (A) A photomicrograph of the mapped region, stained with Congo red after IR mapping. The mapped region is in the cortex. There is a congophilic blood-vessel in the top-right corner of the map. (B) The map processed to show elevated β-sheet proteins. The congophilic blood-vessel contains aggregated β-sheet. (C) The map processed with the methods outlined in Table 3.1. Scale bar = 100 μm.

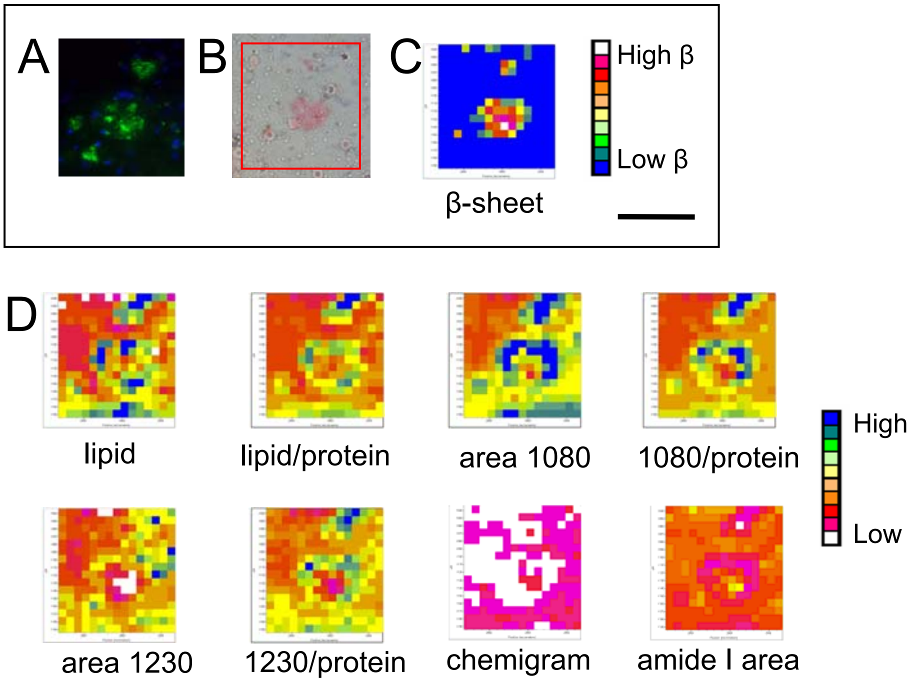

Figure 14.31. Dense-cored plaques from a 21-month-old TgCRND8 mouse. Photomicrographs of (A) a serial section immunostained with antibodies against the Aβ-peptide and (B) the mapped region, stained with Congo red after IR mapping. The multicored plaque is in the cortex. (C) The map processed to show elevated β-sheet proteins. (D) The map processed with the methods outlined in Table 3.1. Scale bar = 100 µm.

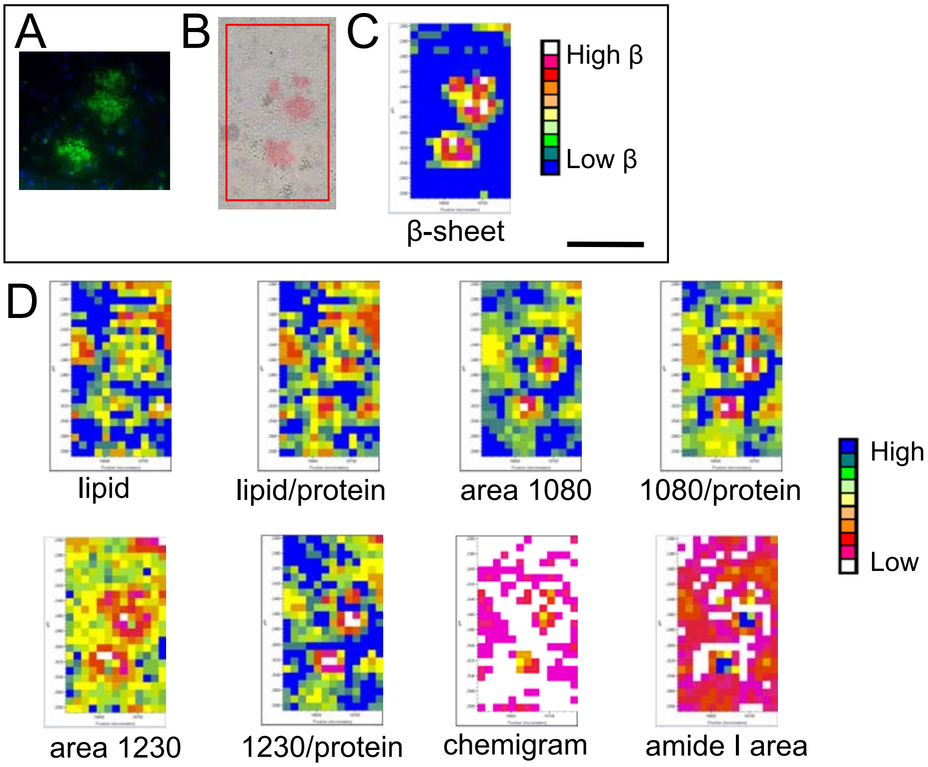

Figure 14.32. Dense-cored plaques from a 21-month-old TgCRND8 mouse. Photomicrographs of (A) a serial section immunostained with antibodies against the Aβ-peptide and (B) the mapped region, stained with Congo red after IR mapping. The plaques are found in the cortex. (C) The map processed to show elevated β-sheet proteins. (D) The map processed with the methods outlined in Table 3.1. Scale bar = 100 μm.

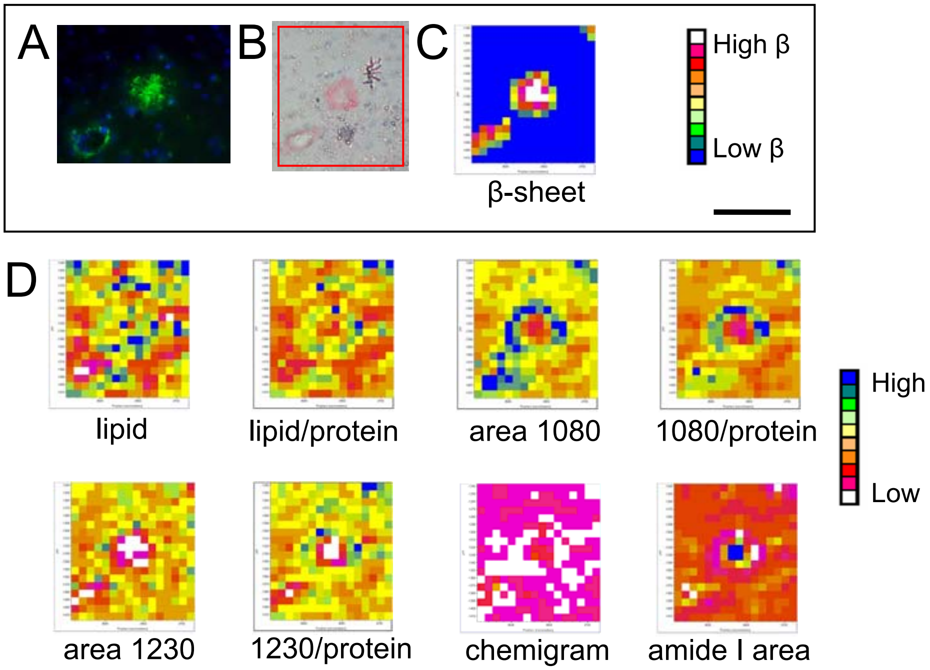

Figure 14.33. Dense-cored plaques from a 21-month-old TgCRND8 mouse. Photomicrographs of (A) a serial section immunostained with antibodies against the Aβ-peptide and (B) the mapped region, stained with Congo red after IR mapping. The mapped region is in the cortex, and includes a plaque and a congophilic blood-vessel in the lower-left corner. The spidery-looking object to the top right of the plaque core is a bit or dust or fiber in the embedding medium applied after staining. (C) The map processed to show elevated β-sheet proteins. The blood vessel, like the plaque core, contains aggregated β-sheet. (D) The map processed with the methods outlined in Table 3.1. Scale bar = 100 µm.

Chapter 15. Appendix 2. Additional Mouse Information

Table 15.1. Information about second set of transgenic AD mice

ID	Gender	Genotype	Age (Months)
TgCRND8			
A01	F	Tg(swe+V717F)8 +/- (C3H/C57)	21
A02	F	Tg(swe+V717F)8 -/- (C3H/C57)	21
A03	F	Tg(swe+V717F)8 +/- (C3H/C57)	17
A04	M	Tg(swe+V717F)8 -/- (C3H/C57)	17
A05	M	Tg(swe+V717F)8 +/- (C3H/C57)	16
A06	M	Tg(swe+V717F)8 -/- (C3H/C57)	16
A07*	F	Tg(swe+V717F)8 -/- (C3H/C57)	15
A08*	F	Tg(swe+V717F)8 -/- (C3H/C57)	15
A09*	F	Tg(swe+V717F)8 -/- (C3H/C57)	15
A10	F	Tg(swe+V717F)8 -/- (C3H/C57)	15
A11	F	Tg(swe+V717F)8 +/- (C3H/C57)	15
A12*	M	Tg(swe+V717F)8 +/- (C3H/C57)	14.5
A13	F	Tg(swe+V717F)8 -/- (C3H/C57)	14
A14	F	Tg(swe+V717F)8 +/- (C3H/C57)	14
A15	M	Tg(swe+V717F)8 -/- (C3H/C57)	14
A16	M	Tg(swe+V717F)8 +/- (C3H/C57)	14
A17*	F	Tg(swe+V717F)8 +/- (C3H/C57)	14
A18*	F	Tg(swe+V717F)8 +/- (C3H/C57)	14
A19*	M	Tg(swe+V717F)8 -/- (C3H/C57)	14
A20*	M	Tg(swe+V717F)8 -/- (C3H/C57)	14
Tg19959			
A21	F	Tg(swe+V717F)19959 -/-	9
A22	F	Tg(swe+V717F)19959 +/-	9
A23	F	Tg(swe+V717F)19959 -/-	9
A24	M	Tg(swe+V717F)19959 -/-	8
A25	M	Tg(swe+V717F)19959 +/-	8

* These animals were not used in the analysis because they lacked proper age-matched controls.

References

Adlard, P. A., & Vickers, J. C. (2002) Morphologically distinct plaque types differentially affect dendritic structure and organization in the early and late stages of Alzheimer's disease. Acta Neuropathol, 103, 377-383.

Aksenov, M. Y., Aksenova, M. V., Butterfield, D. A., Geddes, J. W., & Markesberry, W. R. (2001) Protein oxidation in the brain in Alzheimer's disease. Neuroscience, 1003, 373-383.

Aksenov, M. Y., Aksenova, M. V., J. W., and Markesberry, & Butterfield, D. A. (1998) Amyloid β-peptide(1-40)-mediated oxidative stress in cultured neurons. J Mol Neurosci, 10, 181-192.

Aksenov, M., Aksenova, M., Butterfield, A., & Markesbery, W. R. (2000) Oxidative modification of creatine kinase BB in Alzheimer's disease brain, J Neurochem, 74, 2520-2527.

Aksenova, M. V., Aksenov, M. Y., Payne, R. M., Trojanowski, J. Q., Schmidt, M. L., Carney, J. M., Butterfield, D. A., & Markesberry, W. R. (1999) Oxidation of cytosolic proteins and expression of creatine kinase BB in frontal lobe in different neurodegenerative disorders, Dement Geriatr Cogn Disord, 10, 158-165.

Ambrose, E. J., & Elliott, J. (1951) Infra-red spectra and structure of fibrous proteins. Proc Roy Soc A, 260, 206-219.

Ambrose, E. J., & Elliott, J. (1951) Infra-red spectroscopic studies of globular protein structure. Proc Roy Soc A, 208, 75-90.

Ames III, A. (2000) CNS energy metabolism as related to function. Brain Res Brain Res Rev, 34, 42-68.

Anderson, D. K., & Hall, E. D. (1993) Pathophysiology of spinal cord trauma. Ann Emerg Med, 22, 987-922.

Anderson, M. E. (1998) Glutathione: an overview of biosynthesis and modulation. Chem Biol Interact, 111-112, 1-14.

Anderson, M. E., & Meister, A. (1989) Marked increase of cysteine levels in many regions of the brain after administration of 2-oxothiazolidine-4-carboxylate. FASEB J, 3, 1632-1636.

Ardies, C. M. (2003) Inflammation as cause for scar cancers of the lung. Integr Cancer Ther, 2, 238-246.

Armstrong, R. A. (1994) The spatial patterns of β/A4 deposit subtypes in Down's syndrome. Acta Neuropathol, 88, 353-358.

Armstrong, R. A. (1998) β-Amyloid plaques: Stages in life history or independent origin? Dement Geriatr Cogn Disord, 9, 227-238.

Bandekar, J. (1992) Amide modes and protein conformation. Biochim Biophys Acta, 1120, 123-143.

Barth, A., & Zscherp, C. (2002) What vibrations tell us about proteins. Q Rev Biophys, 35, 369-430.

Beal, M. F. (1995) Aging, energy, and oxidative stress in neurodegenerative diseases. Ann Neurol, 38, 357-366.

Bell, K. F., de Kort, G. J., Steggerda, S., Shigemoto, R., Ribeiro-da-Silva, A., & Cuello, A.C. (2003) Structural involvement of the glutamatergic presynaptic boutons in a transgenic mouse model expressing early onset amyloid pathology. Neurosci Lett, 353, 143-147.

Bellucci, A., Luccarini, I., Scali, C., Prosperi, C., Giovannini, M. G., Pepeu, G., & Casamenti, F. (2006) Cholinergic dysfunction, neuronal damage and axonal loss in TgCRND8 mice. Neurobiol Dis, 23, 260-272.

Bitan, G., Kirkitadze, M. D., Lomakin, A., Vollers, S. S., Benedek, G. B., & Teplow, D. B. (2003) Amyloid β-protein (Aβ) assembly: Aβ40 and Aβ42 oligomerize through distinct pathways. Proc Natl Acad Sci, 100, 330-335.

Blasko I., Stampfer-Kountchev, M., Robatscher, p., Veerhuis, R., Eikelenboom, P., & Grubeck-Loebenstein, B. (2004) How chronic inflammation can affect the brain and support the development of Alzheimer's disease in old age: The role of microglia and astrocytes. Aging Cell, 3, 169-176.

Blass, J. (2001) Brain metabolism and brain disease: Is metabolic deficiency the proximate cause of Alzheimer dementia? (2001) J Neurosci Res, 66, 851-856.

Blass, J., Gibson, G. E., & Hoyer, S. (2002) The role of the metabolic lesion in Alzheimer's disease. J Alzheimers Dis , 4, 225-232.

Boydston-White, S., Gopen, T., Houser, S., Bargonetti, J., & Diem, M. (1999) Infrared spectroscopy of human tissue. V. Infrared spectroscopic studies of myeloid leukemia (ML-1) Cells at different phases of the cell cycle. Biospectroscopy, 5, 219-227.

Bottomley, P. A. (1992) The trouble with spectroscopy papers. J Magn Reson Imaging, 2, 1-8.

Bottomley, P., Cousins, J. P., Pendrey, D. L., Wagle, W. A., Hardy, C. J., Eames, F. A., McCaffrey, R. J. & Thompson, D. A. (1992) Alzheimer dementia: Quantification of energy metabolism and mobile phosphoesters with P-31 NMR spectroscopy, Radiology, 183, 695-699.

Braak, H., & Braak, E. (1991) Neuropathological stageing of Alzheimer-related changes. Acta Neuropathol, 82, 239-259.

Braissant, O., Henry, H., Loup, M., Eilers, B., & Bachmann, C. (2001) Endogenous synthesis and transport of creatine in the rat brain: An *in situ* hybridization study. Brain Res Mol Brain Res, 86. 193-201.

Brandenburg, K., & Seydel, U. (2002) Vibrational spectroscopy of carbohydrates and glycoconjugates. In J. M. Chalmers & P. R. Griffiths (Eds.) Handbook of vibrational spectroscopy (3481-3507). Chichester: John Wiley & Sons.

Brendza, R. P., O'Brien, C., Simmons, K., McKeel, D. W., Bales, K. R., Paul, S. M., Olney, J. W., Sanes, J. R., & Holtzman, D. M. (2003) PDAPP;YFP Double transgenic mice: A toll to study amyloid-β associated changes in axonal, dendritic, and synaptic structures. J Comp Neurol, 456:375-383.

Brewer, G. J., & Wallimann, T. W. (2000) Protective effect of the energy precursor creatine against toxicity of glutamate and β-Amyloid in rat hippocampal neurons. J Neurochem, 74, 1968-1978.

Burklen, T. S., Schlattner, U., Homayouni, R., Gough, K., Rak, M., Szeghalmi, A., & Wallimann, T. (2006) The creatine kinase/creatine connection to Alzheimer's disease: CK-inactivation, APP-CK complexes and focal creatine deposits. J Biomed Biotechnol. 2006, 1-11.

Burton, C. V., Kirkaldy-Willis, W. H., Yong-Hing, K., & Heithoff, K. B. (1981) Causes of failure of surgery on the lumbar spine. Clin Ortho, 157, 191-199.

Butterfield, A. D., Griffin, S., Munch, G., & Pasinetti, G. M. (2002) Amyloid β-peptide and amyloid pathology are central to the oxidative stress and inflammatory cascades under which Alzheimer's disease brain exists. J Alzheimers Dis, 4, 193-201.

Byler, D. M., & Susi, H. (1986) Examination of the secondary structure of proteins by deconvolved FTIR spectra, Biopolymers, 25, 469-487.

Camacho, N. P., Rinnerthaler, S., Paschalis, E. P., Mendelsohn, R., Boskey, A. L. & Fratzl, P. (1999) Complementary information on bone ultrastructure from scanning small angle X-ray scattering and Fourier-transform infrared microspectroscopy. Bone (1999) 25, 287-293.

Camacho, N. P., West, P., Torzilli, P. A., & Mendelsohn, R. (2001) FTIR microscopic imaging of collagen and proteoglycan in bovine cartilage. Biopolymers, 62, 1-8.

Campbell, I. D., & Dwek, R. A. (1984) Biological spectroscopy. Benjamin/Cummings Publishing Company: Menlo Park.

Canadian Study of Health and Aging Working Group (1994) Canadian Study of Health and Aging: Study methods and prevalence of dementia. Can Med Assoc J, 150, 899–913.

Carr, G. L. (2001) Resolution limits for infrared microspectroscopy explored with synchrotron radiation. Rev Sci Instrum, 72, 1613-1619.

Carr, G. L., Reffner, J. A. & Williams, G. P. (1995) Performance of an infrared microspectrometer at the NSLS. Rev Sci Instrum, 66, 1490-1492.

Carter, D. B., & Chou, K. C. (1998) A model for structure-dependent binding of congo red to Alzheimer β-amyloid fibrils. Neurobiol Aging, 19, 37-40.

Casal, H. L., & Mantsch, H. H. (1984) Polymorphic phase behaviour of phospholipid membranes studied by infrared spectroscopy. Biochimica et Biophysica Acta, 79, 381-401.

Casley, C. S., Canevari, L., Land, J. M., Clark, J. B., & Sharpe, M. A. (2002) β-Amyloid inhibits integrated mitochondrial respiration and key enzyme activities. J Neurochem, 80, 91-100.

Castegna, A., Aksenov, M., Aksenova, M., Thongboonkerd, V., Klein, J. B., Pierce, W. M., Booze, R., Markesbery, W. R., & Butterfield, D. A. (2002) Proteomic identification of oxidatively modified proteins in Alzheimer's disease brain. Part I: Creatine kinase BB, glutamine synthase, and ubiquitin carboxy-terminal hydrolase L-1. Free Radic Biol Med, 33, 562-571.

Castellani, R., Hirai, K., Aliev, G., Drew, K. L., Nunomura, A., Tadeka, A., Cash, A. D., Obrenovich, M. E., Perry, G., & Smith, M. A., (2002) Role of mitochondrial dysfunction in Alzheimer's disease. J Neurosci Res, 70, 357-360.

Cavanagh, J. B. (1999) Corpora-amylacea and the family of polyglucosan diseases. Brain Res Rev, 29, 265-295.

Chantal, S., Labelle, M., Bouchard, R. W., Braun, C. M. J., & Boulanger, Y. (2002) Correlation of regional proton magnetic resonance spectroscopic metabolite changes with cognitive deficits in mild Alzheimer disease. Arch Neurol, 955-962.

Chauhan, N. B., & Siegel, G. J. (2005) Efficacy of anti-Aβ antibody isotypes used for intracerebroventricular immunization in TgCRND8. Neurosci Lett, 375, 143-147.

Chiriboga, L., Xie, P., Yee, H., Vigorita, V., Zarou, D., Zakim, D., & Diem, M. (1998) Infrared spectroscopy of human tissue. I. Differentiation of maturation of epithelial cells in the human cervix. Biospectroscopy, 4, 47-53.

Chishti, M. A., Yang, D., Janus, C., Phinney, A. L., Horne, P., Pearson, J., Strome, R., Zuker, N., Loukides, J., French, J., Turner, S., Lozza, G., Grilli, M., Kunicki, S., Morissette, C., Paquette, J., Gervais, F., Bergeron, C., Fraser, P. E., Carlson, G. A., St. George-Hyslop, P., & Westaway, D. (2001) Early-onset amyloid deposition and cognitive deficits in transgenic mice expressing a double mutant form of amyloid precursor protein 695**.** J Biol Chem, 276, 21562-21570.

Choo, L. P., Wetzel, D. L., Halliday, W. C., Jackson, M., LeVine, S. M., & Mantsch, H. H. (1996) *In situ* characterization of β-amyloid in Alzheimer's diseased tissue by synchrotron Fourier transform infrared microspectroscopy. Biophys J, 71, 1672-1679.

Chromy, B. A., Nowak, R. J., Lambert, M. P., Viola, K. L., Chang, L., Velasco, P. T., Jones, B. W., Fernandez, S. J., Lacor, P. N., Horowitz, P., Finch, C. E., Krafft, G. A. & Klein, W. L. (2003) Self-assembly of $A\beta_{1\text{-}42}$ into globular neurotoxins. Biochemistry, 42, 12749-12760.

Citron, M., Westaway, D., Xia, W., Carlson, G., Diehl, T., Levesque, G., Johnson-Wood, K., Lee, M., Seubert, P., Davis, A., Kholodenko, D., Motter, R., Sherrington, R., Perry, B., Yao, H., Strome, R., Lieberburg, I., Rommens, J., Kim, S., Schenk, D., Fraser, P., St George Hyslop P., & Selkoe, D. J. (1997) Mutant presenilins of Alzheimer's disease increase production of 42-residue amyloid beta-protein in both transfected cells and transgenic mice. Nature Medicine 3, 67-72.

Collier, G. L., & Singleton, F. (1956) Infrared analysis by the derivative method. J Appl Chem, 6, 495-510.

Colthup, N. B., Daly, L. H., & Wiberley, S. E. (1975) Introduction to infrared and raman spectroscopy. Academic Press: New York.

Coskun, E., Suzer, T., Topuz, O., Zencir, M., Pakdemirli, E, & Tahta, K. (2000) Relationships between epidural fibrosis, pain, disability, and psychological factors after lumbar disc surgery. Eur Spine J, 9, 218-223.

Cummings, J. L., Vinters, H. V., Cole, G. M., & Khachaturian, Z. S. (1998) Alzheimer's disease: Etiologies, pathophysiology, cognitive reserve, and treatment opportunities. Neurology, 51, S2-S17.

David, S., Shoemaker, M., & Haley, B. E. (1998) Abnormal properties of creatine kinase in Alzheimer's disease brain: Correlation of reduced enzyme activity and active site photolabeling with aberrant cytosol-membrane partitioning. Brain Res Mol Brain Res, 54, 276-287.

Davies, C. A., & Mann, D. M. (1993) Is the “preamyloid” of diffuse plaques in Alzheimer’s disease really nonfibrillar? Am J Pathol, 143, 1594-1605.

Davidson, J. M., & Berg, R. A. (1981) Posttranslational events in collagen biosynthesis. Methods Cell Biol, 23, 119-136.

De Stropper, B., (2003) Aph-1, Pen-2, and nicastrin with presenilin generate an active γ-secretase complex. Neuron, 38, 9-12.

Dechent, P., Pouwels, P. J., Wilken, B., Hanefeld, F., & Frahm, J. (1999) Increase of total creatine in human brain after oral supplementation of creatine-monohydrate. Am J Physiol, 277, 698-704.

Deshpande, A., Mina, E., Glabe, C., & Busciglio, J. (2006) Different conformations of amyloid β induce neurotoxicity by distinct mechanisms in human cortical neurons. J Neurosci, 26, 6011-6018.

Dickson, T. C., & Vickers, J. C. (2001) The morphological phenotype of β-amyloid plaques and associated neuritic changes in Alzheimer’s disease. Neuroscience, 105, 99-107.

Diegelmann, R. F., & Evans, M. C. (2004) Wound healing: An overview of acute, fibrotic and delayed healing. Front Biosci, 9, 283-289.

Dixon, R. M., Bradley, K. M., Budge, M. M., Styles, P., & Smith, A. D. (2002) Longitudinal quantitative proton magnetic resonance spectroscopy of the hippocampus in Alzheimer’s disease. Brain, 125, 2332-2341.

Dodart, J. C., Mathis, C., Bales, K. R., & Paul, S. M. (2002) Does my mouse have Alzheimer’s disease? Genes Brain Behav, 1, 142-155.

Donoff, R. B., Swann, D. A., & Schweidt, S. H. (1984) Glycosaminoglycans of normal and hypertrophic human scar. Exp Mol Pathol, 40, 13-20.

Doussequ, F., & Pezolet, M. (1990) Determination of the secondary structure content of proteins in aqueous solutions from their amide I and amide II infrared bands: Comparison between classical and partial least-squares methods. Biochemsitry, 29, 8771-8779.

Downing, A. K. (2004) Protein NMR techniques. 2nd ed. Humana Press: Totowa.

Dringen, R., Verleysdonk, S, Hamprecht, B., Willker, W., Leibfritz, D., & Brand, A. (1998) Metabolism of glycine in primary astroglial cells: Synthesis of creatine, serine, and glutathione. J Neurochem, 70, 835-840.

Dumas, P. & Miller, L. (2003) The use of synchrotron infrared microspectroscopy in biological and biomedical investigations. Vib Spec, 32, 3-21.

Dumas, P., Jamin, N., Teillaud, J. L., Miller, L. M., & Beccard, B. (2004) Imaging capabilities of synchrotron infrared microspectroscopy. Faraday Discuss, 126, 303-311.

Einhaus, S. L., Robertson, J. T., Curtis, D. F., Wujek, J. R., & Ahmad, S. (1997) Reduction of peridural fibrosis after lumbar laminectomy and discectomy in dogs by a resorbable gel (ADCON-L). Spine, 22, 1440-1446.

Erlund, I. (2004) Review of the flavonoids quercetin, hesperetin, and naringenin: Dietary sources, bioactivities, bioavailability, and epidemiology. Nutr Res, 24, 851-874.

Fabian, H., Choo, L. P., Szendrei, G. I., Jackson, M., Halliday, W. C., Otvos, L. Jr, & Mantsch, H. H. (1993) Infrared spectroscopic characterization of Alzheimer plaques. Appl Spectrosc, 47, 1513-1518.

Firbank, M. J., Harrison, R. M., & O'Brien, J. T. (2002) A comprehensive review of proton magnetic resonance spectroscopy studies in dementia and Parkinson's disease. Dement Geriatr Cogn Disord, 14, 64-76.

Floyd, R. A., & Hensley, K. (2002) Oxidative stress in brain aging: Implications for therapeutics of neurodegenerative diseases. Neurobiol Aging, 23, 795-807.

Forman, M. S., Trojanowski, J. Q., & Lee, V. M. (2004) Neurodegenerative diseases: a decade of discoveries paves the way for therapeutic breakthrough. Nature Medicine, 10, 1055-1063.

Fraser, D. B. (1950) Infra-red microspectrometry with a 0.8 N. A. reflecting microscope. Discuss Faraday Soc, 9, 378-383.

Fraser, P. E., Nguyen, J. T., Inouye, H., Surewicz, W. K., Selkoe, D. J., Podlisny, M. B, & Kirschner, D. A. (1992) Fibril formation by primate, rodent, and Dutch-Hemorrhagic analogues of Alzheimer amyloid β-protein. Biochemistry, 31, 10716-10723.

Fritsch, E. W., Heisel, J., & Rupp, S. (1996) The failed back surgery syndrome: Reasons, intraoperative findings, and long-term results: A report of 182 operative treatments. Spine, 21, 626-633.

Froelich-Fabre, S. & Bhat, R. V. (2004) Mechanisms of tauopathies. Drug Discov Today, 1, 931-398.

Fukasawa, K., Wiener, F., Vande Woude, G. F., & Mai, S. (1997) Genomic instability and apoptosis are frequent in p53 deficient young mice. Oncogene, 15, 1295-1302.

Gadaleta, S. J., Landis, W. J., Boskey, A. L., & Mendelsohn, R. (1996) Polarized FT-IR microscopy of calcified turkey leg tendon. Connect Tissue Res, 34, 203-211.

Gahl, W. A., Thoene, J. G., & Schneider, J. A. (2002) Cystinosis. N Engl J Med, 347, 111-121.

Gallant, M., Rak, M., Szeghalmi, A., Del Bigio, M. R., Westaway, D., Yang, J., Julian, R., & Gough, K. M. (2006) Focally elevated creatine detected in amyloid precursor protein (APP) transgenic mice and Alzheimer disease brain tissue. J Biol Chem, 281, 5-8.

Gasparini, L., Ongini, E., & Wenk, G. (2004) Non-steroidal anti-inflammatory drugs (NSAIDs) in Alzheimer's disease: Old and new mechanisms of action. J Neurochem, 91, 521-536.

Gazit, E. (2002) The "correctly folded" state of proteins: is it a metastable state? Angew Chem Int Ed, 41, 257-259.

Gentleman, S. M., Bruton, C., Allsop, D., Lewis, S. J., Polak, J. M., & Roberts, G. W. (1989) A demonstration of the advantages of immunostaining in the quantification of amyloid plaque deposits. Histochemistry, 92, 355-358.

George, A., & Veis, A. (1991) FTIRS in H_2O demonstrates that collagen monomers undergo a conformational transition prior to thermal self-assembly *in vitro*. Biochemistry, 30, 2372-2377.

Gibson, G. E. (2002) Interactions of oxidative stress with cellular calcium dynamics and glucose metabolism in Alzheimer’s disease. Free Radic Biol Med, 32, 1061-1070.

Glenner, G. G. & Wong, C. W. (1984) Alzheimer’s disease: initial report of the purification and characterization of a novel cerebrovascular amyloid protein. Biochem Biophys Res Commun, 120, 885-890.

Glenner, G. G., Eanes, E. D., & Page, D. L. (1972) The relation of the properties of Congo red-stained amyloid fibrils to the β-conformation. J Histochem Cytochem, 20, 821-826.

Glenner, G. G., Eanes, E. D., Bladen, H. A., Linke, R. P., & Termine, J. D. (1974) β-Pleated sheet fibrils: A comparison of native amyloid with synthetic protein fibrils. J Histochem Cytochem, 22, 1141-1158.

Goate, A., Chartier-Harlin, M., Mullan, M., Brown, J., Crawford, F., Fidani, L., Giuffra, L., Haynes, A., Irving, N., James, L., Mant, R., Newton, P., Rooke, K., Roques, P., Talbot, C., Pericak-Vance, M., Roses, A., Williamson, R., Rossor, M., Owen, M., & Hardy, J. (1991) Segregation of a missense mutation in the amyloid precursor protein gene with familial Alzheimer's disease. Nature, 349, 704-706.

Goedert, M., & Jakes, R. (2005) Mutations causing neurodegenerative tauopathies. Biochim Biophys Acta Mol Basis Dis, 1739, 240-250.

Gorman, P. M., & Chakrabartty, A. (2001) Alzheimer β-amyloid peptides: Structures of amyloid fibrils and alternate aggregation products. Biopolymers, 60, 381-394.

Gotz, J., Chen, F., Dorpe, J. Van, & Nitsch, R. M. (2001) Formation of neurofibrillary tangles in P301L tau transgenic mice induced by Aβ Fibrils. Science, 293, 1491-1495.

Gough, K. M., Rak, M., Bookatz, A., Del Bigio, M., Mai, S., & Westaway, D. (2005) Choices for tissue visualization with IR microspectroscopy. Vib Spectrosc, 38, 133-141.

Gough, K. M., Zelinski, D., Wiens, R., Rak, M. & Dixon, I. M. C. (2003) Fourier transform infrared evaluation of microscopic scarring in the cardiomyopathic heart: Effect of chronic AT_1 suppression. Anal Biochem, 316, 232-242.

Gray, H. (1918) Anatomy of the Human Body. Lea & Febiger: Philadelphia.

Griffiths, P. R. (1975) Chemical infrared Fourier transform spectroscopy. John Wiley and Sons: New York.

Griffiths, P. R., & Pariente, G. L. (1986) Introduction to spectral deconvolution. Trends Analyt Chem, 5, 209-215.

Griffiths, P. R., Sloane, H. J., & Hannah, R. W. (1977) Interferomenters vs. Monochromators: Separating the optical and digital advantages. Appl Spectrosc, 31, 485-495.

Grundman, M., & Delaney, P. (2002) Antioxidant strategies for Alzheimer's disease. Proc Nutr Soc, 61, 191-202.

Gutierrez-Ruiz. M. C., Robles-Diaz, G., & Kershenobich, D. (2002) Emerging concepts in inflammation and fibrosis. Arch Med Res, 33, 595-599.

Halverson, K., Fraser, P. E., Kirschner, D. A., & Lansbury, Jr., P. T. (1990) Molecular determinants of amyloid deposition in Alzheimer's disease: Conformational studies of synthetic β-protein fragments. Biochemistry, 29, 2639-2644.

Hardy, J., & Gwinn-Hardy, K. (1998) Genetic classification of primary neurodegenerative diseases. Science, 282, 1075-1079.

Hardy, J., & Selkoe, D. J. (2002) The amyloid hypothesis of Alzheimer's disease: progress and problems on the road to therapeutics. Science, 297, 353-356.

Harlow, E., & Lane, D. (1988) Antibodies: A laboratory manual. Cold Spring Harbor Laboratory: Cold Spring Harbor.

Harper, J. D., Wong, S. S., Lieber, C. M., & Lansbury, P. T. Jr. (1997) Observation of metastable Aβ amyloid protofibrils by atomic force microscopy. Chem Biol, 4, 119-125.

Hascall, V. C., & Kimura, J. H. (1982) Proteoglycans: Isolation and characterization. Meth Enzymol, 82, 769-800.

Hawkes, S., Maddams, W. F., Mead, W. L., & Southon, M. J. (1982) The measurement of derivative IR spectra - II. Experimental measurements. Spectrochim Acta A Mol Biomol Spectrosc, 38A, 445-457.

Hazard, R. G. (2006) Failed back surgery syndrome. Clin Orthop Relat Res, 443, 228-232.

He, Y., Revel, M., & Loty, B. (1995) A quantitative model of post-laminectomy scar formation: Effects of a nonsteroidal anti-inflammatory drug. Spine, 20, 557-563.

Hemmer, W., & Wallimann, T. (1993) Functional aspects of creatine kinase in brain. Dev Neurosci, 15, 249-260.

Herzberg, G. (1939) Molecular spectra and molecular structure: Diatomic molecules. Prentice-Hall: New York.

Herzberg, G. (1945) Molecular spectra and molecular structure: Infrared and raman spectra of polyatomic molecules. Van Nostrand: Princeton.

Hinton, J. L. Jr, Warejcka, D. J., Mei, Y., McLendon, R. E., Laurencin, C., Lucas, P. A., & Robinson, J. S. Jr (1995) Inhibition of epidural scar formation after laminectomy in the rat. Spine 20, 564-570.

Holman, H. N., Martin, M. C., Blakely, E. A., Bjornstad, K., Mckinney, W. R. (2000) IR spectroscopic characteristics of cell cycle and cell death probed by synchrotron radiation based fourier transform IR spectromicroscopy. Biopolymers, 57, 329-335.

Huang, W., Alexander, G. E., Chang, L., Shetty, H. U., Krasuski, J. S., Papoport, S. I., & Schapiro, M. B. (2001) Brain metabolite concentration and dementia severity in Alzheimer's disease: A ^{1}H MRS study. Neurology 57, 627-632.

Hyde, L. A., Kazdoba, T. M., Grilli, M., Lozza, G., Brussa, R., Zhang, Q., Wong, G. T., McCool, M. F., Zhang, L., Parker, E. M., & Higgins, G. A. (2005) Age-progressive cognitive impairments and neuropathology in transgenic CRND8 mice. Behav Brain Res, 160, 344-355.

Ikeda, M., Shoji, M., Kawarai, T., Kawarabayashi, T., Matsubara, E., Murakami, T., Sasaki, A., Tomidokoro, Y., Ikarashi, Y., Kuribara, H., Ishiguro, K., Hasegawa, M., Yen, S. H., Chishti, M. A., Harigaya, Y., Abe, K., Okamoto, K., St George-Hyslop, P., & Westaway, D. (2005) Accumulation of filamentous tau in the cerebral cortex of human tau R406W transgenic mice. Am J Pathol, 166, 521-531.

Inglesson, M., Fukumoto, H., Newell, K. L., Growdon, J. H., Hedley-Whyte, E. T., Frosch, M. P., Albert, M. S., Hyman, B. T., & Irizarry, M. C. (2004) Early Aβ accumulation and progressive synaptic loss, gliosis, and tangle formation in AD brain. Neurology, 62, 925-931.

Inoue, S., Kuroiwa, M., & Kisilevsky, R. (1999) Basement membranes, microfibrils and β amyloid fibrillogenesis in Alzheimer's disease: High resolution ultrastructural findings. Brain Res Rev, 29, 218-231.

Ipsiroglu, O. S., Stromberger, C., Ilas, J., Hoger, H., Muhl, A., & Stockler-Ipsiroglu, S. (2001) Changes in tissue creatine concentrations upon oral supplementation of creatine-monohydrate in various animal species. Life Sci, 69, 1805–1815.

Jackson Huang, T. H., Yang, D., Fraser, P. E., & Chakrabartty, A. (2000) Alternate aggregation pathways of the Alzheimer β- amyloid peptide: An *in vitro* model of preamyloid. J Biol Chem, 275, 36436-36440.

Jackson, M., Choo, L., Watson, P. H., Halliday, W. C., & Mantsch, H. H. (1995) Beware of connective tissue proteins: assignment and implications of collagen absorptions in infrared spectra of human tissues. Biochim Biophys Acta, 1270, 1-6.

Jakobsen, R. J., Brown, L. L., Hutson, T. B., Fink, D. J., & Veis, A. (1983) Intramolecular interactions in collagen self-assembly as revealed by Fourier transform infrared spectroscopy. Science, 220, 1288-1290.

Jamin, N., Dumas, P., Moncuit, J., Fridman, W., Teillaud, J., Carr, G. L. & Williams, G. P. (1998) Highly resolved chemical imaging of living cells by using synchrotron infrared microspectroscopy. Proc Natl Acad Sci USA, 95, 4837-4840.

Jamin, N., Miller, L., Moncuit, J., Firdman, W., Dumas, P. & Teillaud, J. (2003) Chemical heterogeneity in cell death: Combined synchrotron IR and fluorescence microscopy studies of single apoptotic and necrotic cells. Biopolymers, 72, 366-4373.

Janus, C., Pearson, J., McLaurin, J., Mathews, P. M., Jiang, Y., Schmidt, S.D., Chishti, M.A., Horne, P., Heslin, D., French, J., Mount, H. T. J., Nixon, R. A., Mercken, M., Bergeron, C., Fraser, P. E., St. George-Hyslop, P., & Westaway, D. (2000) Aβ peptide immunization reduces behavioral impairment and plaques in a model of Alzheimer's disease. Nature, 408, 979-982.

Juurlink, B. H. J. (2001) Therapeutic potential of dietary phase 2 enzyme inducers in ameliorating diseases that have an underlying inflammatory component. Can J Physiol Pharmacol, 79, 266-282.

Juurlink, B. H. J., & Paterson, P. G. (1998) Review of oxidative stress in brain and spinal cord: Suggestions for pharmacological and nutritional management strategies. J Spinal Cord Med, 21, 309-334.

Kacurakova, M., & Mathlouthi, M. (1996) FTIR and laser-Raman spectra of oligosaccharides in water: characterization of the glycosidic bond. Carbohydr Res, 284, 145-157.

Kalback, W., Watson, M. D., Kokjohn, T. A., Kuo, Y., Weiss, N., Luehrs, D. C., Lopez, J., Brune, D., Sisodia, S. S., Staufenbiel, M., Emmerling, M., & Roher, A. E. (2002) APP transgenic mice Tg2576 accumulate Aβ peptides that are distinct from the chemically modified and insoluble peptides deposited in Alzheimer's disease senile plaques. Biochemistry, 41, 922-928.

Kamenic, H., Griebel, R. W., Lyon, A. W., Paterson, P. G., & Juurlink, B. H. J. (2001) Promoting glutathione synthesis after spinal cord trauma decreases secondary damage and promotes retention of function. FASEB J, 15, 243-250.

Kauppinen, J. K., Moffatt, D. J., Mantsch, H. H., & Cameron, D. G. (1981) Fourier self-deconvolution: A method for resolving intrinsically overlapped bands. Appl Spectrosc, 35, 271-276.

Kidder, L. H., Kalasinsky, V. F., Luke, J. L., Levin, I. W., & Lewis, E. N. (1997) Visualization of silicone gel in human breast tissue using new infrared imaging spectroscopy. Nat Med, 3, 235-237.

Kim, K. S., Miller, D. L., Sapienza, V. J., Chen, C. J., Bai, C., Grundke-Iqbal, I., Currie, J. R., & Wisniewski, H. M. (1988) Production and characterization of monoclonal antibodies reactive to synthetic cerebrovascular amyloid peptide. Neurosci Res Commun, 2, 121-130.

Kirkitadze, M. D., Condron, M. M., & Teplow, D. B. (2001) Identification and characterization of key kinetic intermediates in amyloid β-protein fibrillogenesis. J Mol Biol, 312, 1103-1119.

Klein, W. L., Krafft, G. A., & Finch, C. E. (2001) Targeting small Aβ oligomers: the solution to an Alzheimer's disease conundrum? Trends Neurosci, 24, 219-224.

Klunk, W. E., Xu, C., Panchalingam, K., McClure, R. J., & Pettegrew, J. W. (1996) Qualitative ^{1}H and ^{31}P MRS of PCA extracts of postmortem Alzheimer's disease brain. Neurobiol Aging, 17, 349-357.

Kneipp, J., Beekes, M., Lasch, P. & Naumann, D. (2002) Molecular changes of preclinical scrapie can be detected by infrared spectroscopy. J Neurosci, 22, 2989-2997.

Kohler, A., Kirschner, C., Oust, A., & Martens, H. (2005) Extended multiplicative signal correction as a tool for separation and characterization of physical and chemical information in Fourier transform infrared microscopy images of cryo-sections of beef loin. Appl Spectrosc, 59, 707-716.

Krimm, S., & Bandekar, J. (1986) Vibrational spectroscopy and conformation of peptides, polypeptides and proteins. Adv Prot Chem, 36, 181-364.

Kumar, K., Hunter, G., & Demeria, D. D. (2002) Treatment of chronic pain by intrathecal drug therapy compared with conventional pain therapies: a cost-effectiveness analysis. J Neurosurg, 97, 803-810.

Kuo, Y., Kokjohn, T. A., Beach, T. G., Sue, L. I., Brune, D., Lopez, J. C., Kalback, W. M., Abramowski, D., Sturchler-Pierrat, C., Staufenbiel, M., & Roher, A. E. (2001) Comparative analysis of amyloid-β chemical structure and amyloid plaque morphology of transgenic mouse and Alzheimer's disease brains. J Biol Chem, 276, 12991-12998.

Lansbury, Jr., P. T. (1992) In pursuit of the molecular structure of amyloid plaque: New technology provides unexpected and critical information. Biochemistry, 31, 6865-6870.

Lansbury, Jr., P. T. (1999) Evolution of amyloid: What normal protein folding may tell us about fibrillogenesis and disease. Proc Natl Acad Sci USA, 96, 3342-3344.

Lasch, P., & Naumann, D. (1998) FT-IR microspectroscopic imaging of human carcinoma thin sections based on pattern recognition techniques. Cell Mol Biol, 44, 189-202.

Lasch, P., Haensch, W., Lewis, E. N., Kidder, L. H. & Naumann, D. (2002) Characterization of colorectal adenocarcinoma sections by spatially resolved FT-IR microspectroscopy. Appl Spectrosc, 56, 1-9.

Lasch, P., Haensch, W., Naumann, D., & Diem, M. (2004) Imaging of colorectal adenocarcinoma using FT-IR microspectroscopy and cluster analysis. Biochim Biophys Acta, 1688, 176-186.

Lazarev, Y. A., Grishkovsky, B. A., & Khromova, T. B. (1985) Amide I of IR spectrum and structure of collagen and related polypeptides. Biopolymers, 24, 1449-1478.

Lee, C., Weindruch, R., & Prolla, T. A. (2000) Gene-expression profile of the ageing brain in mice. Nature Genetics, 25, 294-297.

Lee, C.K., & Alexander, H. (1984) Prevention of postlaminectomy scar formation. Spine, 9, 305-312.

Lee, D. C., Haris, P. I., Chapman, D., & Mitchell, R. C. (1990) Determination of protein secondary structure using factor analysis of infrared spectra. Biochemsitry, 29, 9185-9193.

Lee, J., Stenzel, W., Ebel, H, Wedekind, C., Ernestus, R., & Klug, N. (2004) Mitomycin C in preventing spinal epidural fibrosis in a laminectomy model in rats. Spine, 100, 52-55.

Lehninger, A. L., Nelson, D. L., & Cox, M. M. (1993) Principles of biochemistry. Worth Publishers: New York.

Levy-Lahad, E., Wasco, W., Poorkaj, P., Romano, D. M., Oshima, J., Pettingell, W. H., Yu, C., Jondro, P. D., Schmidt, S. D., Wang, K., Crowley, A. C., Fu, Y., Guenette, S. Y., Galas, D., Nemens, E., Wijsman, E. M., Bird, T. D., Schellenberg, G. D., Tanzi, R. E. (1995) Candidate gene for the chromosome 1 familial Alzheimer's disease locus. Science, 269, 973-977.

Lewis, E. N., Treado, P. J., Reeder, R. C., Story, G. M., Dowrey, A. E., Marcott, C. & Levin, I. W. (1995) Fourier transform spectroscopic imaging using an infrared focal-plane array detector. Anal Chem, 67, 3377-3381.

Lewis, J., Dickson, D. W., Lin, W., Chisholm, L., Corral, A., Jones, G., Yen, S., Sahara, N., Skipper, L., Yager, D., Eckman, C., Hardy, J., Hutton, M., & McGowan, E. (2001) Enhanced neurofibrillary degeneration in transgenic mice expressing mutant tau and APP. Science, 293, 1487-1491.

Li, B. S. Y., Wang, H., & Gonen, O. (2003) Metabolite ratios to assumed stable creatine level may confound the quantification of proton brain MR spectroscopy. Magn Reson Imaging, 21, 923-928.

Lim, K. H., Collver, H. H., Le, Y. T. H., Nagchowdhuri, P., & Kenney, J. M. (2007) Characterization of distinct amyloidogenic conformations of the Aβ (1-40) and (1-42) peptides. Biochem Biophys Res Commun, 353, 443-449.

Linke, R. P. (2000) Highly sensitive diagnosis of amyloid and various amyloid syndromes using Congo red fluorescence. Virchows Arch, 436, 439-448.

Liquier, J., & Taillandier, E. (1996) Infrared spectroscopy of nucleic acids. In H. H., Mantsch & D. Chapman (Eds.) Infrared spectroscopy of biomolecules (131-158). New York: Wiley-Liss.

Litchfield, S., & Nagy, Z. (2001) New temperature modification makes the Bielschowsky silver stain reproducible. Acta Neuropathol, 101, 17-21.

Longas, M. O., & Garg, H. G. (1992) Sulfate composition of dermatan sulfate from scar tissue. Carbohydr Res, 237, 319-324.

Lorenzo, A. & Yankner, B. A. (1994) β-Amyloid neurotoxicity requires fibril formation and is inhibited by Congo red. Proc Natl Acad Sci USA, 91, 12243-12247.

Lowe, J., Mayer, J., Landon, M., & Layfield, R. (2001) Ubiquitin and the molecular pathology of neurodegenerative diseases. Adv Exp Med Biol, 487, 169-186.

Lucas, J. H., Wheeler, D. G., Emery, D. G., & Mallery, S. R. (1998) The endogenous antioxidant glutathione as a factor in the survival of physically injured mammalian spinal cord neurons. J Neuropathol Exp Neurol, 57, 937-954.

Lucas, S., Rothwell, N. J., & Gibson, R. M. (2006) The role of inflammation in CNS injury and disease. Br J Pharmacol, 147, S232-S240.

Lyoo, K., Kong, S. W., Sung, S. M., Hirashima, F., Parow, A., Hennen, J., Cohen, B. M., & Renshaw, P. F. (2003) Multinuclear magnetic resonance spectroscopy of high-energy phosphate metabolites in human brain following oral supplementation of creatine-monohydrate. Psychiatry Res: Neuroimaging, 123, 87-100.

Maddams, W. F., & Mead, W. L. (1982) The measurement of derivative IR spectra - I. Background studies. Spectrochim Acta A Mol Biomol Spectrosc, 38A, 437-444.

Maddams, W. F., & Southon, M. J. (1982) The measurement of derivative IR spectra - III. The effect of band width and band shape on resolution enhancement by derivative spectroscopy. Spectrochim Acta A Mol Biomol Spectrosc, 38A, 459-466.

Mantsch, H. H., & Chapman, D. (1996) Infrared spectroscopy of biomolecules. Wiley-Liss: New York.

Mark, R. J., Pang, Z., Geddes, J. W., Uchida, K., & Mattson, M. P. (1997) Amyloid β-peptide impairs glucose transport in hippocampal and cortical neurons: Involvement of membrane lipid peroxidation. J Neurosci , 17, 1046-1054.

Markesbery, W. R., & Carney, J. M. (1999) Oxidative alterations in Alzheimer's disease. Brain Pathol, 9, 133-146.

Martin, P., D'Souza, D., Martin, J., Grose, R., Cooper, L., Maki, R., & McKercher, S. R. (2003) Wound healing in the PU.1 null mouse - Tissue repair is not dependent on inflammatory cells. Curr Biol, 13, 1122-1128.

Martinon, F., & Glimcher, L. H. (2006) Gout: New insights into an old disease. J Clin Invest, 116, 2073-2075.

Masliah, E., Sisk, A., Mallory, M., Mucke, L., Schenk, D., & Games, D. (1996) Comparison of neurodegenerative pathology in transgenic mice overexpressing V717F beta-amyloid precursor protein and Alzheimer's disease. J Neurosci, 16, 5795-5811.

Masters, C. L., Simms, G., Weinman, N. A., Multhaup, G., & McDonald, B. L., Beyreuther K. (1985) Amyloid plaque core protein in Alzheimer disease and Down syndrome. Proc Natl Acad Sci USA, 82, 4245-4249.

Maury, C. P. J. (1995) Molecular pathogenesis of β-amyloidosis in Alzheimer's disease and other cerebral amyloidoses. Lab Invest, 72, 4-16.

McGowan, E., Pickford, F., Kim, J., Onstead, L., Eriksen, J., Yu, C., Skipper, L., Murphy, M. P., Beard, J., Das, P., Jansen, K., DeLucia, M., Lin, W., Dolios, G., Wang, R., Eckman, C. B., Dickson, D. W., Hutton, M., Hardy, J., & Golde, T. (2005) Aβ42 is essential for parenchymal and vascular amyloid deposition in mice. Neuron, 47, 191-199.

McHale, J. L. (1999) Molecular spectroscopy. Prentice Hall: Upper Saddle River.

McLaurin, J., & Chakrabartty, A. (1997) Characterization of the interactions of Alzheimer β-amyloid peptides with phospholipid membranes. Eur J Biochem, 245, 355-363.

Mendelsohn, R., Paschalis, E. P., & Boskey, A. L. (1999) Infrared spectroscopy, microscopy, and microscopic imaging of mineralizing tissues: Spectra-structure correlations from human iliac crest biopsies. J Biomed Opt, 4, 14-21.

Mendelsohn, R., Rerek, M., & Moore, D. (2000) Infrared spectroscopy and microscopic imaging of stratum corneum models and skin. Phys Chem Chem Phys, 2, 4651-4657.

Mesina, J. E., Page, R. H., Hetzel, F. W., Chopp, M. (1989) Administration of L-2-oxothiazolidine-4-carboxylate increases glutathione levels in rat brain. Brain Res, 478, 181-183.

Miller, E. J., & Gay, S. (1982) Collagen: An Overview. Meth Enzymol, 82, 3-32.

Miller, L. M., & Smith, R. J. (2005) Synchrotron versus globars, point-detectors versus focal plane arrays: Selecting the best source and detector for specific infrared microspectroscopy and imaging applications. Vib Spectrosc, 38, 237-240.

Miller, L. M., Wang, Q., Telivala, T. P., Smith, R. J., Lanzirotti, A., & Miklossy, J. (2006) Synchrotron-based infrared and X-ray imaging shows focalized accumulation of Cu and Zn co-localized with β-amyloid deposits in Alzheimer's disease. J Struct Biol, 155, 30-37.

Miyazawa, T., & Blout, E. R. (1961) The infrared spectra of polypeptides in various conformations: Amide I and II bands. J Am Chem Soc, 83, 712-719.

Mohlenhoff, B., Romeo, M., Diem, M., & Wood, B. R. (2005) Mie-type scattering and non-beer-lambert absorption behavior of human cells in infrared microspectroscopy. Biophys J, 88, 3635-3640.

Monaco, J. L. & Lawrence, W. T. (2003) Acute wound healing: An overview. Clin Plastic Surg. 20, 1-12.

Morris, J. H. (1997) Alzheimer's disease. In M. M. Esiri & J. H. Morris (Eds.) The neuropathology of dementia (70-121). Cambridge: Cambridge University Press.

Mudher, A. & Lovestone, S. (2002) Alzheimer's disease – do tauists and babtists finally shake hands? Trends Neurosci, 25, 22-26.

Munch, G., Schinzel, R., Loske, C., Wong, A., Durany, N., Li, J. J., Vlassara, H., Smith, M. A., Perry, G., & Riederer, P. (1998) Alzheimer's disease – synergistic effects of glucose deficit, oxidative stress and advanced glycation endproducts. J Neural Transm, 105, 439-461.

Myhrstad, M. C. W., Carlsen, H., Nordstrom, O., Blomhoff, R., & Moskaug, J. O. (2002) Flavanoids increase the intracellular glutathione level by transactivation of the γ-glutamylcysteine synthetase catalytical subunit promoter. Free Rad Biol Med, 32, 386-393.

Naumann, D. (2000) Infrared spectroscopy in microbiology. In R. A. Meyers (Ed.) Encyclopedia of analytical chemistry (102-131). Chichester: John Wiley & Sons.

Neuroinflammation Working Group (2000) Inflammation and Alzheimer's disease. Neurobiol Aging, 21, 383-421.

Ogg, M. T. J. (2002) Vibrational microspectroscopy of Alzheimer diseased hippocampal tissue. M. Sc. Thesis, University of Manitoba.

Ohtsuki, S., Tachikawa, M., Takanaga, H., Shimizu, H., Wanatabe, M., Hosoya, K., & Shimizu, H. (2002) The blood-brain barrier creatine transporter is a major pathway for supplying creatine to the brain. J Cereb Blood Flow Metab, 22, 1327-1335.

O'Leary, T. J., & Levin, I. W. (1985) Secondary structure of endocrine amyloid: infrared spectroscopy of medullary carcinoma of the thyroid. Lab Invest, 53, 240-242.

O'Leary, R., Wood, E. J., & Guillou, P. J. (2002) Pathological scarring: Strategic interventions. Eur J Surg, 168, 523-534.

Onesti, S. T. (2004) Failed back syndrome. Neurologist, 10, 259-264.

Park, J. E., & Barbul, A. (2004) Understanding the role of immune regulation in wound healing. Am J Surg, 187, 11S-16S.

Parker, F. S. (1983) Applications of infrared, Raman and resonance Raman spectroscopy in biochemistry. Plenum Press: New York.

Parnetti, L., Tarducci, R., Presciutti, O., Lowenthal, D. T., Pippi, M., Palumbo, B., Gobbi, G., Pelliccioli, G. P., & Senin, U. (1997) Proton magnetic resonance spectroscopy can differentiate Alzheimer's disease from normal aging. Mech Ageing Dev, 97, 9-14.

Paschalis, E. P., Verdelis, K., Doty, S. B., Boskey, A. L., Mendelsohn, R., & Yamauchi, M. (2001) Spectroscopic characterization of collagen cross-links in bone. J Bone Miner Res, 16, 1821-1828.

Payne, K. J., & Veis, A. (1988) Fourier transform IR spectroscopy of collagen and gelatin solutions: Deconvolution of the amide I band for conformational studies. Biopolymers, 27, 1749-1760.

Pearson, H. A., & Peers, C. (2006) Physiological roles for amyloid β peptides. J Physiol, 575, 5-10.

Petkova, A. T., Leapman, R. D., Guo, Z., Yau, W., Mattson, M. P., & Tycko, R. (2005) Self-propagating, molecular-level polymorphism in Alzheimer's β-amyloid fibrils. Science, 307, 262-265.

Pettegrew, J. W., Klunk, W. E., Panchalingam, K., McClure, R. J., & Stanley, J. A. (1997) Magnetic resonance spectroscopic changes in Alzheimer disease. Ann N Y Acad Sci, 826, 282-306.

Pettegrew, J. W., Panchalingam, K., Klunk, W. E., McLure, R. J., & Muenz, L. R. (1994) Alternations of cerebral metabolism in probable Alzheimer's disease: A preliminary study. Neurobiol Aging, 15, 117-132.

Pfefferbaum, A., Adalsteinsson, E., Spielman, D., Sullivan, E. V., & Lim, K. O. (1999) *In vivo* brain concentrations of N-acetyl compounds, creatine, and choline in Alzheimer disease. Arch Gen Psychiatry, 56, 185-192.

Phan, T., Lim, I., J., Chan, S., Tan, E., Lee, S., & Longaker. M. T. (2004) Suppression of transforming growth factor beta/Smad signaling in keloid-derived fibroblasts by quercetin: Implications for the treatment of excessive scars. J Trauma, 57, 1032-1037.

Phan, T., See, P., Tran, E., Nguyen, T. T. T., Chan, S. Y, Lee, S. T., & Huynh. H. (2003) Suppression of insulin-like growth factor signaling pathway and collagen expression in keloid-derived fibroblasts by quercetin: Its therapeutic potential use in the treatment and prevention of keloids. Br J Dermatol, 148, 544-552.

Phinney, A. L., Deller, T., Stalder, M., Calhoun, M. E., Frotscher, M., Sommer, B., Staufenbiel, M., & Jucker, M. (1999) Cerebral amyloid induces aberrant axonal sprouting and ectopic terminal formation in amyloid precursor protein transgenic mice. J Neurosci, 19, 8552-8559.

Phinney, A.L., Horne, P., Yang, J., Janus, C., Bergeron, C., & Westaway, D. (2003) Mouse models of Alzheimer's disease: The long and filamentous road. Neurol Res, 25, 590-600.

Pike, C. J., Walencewich-Wasserman, A. J., Kosmoski, J., Cribbs, D. H., Glabe, C. G., & Cotman, C. W. (1995) Structure-activity analyses of β-amyloid peptides: Contributions of the β25-35 region to aggregation and neurotoxicity. J Neurochem, 64, 253-265.

Puchtler, H., Sweat, F., & Levine, M. (1962) On the binding of Congo red by amyloid. J Histochem Cytochem, 10, 355-364.

Puchtler, H., Waldrop, F. S., & Meloan, S. N. (1985) A review of light, polarization and fluorescence microscopic methods for amyloid. Appl Pathol, 3, 5-17.

Redd, M. J., Cooper, L., Wood, W., Stramer, B., & Martin, P. (2004) Wound healing and inflammation: embryos reveal the way to perfect repair. Phil Trans R Soc Lond B, 359, 777-784.

Reffner, J. A. (1998) Instrumental factors in infrared microspectroscopy. Cell Mol Biol, 44, 1-7.

Reffner, J. A., & Martoglio, P. A. (1995) Uniting microscopy and spectroscopy. In H. J. Humecki (Ed.) Practical guide to infrared microspectroscopy (41-84). New York: Marcel Dekker, Inc.

Reginato, A. J., Falasca, G. F., & Usmani, Q. (1999) Do we really need to pay attention to the less common crystals? Curr Opin Rheumatol, 11, 446-452.

Robertson, J. T. (1996) Role of peridural fibrosis in the failed back: a review. Eur Spine J, 5(Suppl 1), S2-S5.

Rogaev, E. I., Sherrington, R., Rogaeva, E. A., Levesque, G., Ikeda, M., Liang, Y., Chi, H., Lin, C., Holman, K., Tsuda, T., Mar, L., Sorbi, S., Nacmias, B., Piacentini, S., Amaducci, L., Chumakov, I., Cohen, D., Lannfelt, L., Fraser, P. E., Rommens, J. M., & St George-Hyslop, P. H. (1995) Familial Alzheimer's disease in kindreds with missense mutations in a gene on chromosome 1 related to the Alzheimer's disease type 3 gene. Nature, 376, 775-778.

Rogaeva, E., Meng, Y., Lee, J. H., Gu, Y., Kawarai, T., Zou, F., Katayama, T., Baldwin, C. T., Cheng, R., Hasegawa, H., Chen, F., Shibata, N., Lunetta, K. L., Pardossi-Piquard, R., Bohm, C., Wakutani, Y., Cupples, L. A., Cuenco, K. T., Green, R. C., Pinessi, L., Rainero, I., Sorbi, S., Bruni, A., Duara, R., Friedland, R. P., Inzelberg, R., Hampe, W., Bujo, H., Song, Y. Q., Andersen, O. M., Willnow, T. E., Graff-Radford, N., Petersen, R. C., Dickson, D., Der, S. D., Fraser, P. E., Schmitt-Ulms, G., Younkin, S., Mayeux, R., Farrer, L. A., St George-Hyslop, P. (2007) The neuronal sortilin-related receptor SORL1 is genetically associated with Alzheimer disease. Nat Genet, 39, 168-177.

Romeo, M., & Diem, M (2005) Correction of dispersive line shape artifact observed in diffuse reflection infrared spectroscopy and absorption/reflection (transflection) infrared micro-spectroscopy. Vib Spectrosc, 38, 129-132.

Rose, S. E., de Zubicaray, G. I., Wang, D., Galloway, G. J., Chalk, J. B., Eagle, S. C., Semple, J., & Doddrell, D. M. (1999) A 1H MRS study of probable Alzheimer's disease and normal aging: Implications for longitudinal monitoring of dementia progression. Magn Reson Imaging, 17, 291-299.

Ross, J. S., Robertson, J. T., Frederickson, R. C. A., Petrie, J. L., Obuchowski, N., Modic, M. T., & deTribolet, N. (1996) Association between peridural scar and recurrent radicular pain after lumbar discectomy. Neurosurgery, 38, 855-861.

Samura, E., Shoji, M., Kawarabayashi, T., Sasaki, A., Matsubara, E., Murakami, T., Wuhua, X., Tamura, S., Ikeda, M., Ishiguro, K., Saido, T. C., Westaway, D., St George Hyslop, P., Harigaya, Y., & Abe, K. (2006) Enhanced accumulation of tau in doubly transgenic mice expressing mutant betaAPP and presenilin-1. Brain Res, 1094, 192-199.

Savitzky, A., & Golay, M. J. E. (1964) Smoothing and differentiation of data by simplified least squares procedures. Anal Chem, 1627-1639.

Schenk, D., Barbour, R., Dunn, W., Gordon, G., Grayed, H., Guide, T., Hun, K., Huang, J., Johnson-Wood, K., Khan, K., Kholodenko, D., Lee, M., Liam, Z., Lieberburg, I., Motter, R., Mutter, L., Soprano, F., Shop, G., Vasquez, N., Andover, C., Walker S., Moguls, M., Redneck, T., Games, D., & Seubert, P. (1999) Immunization with amyloid-β attenuates Alzheimer-disease-like pathology in the PDAPP mouse. Nature, 400, 173-177.

Scheuner, D., Eckman, C., Jensen, M., Song, X., Citron, M., Suzuki, N., Bird, T. D., Hardy, J., Hutton, M., Kukull, W., Larson, E., Levy-Lahad, E., Viitanen, M., Peskind, E., Poorkaj, P., Schellenberg, G., Tanzi, R., Wasco, W., Lannfelt, L., Selkoe, D., & Younkin, S. (1996) Secreted amyloid β-protein similar to that in the senile plaques of Alzheimer's disease is increased *in vivo* by the presenilin 1 and 2 and APP mutations linked to familiar Alzheimer's disease. Nat Med, 2, 864-870.

Schimizzi, A. L., Massie, J.B., Murphy, M., Perry, A., Kin, C. W., Garfin, S. R., & Akenson, W. H. (2006) High-molecular-weight hyaluronan inhibits macrophage proliferation and cytokine release in the early wound of a preclinical postlaminectomy rat model. Spine J, 6, 550-556.

Schirmer, T., & Auer, D. P. (2000) On the reliability of quantitative clinical magnetic resonance spectroscopy of the human brain. NMR Biomed, 13, 27-36.

Schlattner, U., Tokarska-Schlattner, M., & Wallimann, T. (2006) Mitochondrial creatine kinase in human health and disease. Biochim Biophys Acta, 1762, 164-180.

Schmitt, J., & Udelhoven, T. (2001) Use of artificial neural networks in biomedical diagnosis. In Gremlich, H., & Yan, B. (Eds.) Infrared and Raman spectroscopy of biological materials (378-419). New York: Marcel Dekker, Inc.

Schuff, N., Amend, D., Ezekiel, F., Steinman, S. K., Tanabe, J., Norman, D., Jagust, W., Kramer, J., Mastrianni, J. A., Fein, G., & Weiner, M. W. (1997) Changes of hippocampal N-acetyl aspartate and volume in Alzheimer's disease: A proton MR spectroscopic imaging and MRI study. Neurology, 49, 1513-1521.

Schuff, N., Capizzano, A. A., Du, A. T., Amend, D. L., O'Neil, J., Norman, D., Kramer, J., Jagust, W., Miller, B., Wolkowitz, O. M., Yaffe, K., & Weiner, M. W. (2002) Selective reduction of N-acetyl aspartate in medial temporal and parietal lobes in AD. Neurology, 58, 928-935.

Schuff, N., Ezekiel, F., Gamst, A. C., Amend, D. L., Capizzano, A. A., Maudsley, A. A., & Weiner, M. W. (2001) Region and tissue differences of metabolites in normally aged brain using multislice 1H magnetic resonance spectroscopic imaging. Magn Reson Med, 45, 899-907.

Schultke, E., Kendall, E., Kamenic, H., Ghong, Z., Grieble, R. W., & Juurlink, B. H. J. (2003) Quercetin promotes functional recovery following acute spinal cord injury. Journal of Neurotrauma, 20, 583-591.

Schulze, A. (2003) Creatine deficiency syndromes. Mol Cell Biol, 244, 143-150.

Seeds, W. E. (1953) Infra-red absorption and collagen structure. Nature and Structure of Collagen, Papers Presented for a Discussion, 250-252.

Selkoe, D. J. (2001) Alzheimer's disease: Genes, proteins and therapy. Physiol Rev, 81, 741-766.

Selkoe, D. J. (2003) Folding proteins in fatal ways. Nature, 426, 900–904.

Serpell, L. C. (2000) Alzheimer's amyloid fibrils: structure and assembly. Biochim Biophys Acta, 1502, 16-30.

Sherrington, R., Rogaev, E. I., Liang, Y., Rogaeva, E. A., Levesque, G., Ikeda M., Chi, H., Lin, C., Li, G., Holman, K., Tsuda, T., Mar, L., Foncin, J. F., Bruni, A. C., Montesi, M. P., Sorbi, S., Rainero, I., Pinessi, L., Nee, L., Chumakov, I., Pollen, D., Brookes, A., Sanseau P., Polinsky, R. J., Wasco, W., Da Silva, H. A. R., Haines, J. L., Pericak-Vance, M. A., Tanzi, R. E., Roses, A. D., Fraser, P. E., Rommens, J. M. & St George-Hyslop, P. H. (1995) Cloning of a gene bearing missense mutations in early-onset familial Alzheimer's disease. Nature, 375, 754-760.

Slipman, C. W., Shin, C. H., Patel, R. K., Isaak, Z., Huston, C. W., Lipetz, J. S., Lenrow, D. A., Braverman, D. L., & Vresilovic, E. J. (2002) Etiologies of failed back surgery syndrome. Pain Med, 3, 200-214.

Smith, C. D., Carney, J.M., Starke-Reed, P. E., Oliver, C. N., Stadtman, E. R., Floyd. R. A., & Markesbery, W. R. (1991) Excess brain protein oxidation and enzyme dysfunction in normal aging and Alzheimer's disease. Proc Natl Acad Sci USA, 88, 10540-10543.

Smith, G. D., & Palmer, R. A. (2002) Fast time-resolved mid-infrared spectroscopy using an interferometer. In J. M. Chalmers & P. R. Griffiths (Eds.) Handbook of vibrational spectroscopy (625-640). Chichester: John Wiley & Sons.

Smith, M. A., Drew, K. L., Numomura, A., Takeda, A., Hirai, K., Zhu, X., Atwood, C. S., Raina, A. K., Rottkamp, C. A., Sayre, L. M., Friedland, R. P., & Perry, G. (2002) Amyloid-β, tau alterations and mitochondrial dysfunction in Alzheimer disease: the chickens or the eggs. Neurochem Int, 40, 527-531.

Smith, T. I. (2002) The source issue in infrared microspectroscopy. Nucl Instrum Methods Phys Res A, 483, 565-570.

Snyder, R. G., & Schachtschneider, J. H. (1963) Vibrational analysis of the n-paraffins – I: Assignements of infrared bands in the spectra of C_3H_8 through n-$C_{19}H_{40}$. Spectrochimica Acta, 19, 85-116.

Songer, M. N., Rauschning, W., Carson, E, W., & Pandit, S. M. (1995) Analysis of peridural scar formation and its prevention after lumbar laminectomy and discectomy in dogs. Spine, 20, 571-580.

St. George-Hyslop, P. H. & Petit, A. (2005) Molecular biology and genetics of Alzheimer's disease. C. R. Biologies, 328, 119-130.

Stalder, M., Phinney, A., Probst, A., Sommer, B., Staufenbiel, M., & Jucker, M. (1999) Association of microglia with amyloid plaques in brains of APP23 transgenic mice. Am J Pathol, 154, 1673-1684.

Stampfer, M. J. (2006) Cardiovascular disease and Alzheimer's disease: common links. J Intern Med, 260, 211-223.

Stoppe, G., Bruhn, H., Pouwels, P. J. W., Hanicke, W., & Frahm, J. (2000) Alzheimer disease: Absolute quantification of cerebral metabolites *in vivo* using localized proton magnetic resonance spectroscopy. Alzheimer Dis Assoc Disord, 14, 112-119.

Streijger, F., Oerlemans, F., Ellenbroek, B. A., Jost, C. R., Wieringa, B., & Van der Zee, C. (2005) Structural and behavioral consequences of double deficiency for creatine kinases BCK and UbCKmit. Behav Brain Res, 157, 219-234.

Surewicz, W. K., Mantsch, H. H., & Chapman, D. (1993) Determination of protein secondary structure by Fourier transform infrared spectroscopy: A critical assessment. Biochemistry, 32, 389-394.

Susi, H., & Byler, D. M. (1983) Protein structure by Fourier transform infrared spectroscopy: Second derivative spectra. Biochem Biophys Res Commun, 115, 391-397.

Swerdlow, R. H., & Khan, S. M. (2004) A "mitochondrial cascade hypothesis" for sporadic Alzheimer's disease. Med Hypotheses, 63, 8-20.

Szumanska, G., Vorbrodt, A. W., Mandybur, T. I., & Wisniewski, H. M. (1987) Lectin histochemistry of plaques and tangles in Alzheimer's disease. Acta Neuropathol, 73, 1-11.

Taboada, P., Barbosa, S., Castro, E., Mosquera, V. (2006) Amyloid fibril formation and other aggregate species formed by human serum albumin association. J Phys Chem B, 110, 20733-20736.

Tachikawa, M., Fukaya, M., Terasaki, T., Ohtsuki, S., & Watanabe, M. (2004) Distinct cellular expression of creatine synthetic enzyme GAMT and creatine kinases uCK-Mi and CK-B suggest a novel neuron-glial relationship for brain energy homeostasis. Eur J Neurosci, 20, 144-160.

Tarnopolsky, M. A., & Beal, F. M. (2001) Potential for creatine and other therapies targeting cellular energy dysfunction in neurological disorders. Ann Neurol, 49, 561-574.

Terzi, E., Holzemann, G., & Seelig, J. (1994) Alzheimer β-amyloid peptide 25-35: Electrostatic interactions with phospholipid membranes. Biochem, 33, 7434-7441.

Terzi, E., Holzemann, G., & Seelig, J. (1999) Self-association of β-amyloid peptide (1-40) in solution and binding to lipid membranes. J Mol Biol, 252, 633-642.

Treuting, P.M., Hopkins, H. C., Ware, C. A., Rabinovitch, P. R., & Ladiges, W. C. (2002) Generation of genetically altered mouse models for aging studies. Exp Mol Pathol, 72, 49-55.

Turk, D., & Johnson, L. (2001) Methods in macromolecular crystallography. IOS Press: Amsterdam.

Tycko, R. (2003) Insights into the amyloid folding problem from solid-state NMR. Biochemistry, 42, 3151-3159.

Urbanc, B., Cruz, L, Le, R., Sanders, J., Ashe, K. H., Duff, K., Stanley, H. E., Irizarry, M. C., & Hyman, B. T. (2002) Neurotoxic effects of thioflavin S-positive amyloid deposits in transgenic mice and Alzheimer's disease. Proc Natl Acad Sci U S A, 99, 13990-13995.

Urenjak, J., Williams, S. R., Gadian, D. G., & Noble, M. (1993) Proton nuclear magnetic resonance spectroscopy unambiguously identified different neural cell types. J Neurosci, 13, 981–989.

Uversky, V.N., Talapatra, A., Gillespie, J. R., & Fink, A. L. (1999) Protein deposits as the molecular basis of amyloidosis. Part II. Localized amyloidosis and neurodegenerative diseases. Med Sci Monit, 5, 1238-1254.

Valensuela, M. J. & Sachdev, P. (2001) Magnetic resonance spectroscopy in Ad. Neurology, 56, 592-598.

Vallet, P. G., Guntern, R., Hof, P. R., Golaz, J., Delacourte, A., Robakis, N. K., & Bouras, C. (1992) A comparative study of histological and immunohistochemical methods for neurofibrillary tangles and senile plaques in Alzheimer's disease. Acta Neuropathol, 83, 170-178.

Van Groen, T., Liu, L., Ikonen, S., & Kadish, I. (2003) Diffuse amyloid deposition, but not plaque number, is reduced in amyloid precursor protein/presenilin 1 double-transgenic mice by pathway lesions. Neuroscience, 119, 1185–1197.

Varadarajan, S., Yanit, S., Aksenova, M., & Butterfield, A. D. (2000) Review: Alzheimer's amyloid β-peptide-associated free radical oxidative stress and neurotoxicity. J Struct Biol, 130, 184-208.

Varga, J., & Jimenez, S. A. (1995) Modulation of collagen gene expression: its relation to fibrosis in systemic sclerosis and other disorders. Ann Intern Med, 122, 60-62.

Vassar, R., & Citron, M. (2000) Aβ-Generating enzymes: Recent advances in β- and γ-secretase research. Neuron 27, 419-422.

Walsh D. M., Lomakin, A., Benedek, G. B., Condron, M. M., & Teplow, D. B. (1997) Amyloid β-protein fibrillogenesis: Detection of a protofibrillar intermediate. J Biol Chem, 272, 22364-22372.

Walsh, D. M., Hartley, D. M., Kusumoto, Y., Fezoui, Y., Condron, M. M., Lomakin, A., Benedek, G. B., Selkoe, D. J., & Teplow, D. B. (1999) Amyloid β-protein fibrillogenesis: Structure and biological activity of protofibrillar intermediates. J Biol Chem, 274, 25945-25952.

Wang, C., Wurtman, R. J., & Lee, R. K. K., (2000) Amyloid precursor protein and membrane phospholipids in primary cortical neurons increase with development, or after exposure to nerve growth factor or $A\beta_{1\text{-}40}$. Brain Res, 865, 157-167.

Waschuk, S. A., Elton, E. A., Darabie, A. A., Fraser, P. E., & McLaurin, J. (2001) Cellular membrane composition defines Aβ-lipid interactions. J Biol Chem, 276, 33561-22568.

Watson, D., Castano, E., Kokjohn, T. A., Kuo, Y., Lyubchenko, Y., Pinsky, D., Connolly, E. S., Esh, C., Luehrs, D. C., Stine, W. B., Rowse, L. M., Emmerling, Mark R., & Roher, A. E. (2005) Physicochemical characteristics of soluble oligomeric Aβ and their pathologic role in Alzheimer's disease. Neurol Res, 27, 869-881.

Watzel, B., Speer, O., Zanolla, E., Eriksson, O., Bernardi, P., & Wallimann, T. (2002) Novel mitochondrial creatine transport activity: Implications for intracellular creatine compartments and bioenergetics. J Biol Chem, 277, 37503-37511.

Wegiel, J., Bobinski, M., Tarnawski, M., Dziewiatkowski, J., Popovitch, E., Bobinski, M., Lach, B., Reisberg, B., Miller, D. C., de Santi, S., & de Leon, M. J. (2001) Shift from fibrillar to nonfibrillar Aβ deposits in the neocortex of subjects with Alzheimer disease. J Alzheimers Dis, 3, 49-57.

Wegiel, J., Wang, K., Imaki, H., Rubenstein, R., Wronska, A., Osuchoski, M., Lipinski, W. J., Walker, L. C., & LeVine, H. (2001b) The role of microglial cells and astrocytes in fibrillar plaque evolution in transgenic APPSW mice. Neurobiology of Aging, 22, 49-61.

Wendt, S., Dedeoglu, A., Speer, O., Wallimann, T., Beal, M. F., & Andreassen, O. A. (2002) Reduced creatine kinase activity in transgenic amyotrophic lateral sclerosis mice. Free Rad Biol Med, 32, 920-926.

Westermark, G. T., Johnson, K. H., & Westermark, P. (1999) Staining methods for identification of amyloid in tissue. Methods Enzymol, 309, 3-25.

Wetzel, D. L., & LeVine, S. M. (1993) *In situ* FT-IR microspectroscopy and mapping of normal brain tissue. Spectroscopy, 8, 40-45.

Wiedemann, H. (2003) Synchrotron radiation. Springer: Berlin.

Wiens R., Rak, M., Cox, N., Abraham, S., Juurlink, B. H., Kulyk, W. M., Gough, K. M. (2007) Synchrotron FTIR microspectroscopic analysis of the effects of anti-inflammatory therapeutics on wound healing in laminectomized rats. Anal Bioanal Chem.

Wilder, C. L., Friedrich, A. D., Potts, R. O., Daumy, G. O, & Francoeur, M. L. (1992) Secondary structural analysis of two recombinant murine proteins, inteleukins 1α and 1β: Is infrared spectroscopy sufficient to assign structure? Biochemistry, 31, 27-31.

Wilgus, T. A., Bergdall, V. K., Dipietro, L. A., & Oberyszyn, T. M. (2005) Hydrogen peroxide disrupts scarless fetal wound repair. Wound repair and regeneration. 13, 513-519.

Wirths, O., Multhaup, G., & Bayer, T. A. (2004) A modified β-amyloid hypothesis: Intraneuronal accumulation of the β-amyloid peptide - the first step of a fatal cascade. J Neurochem, 91, 513-520.

Wisniewski, H. M., Sadowski, M., Jakubowska-Sadowska, K., Tarnawski, M., & Wegiel, J. (1998) Diffuse, lake-like amyloid-β deposits in the parvopyramidal layer of the presubiculum in Alzheimer disease. J Neuropathol Exp Neurol, 57, 674-683.

Wong, C. P., Cai, H., Borchelt, D. R., & Price, D. L. (2002) Genetically engineered mouse models of neurodegenerative diseases. Nature Neurosci, 5, 633-639.

Woodhead-Galloway, J. (1980) Collagen: The anatomy of a protein. Camelot Press: Southampton.

Wyss, M., & Kaddurah-Daouk, R. (2000) Creatine and creatinine metabolism. Physiol Rev, 80, 1107-1213.

Wyss, M., & Schulze, A. (2002) Health implications of creatine: Can oral creatine supplementation protect against neurological and atherosclerotic disease? Neuroscience, 112, 243-260.

Yamaguchi, H., Hirai, S., Morimatsu, M., Shoji, M., & Nakazato, Y. (1989) Diffuse type of senile plaques in the cerebellum of Alzheimer-type dementia demonstrated by β protein immunostain. Acta Neuropathol, 77, 314-319.

Yamaguchi, H., Maat-Schieman, M. L. C., van Duinen, S. G., Prins, F. A., Neeskens, P., Natte, R., & Roos, R. A. C. (2000) Amyloid β protein (Aβ) starts to deposit as plasma membrane-bound form in diffuse plaques of brains from hereditary cerebral hemorrhage with amyloidosis-Dutch type, Alzheimer disease and nondemented aged subjects. J Neuropathol Exp Neurol, 59, 723-732.

Yan, Y., & Wang, C. (2006) Aβ42 is more rigid than Aβ40 at the C terminus: Implications for Aβ aggregation and toxicity. J Mol Biol, 364, 853-862.

Zandemeneghi, G., Krebs, M. R. H., McCammon, M. G., & Fandrich, M. (2004) FTIR reveals structural differences between native β-sheet proteins and amyloid fibrils. Protein Sci, 13, 3314-3321.